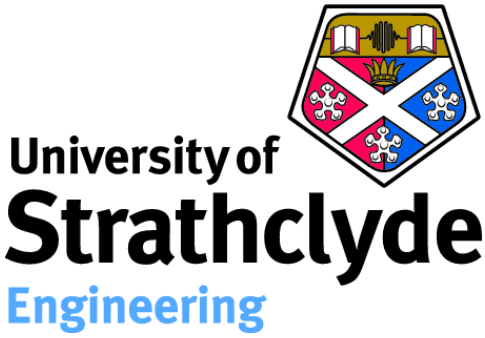
UNIVERSITY OF STRATHCLYDE



DOCTORAL THESIS

A nonlocal thermodynamic framework for mass transfer and phase separation in antisolvent crystallisation

Author:
Irene MORENO FLORES

Academic supervisors:
Dr Javier CARDONA
Dr Leo LUE

A thesis submitted in fulfilment of the requirements for the degree of Doctor of Philosophy

in the

Department of Chemical and Process Engineering

31st July, 2026

Declaration of Authorship

This thesis is the result of the author's original research. It has been composed by the author and has not been previously submitted for examination which has led to the award of a degree.

The copyright of this thesis belongs to the author under the terms of the United Kingdom Copyright Acts as qualified by University of Strathclyde Regulation 3.50. Due acknowledgement must always be made of the use of any material contained in, or derived from, this thesis.

Signed: Irene Moreno Flores

Date: 31/07/2026

Inspiration exists, but it has to find you working.

— PABLO PICASSO

Scientia non quiescit

— AUTHOR'S MOTTO

Acknowledgements

For someone who loves writing, I find that words elude me now that it is time to capture the depth of the gratitude I feel towards the people who helped me along this journey. I hope these words, however imperfect or corny, convey what I know to be true with complete certainty: the doctorate, the thesis, the growth—I owe all of it to you and your support.

I would like to thank my academic supervisors, Dr Javier Cardona Amengual and Dr Leo Lue. To both of you: your door was always open, your expertise, time—and patience—doled out freely. Whatever I have accomplished in this process, it is because of you. Javier, thank you for being my mentor all these years, for supporting me through every curveball and encouraging every side project along the way. Leo, your enthusiasm and dedication gave me the inspiration I needed to complete this work. Thank you for stepping in with such generosity this past year.

I would also like to thank the supervisors of my industrial placement, Dr Massimiliano Mari, Dr Edoardo Mariani and Mr Alessandro Falchi, for their mentorship and guidance throughout my time in Chiesi. Thank you to the rest of my team for the warm welcoming and coffee chats. Bea, Tommaso, Xime, thank you for showing me Parma and making my time there so enjoyable.

I would also like to thank the Department of Chemical and Process Engineering and CMAC for funding my PhD, for helping me navigate life abroad and providing me with a great environment to complete my studies in. Thank you to my supervisors in the Thermal Lance research project, Dr Leo Lue and Dr Jun Li, for their patience and understanding. I have truly enjoyed working with you this past year.

To my research group, thank you for the advice over every talk, poster or report. Chris, David, thank you for your mentorship, guidance and encouragement. Gabriel, thank you for your positivity and encouragement this past few months.

A huge thanks to all my friends, who have celebrated with me every small win and supported me through every hiccup. Alina, thank you for the many adventures, crash-out sessions and dry humour. Farha, Sahil, thank you for the advice, support, the long evening chats over chai and all the memories. Shiva, Samuel, you made the days feel lighter and brighter; thank you for everything. Mais, thank you for your help, kindness and particular brand of funny. Suruthi, thank you for inspiring me to do the work and love it. Samira, Musab, Lujain, Shaan, Sara, and the rest of the department, thank you. Mónica, Lucía, gracias por traerme la tierra a Glasgow durante los meses mas difíciles de este doctorado. Darrell, desde el primer día. Saray, gracias por todas las charlas, apoyo y aventuras.

A toda mi familia, muchas gracias por vuestro apoyo y aliento durante todos estos años. Os quiero mucho. Mamá, Papá, Sergio, sin vosotros no habría llegado hasta aquí. Papá, gracias por empujarme a empezar este doctorado, que me ha hecho descubrir que me encanta la investigación. Yaya, Pepi, Abuela, gracias por pensar en mí siempre. Yayo, te quiero muchísimo. Sudha and Haresh, thank you so much for welcoming me into your home and helping me during the last stage of this PhD.

And, finally, to my partner, Keshav, who has listened to me talk—and complain—about my research for five years, and convinced me to get up and try again more times than I can count.

Contents

Declaration of Authorship iii

Acknowledgements vii

Contents ix

List of Figures xii

List of Tables xxvi

List of Abbreviations xxix

Abstract xxxi

1 Introduction 1

1.1 Thesis aim and objectives . . . 3
1.2 Thesis contributions . . . 4
1.3 Thesis outline . . . 5

2 Background 7

2.1 Crystallisation fundamentals . . . 7
2.1.1 The crystal formation process . . . 7
2.1.2 Overview of the main crystallisation methods . . . 9
2.1.3 General process configurations . . . 11
2.1.4 Ethos: Quality by Digital Design . . . 12
2.2 Challenges within antisolvent crystallisation . . . 13
2.3 Modelling mixing in antisolvent crystallisation . . . 15
2.4 Phase-field models: bases and application . . . 19

3 Diffusion and phase behaviour in binary systems: the effect of a non-local contribution to the chemical potential 23

3.1 Introduction . . . 23
3.2 Theoretical background . . . 25
3.2.1 The driving force for mass transfer . . . 25
3.2.2 General thermodynamic framework . . . 26
3.2.3 Diffusion dynamics . . . 40
3.3 Simulation methodology . . . 41

3.4 Results and discussion . . . 44
3.4.1 Definition of the gradient coefficient . . . 45
3.4.2 Differences between mass transfer models . . . 49
3.4.3 Effect of the interfacial free energy on mixed and demixed systems . . . 51
3.4.4 Phase behaviour under crash-cooling conditions . . . 53
3.5 Conclusions . . . 56

4 Diffusion and phase behaviour in antisolvent crystallisation 59
4.1 Introduction . . . 59
4.2 Theoretical background . . . 61
4.2.1 General thermodynamic framework . . . 62
4.2.2 Diffusion dynamics . . . 70
4.3 Methodology . . . 71
4.3.1 Selection of initial conditions . . . 72
4.3.2 Computational details . . . 75
4.4 Results and discussion . . . 77
4.4.1 Phase behaviour under different regions of the diagram . . . 78
4.4.2 Diffusion and equilibrium across the miscibility gap . . . 88
4.4.3 Study on the effect of different antisolvents . . . 91
4.5 Conclusions . . . 98

5 Generating diffusive mixing fingerprints via Raman microscopy 101
5.1 Introduction . . . 102
5.2 Materials and methods . . . 103
5.2.1 Materials . . . 104
5.2.2 Raman spectroscopy: working principle . . . 104
5.2.3 Experimental setup . . . 105
5.2.4 Experimental procedure . . . 106
5.2.5 Raman spectra preprocessing . . . 108
5.2.6 Transforming spectra into compositions . . . 113
5.2.7 Extraction of mass transfer model parameters . . . 116
5.3 Experimental results . . . 121
5.3.1 Optical microscopy . . . 121
5.3.2 Raman microscopy . . . 122
5.4 Computational results . . . 135
5.4.1 Experimental vs simulated maps . . . 135
5.4.2 Comparison with literature diffusion coefficients . . . 139
5.4.3 Velocity scaling . . . 141
5.5 Conclusions . . . 142

6 Conclusions and future work **143**
6.1 Conclusions . . . 143
6.2 Future work . . . 145
6.2.1 General model development . . . 145
6.2.2 Development of a ternary model . . . 146
6.2.3 Leveraging microfluidics and Raman microscopy to isolate diffusion . . . 146

Bibliography **149**

Appendices **164**

A The fundamental diffusion models **165**
A.1 Fick's law of binary diffusion . . . 167
A.2 Fick's second law of diffusion . . . 167
A.3 Maxwell-Stefan model . . . 168

B Formulation of the nondimensional Helmholtz free energy density **173**

C Interfacial tension in one-dimensional multicomponent systems **177**

D Supplementary material on the experimental microfluidic platform **181**

E Building the ternary diagram **185**
E.1 Binodal curve and tie lines . . . 186
E.2 Spinodal curve . . . 187
E.3 Solubility curve . . . 188

F Supplementary material on the ternary mass transfer model development **189**
F.1 Towards defining the correct chemical potential . . . 189
F.2 Additional results . . . 193

List of Figures

1.1 Depiction of the potential effect of different mass transfer pathways across the ternary phase diagram. L-L stands for liquid-liquid; S-L, for solid-liquid; and AS, for antisolvent. Commonly, mixing models assume ideality, and thus, a straight pathway between streams (green line) predicting no breach into the binodal/spinodal regions. Non-idealities in the system can lead to different evolutions (red and blue lines), which could result in unwanted properties within the crystal product. 2

2.1 Generic solubility curve and metastable zone representation for a solute in a certain solvent. A typical cooling crystallisation process would follow the points (1)-(2)-(4). The difference in concentration between (2) and (3) is the supersaturation. 8

2.2 Diagram of the mechanisms that occur during a crystallisation process. Adapted from [28]. 8

2.3 Examples of oiling out in a binary salicylic acid–n-heptane system, at subsequent times (a)–(c). Images collected by Dr Thomas Pickles as part of the CMAC DataFactory [67, 68]. 14

2.4 Diagram illustrating the different scales within a crystalliser unit. 15

3.1 Free energy landscape under different values of A. (a) Free energy density evolution with x_A, where $\tilde{f} = (f - \sum_i c_i \beta \mu_i^\circ - \beta p_0)/c$. (b) Phase diagram showing the critical point and the binodal and spinodal regions, shaded in light and dark blue, respectively, with the first conforming the boundaries of the miscibility gap. (c) Free energy density for $A = 3$, marking the chemical potentials of the pure components, the equilibrium compositions and common tangent, and the spinodal points. Note that the critical points of this case have been translated onto the phase diagram in (b). 29

3.2 Diagram of potential system configurations after undergoing phase separation. Note that, if the gradient term is not incorporated into the free energy functional, both of these configurations are equally probable. 30

3.3 Diagram of the heterogeneous system in equilibrium. The continuous black line depicts its concentration profile, whereas the dashed lines correspond with the concentration of the individual, unconnected bulk phases: c^I and c^{II}. The location of the interface, z_G, is chosen so that the shaded grey and striped areas are equal in magnitude but of opposite sign. 36

3.4 Evolution of the non-dimensional interfacial tension with respect to (a) the non-dimensional interfacial free energy coefficient $\tilde{\kappa}$, with a fixed $A = 3$, and (b) with respect to the Margules parameter A, with a fixed $\tilde{\kappa} = 0.2$. 37
3.5 Equilibrium composition profiles at different conditions (solid lines) and their respective bulk equilibrium compositions (dashed lines). (a) Equilibrium behaviour at $A = 2.5$ and different values of $\tilde{\kappa}$. (b) Equilibrium behaviour for $\tilde{\kappa} = 0.2$ and different values of the Margules parameter. 38
3.6 Schematic diagram of the discretised 1D system. 42
3.7 Diagram of the two different initial conditions employed within this work. (a) Step-like, aiming to reproduce two streams put in contact with each other. (b) Gaussian noise, randomly sampled from a distribution with $\overline{x}_1 = 0.35$ and $\sigma^2 = 10^{-4}$. 42
3.8 Evolution with time of the mole fraction and chemical potential profile of species 1, for three different definitions of κ: (I) constant, (II) $\kappa \propto c^{-3}$ and (III) $\kappa \propto c^{-5}$. Note that these three definitions yield the same nondimensional mass transfer equation, and thus the diffusion dynamics presented in the mole fraction profiles are the same in all three cases. The value of the nondimensional gradient energy parameter used in the equation dynamics was kept at 0.2, and two values of A have been evaluated: $A = 1$ (a, c) and $A = 3$ (b, d). The dashed lines in (d) correspond with the coexistence compositions. The equilibrium composition profile has been considered to be the last saved value of each simulation. In (a), the equilibrium chemical potential profiles overlap. 47
3.9 Mass transfer performance for Fickian ($A = 0$, $\tilde{\kappa} = 0$), Maxwell-Stefan ($A = 1$, $\tilde{\kappa} = 0$), and CaHiMaS ($A = 1$, $\tilde{\kappa} = 0.2$) diffusion. (a) Evolution with time of the mole fraction at two points in the system, located at $z = 2.25$ (bottom) and 3.75 (top). (b) Chemical potential profiles across the system throughout the simulation, where the equilibrium composition profile has been considered to be the last saved value of each simulation. Note that the Maxwell-Stefan and CaHiMaS equilibrium chemical potential profiles overlap, since there is no gradient contribution when the composition profile is flat. 50
3.10 Mass transfer performance for an ideal system ($A = 0$) combined with different magnitudes of the interfacial free energy coefficient. (a) Evolution with time of the mole fraction for two points symmetric with respect to the original interface, and located at $z = 2.5|3.5$, $2|4$ and $0.1|5.9$. In all cases, the first number corresponds to the bottom trend, and the second, to the top. (b) Chemical potential profiles across the system throughout the simulation, where the equilibrium composition profile has been considered to be the last saved value of each simulation. Note that the equilibrium chemical potential profiles for all $\tilde{\kappa}$ overlap, in this case because there is no gradient contribution when the composition profile is flat. 51

3.11 Mass transfer performance for a system undergoing phase separation ($A = 3$) combined with different magnitudes of the interfacial free energy coefficient. (a) Evolution with time of the mole fraction at several points, located at $z = 0.1$, 2.0 and 2.5. (b) Chemical potential profiles across the system throughout the simulation, where the equilibrium composition profile has been considered to be the last saved value of each simulation. Note that the equilibrium chemical potential profiles for all $\tilde{\kappa}$ overlap. 52

3.12 Crash-cooling of a binary system, modelled with $A = 3$ and $\tilde{\kappa} = 0.025$ for (a), (c), (e) and (f), and with $\tilde{\kappa} = 0.2$ for (b) and (d). (a-b) Mole fraction evolution with time; same colorbar applies to both cases. The grey dashed lines correspond with the coexistence compositions for the studied conditions. (c-d) Chemical potential profile evolution with time; same colorbar applies to both cases. (e-f) Cmposition and chemical potential profiles, respectively, for selected times showing phase coalescence, within the $\tilde{\kappa} = 0.025$ study. Same colorbar applies to both cases. 54

3.13 Free energy evolution in the crash-cooling of a binary system, modelled with $A = 3$ and $\tilde{\kappa} = 0.025$ and 0.2 for (a) and (b), respectively. Both the total free energy and the individual contribution of the ideal, non-ideal (Margules) and interfacial (gradient) terms are included. They have each been scaled by deducting their value in equilibrium, taken to be that at the end of the simulation. 55

4.1 Local nondimensional free energy density contributions, where $\tilde{f} = f/c = \sum_{i=0}^{2} x_i \ln x_i + A x_1 x_0$. (a) Free energy landscape across the ternary diagram for a system with $A = 3$ (non-ideality in the API-antisolvent pair) and ideal interactions between API-solvent and solvent-antisolvent. The continuous and dashed black lines correspond with the binodal and spinodal curves, respectively; the black circle marks the critical point. (b) Nondimensional free energy density for all binary pairs within the system; the profiles correspond to those found along the triangle axes in (a). 64

4.2 Effect of A and of the solubility parameter $\beta\mu_1^{\circ,(S)} - \beta\mu_1^{\circ,(L)}$ on the shape of the miscibility gap, affected only by the former, and the solubility curve, affected by both. 65

4.3 Projection on the ternary diagram of the initial conditions studied on the first (a) and second (b) subset of results, which respectively correspond with a study of mass transfer and phase behaviour under different regions of the ternary diagram, and with a study of mass transfer across the miscibility gap. These initial conditions are step-like, and the points located in the API-S and S-AS axis indicate the compositions of the two streams being put in contact. The same colors belong to the same experiment. Moreover, these two compositions are joint by a dashed line that indicates the pathway that a linear mass transfer process would follow. The white circle located on each respective line indicates the mixing point between the two streams, would the system evolve towards a homogeneous final state. 74

4.4 Adaptive time-stepping algorithm and tolerance thresholds for the ternary simulations. 76

4.5 Evolution of the composition with time in a system mixing pure antisolvent with a 25% API solution, considering that $A = 3$ and $\beta\mu_1^{\circ,(S)} - \beta\mu_1^{\circ,(L)} = -1$. The gradient coefficient values are (a, c, e) $\tilde{\kappa}_{aa} = \tilde{\kappa}_{bb} = \tilde{\kappa}_{ab} = 0$ and (b, d, f) $(\tilde{\kappa}_{aa}, \tilde{\kappa}_{ab}, \tilde{\kappa}_{bb}) = (0.05, 0.016, 0.05)$. In particular, the compositional pathways through the ternary diagram are depicted in (a-d), with (a, b) presenting a subset of times, as per the legend, and (c, d) showcasing the the entire evolutions. In them, the solid blue line corresponds with the solubility curve, and the dotted line joins the two initial compositions, marked by a white circle. The last recorded profile for the system has been plotted in white. Lastly, (e, f) present the spatial composition profiles at the same times showcased in (a, b), in this case indicated by the coloured legend. 79

4.6 Chemical potential and diffusive flux exploration in a system mixing pure antisolvent with a 25% API solution, and considering that $\tilde{\kappa}_{aa} = \tilde{\kappa}_{bb} = \tilde{\kappa}_{ab} = 0$, $A = 3$ and $\beta\mu_1^{\circ,(S)} - \beta\mu_1^{\circ,(L)} = -1$. (a) Evolution of the chemical potential profiles with the times reported in the legend. (b) Chemical potential, mole fraction and diffusive flux of API for two consecutive saved iterations. 81

4.7 Evolution of the supersaturation profiles across the entire time range within a system of two mixing streams, one of pure antisolvent and another formed by 25% of API and 75% of solvent. It is considered that $A = 3$ and $\beta\mu_1^{\circ,(S)} - \beta\mu_1^{\circ,(L)} = -1$. Two subsets of the interfacial free energy coefficient are presented: (a) $\tilde{\kappa}_{aa} = \tilde{\kappa}_{bb} = \tilde{\kappa}_{ab} = 0$, and (b) $(\tilde{\kappa}_{aa}, \tilde{\kappa}_{ab}, \tilde{\kappa}_{bb}) = (0.05, 0.016, 0.05)$. 82

4.8 Evolution of the composition with time in a system mixing pure antisolvent with a 45% API solution, considering that $A = 3$ and $\beta\mu_1^{\circ,(S)} - \beta\mu_1^{\circ,(L)} = -1$. The gradient coefficient values are (a, c) $(\tilde{\kappa}_{aa}, \tilde{\kappa}_{ab}, \tilde{\kappa}_{bb}) = (0.025, 0.008, 0.025)$ and (b, d) $(\tilde{\kappa}_{aa}, \tilde{\kappa}_{ab}, \tilde{\kappa}_{bb}) = (0.1, 0.032, 0.1)$. In particular, (a, b) depict the compositional pathways through the ternary diagram. The blue line in them is the solubility curve, and the dotted line joins the two initial compositions, marked by a white circle. To ease visualisation, the last recorded profile has been plotted in white. (c, d) present the spatial composition profiles at the times indicated by the coloured legend. 83

4.9 Mass transfer evolution across the ternary phase diagram (a) and as composition profiles (b) within a system of two mixing streams, one of pure antisolvent and another formed by 55% of API and 45% of solvent. It is considered that $A = 3$ and $\beta\mu_1^{\circ,(S)} - \beta\mu_1^{\circ,(L)} = -1$. The interfacial free energy coefficients are set to $(\tilde{\kappa}_{aa}, \tilde{\kappa}_{ab}, \tilde{\kappa}_{bb}) = (0.025, 0.008, 0.025)$. (a) The solid blue line corresponds with the solubility curve, and the dotted line joins the two initial compositions, which have been marked by a white circle. The last recorded profile for the system has also been plotted as a series of white markers. (b) The coloured legend corresponds with the presented times, which are shown for all three species. . . 85

4.10 Mass transfer evolution across the ternary phase diagram within a system of two mixing streams, one formed by 45% of API and 55% of solvent, and the other, by 80% antisolvent and 20% solvent. It is considered that $A = 3$ and $\beta\mu_1^{\circ,(S)} - \beta\mu_1^{\circ,(L)} = -1$. The interfacial free energy coefficients are $(\tilde{\kappa}_{aa}, \tilde{\kappa}_{ab}, \tilde{\kappa}_{bb}) = (0.025, 0.008, 0.025)$. (a) Composition evolution throughout the ternary phase diagram. The solid blue line corresponds with the solubility curve, and the dotted line joins the two initial compositions, which have been marked by a white circle. The last recorded profile for the system has also been plotted as a series of white markers. (b) Composition profiles of the three species at selected times. Note that the times have been represented through colours of increasing intensity, and they are the same for all three species. 87

4.11 Summary of system evolution during diffusion for initial conditions positioned across the miscibility gap and parallel to tie lines; 10, 20 and 30% initial solvent composition in both streams were considered. The degree of non-ideality between API and antisolvent was fixed at $A = 3$; $\beta\mu_1^{\circ,(S)} - \beta\mu_1^{\circ,(L)} = -1$; and the interfacial free energy coefficients were $(\tilde{\kappa}_{aa}, \tilde{\kappa}_{ab}, \tilde{\kappa}_{bb}) = (0.025, 0.008, 0.025)$. (a) Mass transfer pathways across the ternary diagram, with the last recorded profile plotted as a series of white markers. (b) Subset of times, from $\tilde{t} = 1$–5, for the $x_S = 30\%$ case. (c) Composition profiles at selected times for the $x_S = 30\%$ case. The times have been represented through colours of increasing intensity, and they are the same for all three species. (d) Total unscaled nondimensional free energy in all three systems with time. 89

4.12 Free energy landscape of a system in which $A = 3$ and $\beta\mu_1^{\circ,(S)} - \beta\mu_1^{\circ,(L)} = -1$, without considering the gradient term. (a) Unscaled free energy across the ternary phase diagram. (b) Unscaled free energy profiles for the three fixed solvent contents explored in this study: 10, 20 and 30%. 90
4.13 Evolution of the composition and supersaturation with time in a system mixing a stream of pure antisolvent with a 25% API solution. The Margules parameter between API and AS was fixed at $A = 3$; $\beta\mu_1^{\circ,(S)} - \beta\mu_1^{\circ,(L)} = -1$; and the interfacial free energy coefficients, at $(\tilde{\kappa}_{aa}, \tilde{\kappa}_{ab}, \tilde{\kappa}_{bb}) = (0.025, 0.008, 0.025)$. (a, b) Composition trajectories across the ternary phase diagram for $\widetilde{D}_{10} = 0.1$ and 0.5, respectively. Note that the last profile was plotted in white to aid its visualisation. (c, d) Comparison of their spatial composition and supersaturation profiles, respectively. (e, f) Trajectories across the ternary phase diagram for $\tilde{t} = 0.0016$–0.1, for $\widetilde{D}_{10} = 0.1$ and 0.5, respectively. 93
4.14 Evolution of the composition and supersaturation with time in a system mixing a stream of pure antisolvent with a 25% API solution. The diffusion coefficients were fixed at $(\widetilde{D}_{10}, \widetilde{D}_{20}, \widetilde{D}_{12}) = (0.1, 0.1, 1)$. The Margules parameter between API and AS was fixed at $A = 3$; $\beta\mu_1^{\circ,(S)} - \beta\mu_1^{\circ,(L)} = -1$; and the interfacial free energy coefficients, at $(\tilde{\kappa}_{aa}, \tilde{\kappa}_{ab}, \tilde{\kappa}_{bb}) = (0.025, 0.008, 0.025)$. (a, b) Composition pathways throughout the ternary diagram. (a) The last composition profile has been plotted in white, to aid in its visualisation. (b) comprises a smaller subset of times to help in their visualisation. (c) Spatial supersaturation profiles. Note that the profiles of the $(\widetilde{D}_{10}, \widetilde{D}_{20}, \widetilde{D}_{12}) = (0.5, 1, 1)$ case were included for comparison purposes. 94
4.15 Evolution of the composition and supersaturation with time in a system mixing pure antisolvent with a 25% API solution, considering that $A = 3.75$, $\beta\mu_1^{\circ,(S)} - \beta\mu_1^{\circ,(L)} = -1$, and that the interfacial free energy coefficients had values of $(\tilde{\kappa}_{aa}, \tilde{\kappa}_{ab}, \tilde{\kappa}_{bb}) = (0.025, 0.008, 0.025)$. (a, b) Evolution across the entire simulation time and from $\tilde{t} = 4$–200, respectively, across the ternary phase diagram. (c, d) Selected spatial mole fraction and supersaturation profiles, respectively, throughout the entire simulation time. Note that in these, the solid lines correspond with the evolutions of the same system but considering $A = 3$, included for comparison purposes. 96

5.1 Diagram summarising the experimental and in-silico methodology built to extract the value of the benchmark parameters in a mass transfer model. The spectral maps collected via Raman microscopy are translated into composition maps using a PLS model. In turn, these are used as the ground truth for an optimisation loop to parameterise the models. 101
5.2 Energy diagrams depicting the different types of scattering present when performing Raman spectroscopy. 104
5.3 Y-junction microfluidic chip from Dolomite Microfluidics, fabricated with hydrophilic glass. Taken from [169]. 105

5.4 Experimental setup used for the collection of the microfluidic maps. The different pieces are labelled as follows: (A) and (B) conform the syringe pump, with (A) being the remote control unit and (B) the pushing block; (C) microfluidic syringe; (D) inlet tubing; (E) 4-way linear connector; (F) microfluidic chip; (G) 3D printed plastic support; (H) H interface; (I) outlet tubing; and (J) waste disposal. 106
5.5 Experimental setup used for the collection of the microfluidic mixing maps (not to scale). (a) Two syringes pumping the different solvents into a microfluidic channel, where their mixing is mapped by collecting Raman measurements in columns along this channel. (b) Depiction of the meaning given to the terms "columns" and "measurements along the channel" in this work; the columns also correspond with the channel height. (c) Channel cross-sectional profile adapted from the manual, depicting the meaning given to depth, also called z measurements, in this work. 106
5.6 Diagram of the experimental procedure followed during the collection of the Raman microscopy maps. There were 11 columns collected in each system, and thus the last block was repeated 11 times. 107
5.7 Diagram outlining the steps involved in preparing the system for data collection. The system is first filled up through capillarity by holding the syringe under the vessel with solution, in order to minimise the presence of air bubbles (1-2), and then fixed onto the stage of the Raman microscope (3). To minimise any potential contamination in steps (1-2) due to ethanol's hygroscopic nature, the opening of the vessel was sealed with parafilm, and a razor was used to make a thin cut through which to introduce the tubing. 107
5.8 Top: Step by step description of the data processing followed for calibration runs. Note that 0–100wt% corresponds with the mass percentage of ethanol. The spectra correction step is further described in Section 5.2.6. Bottom: Step by step description of the data processing followed in the case of mixing experiments. 109
5.9 Example of how the airPLS baseline removal method, with $\lambda = 100$ and first-order difference penalties, affects spectra across the whole range of mass compositions (wt%) for the ethanol-water system. (a) Raw spectra. (b) Same spectra, after baseline removal. 110
5.10 Example of how the cosmic rays in spectra are filtered without compromising the ethanol signal. (a, b) Complete spectra. (c, d) Zoom into the relevant intensity range for enhanced visibility. (a, c) Spectra for an ethanol mass fraction of 0.8. (b, d) Spectra for an ethanol mass fraction of 1. Both (a, c) and (b, d) share the legend, where y and *Rep* indicate, respectively, at what Y position and in what repetition (1, 2 or 3) the spectra was found on. There are multiple repetitions because the spectra shown in these examples is part of the calibration dataset, for which each measurement was repeated three times. 111

5.11 Example of how the intensities marked as zero in some spectra within the calibration dataset have been corrected by replacing these with the average of the other two repetitions. The labels *Og. R1*, *Og. R2* and *Og. R3* denote the original raw spectra, while the labels *Avg. R3 (corrected)* and *Avg. R3 (Unchanged)* refer to the two parts of the modified spectra: the corrected, averaged intensities from the beginning, and the unchanged intensities across the rest of the wavenumber range. The spectra shown in this example correspond to a pure water measurement. 112
5.12 Example of a spectra showing a disproportionately large baseline in comparison to other measurements in the same column, resulting in the deformation of the spectral shape. Note that each Y position in the legend corresponds with a discrete colour, with 0 and 205 being the top and bottom of the channel, respectively. 112
5.13 Average normalised area under the signal peak, as used to determine the borders of the channel. The shadowed area corresponds with the standard deviation of each average. In all cases except pure water, the $2800 - 3040\,\mathrm{cm}^{-1}$ ethanol peak was used; the former considered instead the $3060 - 3690\,\mathrm{cm}^{-1}$ water peak. A close-up of this figure is displayed on the right to showcase the adequacy of the selected threshold value, 0.04, indicated by the red dashed line. 113
5.14 (a) Average Raman spectra for each concentration in the calibration dataset, after baseline removal; the shadowed area corresponds with the standard deviation. (b) Average and standard deviation of the highest ethanol intensity for each composition of the calibration dataset. Two values for the pure ethanol value were presented, collected at different times; the earlier one corresponds with the pink marker. Note that the error bars showcasing the standard deviation may be too small in comparison to the marker size to be appreciated. 114
5.15 (a) Average ethanol intensity across the entire channel height for the two calibration measurements of pure ethanol, labelled by the date they were acquired. The error bars correspond with the standard deviation between repetitions. (b) Value of the calculated scaling factor for each y position along the channel height. 115
5.16 (a) Spectra from the 90 wt% calibration measurement at $y = 125$, before (solid line) and after (dashed line) correction. (b) Original and corrected average and standard deviation of the ethanol signal for each calibration composition, and their linear fit. 115
5.17 Area under the ethanol peak across the height of the channel for selected x positions recorded in the experiment 50–0 wt%. The (x, y) coordinates of the points that were identified as air bubbles and subsequently eliminated are $(3750, 90)$ and $(11250, 105)$. 117
5.18 Step-by-step flowchart for the optimisation process. For clarity, it has been indicated what form of composition each step was conducted in. The results of the first interpolation, labelled as "Generate left BCs", are only used to define the left boundary conditions of the simulation, but the interpolated missing values are not considered when evaluating the error function. 119

5.19 Depiction of how the linear interpolation of missing datapoints within the first column of experiments 4 (a) and 5 (b) affects the overall trend. In both cases, the original trend is preserved, including when estimating an end value, as seen in (b). 120
5.20 Coordinates at which the data in the experimental and simulated maps are located. Since the simulation mesh is finer across the y axis, with the equations solved at the centre of each cell, an interpolation of this map onto the experimental grid was required, as illustrated in the middle map. The red-shaded cells indicate the points trimmed out of this interpolated map to match the number of discarded rows in the experimental maps. 120
5.21 Mixing of water–ethanol solutions as observed with the Leica M165 C optical microscope: (a) Mixing of pure ethanol and pure water streams under increasing flow rates (top to bottom). (b) Mixing of a pure water stream with a water–ethanol solution of increasing ethanol composition (top to bottom) at $10\,\mu L\,min^{-1}$. The red arrows are a guide to the eye. 122
5.22 Example of the effect that the SGS filter (a) and combined (b) baseline removal methods have on the calibration dataset, at $y = 100\,\mu m$. Note that the combined methodology consists on applying airPLS baseline removal first, followed by a SGS filter. 123
5.23 Performance of PLS models at different channel y positions trained under different combinations of number of latent variables, scaling of the data and baseline removal methods: (a) airPLS; (b) SGS filter; (c) combined (airPLS + SGS filter). The λ value was kept constant at 100 for these studies (a-c). Finally, (d) presents the performance of PLS models with 4 latent variables at different channel y positions, trained on unscaled data which baseline was removed through airPLS, but at different values of λ. The performance was quantified following the average RMSE calculated from the LOGO-CV process, as well as its standard deviation. 124
5.24 Overview of the performance of the final PLS model configuration. (a) Average RMSE across all LOGO-CV iterations, except for those in which 0 and 100 wt% were used as the test set. (b) Example of prediction plot for one of the LOGO-CV iterations of the 105 µm model. 126
5.25 Evolution of the Raman spectra captured during the study of the pure EtOH-H_2O system flowing at $4\,\mu L\,min^{-1}$, without applying any baseline correction. Note that $y = 0$ corresponds with the top edge of the channel where ethanol was introduced. (a) At x =3750 µm, along the y axis, and (b) at y =30 µm, along the x direction. 126

5.26 Raman composition mixing maps for a pure water–ethanol system studied at different flowrates: (a) $2\,\mu L\,min^{-1}$; (b) $3\,\mu L\,min^{-1}$; and (c) $4\,\mu L\,min^{-1}$; these correspond with experiments 1, 4 and 7 in Table 5.2, respectively. Composition is given as the ethanol mass fraction; the white squares represent eliminated outliers, and the white column indicates a missed collection point in the x axis. (d) Selected composition profiles extracted from these mixing maps at two x positions: the channel inlet, and 11 250 µm. Those points at which the trendline breaks correspond to discarded outliers. The larger pixels in the second and third columns in (b) are due to the $x = 2500\,\mu m$ column being missing in this map. . 128
5.27 Raman composition mixing maps for a system at $3\,\mu L\,min^{-1}$. (a) 25–100 wt% EtOH; (b) 50–100 wt% EtOH; (c) 75–100 wt% EtOH. These correspond, respectively, with experiments 8–10 in Table 5.2. Composition is given as the ethanol mass fraction; the white squares represent eliminated outliers. (d) Composition profiles at $x = 0$ and 11 250 µm for the three systems. Those points at which the trendline breaks correspond to discarded outliers. 129
5.28 Raman composition mixing maps for a system at $3\,\mu L\,min^{-1}$. (a) 25 wt% EtOH–H_2O; (b) 50 wt% EtOH–H_2O; (c) 75 wt% EtOH–H_2O. These correspond, respectively, with experiments 11–13 in Table 5.2. Composition is given as the ethanol mass fraction; the white squares represent eliminated outliers. (d) Composition profiles at $x = 0$ and 11 250 µm for the three systems. Those points at which the trendline breaks correspond to discarded outliers. 130
5.29 Repeated Raman composition mixing maps for pure ethanol–water flowing at $2\,\mu L\,min^{-1}$ (a, b), and $3\,\mu L\,min^{-1}$ (c, d). In particular, the maps correspond with experiments 2 (a), 3 (b), 5 (c) and 6 (d), as per Table 5.2. Composition is given as the ethanol mass fraction; the white squares represent eliminated outliers, and a white column indicates a missed collection point in the x axis. . . . 131
5.30 Composition profiles for pure ethanol–water flowing at (a) $2\,\mu L\,min^{-1}$, and (b) $3\,\mu L\,min^{-1}$ at different x positions along the channel. R1, R2 and R3 correspond respectively with experiments 1–3 in (a) and 4–6 in (b), as per Table 5.2. The points at which the trendline breaks correspond to discarded outliers. . . . 132
5.31 Uncertainty test performed in a pure ethanol–water system, consisting on measuring the column at the channel inlet 17 times. (a) Average and standard deviation of the spectra located at $y = 120\,\mu m$. (b) Averaged ethanol signal across the y axis, and its standard deviation. In both cases, the standard deviation is presented as a shadowed area. 133
5.32 Unexpected formations observed during the gathering of the compositional maps. (a) Pocket of air located against the top wall of the channel; (b, c) trail of dot-like bubbles; (d) formation and growth of an air bubble against a channel wall. These formations did not show any Raman signal. 134

5.33 Experimental mole fraction map (a) and best-fit simulated map, given in mole fractions, (b) for experiment 7. The outliers present in (a) were not taken into account when evaluating the loss function, despite their corresponding cells being full in (b). 136
5.34 Comparison between experimental and simulation best-fit composition profiles for experiment 4 (a) and 13 (b), at different points along the channel length. The missing points on the trends reflect discarded outliers. 137
5.35 Comparison between experimental and simulation best-fit composition profiles for experiment 10 (a) and 12 (b) at different points along the channel length. The missing points on the trends reflect discarded outliers. Evolution along the y axis of the spectra captured for experiment 10 at $x = 0$ (c) and $x = 1250\,\mu m$ (d). . . . 138
5.36 Comparison of the predicted interdiffusion coefficient values in this work with literature. Note that the compositions assigned to each of the values reported in this work corresponds with the theoretical final composition of the mixed streams. Literature data taken from [183], [187], [188], [186], [184], [189], [185]. Note that, as pointed out in [190], the value for D at an ethanol mass fraction of 0.8968 was erroneously listed as $2.51 \times 10^{-10}\,m^2\,s^{-1}$ in Table 3 of [189]; however, the correct value of $6.51 \times 10^{-10}\,m^2\,s^{-1}$ was displayed in Fig. 4. Therefore, it is this amended value that was included in this work. 140
5.37 Results of the velocity sensitivity analysis conducted for experiment 7. (a) Selected composition profiles for all studied scaling factors. (b) Variation of the predicted diffusion coefficient based on the applied scaling factor. 141

A.1 Differential volume element over which the mass balance is performed. Adapted from Byron et al. [1] 165
A.2 Differential volume element over which the force balance is performed. 169

C.1 Diagram of the heterogeneous system in equilibrium. The continuous black line depicts its concentration profile, whereas the dashed lines correspond with the concentration of the individual, unconnected bulk phases: c_i^I and c_i^{II}. The location of the interface, z_G, is chosen so that the shaded grey and striped areas are equal in magnitude but of opposite sign. 180

D.1 Comparison between the experimental and the best-fit simulation profiles for experiment 7. 181
D.2 Comparison between the experimental and the best-fit simulation profiles for experiments 1 (a), 2 (b) and 3 (c). 182
D.3 Comparison between the experimental and the best-fit simulation profiles for experiments 4 (a), 5 (b) and 6 (c). 183
D.4 Comparison between the experimental and the best-fit simulation profiles for experiments 11 (a), 8 (b), 12 (c), 9 (d), 13 (e), 10 (f). 184

F.1 Chemical potentials of the two independent species, 1 and 2, for the equilibrium state of a system in which a stream of pure antisolvent was mixed with a solution of 25% API. The results obtained with the form posed by Petrischeva and Abart [121] and with the form initially explored in this work are both presented. The degree of non-ideality was $A = 3$, and the interfacial free energy coefficients correspond with (a) $(\kappa_{aa}, \kappa_{ab}, \kappa_{bb}) = (0, 0, 0)$ and (b) $(\kappa_{aa}, \kappa_{ab}, \kappa_{bb}) = (0.025, 0.008, 0.025)$. 190

F.2 Chemical potential differences between the independent and the dependent species for the equilibrium state of a system in which a stream of pure antisolvent was mixed with a solution of 45% API. In particular, (a) presents $\beta\mu_a = \beta\mu_1 - \beta\mu_0$, and (b), $\beta\mu_b = \beta\mu_2 - \beta\mu_0$. The results obtained with the form posed by Petrischeva and Abart [121] and with the form initially explored in this work are both presented. The degree of non-ideality was $A = 3$, and the interfacial free energy coefficients correspond with $(\kappa_{aa}, \kappa_{ab}, \kappa_{bb}) = (0.025, 0.008, 0.025)$. 190

F.3 Chemical potentials of the two independent species for the equilibrium state of a system in which a stream of pure antisolvent was mixed with a solution of 45% API. The results obtained with the form posed by Petrischeva and Abart [121] and with the form initially explored in this work are both presented. The degree of non-ideality was $A = 3$, and the interfacial free energy coefficients correspond with (a) $(\kappa_{aa}, \kappa_{ab}, \kappa_{bb}) = (0.025, 0.008, 0.025)$ and (b) $(\kappa_{aa}, \kappa_{ab}, \kappa_{bb}) = (0.1, 0.032, 0.1)$. 191

F.4 Evolution of the composition with time in a system mixing pure antisolvent with a 45% API solution, considering that $A = 0$ and $\beta\mu_1^{\circ,(S)} - \beta\mu_1^{\circ,(L)} = -1$. The gradient coefficient values are (a) $(\tilde{\kappa}_{aa}, \tilde{\kappa}_{ab}, \tilde{\kappa}_{bb}) = (0, 0, 0)$ and (b) $(\tilde{\kappa}_{aa}, \tilde{\kappa}_{ab}, \tilde{\kappa}_{bb}) = (0.1, 0.032, 0.1)$. In particular, (a, b) depict the compositional pathways through the ternary diagram. The blue line in them is the solubility curve, and the dotted line joins the two initial compositions, marked by a white circle. To ease visualisation, the last recorded profile has been plotted in white. 193

F.5 Evolution of the composition with time in a system mixing pure antisolvent with a 45% API solution, considering that $A = 3$ and $\beta\mu_1^{\circ,(S)} - \beta\mu_1^{\circ,(L)} = -1$. The gradient coefficient values are $(\tilde{\kappa}_{aa}, \tilde{\kappa}_{ab}, \tilde{\kappa}_{bb}) = (0.05, 0.016, 0.05)$. In particular, (a) depicts the compositional pathways through the ternary diagram. The blue line in them is the solubility curve, and the dotted line joins the two initial compositions, marked by a white circle. To ease visualisation, the last recorded profile has been plotted in white. (b) Spatial evolution of the composition profile. . . . 194

F.6 Evolution of the composition with time in a system mixing a 45% API solution with a solution of 80/20% antisolvent/solvent, considering that $A = 3$ and $\beta\mu_1^{\circ,(S)} - \beta\mu_1^{\circ,(L)} = -1$. The gradient coefficient values are (a) $(\tilde{\kappa}_{aa}, \tilde{\kappa}_{ab}, \tilde{\kappa}_{bb}) = (0,0,0)$ and (b) $(\tilde{\kappa}_{aa}, \tilde{\kappa}_{ab}, \tilde{\kappa}_{bb}) = (0.1, 0.032, 0.1)$. The blue line in them is the solubility curve, and the dotted line joins the two initial compositions, marked by a white circle. To ease visualisation, the last recorded profile has been plotted in white. 195

F.7 Evolution of the composition with time in a system mixing a 25/75% API/solvent solution with a stream of pure antisolvent, considering that $A = 2.5$ and $\beta\mu_1^{\circ,(S)} - \beta\mu_1^{\circ,(L)} = -1$. The gradient coefficient values are (a) $(\tilde{\kappa}_{aa}, \tilde{\kappa}_{ab}, \tilde{\kappa}_{bb}) = (0,0,0)$ and (b) $(\tilde{\kappa}_{aa}, \tilde{\kappa}_{ab}, \tilde{\kappa}_{bb}) = (0.025, 0.008, 0.025)$. The blue line in them is the solubility curve, and the dotted line joins the two initial compositions, marked by a white circle. To ease visualisation, the last recorded profile has been plotted in white. 195

List of Tables

2.1 Summary of the advantages and disadvantages of the main crystallisation techniques. 10

3.1 Selected simulation parameters. Left: parameters shared between all performed simulations. Right: variable set of studied conditions. Attending to the left, `nx` and `dx` correspond with the number of volume elements in the discretised system and their width, respectively; `res tol` with the tolerance allowed within the residual step of the solver; `stag tol` with the tolerance considered to decide whether the minimum possible residual has been reached, or the solver has stagnated; `save freq` with the frequency with which a timestep was saved; lastly, `dt fcn` is the function used to define timestepping, and `dt` and `n` are its variables. Attending to the right, ICs corresponds with initial conditions; **G** to the group of studies those simulations belong to; the three functions tested as part of group 1 have been detailed in Section 3.4.1; GN stands for Gaussian noise, defined through mean ($\overline{x}_1$) and variance (σ^2); and, lastly, $\tilde{\kappa}$ and A correspond with the nondimensionalised gradient coefficient and Margules parameter, respectively. 43

3.2 Summary of all forms of composition dependence for κ_{ij} tried in this work and their resulting chemical potential. To calculate that of form I, it was assumed that $(\tilde{\kappa}_{11} - \tilde{\kappa}_{10}) = 0.5\tilde{\kappa}$. 45

4.1 Summary of conditions studied in this work. The composition indicated in the top and bottom streams is in the form (x_{API}, x_S, x_{AS}). The abbreviations employed in the diffusion coefficients correspond with 1 for API, 2 for solvent and 0 for antisolvent. 73

4.2 Tolerance thresholds accepted in the solver residual for the first four time iterations. The compositions indicated in both streams are in the form (x_{API}, x_S, x_{AS}). 77

5.1 Weights and ethanol mass percentages of the solutions used within the calibration dataset, and temperatures at which each calibration measurement was performed. 108

5.2 List of experiments performed for the spectroscopical analysis of the EtOH–H_2O system, and the room temperatures at which they were performed. C_1 and C_2 correspond to the ethanol mass percentages of the two solutions used and Q corresponds with the total flowrate, reported in $\mu L\,min^{-1}$. 108

5.3 Properties of the system studied in each experiment. Left to right: experiment identification number; average temperature $\overline{T}$ (°C); ethanol mole fractions of the inlet streams; and molar volumes ($cm^3\,mol^{-1}$) of ethanol and water at that average temperature. Note that the mole fractions correspond with the theoretical composition of each stream, not with measured values. 118
5.4 Hyperparameters analysed during the optimisation of the features of the PLS model, and the different values tested for each of them. Note that the combined baseline removal method consists of applying first airPLS to the spectra and then a Savitzky-Golay filter, with parameters $(9, 2, 1)$ for window length, polynomial order and derivative order, respectively. 123
5.5 Interdiffusion coefficient values predicted by the optimisation algorithm after fitting Fickian diffusion to the experimentally measured composition mixing maps. 140

List of Abbreviations

API	**A**ctive **P**harmaceutical **I**ngredient
CFD	**C**omputational **F**luid **D**ynamics
CQA	**C**ritical **Q**uality **A**ttribute
CSD	**C**rystal **S**ize **D**istribution
FVM	**F**inite **V**olume **M**ethod
LLPS	**L**iquid **L**iquid **P**hase **S**eparation
MSMPR	**M**ixed **S**uspension **M**ixed **P**roduct **R**emoval
PAT	**P**rocess **A**nalytical **T**echnology
PBE	**P**opulation **B**alance **E**quation
PBM	**P**opulation **B**alance **M**odel
PDF	**P**robability **D**ensity **F**unction
PFC	**P**lug **F**low **C**rystalliser
PFM	**P**hase **F**ield **M**odel
PIV	**P**article **I**mage **V**elocimetry
QbD	**Q**uality by **D**esign
QbDD	**Q**uality by **D**igital **D**esign

UNIVERSITY OF STRATHCLYDE

Abstract

Faculty of Engineering
Department of Chemical and Process Engineering

Doctor of Philosophy

A nonlocal thermodynamic framework for mass transfer and phase separation in antisolvent crystallisation

by Irene MORENO FLORES

A central challenge in pharmaceutical manufacturing is the reliable prediction of when and where crystallisation will occur, as this governs product quality, yield, and process robustness. In antisolvent crystallisation, supersaturation is generated by mixing a solvent–API solution with an antisolvent in which the API has low solubility. Despite its widespread use, antisolvent crystallisation remains difficult to control, often leading to unwanted outcomes such as unexpected crystal forms or liquid–liquid phase separation. This stems from the complex, multiscale nature of the process. At the scales relevant to crystal nucleation, mass transfer is dominated by diffusion, and mixing creates localised composition inhomogeneities that result in regions of high supersaturation. Accurately describing diffusion is therefore critical, as oversimplified models can lead to erroneous conclusions about the onset of supersaturation and nucleation. Traditionally, diffusion has been modelled using Fick's law, which assumes concentration gradients as the driving force. Yet observations such as uphill diffusion and oiling out demonstrate its limitations in highly non-ideal antisolvent systems. Recent studies have shown that the Maxwell–Stefan framework, which formulates diffusion in terms of chemical potential gradients, provides a more appropriate description. The key challenge now lies in accurately formulating the chemical potential. This work incorporates a nonlocal contribution rooted in the Cahn–Hilliard formulation, which accounts for the free energy cost of composition inhomogeneities and, thus, interfaces. This term enables the modelling of liquid–liquid phase separation and provides a more physically consistent description of diffusion, improving predictions of where and when supersaturation and nucleation are likely to occur. By highlighting the importance of interfacial effects in diffusion, this work provides a powerful framework for understanding supersaturation profiles in antisolvent crystallisation and controlling or avoiding phase separation phenomena such as oiling out. The study systematically examines non-ideality and interfacial contributions in binary and ternary systems, and develops an experimental methodology based on Raman microscopy to obtain composition mixing maps for future model validation.

Chapter 1

Introduction

Crystallisation is one of the most widespread separation techniques within the food, chemical and pharmaceutical industries. In particular, crystallisation from solution of the Active Pharmaceutical Ingredient (API) is a core step in upstream drug manufacturing.

The properties of the final drug substance, that is, the API, play an essential role in the safety and reliability of the final drug product, impacting its bioavailability and effect on the human body. They also impact the downstream processing, with certain attributes associated with problems at the filtering, blending, and tableting stages [1]. Some of the most relevant Critical Quality Attributes (CQAs) of the API are the crystal size distribution, the crystal shape and habit, and the polymorphic form [1]. Their importance has been highlighted by high-profile cases such as ritonavir and rotigotine, in which the formation of an unexpected polymorph led to their temporary withdrawal from the market [2].

Antisolvent crystallisation is one of the most commonly applied varieties of this unit operation. The key principle is that a solute of interest, dissolved in a suitable solvent, is crystallised by mixing the solution with a third species, denominated antisolvent, in which the solute has poor solubility. This technique is particularly suited to purify heat-sensitive compounds, and can have a lower energetic cost than its counterparts [1]. Its combination with cooling crystallisation can lead to increased yields, making this a common approach in industrial pharmaceutical processes [3].

Despite its widespread use within the pharmaceutical industry, the observation of undesired outcomes remains a prevalent problem in antisolvent crystallisation. Examples of this are the formation of unwanted and unexpected crystal polymorphs, shapes, or habits [4, 5], and the formation of a solute-rich secondary liquid phase within the mother liquor instead of solid nuclei, referred to as oiling out or liquid-liquid phase separation (LLPS) [6]. These occurrences are rooted in a lack of sufficient understanding of mass transfer within the antisolvent crystallisation context and inevitably hinder the control over the CQAs.

Mass transfer in antisolvent crystallisation is governed by the mixing of the two streams, i.e., solution and antisolvent. When first put in contact, it is expected to find local regions within the system with vastly different concentrations separated by interfaces which, as mixing develops, disappear. These compositional inhomogeneities are in turn translated into spatial gradients in supersaturation. Thus, the system may not be locally operating at the mixing point and supersaturation that the macroscopic system was designed for. Parts of the system could be brought into unexpected regions of the ternary phase diagram and potentially cause it to exit the design

envelope; this concept is illustrated in Figure 1.1. This could cause the formation of unexpected polymorphs, crystal shapes, or oiling out.

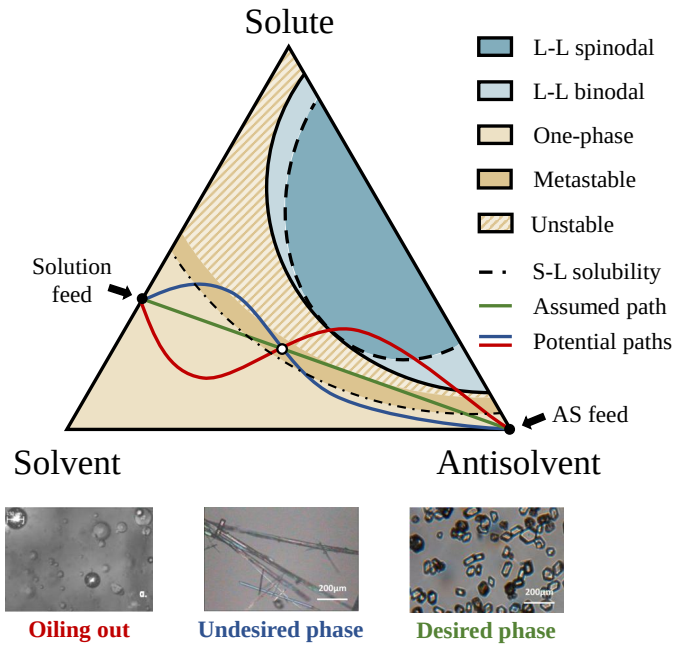


FIGURE 1.1: Depiction of the potential effect of different mass transfer pathways across the ternary phase diagram. L-L stands for liquid-liquid; S-L, for solid-liquid; and AS, for antisolvent. Commonly, mixing models assume ideality, and thus, a straight pathway between streams (green line) predicting no breach into the binodal/spinodal regions. Non-idealities in the system can lead to different evolutions (red and blue lines), which could result in unwanted properties within the crystal product.

Although the problematic of oiling out and of reaching undesired crystal properties during antisolvent crystallisation is well-known [4, 6], modelling in this context has been more dedicated to reproducing the properties of the crystal population rather than understanding the fundamentals of mass transfer behind these [7]. Only a small number of studies [8, 9] dedicate themselves to this problem, and an even smaller number [10] tackle oiling out within their theory.

Mass transfer at the relevant scale for local composition gradients is governed by diffusion, making its accurate description crucial. Diffusion in antisolvent crystallisation is most commonly described by Fick's law [8], which defines the driving force for mass transfer as proportional to the spatial gradients in concentration. This in turn enforces the assumption of ideal behaviour, as well as a linear trajectory across the ternary phase diagram, as depicted in Figure 1.1 in the assumed path. Therefore, within this framework, the system always strives towards homogeneity. However, this assumption does not hold even for the most intuitive systems: considering an emulsion of oil and water, one does not expect the phases to interdiffuse and fully mix, and yet, that is the behaviour that the Fickian framework would predict. Therefore, it cannot be expected to provide an accurate description of diffusion in a process of the complexity of antisolvent crystallisation. This is evidenced by the occurrence of uphill diffusion, in which a species diffuses against its concentration gradient [8, 11].

Fundamentally, all spontaneous processes are driven to decrease the free energy of the system, which is equivalent to the dissipation of spatial gradients in the chemical potential. This way, in spontaneous processes, particles move from regions of high to low chemical potential until chemical equilibrium is reached. This makes a framework that considers that the driving force for mass transfer is proportional to the gradient in chemical potential—such as the Maxwell-Stefan diffusion model [12, 13]—a more accurate alternative. For instance, such a framework explains the uphill diffusion phenomenon as a case in which the chemical potential and concentration gradients evolve in opposite directions. It also avoids assuming linear trajectories through the phase diagram, enabling the prediction of the formation of potentially undesired crystal forms, as depicted in the potential paths in Figure 1.1. However, the Maxwell-Stefan model still exhibits limitations, namely, its incapability to contemplate the dynamics of phase transformations, reducing its usefulness for the study and understanding of the liquid-liquid phase separation occurring during oiling out. Moreover, this model neglects the effects that the temporary interfaces formed during the mixing of the two streams may have on the system.

1.1 Thesis aim and objectives

This work aims to cover this gap through the formulation of a diffusion model capable of accounting for these interfaces and of predicting and simulating phase transformations, so as to improve the accuracy of the mass transfer description within antisolvent crystallisation, and apply it to the problematic of oiling out and unexpected crystal properties.

In particular, this gap has been addressed through the incorporation of a non-local gradient term in the free energy definition, adapting the framework devised by Cahn and Hilliard [14] to model spinodal decomposition. This will lead to the apparition of additional terms in the chemical potential, which are expected to help provide a better evaluation of supersaturation in time and space. This, in turn, will translate into better estimations of nucleation rates, and potential times and regions where nucleation could occur. Moreover, it is expected to better track the composition trajectories throughout the ternary phase diagram, helping explain oiling out and the formation of unexpected polymorphic forms or crystal shapes. It could thus be employed for design of experiments, helping avoid conditions predicted by the model to veer outside of the design envelope. This aim has been divided in the following objectives:

- **To study the effect of the non-local term on diffusion in a binary system.**
  - Provide a detailed introduction to the theory behind the model for a binary system, including its main scientific motivation, physical relevance and relation to known physical variables, behaviour in equilibrium, and main limitations.
  - Compare the temporal and spatial composition and supersaturation profiles predicted by the model with those of the two other most relevant diffusion frameworks, Fick's law and Maxwell-Stefan, in the context of a non-ideal system.
  - Confirm the effectiveness of the model in simulating LLPS within the spinodal region and analyse the effect that the magnitude of the gradient term has on diffusion and

supersaturation, in the context of an ideal system and of a system undergoing phase separation.

- Explore the mass transfer and phase behaviour of a system under crash-cooling conditions. This proves the uniqueness of the model, as both Fick and Maxwell-Stefan are unable to predict diffusion within the spinodal region.

- **To study the effect of the non-local term on diffusion in a ternary system, aimed towards antisolvent crystallisation.**

  - Provide a detailed introduction to the theory generalised to a multicomponent system, including its main scientific motivation, physical relevance and relation to known physical variables, behaviour in equilibrium, and main limitations.
  - Explore the phase and mass transfer behaviour under the one-phase, binodal and spinodal regions of the ternary diagram through the predicted compositional and supersaturation spatial profiles, and compositional pathways through the ternary diagram.
  - Explore the effect that different diffusion coefficients and degrees of nonideality between species have upon the phase and mass transfer behaviour for a system of fixed initial conditions through the predicted compositional and supersaturation spatial profiles, and compositional pathways through the ternary diagram. This aimed to replicate the behaviour of different interactions between the species.

- **To develop an experimental framework isolating diffusion as the dominant mass transfer mechanism in order to facilitate the qualitative validation of the predictions of the proposed model.**

  - Develop a microfluidic platform scalable to multicomponent systems through which to study mass transfer in combination with Raman microscopy.
  - Perform experimental diffusion studies of a binary water–ethanol system under different initial compositions and flow rates.
  - Replicate the experimental system through a digital model and develop a digital optimisation framework through which to estimate benchmark mass transfer parameters.

1.2 Thesis contributions

The following scientific contributions have been made as a result of this work:

- The development of a diffusion model, applied to binary and ternary systems, better suited to describing antisolvent crystallisation by accounting for non-ideal and non-local thermodynamics, thus overcoming the limitations of current approaches. The model features a driving force rooted in chemical potential gradients, allowing the incorporation of an activity model to describe non-idealities. Moreover, an additional non-local term was included

in the free energy formulation, inspired on the Cahn-Hilliard equation [14]. This term describes the contributions of compositional inhomogeneities, and thus, of interfaces, making it capable of modelling the dynamics of LLPS and of representing the thermodynamic effect of transient interfaces formed during mixing. An exploration on the effects of this term on the prediction of composition and supersaturation in time and space (binary and ternary) and of the evolution of non-linear compositional pathways on the ternary phase diagram is presented.

- While the non-local gradient term studied in this work has been extensively applied in other fields, such as material science and polymers, this knowledge is not easily accessible by scientists in adjacent fields. Many texts rely on the reader possessing a baseline knowledge of the topic, lacking the level of algebraic detail needed for a newcomer to be introduced into the theory. This work bridges this gap, providing a detailed derivation and analysis of the main features of the theory and of the relationship between the gradient term and other known physical variables, such as the surface tension. This thus brings the theory to the pharmaceutical crystallisation community, and to antisolvent crystallisation in particular.

- Despite the extensive study of the dynamics of models incorporating the gradient term observed in other fields, this work has identified an inconsistency with the equilibrium states recovered from approaches found in literature. In particular, certain definitions of the chemical potential proposed in literature do not result in a flat profile when in equilibrium. This work proposes, for a binary system, a revised definition of the gradient term coefficient that does not alter the model dynamics and recovers a flat chemical potential profile in equilibrium. It also provides insights as to what pieces of the theory one would inspect to replicate this for ternary systems.

- This work proposes an experimental framework in which diffusion is isolated as the main mass transfer mechanism, leveraging microfluidics and Raman microscopy to collect liquid composition maps of two solvents during mixing. This could be used to qualitatively validate the proposed modelling framework in the future, exploring whether the anomalous phenomena predicted by the model are observed in the microfluidic setup. Moreover, an optimisation algorithm is built for the quantitative estimation of mass transfer model parameters from the collected maps, and a case study applied to a Fickian diffusion model is provided.

1.3 Thesis outline

Given the completely computational nature of the first two results chapters and the considerably lengthy methodology description required to explain the development of the experimental microfluidic platform, each chapter was structured as a self-contained unit, comprising a brief introduction, methodology, results and discussion, and conclusions. This approach was adopted

to improve the accessibility of the thesis, reducing the need for readers to locate relevant methodological and contextual information across multiple chapters when interpreting a particular set of results. The thesis has been organised as follows:

- **Chapter 2** provides an overview of the relevant literature focusing on the general principles behind crystallisation, the most pressing problems within antisolvent crystallisation, the most commonly applied models to describe this technique, and some background on the models proposed in this work.
- **Chapter 3** develops a binary diffusion model incorporating a non-local gradient term into the free energy landscape, analyses its equilibrium behaviour and its performance in comparison to other diffusion models, and studies its application to a crash-cooling system.
- **Chapter 4** develops a multicomponent diffusion model incorporating a non-local gradient term into the free energy landscape, and analyses its performance under different scenarios relevant to ternary systems and antisolvent crystallisation processes.
- **Chapter 5** describes an experimental microfluidic platform leveraging Raman microscopy to perform diffusion studies, tested in an ethanol–water system, and develops an optimisation routine to extract benchmark mass transfer parameters of diffusion models.
- **Chapter 6** summarises the main findings arisen from this research and proposes directions for future work.

Chapter 2

Background

2.1 Crystallisation fundamentals

Crystallisation can be considered the oldest separation technique applied in chemical engineering, since the obtention of salt through this method dates back to the earliest civilisations, playing a major role in their development [15]. It can be defined as a process concerned with the formation of a solid product from an original fluid, the mother liquor, through the rearrangement of atoms into a three-dimensional lattice. It plays an essential role in several natural processes, such as geologic crystallisation and the crystallisation of biominerals in living creatures [16].

From a manufacturing perspective, crystallisation is applied as a separation technique across a multitude of industries for the production of both intermediates and products, such as (bio)pharmaceutical, agricultural and other fine chemicals [17], food manufacturing, waste management [18, 19] and production of metallic materials [20], among others. In food technology it is used in the production of sucrose, salt, fatty acids and artificial sweeteners [21, 22], as well as other products such as ice-cream [23]. In the agricultural industry it is employed in the manufacturing of fertilizers [24], pesticides [25] and other agrochemicals. Within the wider fine chemical industry, the production of most dyes and explosives employ crystallisation as a part of the manufacturing process [16]. Finally, within the pharmaceutical industry, 80% of the drugs available on the market are formulated as crystals [26]; in particular, crystallisation is the final upstream step in the manufacturing of most Active Pharmaceutical Ingredients (APIs) [27]. The wide applications of crystallisation in industry make its understanding and optimisation paramount for the achievement of the highest possible operating efficiency.

2.1.1 The crystal formation process

The solubility of a compound in a solvent is defined as the amount of that compound that a certain amount of solvent at a certain temperature can dissolve. A generic solubility curve is presented in Figure 2.1.

In a cooling crystallisation process, temperature is decreased from point (1) to (2) in Figure 2.1 in order to decrease the solubility of the API in the solution and generate supersaturation. The thermodynamic driving force in a crystallisation process is denominated supersaturation, which in Figure 2.1 corresponds with the difference in concentrations between (2) and (3). It can also be defined as a deviation from equilibrium, accounted for through the difference in

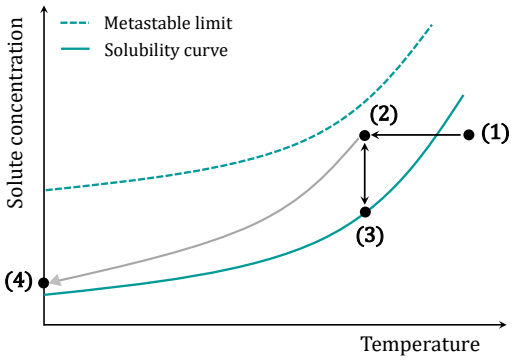


FIGURE 2.1: Generic solubility curve and metastable zone representation for a solute in a certain solvent. A typical cooling crystallisation process would follow the points (1)-(2)-(4). The difference in concentration between (2) and (3) is the supersaturation.

chemical potential between the dissolved solute and the crystalline phase [15]. The supersaturation value indicates in what region of the solubility diagram the solution is situated at, as can be seen in Figure 2.1. If, at a given temperature, the solution is placed at the solubility curve, it is said that it is saturated. If it is located above or below the curve, it will be supersaturated or undersaturated, respectively [23]. The degree of supersaturation of the solution plays an essential role in the crystallisation, dictating what mechanisms will dominate the crystal formation.

Crystallisation is constituted by seven mechanisms, as depicted in Figure 2.2. The initial phase separation occurs during the primary nucleation stage, in which solid crystals appear for the first time in the solution. This is followed by a stage of crystal growth in which the small nuclei previously formed increase their size. Thus, a trade-off is established between these two phenomena, since if nucleation consumes the majority of the supersaturation, numerous small crystals will be obtained, whereas a the process majorly controlled by the growth stage will result in fewer, larger crystals. Potentially, agglomeration can also occur, with two small particles colliding and remaining close during enough time for a crystalline bridge to be formed between them [23].

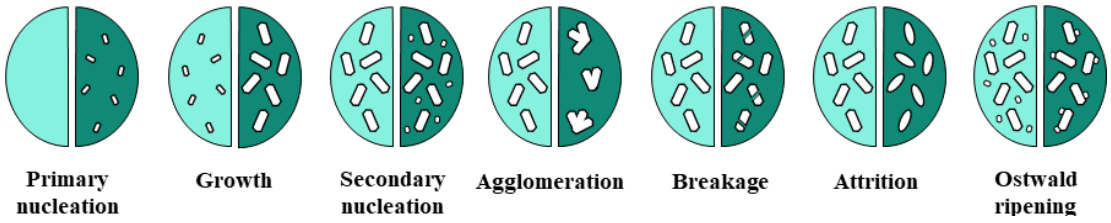


FIGURE 2.2: Diagram of the mechanisms that occur during a crystallisation process. Adapted from [28].

The crystals formed by these three mechanisms can be denominated as parent crystals, and they exert a catalytic effect on the nucleation phenomena. Thus, it is possible for a new batch of nuclei to appear despite the lower overall supersaturation, following a process of secondary nucleation from solution [16]. In addition, several other subprocesses can take place during crystallisation. Due to collisions with other crystals, against the mixer, or because of strong turbulences, the breakage or fragmentation of crystals can occur [29]. Moreover, it is possible

for the roughness present in the surface of the crystals to be gradually removed, in a process denominated attrition [30]. Lastly, Ostwald ripening consists in the dissolution of small crystals, increasing the supersaturation in solution, and the consumption of this supersaturation through the growth of other crystals. Occurring over long periods of time, it reduces the total surface area of crystals in contact with the solution, therefore reducing the overall free energy of the system [23].

The properties of the final crystalline product are highly dependent on what mechanisms have occurred during crystal formation, and to what extent. Given the high risk associated to the inadequate performance of a drug product, processes within the pharmaceutical industry undergo thorough final quality controls, partly based on two parameters: the Crystal Size Distribution (CSD) and the crystal morphology. The importance of the size distribution resides on its heavy influence on the bioavailability of the final API [16], which dictates how well it will absorb in the human body. Bioavailability is also affected by polymorphism, the ability of a compound to crystallise with different morphologies. The different lattice can impact the solubility of the crystals, and thus their performance [31]. From a manufacturing perspective, the performance of downstream processes such as filtration [16] is affected by the CSD, as well as by the crystal shape [23]. Finally, the purity of the final product is another of its critical characteristics, due to the possibility of the mother liquor and/or impurities to have been included within the crystal lattice [23].

2.1.2 Overview of the main crystallisation methods

The available crystallisation techniques can be classified in two distinct categories depending on whether the crystals are obtained from solution or from the melt.

A melt is defined as as a pure molten solid or liquid mixture close to its melting point; when brought to this temperature, it freezes, forming crystals. Melt crystallisation is mainly used for the production of highly pure compounds, in the range of 99.9 to 99.999%. This purification potential constitutes one of the main advantages of this process, together with the ability of separating compounds with close boiling points and the possibility of crystallising thermally sensitive products, if their melting temperature is not high [23]. The process is normally carried out over several steps, helping achieve higher final purity [32]. Therefore, the energy consumption per kilogram of product can be relatively high [23].

Melt crystallisation differs from crystallisation from the solution in three main aspects. Firstly, the crystals obtained are formed by either the melt itself or the solvent used for the mixture, depending on the application. Secondly, by definition, this process operates close to the freezing point of the component of interest [23]. And thirdly, this process is dominated by heat transfer effects, in opposition to crystallisation from the solution, in which crystallisation is controlled by mass transfer [15].

Crystallisation from solution can be applied in a single step while still achieving high purities, due to the higher rigidity of the obtained crystal lattice. It is comprised by four main techniques, of which a brief overview is provided below: cooling, evaporative and anti-solvent

crystallisation, and precipitation. The main advantages and disadvantages of each technique are summarised in Table 2.1.

The basic principle of cooling crystallisation is the reduction of the temperature of the solution until the solubility of the API falls below the actual concentration of the solution. This drives the solution into the metastable zone and creates supersaturation, point at which nucleation can occur. Its main advantage are the generation of narrow CSDs, and its main limitation is the solubility of the solute at the lowest achieved temperature, which, if high, could lead to lower yields [16].

Evaporative crystallisation induces supersaturation through the evaporation of the solvent, leading to an increase in the solute concentration which, eventually, causes supersaturation. It is suitable for thermally stable compounds which solubility is not a strong function of temperature. Its main potential limitation is the possible build-up of non-volatile impurities in the remaining mother liquor, which may be incorporated into the crystal lattice and change the solubility of the remaining solution [23].

TABLE 2.1: Summary of the advantages and disadvantages of the main crystallisation techniques.

Technique	**Advantages**	**Disadvantages**
Melt	Ultrapurification is feasible, potentially adequate for heat-sensitive compounds.	Low separation efficiencies can lead to high energy consumption depending on process efficiency.
Cooling	Adequate for high temperature dependency in solubility. Narrow CSDs.	Limited yield dependent on solute solubility at lowest temperature.
Evaporative	Potential yields of near 100%, adequate for low solubility dependence on temperature.	Accumulation of non-volatile impurities in mother liquor.
Precipitation/Antisolvent crystallisation	Adequate for thermally sensitive compounds and low solubility dependence on temperature; high product yields.	Locally high supersaturations may lead to unexpected crystal attributes.

Precipitation is the only crystallisation process that involves a chemical reaction. It consists in the mixing of two concentrated reactants in order to obtain a product poorly soluble in the solution formed. This process achieves considerably high yields, albeit it is also linked to locally high supersaturation values, which can translate into unexpected crystal polymorphs [23].

Antisolvent crystallisation, also known as salting out or drowning out crystallisation, is based on the formation of the solid solute via its dissolution in a solvent and a posterior addition of an antisolvent or nonsolvent, i.e., a liquid in which the solubility of the solute is poor. The similitude with precipitation can be drawn immediately, with the only exception of no chemical reaction occurring in this case.

Since this process does not rely on large temperature differences to create supersaturation, it is generally used for the crystallisation of thermally sensitive compounds. In the context of pharmaceutical crystallisation, it is applied when working with compounds which solubility is only a weak function of temperature [33]. It has been applied across a wide breadth of fields beyond the pharmaceutical, such as for the development of piezoelectric nerve conduits in the context of nerve tissue engineering [34], for electrode manufacturing in redox flow batteries [35], for the preparation of perovskite films used in solar cells [36], and for the formation of polymer membranes, field in which it receives the name of nonsolvent induced phase separation (NIPS) [37].

Within pharmaceutical crystallisation, it is commonly used in the preparation of poorly water-soluble drugs, such as paracetamol [1], ibuprofen, curcumin and siramesine [38]. Some examples of systems in which water is not part of the solvent/antisolvent pair are, as given in [1], the crystallisation of indomethacin in acetone/heptane [39], pyrazinamide in 1,4–dioxane/cyclohexane [40], or ammonium perchlorate in acetone/ethyl acetate [41]. Moreover, antisolvent crystallisation is considered an effective preparation method of micro or nanoparticles [33, 42], and it has been applied for the polymer coating of particles [43, 44].

From a crystal engineering perspective, antisolvent crystallisation can help in the control of key particle properties such as shape and size. Examples of this, as given in [1], are the preparation of paracetamol in acetone/water, which helps decrease the occurrence of agglomeration [45]; the crystallisation of carbamazepine in methanol/water to produce hollow crystals [46]; or the formation of spherical nitrendipine crystals [47]. Moreover, some systems have been linked with the formation of a specific polymorph, such as β–glycine in water/2–propanol [48], or γ–indomethacin in 1,4–dioxane/cyclohexane [39].

Lastly, antisolvent crystallisation can be deployed as a second purification step after cooling crystallisation, allowing to increase the yield and profitability of this process [23, 49–51].

2.1.3 General process configurations

Industrial crystallisation processes are focused around two main operational modes: batch and continuous. A batch crystalliser operates in discrete cycles [52], while in a continuous configuration the inlet/outlet streams of feed and product flow continuously into and out of the system without interruption [53]. Semibatch mode, relevant for antisolvent crystallisation, is characterised by the incorporation of one or more feed streams to the equipment during all or part of the operation [52].

Batch crystallisation offers a higher flexibility of operation and lower maintenance than its continuous counterparts; moreover, cycle operation helps avoid fouling between loads, albeit at the cost of a higher downtime. It is particularly suitable for products with slow growth speeds, or which exhibit difficulties in their processing. It remains more economically favourable up to a capacity demand of $500\,\mathrm{kg\,h^{-1}}$, after which point continuous operation is more advantageous. Batch crystallisers can be classified based on the type of crystallisation they perform; some industrially applied examples are the calandria batch evaporative crystalliser, the vacuum crystalliser with forced recirculation, and the Buflovak draft-tube crystalliser [52].

Continuous crystallisation offers a reduced downtime and a higher efficiency regarding space demands abd API, solvent and energy consumption, leading to reduced waste production and helping maximise yield. Moreover, while batch operation relies on the variation of process conditions to maintain supersaturation during operation [54], often leading to batch-to-batch inconsistencies, continuous operation avoids this by maintaining the selected conditions across the entire crystalliser [55]. The three most common crystallisers within this process configuration are the mixed-suspension mixed-product-removal (MSMPR), plug flow, and oscillatory baffled crystalliser [54].

Microfluidic crystallisation has recently gained attention from the scientific community. It offers several advantages over traditional batch/continuous operation, such as enhanced mass and heat transfer, and a more accurate control over the process conditions and thus over crystal nucleation and the properties of the crystalline product [56, 57]. Its reduced scale leads to significantly lower API and solvent requirements, improving their cost-effectiveness and helping reduce operational risks [56]. It also enables the high-throughput screening of different process conditions and their impact on the crystal properties [57]. Moreover, they can be easily coupled with in-line Process Analytical Tools (PATs) and integrated with real-time control systems, facilitating their automation [56].

Despite their vastly different scales, diffusion exerts a great control over local mixing in all three presented process configurations. The geometry of general microfluidic systems is associated with Peclet numbers significantly lower than 1, indicating that mixing is dominated by diffusion [8]; thus, they are able to achieve conditions of free interface diffusion [57]. In industrial batch and continuous crystallisers the Peclet number can be much larger than 1, in which case mixing is controlled by fluid bulk motion and diffusion. The former works by rearranging the location of fluid elements within the system without altering the composition of each element. That can only occur via molecular diffusion between two adjacent fluid elements, indicating that at a small enough length scale, mixing in such a system is also controlled by diffusion [8]. Given that supersaturation is a function of composition, its local profile is therefore also controlled by diffusion, highlighting the importance of correctly describing this phenomenon.

2.1.4 Ethos: Quality by Digital Design

In a wider context, the challenges outlined above regarding the design and operation of crystallisation processes are occurring amid a regulatory framework shift. Rather than the traditionally favoured end-quality testing, the past two decades have seen the main regulatory agencies promote the application of Quality by Design (QbD) [58, 59]. Based on the idea that quality should be built in the manufacturing process through adequate product and process design, it emphasises the thorough exploration of the design space through PAT testing [60].

More recently, the Quality by Digital Design (QbDD) [61, 62] framework has drawn from the principles behind QbD and aims to incorporate emerging capabilities in digital technologies. It encourages the application of both physics and data-driven models to enhance the understanding of a process, helping elucidate the relationship between its critical parameters and the critical quality attributes of the product. In the context of crystallisation, QbDD would entail, among

others, studying the mechanisms involved in crystal formation, such as nucleation and growth, and, consequently, diffusion and supersaturation generation.

2.2 Challenges within antisolvent crystallisation

Traditionally, antisolvent crystallisation has been conducted in a stirred vessel with several potential feed configurations, such as single or double jets, or with an additional premixing device, such as an impinging jet [32]. Given their effect upon the turbulent and/or diffusive mass transfer process, some of the operating conditions that dictate the quality of the crystalline product are the temperature of the overall process; the solvent/antisolvent pair selected; the velocity of the inlet streams, their flow ratio and their mode of addition; the size of the crystalliser, and the agitation rate [33, 63]. These parameters are also crucial when operating in a continuous context, with literature highlighting the effect of the supersaturation profiles, the residence time, the feed concentration, and the addition and mixing of the antisolvent as relevant [55, 64]. The selection of the operating value for each variable must be as informed and tailored to each application as possible, in order to ensure maximum efficiency.

In addition to these, local composition profiles also affect the properties of the final product. The local composition, and therefore the local supersaturation, vary considerably within the crystalliser. It is expected to find higher supersaturation values near the feed point of the antisolvent due to the larger mass fraction of this compound in that region. This in turn influences the nucleation and growth rates, as well as the characteristics of the final crystalline product, being common, for example, the formation of unexpected polymorphs due to the large local supersaturation values [65]. Since supersaturation is a function of composition, it is affected by its local variations, which are governed by diffusion [8]. Remarkably, local mixing is also tightly linked to the scale-up problem. In antisolvent crystallisation, scaling issues are rooted in the different equipment size drastically altering the mixing conditions and, thus, the local supersaturation profiles, resulting in many cases in unexpected and undesired product properties [65, 66]. Hence, local mass transfer has a considerable impact on the overall performance of the crystallisation process and the quality of the drug product.

This way, mixing between solution and antisolvent emerges as an important operating aspect, which optimisation is already object of considerable effort [33]. Operating variables such as stirring speed and mixer geometry aim to enhance it from a macroscale perspective, while parameters such as composition feed and ratio of solution to antisolvent greatly influence local composition and thus local supersaturation. While perhaps unaware, operators tailoring such variables to the desired CQAs were indirectly optimising diffusive mixing.

The incorrect selection of process variables can lead to one or more of the unwanted phenomena commonly reported within crystallisation units. As mentioned before, the crystal morphology can differ from the desired one, which could drastically affect the properties of the product. A general example of this are the cases of ritonavir and rotigotine, which had to be temporarily withdrawn from the market due to the appearance of an unexpected polymorph [2]. Traditionally, the main other problem that can be encountered during crystallisation is the so-called oiling

out process, or liquid-liquid phase separation. It consists in the formation of a secondary solute-enriched liquid phase, previous to the potential crystal nucleation and growth steps. Figure 2.3 provides an example of this phenomenon for a binary system of salicylic acid and n-heptane.

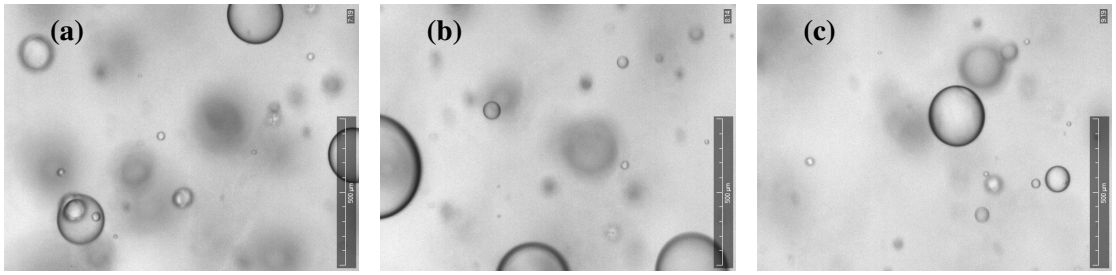


FIGURE 2.3: Examples of oiling out in a binary salicylic acid–n-heptane system, at subsequent times (a)–(c). Images collected by Dr Thomas Pickles as part of the CMAC DataFactory [67, 68].

Oiling out is highly affected by the diffusive mixing process, since it is the local composition of the system that determines in what region of the phase diagram the process operates and whether LLPS will occur [6]. Its occurrence considerably hinders the reproducibility of crystallisation batches, thus damaging the overall reliability of the pharmaceutical process [69]. It also often leads to impure crystals, since impurities are normally soluble in the secondary liquid phase formed, to which most of the solute migrates [70]. Finally, oiling out has also been linked with excessively time-consuming batches, 'desert rose' crystal morphology and difficulties in nucleation occurring spontaneously [71]. Interestingly, recent studies [6, 72] pinned LLPS as a possible tool to be harnessed to aid crystallisation in certain systems, highlighting potential advantages such as enhanced product sphericity [73], enhanced favourability of certain polymorphs [74] and aid in the control of crystal size and aspect ratio [75, 76].

The emergence of these phenomena is clearly rooted in complex mass transfer mechanisms, which, as mentioned above, are greatly influenced by diffusion regardless of scale. The thorough understanding of these phenomena and the ability to predict their occurrence and follow their evolution plays a key role in both their avoidance or deployment, through better informed design of antisolvent crystallisation processes. These benefits evidence the high importance of this field of study, given its great optimisation potential for processes containing crystallisation units.

Considering these challenges, the application of the QbDD framework to antisolvent crystallisation could be translated into the study of the fundamental physics of diffusion, given its relation with local supersaturation profiles and thus the nucleation mechanism [8, 65]. It could also motivate the prediction and simulation of polymorph formation and oiling out phenomena, processes highly affected by the mixing process [6, 65], in order to understand their behaviour and the conditions leading to them.

For these reasons, this project is concerned with producing a model capable of simulating diffusion and spontaneous phase transformations, which are a subset of oiling out dynamics [77]. It also aims to gather a collection of rich experimental data in a diffusion-controlled environment, that can serve to qualitatively validate the translation of the local phenomena observed within the model in a larger scale.

Therefore, the computational study proposed in this work is framed in the relevant scale for diffusion, as proposed by Miller *et al.* [8]. As illustrated in Figure 2.4, it is assumed that at this scale the system can be described initially as a layer of solvent-rich solution opposite to a layer of antisolvent. This spatial scale was selected due to its high direct effect on local supersaturation, in contrast with the indirect effect of macromixing [8, 16, 66]. Additionally, this is the most relevant scale for the simulation of the phase change associated with the nucleation process.

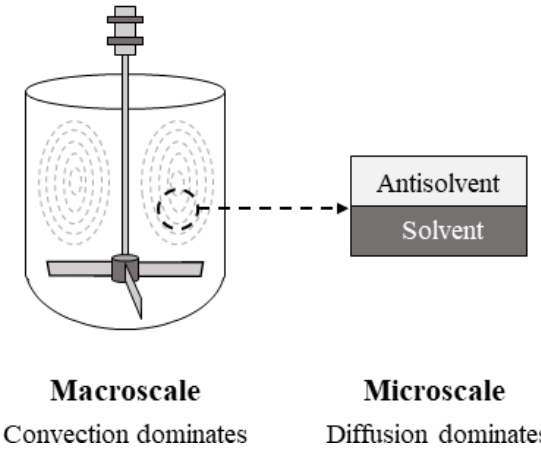


FIGURE 2.4: Diagram illustrating the different scales within a crystalliser unit.

2.3 Modelling mixing in antisolvent crystallisation

Having established the main reasoning behind studying diffusive mass transfer in antisolvent crystallisation, there are several questions that derive naturally from this motivation. It is necessary to consider how the micromixing process has been described so far in antisolvent crystallisation processes, and, in particular, consider how has diffusive mixing been described in the field.

The main critical quality attributes of a crystallisation process are normally the purity of the crystal product, its CSD, polymorphic form, shape, and yield. The Population Balance Model (PBM) framework is capable of taking into account these properties, making it one of the most popular choices for the modelling of crystallisation processes. These models rely on the Population Balance Equation (PBE), which describes the different mechanisms occurring in the crystallisation process through empirical and/or semi-empirical equations, following the suspended crystals as a disperse phase. These are combined with mass and energy balances to track the properties of the mother liquor that affect the crystallisation process, such as concentration and temperature [7]. However, these balances are not always resolved, and when they are, it is with different degrees of accuracy.

In many cases, the crystallisation process is still modelled through the PBM alone [78, 79]. If working with an MSMPR crystalliser, this implies assuming perfect mixing and isothermal conditions at every single point in the unit, as well as assuming that the properties of the removed slurry are identical to those remaining inside the reactor. If working with a Plug Flow

Crystalliser, it entails assuming perfect mixing on the radial direction, and null axial mixing [7]. Thus, this option completely neglects any mixing or heat transfer effects at any scale.

Following the classification given in [80], mixing can be included in the modelling ecosystem in three ways. (1) resolved exclusively at the macroscale, by coupling the PBE with a Computational Fluid Dynamics (CFD) simulation; (2) through a mechanistic micromixing model coupled with the PBE and a simplified macromixing model; and (3) by combining the PBE with CFD to solve macromixing, and using a Probability Density Function (PDF) to close micromixing.

These three options all represent diffusion from different perspectives, and none are without limitations. The first case presents the crudest assumption, directly considering ideal subgrid mixing. The mechanistic models employed in the second case are more directed towards describing how different fluid elements rearrange themselves to facilitate diffusion, but all of them assume that this process happens according to Fick's law [81]. Lastly, the combination of a PDF with CFD and PBM can be done in two ways: by transporting the PDF, or by presuming its shape [80]. In the first case, the system tracks the probability distribution of the continuous property—concentration, for example—in time and space. In the second, the shape of the distribution is assumed at each point of space and time [80]. The closure schemes employed in the first enforce the relaxation of gradients in the continuous property as the consequence of diffusion; similarly, in the second, the variance of the continuous property at a diffusion scale is only of dissipative nature, and thus cannot grow to influence the meso and macroscales. Considering the evolution of concentration, this evidences that these three approaches have been built on the Fickian physical interpretation of molecular diffusion, which stipulates that this phenomenon ultimately just leads to a relaxation of concentration gradients.

It is true, however, that a crystallisation macroscopic model accounting for the crystal PBE and bulk flow in addition to micromixing is inherently complex, which could drive the need for a more simplified accounting of diffusion. Thus, the next question that must be answered is: how is diffusion described when operating at its dominant scale?

In most scientific fields, molecular diffusion is most widely described through Fick's law, which states that the driving force for mass transfer is proportional to the spatial gradients in concentration. This leads to the continuity expression shown in Equation (2.1).

$$\frac{\partial c_i}{\partial t} = D_{ij} \nabla^2 c_i \tag{2.1}$$

where c_i is the molar concentration of component i and $D_{ij} = D_{ji}$ is the diffusion coefficient of the mixture, always > 0. In several books this is the only diffusion model covered, and only certain dedicated texts explore other alternatives. A detailed derivation of Fick's model for a binary mixture can be found in Appendix A.

Research on microfluidic devices offers perhaps one of the best areas in which to look to understand how the scientific community understands molecular diffusion, given that it heavily controls mass transfer in these devices. This review focuses first on antisolvent crystallization. Although the available studies of molecular diffusion within this context are scarce, some key

works have been summarized below, with their combination of experimental and modelling approaches highlighting how the Fickian framework dominates the understanding of diffusion.

Thorson *et al.* [65] presented a microfluidic approach to polymorph screening of APIs in an antisolvent crystallization system. This rapid screening under a broad range of operating conditions led to the identification of the most stable polymorph, with its success partly due to the high level of control over diffusion offered by the microfluidic platform. These experimental results were qualitatively compared to, and found to be in good agreement with, simulated supersaturation profiles in time, generated through Fickian diffusion. Similarly, Bhamidi *et al.* [48] designed a microfluidic device for the polymorph screening of glycine in an antisolvent crystallisation system. The diffusive mixing and supersaturation effects were correlated with an empirical parameter that allowed to determine the recovered polymorph in most cases. Their experimental device was modeled through combining the steady-state Navier-Stokes equation and convection-diffusion equation, which, again, comprised a Fickian approach to molecular diffusion. In a more recent study, Zhao *et al.* [82] employed a microfluidic device for the production, through antisolvent crystallization, of solid ultrafine particles of hexanitrostilbene (HNS). Their analysis was also based on the Fickian framework.

This preference is maintained across a wide range of fields. Wu *et al.* [83] developed a nonlinear convection-diffusion model which considered the dependence of the diffusion coefficient with the concentration, and modelled diffusive mixing through Fick's law. In a posterior study of this group, Wu and Nguyen [84] built several devices based on the hydrodynamic focusing principle, in which a stream is contained between two identical other inlets. Two-dimensional Fick's law was used to build the convection-diffusion model used to describe the mass transfer between these streams. Sullivan *et al.* [85], in a similar study, applied the lattice Boltzmann method to simulate diffusive mixing in a Y-shaped micromixer, again considering Fickian diffusion. Finally, another metric of the popularity of this model is the considerable amount of research devoted to the study and application of its diffusion coefficient, even today [86–90].

While undoubtedly widespread and useful, Fickian diffusion presents some limitations that gain relevance the moment a system steps away from ideality, which have been reported in [11, 91–94]. The most important is its definition of the driving force for mass transfer as proportional to the concentration gradient. Considering a simple system of oil and water, we would intuitively not expect one to diffuse into the other, despite the large concentration gradient between the two layers. This thus constitutes an incorrect definition of the driving force, which can lead to erroneous conclusions regarding how diffusion will occur. A good example of this is the so-called uphill diffusion: a phenomenon in which a species naturally diffuses against its concentration gradient, that is, from a region of low to high concentration. The Fickian framework cannot cope with such a system, as extensively reviewed by Krishna [11] across several fields. In a process as inherently complex as is antisolvent crystallisation, diffusion is unlikely to behave according to the Fickian framework, and describing it in this way is expected to lead to errors. Considering that, to the author's knowledge, all micromixing models coupled with macromixing have been designed to replicate the behaviour of Fick's law, the poor suitability of this model to describe diffusion in antisolvent crystallisation systems is motive of concern.

The most recent literature studying diffusion in an antisolvent crystallisation context has focused on addressing this gap, proposing Maxwell-Stefan diffusion [12, 13] as a suitable alternative. Unlike Fick's law, this framework considers the driving force for diffusion to be proportional to the gradient in chemical potential of a species. This definition is thermodynamically correct, since, unlike the gradient in concentrations, this is indicative of the system reducing its free energy [95].

To the author's knowledge, only four relevant studies have been published on this topic. Miller *et al.* [95] presented a comparison between the Maxwell-Stefan and Fickian frameworks, finding that the supersaturation behaviour during the diffusive mixing process differed between them: the ideal model led to the prediction of large supersaturation overshoots, whereas the Maxwell-Stefan output predicted the solution would remain unsaturated. Given the more physically accurate nature of this model, it is thus expected that supersaturation would not be observed in the real system, highlighting how the Fickian framework could lead to erroneous conclusions. Moreover, the authors were able to predict when spinodal decomposition may occur by tracking the evolution of the composition profile in the system during the diffusion process, albeit the simulation had to be stopped once the system entered this region. An interesting finding was that this could occur even for systems which final composition was located outside of the spinodal region, highlighting the importance of correctly describing local mixing pathways for understanding the outcome of the process.

Afterwards, Zhang *et al.* presented two consecutive studies on the thermodynamics of oiling out. The first [96] explored the construction of the ternary phase diagram of a DBDCS-water-[1,4-dioxane] antisolvent crystallisation system through the CALPHAD method, which showed good agreement with an experimentally constructed diagram used for its validation. An interesting observation of this study is what the authors call "antisolvent focusing", which is nothing more than the uphill diffusion of the solute upon its mixing with the antisolvent-rich stream. The authors observe that the sharper the antisolvent concentration gradient is between the two streams, the more pronounced the solute uphill diffusion becomes.

Their second study [9] explored the suitability of Maxwell-Stefan as a framework from which to describe diffusion in the antisolvent crystallisation system of the first study. By performing time-resolved advection-diffusion simulations of a 1D diffusion couple and analysing their corresponding mixing profiles, the authors identified three general stages in the diffusion of the two streams. If no phase separation occurred, upon their initial contact, the solute experiences uphill diffusion and gathers in the vicinity of the interface, on the solvent-rich side, albeit the composition in the bulk of the solvent-rich stream remains unchanged. The solute front then travels rapidly through the solvent-rich region, until reaching a maximum when colliding with the boundary of the system. After this point, it starts slowly diffusing downhill. Interestingly, the authors identified the onset of spinodal decomposition in the same way that Miller *et al.* [95] did: by observing whether the simulation diverged. While the Maxwell-Stefan framework can diagnose whether a set of conditions will lead to spinodal decomposition, it is unable to model the separation itself, thwarting the level of understanding that this model can provide on the dynamic and thermodynamic behaviour of oiling out. This also compromises the ability to study

diffusion in the vicinity of the spinodal region, since, as Miller *et al.* [95] identified, even systems which mixing point is outside of this region can venture into it during the mass transfer process.

To address this gap, this work proposes the incorporation of a non-local term to the free energy landscape of the model, penalising composition gradients, and thus enabling the simulation of spinodal decomposition. This was inspired by phase-field models, which have been extensively applied in material science to model very similar mass transfer problems in material science, among other fields [97].

2.4 Phase-field models: bases and application

The coexistence, temporal or permanent, of different phases within a system necessarily implies the formation of an interface, which must be accounted for in the thermodynamic modelling of such systems. Traditionally, this has been done explicitly, through the combination of several equations to describe the mass transfer, heat production and transfer, and boundary conditions that occur at the interface. This formulation is called the sharp-interface model, also referred to as the Stefan Problem [98].

While in theory a combination of these expressions exists containing the necessary physics to track the natural evolution of the interface through space and time, a notorious limitation of the sharp-interface model is that the most appropriate form of these expressions is, in many cases, not known. Moreover, certain phase transformations, such as the formation of dendrites, are associated with the formation of considerably complex interface morphologies [98]. The phase-field model (PFM) approach was developed as a solution to these limitations.

Phase-field models are situated in the mesoscale, spanning approximately from 100 nm to 100 µm [97]. They describe the system through a continuous variable, called the order parameter (ϕ), which is used to formulate the free energy landscape. It will thus be possible to describe any coexisting phases within the system through different values of this order parameter; as a result, the interfaces are described as smooth. That means that they are no longer an infinitely sharp jump between phases, but a progressive transition. This proposition is regarded as fundamentally correct, and the phase-field theory can be theoretically related to the mean-field approximation of phase transformations performed within statistical mechanics. A detailed description of their relationship was established by Provatas and Elder in [98].

Depending on the nature of their order parameter, phase-field models can be classified into two groups: conserved and non-conserved. As their name suggests, conserved order parameters must be naturally preserved within the field, as stipulated by a physical law; composition and concentration of a species are classic examples. In contrast, non-conserved order parameters do not need to be maintained in space. Solidification is a good example of this: the total amount of solid phase within the system is expected to change, as the system goes from completely liquid to solid. Other examples are magnetic domain growth and ordered/disordered transitions [98]. Non-conserved dynamics are traditionally described through the Allen-Cahn equation (2.2) [99],

whereas conserved dynamics are modelled with the Cahn-Hilliard equation (2.3) [14, 100].

$$\frac{\partial \phi}{\partial t} = -M \frac{\delta F}{\delta \phi} \tag{2.2}$$

$$\frac{\partial \phi}{\partial t} = \nabla \cdot \left(M \nabla \frac{\delta F}{\delta \phi} \right) \tag{2.3}$$

where M, normally referred to as the mobility coefficient, is a kinetic parameter, and F corresponds with the free energy of the system.

Phase transformations are normally classified into first- and second-order. First-order transformations present a discontinuity in the possible states of the order parameter. This means that above a certain transition temperature, the order parameter has one distinct value ($\phi = \phi_0$, for example), but jumps to a different one ($\phi = \phi_1$) when below this temperature; moreover, it does not approach the previous value as the temperature of the system tends toward the transition temperature [98]: $\lim_{T \to T_c^-} \phi \neq \phi_0$. Additionally, these transformations are normally accompanied by a discontinuity in the first derivatives of the thermodynamic potentials [98]: if working in the Gibbs free energy framework, this could mean a release/consumption of latent heat, or a change in volume; for the Helmholtz free energy, it could also entail a change in latent heat, or in pressure. Lastly, if the transformation occurs between phases of the same symmetry, such two liquids, or a liquid and a gas, they normally finish at a critical point, and at this point, a second-order transformation takes place. If the two phases have different symmetries, such as a liquid and a solid, the transformation need not terminate at a critical point.

In contrast, second-order transformations entail a continuous transition from a specific value of ϕ (again, $\phi = \phi_0$ as an example) when above a critical temperature to several values different from ϕ_0 when below this temperature. The second derivatives of thermodynamic potentials are discontinuous for this type of transformation, while their first derivatives maintain continuity, indicating that these processes are not associated with a release or consumption of latent heat. Lastly, another mark of this class is the phase transformation being spontaneous, without needing to overcome a free energy barrier to occur [98].

At this point, it is convenient to bring the analysis to our topic of interest and answer: where does oiling out lie within this classification? Literature on the topic is notoriously sparse, and the definitions above can be seemingly contradicting in some cases. Oiling out refers to the formation of a secondary liquid phase from the original mother liquor. There are two different dynamics it can follow, depending on the region of the phase diagram where it takes place. If stemming from the binodal region, it will follow nucleation and growth dynamics, meaning that it will have to overcome a free energy barrier to occur. However, if resulting from within the spinodal region, it will follow spinodal decomposition dynamics, in which case the separation is spontaneous, since the system is linearly unstable to all fluctuations [98].

This way, nucleation and growth and spinodal decomposition refer to the two different dynamics oiling out can follow, when occurring within the binodal or the spinodal region, respectively. The nature of the separation itself is unclear, and if the dynamic criteria outlined above

are applied, binodal and spinodal oiling out would be considered first- and second-order, respectively. However, these two mechanisms result in the same equilibrium state: two distinct phases with the same respective coexistence compositions. In this regard, both instances would be considered first-order transitions.

Phase-field models have been applied across a wide range of fields, including multiphase flow description [101] and material science, where they have been applied to the prediction of solidification [100, 102–104], microstructure evolutions [105, 106], modelling of material failure [107–110], sintering [111, 112] and liquid metal dealloying [113, 114], among others [97]. In polymers, they have been extensively used to study different types of phase separation, including thermally, evaporation, nonsolvent and polymerization-induced phase separation [115]. In the realm of biology, they have been applied to the modelling of biological tissues [116], including tumour growth [117, 118] and cell migration [119, 120]. There clearly is a wealth of information available for their development, and yet, this has not been leveraged for applications within the pharmaceutical industry. While the knowledge is available, it is perhaps not accessible, with many texts lacking the level of algebraic detail needed for a newcomer to truly understand the theory. This is one of the gaps that this work intends to bridge.

To the author's knowledge, there is only one published study where phase-field models are applied to the problem of oiling out. Performed by Tsugawa *et al.* [10], it investigated phase separation through a 2D rendition of the Cahn-Hilliard equation in a ternary system of ethanol, water and butylparaben. A very interesting output from their study is the confirmation that the model's prediction of the growth of the secondary liquid phase in the spinodal follows the expected dynamics: Ostwald ripening when close to the edges of the spinodal region, and bi-continuous dynamics when further inside it. However, there are several gaps that remain unaddressed in this study. Firstly, the outputs were not analysed in the context of their position within the ternary phase diagram, missing the opportunity to explore the compositional pathways followed by the system during the mass transfer process. Moreover, only the composition profiles and maps of the solute were reported, missing important nuances on the behaviour of the other species. It was not confirmed whether the final compositions correspond with the expected coexistence values. Lastly, the applied theory considered the same gradient coefficient for all species. Despite these limitations, the study was able to prove the great potential that phase-field models hold when it comes to the understanding of oiling out.

This thesis leveraged the more detailed literature provided in other fields to establish the foundation of the method. The work by Petrischeva *et al.* [121] was of particular usefulness, given the similitude between applications—spinodal decomposition in mineral solutions, in their case—and the good level of detail provided regarding the involved equations. Their methodology echoes that developed by Nauman and He [122], and was more recently applied by Inguva *et al.* [123] to study the effect that different activity models have on the model outcomes.

The application of phase-field models is expected to gain considerable attention in the coming years for the description of mixing and phase transformations in the context of the pharmaceutical industry. It is the hope of the author that this work will serve as the blueprint from which these applications will be developed.

Chapter 3

Diffusion and phase behaviour in binary systems: the effect of a non-local contribution to the chemical potential

Conventional diffusion models neglect interfacial contributions to the chemical potential. This limits their ability to accurately describe systems with strong composition gradients, such as antisolvent crystallisation processes, and prevents them from modelling phase separation altogether. This work investigates the effect of incorporating an interfacial free energy term into the formulation of the chemical potential. Before this approach can be studied in relation to a more complex ternary system, it is first necessary to understand the model behaviour in a simpler liquid binary context. Thus, this chapter explores the equilibrium behaviour and mass transfer dynamics of the proposed model, analysing it in comparison with local approaches and Fickian diffusion.

3.1 Introduction

Crystallisation is one of the most widely applied techniques within the pharmaceutical industry, with 80% of the drugs available on the market formulated as crystals [26]. Two of its most common variants are cooling and antisolvent crystallisation, in which supersaturation—the driving force for nucleation and growth—is generated by reducing the temperature of the solution until crossing the solubility line, in the first case, and by reducing the solubility through the incorporation of an additional solvent in which the solute has poor solubility, in the second case. This additional solvent is called the antisolvent.

The rates of nucleation and growth are highly dependent on supersaturation, and thus this variable has a significant impact on a number of CQAs of the crystalline product, such as particle size distribution, shape, habit, and polymorphic form [23, 80]. Focusing on antisolvent crystallisation, since supersaturation is generated through the incorporation of the antisolvent, this process is intuitively highly dependent on mixing. During the mixing process it is expected to find great variation in composition between different regions within the system, as well as the formation of temporal interfaces that will disappear as the mixing resolves. It is entirely possible for local regions of the system to venture into unanticipated areas of the phase diagram, which

can lead to unexpected properties in the final crystals. Moreover, since supersaturation depends on composition, this local heterogeneity will lead to local regions of high supersaturation, which can differ significantly from the overall supersaturation level of the bulk system.

This way, it is clear that maintaining a good control over these attributes necessitates of an adequate understanding and control of local mass transfer. Despite this clear relationship, mass transfer in antisolvent crystallisation remains not fully understood, with the formation of unwanted crystal phases or the occurrence of unexpected phenomena, such as liquid-liquid phase separation (LLPS, also known as liquid-liquid demixing and oiling out) being common observances [6].

Diffusive mixing in crystallisation is normally described through Fickian diffusion, which defines the driving force for mass transfer as proportional to the composition gradient. However, this is not thermodynamically accurate, with the real driving force being the gradient in chemical potential. While some recent studies [9, 95] have explored the importance of this distinction via the application of Maxwell-Stefan diffusion [12, 13], the chemical potential definitions considered in them are only able to predict whether spontaneous liquid-liquid demixing—that is, spinodal decomposition—will occur, no further. Moreover, these studies have not accounted for the contribution that the temporal interfaces formed during mixing have on the thermodynamics of the system, and thus, on mass transfer.

This work proposes the incorporation of a nonlocal term to the free energy of the system to bridge this gap, based on the gradient term present in the Cahn-Hilliard equation [14]. While this type of model, part of the phase-field family, has been extensively studied in the context of other scientific fields, such as metals, polymers, and biological systems [97, 115, 116], to the author's knowledge there is only one published article that has leveraged this concept to study oiling out in antisolvent crystallisation. Performed by Tsugawa *et al.* [10], it employed a 2D Cahn-Hilliard-like model to study LLPS through spinodal decomposition in a water/ethanol/butylparabene system. Interestingly, they found that the dynamics of the model followed Ostwald-ripening when in the outer region of the spinodal. Nonetheless, the authors highlight the need for further research on the compositional behaviour of these models when in equilibrium within the spinodal region. Additionally, the theory remains abstruse, with the physical interpretation of the gradient term and its coefficients unclear.

In particular, this work focuses on the study of the mentioned model in the context of a binary system, which is not something covered in the work of Tsugawa *et al.* [10]. While antisolvent crystallisation is undoubtedly a ternary process, by starting with a less complex system the author aims to help build intuition regarding the behaviour of the model under different conditions, as well as to provide a clearer picture of the physics behind the model to crystallisation scientists. Moreover, oiling out has been observed in a number of binary cooling crystallisation systems [124], such as ibuprofen and water [125], vanillin and water [70], or, as shown in Chapter 2, salicylic acid and n-heptane. Therefore, the binary studies conducted in this work can also help explain LLPS in this context.

3.2 Theoretical background

This section explores different approaches for modelling diffusive mass transfer, focusing first on the dynamics of the process and, afterwards, on the definition of a thermodynamic framework that takes into account interfacial contributions.

3.2.1 The driving force for mass transfer

The total flux $\mathbf{N_i}$ of a species i can be defined as $c_i\mathbf{u_i}$, where c_i and $\mathbf{u_i}$ are, respectively, the concentration and average velocity of the species. This total flux can be separated into two contributions: convective ($c_i\mathbf{v}$) and diffusive ($\mathbf{J_i}$). The convective flux is reversible and related to the general flow of the fluid, whereas the diffusive flux is thermodynamically irreversible and represents deviations from this general flow.

$$\mathbf{N_i} = c_i\mathbf{v} + \mathbf{J_i} \tag{3.1}$$

The general mass balance of species i, also referred to as its continuity equation, can be written in terms of its general flux according to Equation (3.2), and thus decomposed into convective and diffusive contributions by substituting Equation (3.1) into it. As explained in Chapter 2, this work is situated at the scale at which mass transfer occurs only by diffusion, and thus convection has not been considered. Therefore, the final continuity equation of species i is presented in (3.3).

$$\frac{\partial c_i}{\partial t} = -\nabla \cdot \mathbf{N_i} \tag{3.2}$$

$$\frac{\partial c_i}{\partial t} = -\nabla \cdot \mathbf{J_i} \tag{3.3}$$

The diffusive flux is most commonly described through Fick's law (3.4), greatly due to the abundant literature available studying a wide variety of systems in the context of this model. Moreover, the research community still dedicates considerable effort and resources to improving the accuracy and speed with which Fickian diffusion coefficients are gathered, and to measuring them for novel systems [87–90, 126, 127]

$$\mathbf{J_i} = -D_{ij}\nabla c_i \tag{3.4}$$

where D_{ij} corresponds with the Fickian mutual diffusion coefficient, also called interdiffusion coefficient, between species i and j.

The main feature of this model is that it considers the driving force for diffusion, $\mathbb{d}_i$, to be inversely proportional to the gradient in concentration of species i: $\mathbb{d}_i^{Fick} = -\nabla_{T,V} c_i$. This presumes diffusion will occur from regions of high to low concentration, and that the system will reach a fully mixed final state. This formulation is incorrect and can be proved so by considering an intuitive system formed by water and oil: according to Fick's law, these two liquids will steadily diffuse until forming a completely homogeneous solution. However, this does not

happen in reality, with the oil and water phases remaining firmly separated, either as an emulsion or, eventually, as two distinct layers.

The correct thermodynamic description of the diffusive driving force is instead given by the gradient of the chemical potential (μ_i) of species i: $\mathbb{d}_i = -\nabla_{T,V}\mu_i$. The chemical potential is defined as the molar partial derivative of the free energy, as presented in Equation (3.5), and thus it indicates how much the free energy will change in a particular point in space when a particle of species i is added to it.

$$\beta\mu_i = \left.\frac{\partial F}{\partial n_i}\right|_{T,V,n_{j\neq i}} \tag{3.5}$$

where n_i corresponds with the number of particles of species i; F corresponds with the nondimensional Helmholtz free energy of the system; and β corresponds with $1/(kT)$, where k corresponds with the Boltzmann constant. This can be related to the product of the ideal gas constant with temperature through $RT = N_A k_B T$, N_A being Avogadro's number. Thus, $\beta\mu_i$ is nondimensional.

Since all spontaneous changes in a system occur in order to minimise its free energy, it follows that transport will take place from regions of high to low chemical potential. The decrease in free energy caused by removing a particle of i from a region of high chemical potential will be larger than the increase in free energy caused by placing this extra particle in a region of low chemical potential, and thus the total free energy of the system will decrease. When the chemical potential is constant across the entire system, there is no drive to maintain a particle flux: the system has reached equilibrium.

The erroneous description of the driving force for mass transfer is a fundamental flaw of Fickian diffusion. The direction of the concentration and chemical potential gradients is not necessarily the same, and, in certain systems, diffusion will occur from regions of low to high concentration, which constitutes the so-called uphill diffusion phenomenon [11, 128]. Despite going against the concentration gradient, the process is still proceeding downhill in terms of chemical potential gradient. Even if these two gradients maintained the same direction, they could differ in magnitude, leading to discrepancies in mass transfer kinetics. Lastly, disregarding chemical potentials enforces the assumption of thermodynamically ideal behaviour, which only contemplates a fully mixed final state as the result of the mass transfer process.

This makes Fick's law inadequate for describing diffusion, especially in antisolvent crystallisation processes, where mixing is highly non-ideal. Considering its widespread use, it is not surprising that certain mass transfer phenomena rooted in non-ideal thermodynamics, such as oiling out, remain largely misunderstood.

3.2.2 General thermodynamic framework

The independent variables through which this work describes the studied system are temperature, volume and concentration of each species throughout the system. The thermodynamic free energy that has these properties as its independent variables is the Helmholtz free energy.

Therefore, this work, which considers an isothermal system of constant volume, is set within the context of the nondimensional Helmholtz free energy (F).

Given that the gradients in chemical potential constitute the driving force for diffusion, and that the chemical potential is a derivative of the free energy, it is clear that to develop an accurate diffusion model the first step is developing a representative free energy description. In this work, four contributions have been considered to form the free energy: (1) that of the pure species, (2) ideal mixing with the other species, (3) non-ideal mixing, and (4) that of non-local compositional gradients within the system.

Let us consider a 1D binary system formed by species 1 and 0, also referred to as S and A, respectively, where $x_0 = 1 - x_1$. Equation (3.6) introduces each of the free energy pieces in the presented order for the chemical potential of species 1. An identical expression mirroring Equation (3.6) could be written to define $\beta\mu_0$. The total chemical potential of the system is given by $\beta\mu = \beta\mu_1 + \beta\mu_0$.

$$\beta\mu_1 = \beta\mu_1^\circ(T, p_0) + \ln x_1 + \beta\mu_1^{nid} + \beta\mu_1^{intf} \tag{3.6}$$

where $\ln x_1$ corresponds with the contribution of ideal mixing, and $\beta\mu_1^{nid}$ and $\beta\mu_1^{intf}$, with the non-ideal mixing and gradient terms, respectively.

Free energy due to mixing non-idealities

This section provides the background and analysis of the local contributions to the free energy: that of the pure species, and of ideal and non-ideal mixing. In this work, the non-idealities in the species interaction have been described through the one-parameter Margules activity model, given in Equations (3.8)–(3.10). This is hereafter referred to as Margules, and in some texts as the symmetrical model [129].

$$G^{\mathrm{ID}} = \sum_{i=0}^{n} n_i(\mu_i^\circ + k_B T \ln x_i) \tag{3.7}$$

$$\frac{G^{\mathrm{EX}}}{k_B T} = \frac{\Omega}{k_B T} x_1 x_2 \equiv A(T,p) x_1 x_2 \tag{3.8}$$

$$\ln \gamma_1 = A(T,p) x_2^2 \tag{3.9}$$

$$\ln \gamma_2 = A(T,p) x_1^2 \tag{3.10}$$

where G^{ID} and G^{EX} correspond with the ideal and excess Gibbs free energy due to non-idealities, respectively; γ_i corresponds with the activity coefficient of species i; A and Ω correspond with the nondimensional and dimensional Margules parameter, respectively; and x_i is the mole fraction of species i, defined as the ratio between the number of particles of that species and the total number of particles in the system, n_i/n.

Since the aim is to qualitatively explore the effect of the interfacial free energy term, it was decided that the simplest nontrivial activity model with the ability to reproduce phase separation would be appropriate. However, this can be easily replaced by any other model suitable for the

intended application, such as the commonly preferred UNIQUAC for small molecules, or Flory-Huggins in the case of polymers. More information on their incorporation and effect on mass transfer can be found in [123].

While the Margules model is originally defined in terms of the Gibbs free energy, the theory proposed in this work is set within the Helmholtz free energy framework. Recasting the Margules contribution in this framework implies considering how the pressure-dependent variables in the free energy, which in this case are $\beta\mu_i^\circ(T,p)$ and $A(T,p)$, will vary with pressure. This pressure dependency has been described through a first-order Taylor expansion, which details are given in Appendix B. Algebraic manipulation subsequently allowed to reduce the definition of these parameters in the final Helmholtz free energy density as dependent only on p_0, a constant reference pressure of the system. Furthermore, an additional βp_0 term arises, coming from the fundamental relations between the two free energies detailed in Equations (3.11)–(3.13).

$$F = U - TS \tag{3.11}$$

$$G = U + pV - TS \tag{3.12}$$

$$F/V = \beta(G - pV)/V \tag{3.13}$$

where F is nondimensional, thus why the RHS of the last expression had to be multiplied by β; moreover, since $f = F/V$, the final relationship can be expressed as $f = \beta g - \beta p$.

Equation (3.14) presents the resulting Helmholtz free energy density, defined as $f = F/V$; f has units of $[1/V]$, and V corresponds with the volume of the system.

$$f(c_1,c_0) = c_1\left[\beta\mu_1^\circ(T,p_0) + \ln x_1\right] + c_0\left[\beta\mu_0^\circ(T,p_0) + \ln x_0\right] + cA(T,p_0)x_1x_0 - \beta p_0 \tag{3.14}$$

Since both the free energy density and the chemical potential are defined up to an additive constant, it is possible to calculate the free energy density without considering the chemical potential of the pure species and βp_0, through $f - \sum_i c_i\beta\mu_i^\circ - \beta p_0$. Similarly, the chemical potential can be calculated through $\beta\mu_i - \beta\mu_i^\circ$.

The behaviour of the system with respect to parameter A is detailed in Figure 3.1. Higher values of A signal a stronger incompatibility between species. The free energy densities presented in Figure 3.1(a) demonstrate that this activity model can describe both systems in which the most energetically favourable configuration is a homogeneous mixture ($A < 2$) and those for which demixing into two distinct phases is more favourable ($A > 2$). The transition between these behaviours occurs at $A = 2$, explaining why the miscibility gap in Figure 3.1(b) exhibits its critical point at that value. Since $A = \Omega/k_BT$, increasing A is equivalent to reducing the temperature of the system. Furthermore, A has opposite effects on the driving force depending on whether it is above or below 2. When $A > 2$, increasing A widens the miscibility gap, increasing the energetic penalty associated with intermediate compositions and thus resulting in a stronger driving force for demixing. In contrast, for $A < 2$, increasing A reduces the depth of the single well, and consequently also the driving force for mass transfer.

The binodal and spinodal curves are defined, respectively, by the minima and the inflexion points in the free energy density curve. An illustration of this is provided in Figure 3.1(c) for

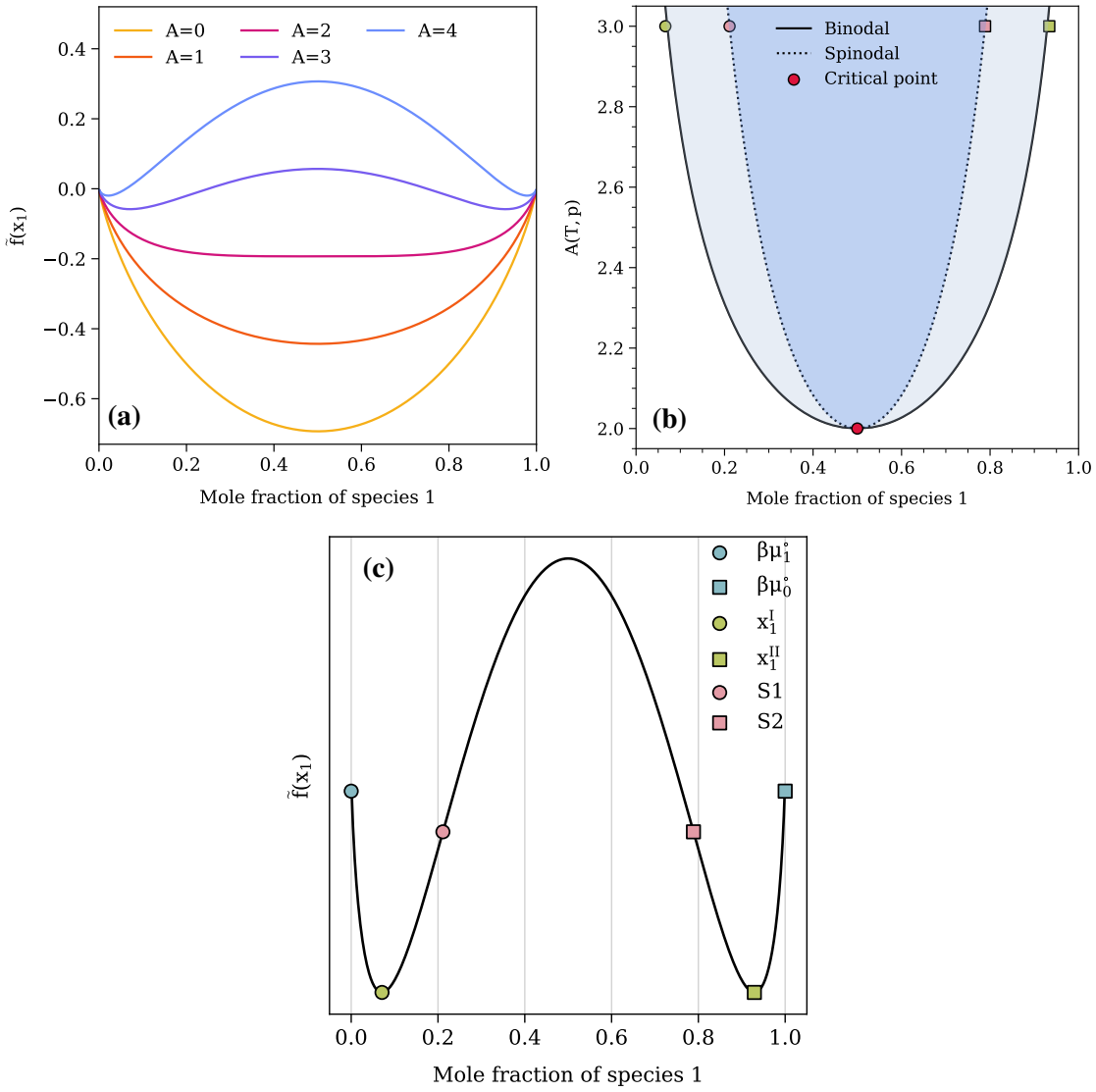


FIGURE 3.1: Free energy landscape under different values of A. (a) Free energy density evolution with x_A, where $\tilde{f} = (f - \sum_i c_i \beta\mu_i^\circ - \beta p_0)/c$. (b) Phase diagram showing the critical point and the binodal and spinodal regions, shaded in light and dark blue, respectively, with the first conforming the boundaries of the miscibility gap. (c) Free energy density for $A = 3$, marking the chemical potentials of the pure components, the equilibrium compositions and common tangent, and the spinodal points. Note that the critical points of this case have been translated onto the phase diagram in (b).

$A = 3$; these markers have also been mapped to their corresponding locations in Figure 3.1(b). Phase separation can occur in both of these regions, with the distinction that it is only spontaneous in the spinodal region [77]. As shown in Figure 3.1(c), a small composition fluctuation in the spinodal region immediately leads to a smaller total free energy than that held by the initial system. Consequently, the free energy always decreases as phase separation proceeds. The opposite happens, however, in the binodal region, since a small composition fluctuation leads to a slightly higher free energy than that of the original configuration. Thus, phase separation in the binodal region must overcome an energy barrier to occur [77]. Furthermore, if the initial composition of the system lies outside of the miscibility gap, a final homogeneous state will be

reached.

The equilibrium compositions of a demixing system are given by the common tangent to both wells. Since we are considering that $A_{10} = A_{01} = A$, this free energy model is completely symmetric. As a result, the common tangent joins both minima together, making them the equilibrium compositions as well as the boundaries of the binodal region. Thus, the distance between compositions increases with A. As mentioned previously, a more refined approach would undo this assumption and allow an asymmetrical free energy landscape, or would consider a different activity model altogether; both out of the scope of this work.

Lastly, while the incorporation of this activity model makes phase separation a possible outcome for the system, the formulation of the free energy as defined so far—with only the pure species, ideal and non-ideal mixing contributions—is not able to accurately reproduce the dynamics of phase separation. This is because it does not provide any constraints regarding the spatial configuration of the final system: to group the bulk phases into two distinct layers would be equally as likely as to reach a chessboard-like configuration, as shown in Figure 3.2. However, intuitively, the contact surface between the two phases is expected to be minimal—consider an oil and water emulsion, eventually coalescing into two layers. In order to overcome this limitation, a new term is included in the free energy formulation, aiming to account for the contribution of having a diffuse interface present in the system.

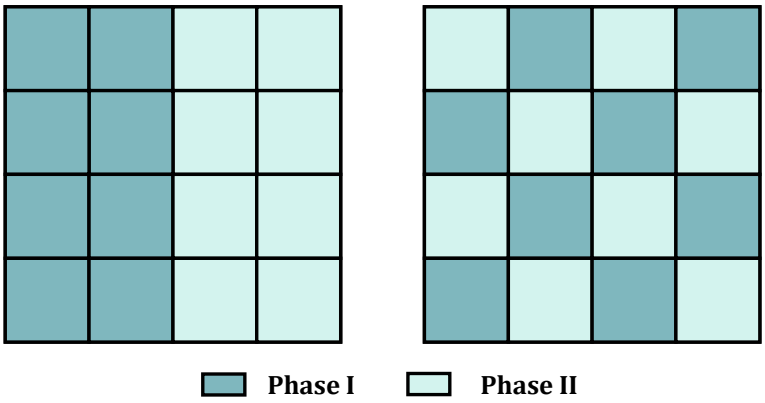


FIGURE 3.2: Diagram of potential system configurations after undergoing phase separation. Note that, if the gradient term is not incorporated into the free energy functional, both of these configurations are equally probable.

Non-locality in the free energy functional

The contributions to the free energy presented until this point are of a local nature. To determine their value at a particular point of the system, only the composition at that specific point is needed. This work studies the addition of a non-local term based on Cahn and Hilliard's formulation [14], making the free energy dependent not only on c_1 and c_0, but also on their spatial gradients: ∇c_1 and ∇c_0. This implies that the free energy in a particular point is also affected by the compositions in its vicinity.

Introducing this term makes the free energy no longer a function of composition, but a functional, as presented in Equation (3.15). While functions take a scalar as input and output another

scalar, a functional takes an entire function as input—the density profile in space, in this case—and produces a scalar.

$$F\left[c_i(\mathbf{r}), \nabla c_i(\mathbf{r})\right] = \int f\left[c_i(\mathbf{r})\right] d\mathbf{r} + \int \left[\frac{1}{2}\sum_{ij=0}^{1} \kappa_{ij} \nabla c_i(\mathbf{r}) \cdot \nabla c_j(\mathbf{r})\right] d\mathbf{r} \tag{3.15}$$

where $\boldsymbol{r}$ is the volume of the system and $\kappa_{ij}\ \left[L^5\right]$ are called gradient energy parameters [14] and can be composition-dependent.

The first term on the right-hand side of Equation (3.15) groups all local contributions to the free energy, as written in Equation (3.14). The following gradient term constitutes the non-local contribution.

The positive sign in the gradient term in Equation (3.15) indicates that it imposes a penalty upon the free energy. In particular, it corresponds with the energetic cost of having compositional inhomogeneities in the system, and thus, any interfaces within it. This means it not only accounts for any temporary interfaces that arise during the mixing of the two streams, but also helps regulate the morphology of the system during liquid-liquid phase separation. A larger gradient coefficient imposes a higher energetic penalty for composition differences, forcing their relaxation and leading to less numerous, smoother and wider interfaces.

From the perspective of a non-separating system, introducing this penalty for composition differences could lead to faster diffusion, as it represents an increase of the driving force for mass transfer. This hypothesis is explored in Section 3.4.3.

Therefore, the gradient term introduces a new length scale into the system, related to the interfacial width. Since this term determines the extent to which the chemical potential at a given point is affected by the compositions of its neighbouring regions, this length scale is also related to the range of molecular interactions. Therefore, the thickness of the interface is also expected to increase with molecule size, with a pharmaceutical solvent-API system exhibiting thinner interfaces than a polymeric one, for example.

The gradient coefficients are typically composition dependent, especially for small molecule systems such as those found in crystallisation; however, this dependency can be ignored for polymer systems in which the molecule size is considerably larger [122]. As Inguva *et al.* [123] laid out, following the approach in [130, 131], these gradient parameters can be written as a sum of an entropic and an enthalpic contribution: $\kappa = \kappa_S + \kappa_H$. If the free energy of mixing can be decomposed into the sum of an ideal and a non-ideal contribution, as occurs in Equation (3.14), distinct expressions can be obtained for κ_H and κ_S. Disregarding the composition dependency in this parameter corresponds with neglecting its entropic contribution [122]. More information on this can be found in [123].

On account of the free energy becoming a functional, the chemical potential must now be calculated through a variational derivative of the free energy with respect to the composition profile, as presented in Equation (3.16). Its physical meaning remains unchanged, describing how the free energy at a given point varies with a small change in the composition at that point. The subtlety is that changing the composition at this location will lead to changes in the neighbouring

slopes of the composition profile; due to the gradient term, these will also affect the value of the free energy at the point of interest. This is why the free energy now must take the entire profile as input, and not just the local composition. Thus, if the gradient term was not included, the chemical potential would again be calculated through Equation (3.5).

$$\beta\mu_i = \left.\frac{\delta F}{\delta c_i(\mathbf{r})}\right|_{T,V,c_{j\neq i}} \tag{3.16}$$

The definition of the chemical potential given in Equation (3.16) can be expanded through a chain rule into the variables (c, x_1), as shown in Equations (3.17) and (3.18). It can be seen that $\delta F/\delta c$ will be a common contribution to the chemical potentials of both species, related to the change that adding a particle into the system makes on its total mass.

$$\frac{\delta F}{\delta c_1} = \frac{\delta F}{\delta c}\frac{\partial c}{\partial c_1} + \frac{\delta F}{\delta x_1}\frac{\partial x_1}{\partial c_1} \tag{3.17}$$

$$\frac{\delta F}{\delta c_1(\mathbf{r})} = \frac{\delta F}{\delta c} + \frac{(1-x_1)}{c}\frac{\delta F}{\delta x_1(\mathbf{r})} \tag{3.18}$$

where $\partial c/\partial c_1 = 1$ and $\partial x_1/\partial c_1 = (1-x_1)/c$.

On the other hand, $\delta F/\delta x_i$ is related to the changes in the composition of the system. A similar chain rule expansion, given in Equations (3.19) and (3.20), shows that this expression corresponds with the difference between the chemical potentials.

$$\frac{\delta F}{\delta x_1} = \frac{\delta F}{\delta c_1}\frac{\partial c_1}{\partial x_1} + \frac{\delta F}{\delta c_0}\frac{\partial c_0}{\partial x_1} \tag{3.19}$$

$$\frac{\delta F}{\delta x_1(\mathbf{r})} = c\left(\beta\mu_1 - \beta\mu_0\right) \tag{3.20}$$

where $\partial c_1/\partial x_1 = c$ and $\partial c_0/\partial x_1 = -c$.

The final form of the chemical potentials is given, for both species, in Equations (3.21)–(3.24), where it can be assumed that the system is incompressible. It was calculated according to Equation (3.16), considering that $\kappa_{ij} = \kappa_{ji}$.

$$\beta\mu_1 = \frac{\partial f}{\partial c_1} + \frac{1}{2}\left[\frac{\partial \kappa_{11}}{\partial c_1} - 2\frac{\partial \kappa_{10}}{\partial c_1} + \frac{\partial \kappa_{00}}{\partial c_1}\right]\left(\nabla c_1\right)^2 - (\kappa_{11}-\kappa_{10})\nabla^2 c_1 - \nabla\left(\kappa_{11}-\kappa_{10}\right)\cdot\nabla c_1 \tag{3.21}$$

$$\beta\mu_0 = \frac{\partial f}{\partial c_0} + \frac{1}{2}\left[\frac{\partial \kappa_{11}}{\partial c_0} - 2\frac{\partial \kappa_{10}}{\partial c_0} + \frac{\partial \kappa_{00}}{\partial c_0}\right]\left(\nabla c_1\right)^2 + (\kappa_{00}-\kappa_{10})\nabla^2 c_1 + \nabla\left(\kappa_{00}-\kappa_{10}\right)\cdot\nabla c_1 \tag{3.22}$$

$$\frac{\partial f}{\partial c_1} = \beta\mu_1^\circ + \ln x_1 + A(1-x_1)^2 \tag{3.23}$$

$$\frac{\partial f}{\partial c_0} = \beta\mu_0^\circ + \ln(1-x_1) + Ax_1^2 \tag{3.24}$$

where $\beta\mu_i^\circ \equiv \beta\mu_i^\circ(T, p_0)$ and $A \equiv A(T, p_0)$.

Note that the contribution of the ideal, non-ideal and interfacial pieces can be separated in different terms, and therefore these expressions allow to recover local diffusion when the gradient coefficient is zero, and Fickian diffusion when both this and the Margules parameter are zero.

The modularity of the model also allows to study the effect of the non-local contribution in an otherwise ideal system, by simply setting A to zero.

Adaptability of the phase-field method to diffusion, nucleation and growth

Recalling from Section 3.2.2, LLPS can follow two different dynamics, attending to the region of the phase diagram where they take place: binodal or spinodal. While LLPS in the spinodal is a spontaneous process in which the free energy is decreasing at all times, transformations in the binodal region must overcome a free energy barrier, forcing it to temporarily increase [77]. This barrier prohibits the modelling of phase separation within this region by the mass transfer model presented in this work, since the free energy can only decrease with time. The aim of this section is to prove this, and give an indication of how this limitation could be circumvented.

The definition of the rate of change of the free energy with time is given in Equation (3.25). Expanding this consecutively through the chain rule, the product rule and the divergence theorem, then describing the diffusive flux as proportional to $\mathbb{d}_i$, and lastly considering that there is no flow out of the boundaries, Equation (3.27) is reached.

$$\frac{dF}{dt} = \sum_{i=1,0} \int d\mathbf{r} \left[\frac{\delta F}{\delta c_i(\mathbf{r})} \frac{\partial c_i}{\partial t} \right] \tag{3.25}$$

$$= - \sum_{i=1,0} \int d\mathbf{r} \left[\beta \mu_i \nabla \cdot \mathbf{J_i} \right] \tag{3.26}$$

$$= - \int d\mathbf{r} \left[\mathrm{D}_{10} \left(\nabla \beta \mu_1 \right)^2 \right] \tag{3.27}$$

It can be seen from Equation (3.27) that for the free energy to increase at any point in time the diffusion coefficient of the system would have to be negative, since the chemical potential gradient has been squared. Since D must remain positive, it is clear that the rate of change of the free energy functional with time is monotonically decreasing.

Consequently, the presented model is not able to describe phase changes occurring within the binodal region, which follow nucleation and growth dynamics and thus must overcome an energy barrier to occur. Nonetheless, this model can predict the time and location of supersaturation spikes, indicating when and where nucleation could happen. Moreover, the model can simulate the dynamics of phase transformations in the spinodal, which will improve the accuracy of supersaturation predictions in the vicinity of this region.

The phenomenon of nucleation and growth has been extensively studied in the context of alloy formation. There are two main methods in which this limitation may be circumvented. The first reproduces the stochastic nature of nucleation by adding a noise term into the governing equations, which results in eventual automatic apparition of nuclei [132–135]. The second alternative treats nucleation explicitly, by artificially inserting nuclei in the simulation when certain criteria are met. For example, the local supersaturation within the domain may be used to calculate the local nucleation rate and subsequently the local nucleation probability. If this probability is higher than a certain threshold, a nucleus is artificially seeded into the location that met the criteria [136]. Note that growth can be handled by the unmodified phase-field model,

which has the capability to determine whether the nuclei will enlarge or dissolve, given that in both alternatives the free energy naturally decreases.

Non-dimensionalisation of the governing equations

The diffusion system presented in this work has been solved in its nondimensional form, since doing so allows to reduce the number of parameters that the system is dependent on. The only parameter in the final system of equations that has units of time is the diffusion coefficient. Thus, by selecting a characteristic time based on it, $\tau = L^2/D_{10}$, it vanishes from the equation.

There are three different parameters that contain length units in the equation, and therefore three different length scales to consider. The first is the total size of the system, L_b. The second is the total concentration, which has units of $1/L^3$ and thus leads to a length scale $L_c = c^{-1/3}$, which is related to the distance between molecules. The last one is the gradient free energy coefficient, which has units of L^5, making the final length scale $L_g = \kappa^{1/5}$. This is related to the range of interactions between molecules, due to the gradient, and to the width of the interface.

Since this work seeks to explore the impact of the gradient coefficient, using L_g as the characteristic length for the nondimensionalisation is discarded. Out of the two other options, selecting L_c for this purpose will be more advantageous, since it will allow to eliminate c from the final equation. Thus, the selected characteristic length is $c^{-1/3}$.

The remainder of the section explores the equilibrium behaviour of this model, in particular, the interfacial tension and equilibrium composition profiles, and their evolution with the Margules and gradient coefficients.

The interfacial tension and its relationship with κ

The gradient term acts as a penalty for sharp spatial compositional changes in the system, hence controlling the formation of interfaces within it. Therefore, it is expected to have a relation with known interfacial properties. To help provide a physical meaning to the gradient coefficients, this section derives its relation with the interfacial tension for a binary system.

Let the system of study be one-dimensional and of infinite length, divided into two bulk phases (I and II) joint by a planar interface and in thermodynamic equilibrium. The coexistence compositions of these bulk phases are given by c^I and c^{II}, respectively.

The free energy functional of the system is defined in Equation (3.28), and the chemical potential for species 1, in Equation (3.29). Since the system is in equilibrium, the chemical potentials of both species (denoted as γ_1 and γ_0 to signal equilibrium) will maintain a constant value at every position.

$$F[c_1(z), c_1'(z)] = \int dz \left[f[c_1(z)] + \frac{1}{2}\left[\kappa_{11}[c_1'(z)]^2 + 2\kappa_{10}c_1'(z)c_0'(z) + \kappa_{00}[c_0'(z)]^2\right]\right] \tag{3.28}$$

$$\gamma_1 = \frac{\partial f}{\partial c_1} - (\kappa_{11}c_1'(z))' - (\kappa_{10}c_0'(z))' + \frac{1}{2}\frac{\partial \kappa_{11}}{\partial c_1}(c_1'(z))^2 + \frac{\partial \kappa_{10}}{\partial c_1}c_1'(z)c_0'(z) + \frac{1}{2}\frac{\partial \kappa_{00}}{\partial c_1}(c_0'(z))^2 \tag{3.29}$$

where c_i' represents the first derivative of c_i in space, dc_i/dz.

The interfacial tension (σ) of a system is defined as the work per unit area required to form an interface between two bulk phases. This can be expressed as the difference between the free energy of the heterogeneous, phase-split system, and the free energy of the two individual bulk phases when existing disconnected from each other, as reflected in Equation (3.30).

$$\beta\sigma = F - \int_I dz f\left(c_1^I\right) - \int_{II} dz f\left(c_1^{II}\right) \tag{3.30}$$

where I goes from $-\infty$ to the interface location, and II, from the interface to $+\infty$. Note that, was this integral posed in 3D, the LHS would be multiplied by the total area of the interface, and in the RHS the differential would have units of volume.

The relation between σ and the gradient coefficients can be found by calculating the equilibrium free energy density of the system (f) from $c_1\gamma_1 + c_0\gamma_0$, as given in Equation (3.31), and substituting this into the definition of σ given in Equation (3.30). Details on the algebra involved can be found in Appendix C.

$$c_1\gamma_1 + c_0\gamma_0 = f - \frac{1}{2}\kappa_{11}(c_1')^2 - \kappa_{10}c_1'c_0' - \frac{1}{2}\kappa_{00}(c_0')^2 + \beta p_0 \tag{3.31}$$

The LHS and RHS of Equation (3.31) correspond respectively with the total Gibbs and Helmholtz free energy densities of the system in equilibrium. A key assumption made during its derivation (see Appendix C) is that the chemical potential of both species is a scalar, that is, maintains a constant value across the entire system. This establishes Equation (3.31) as a key condition for thermodynamic equilibrium, indicating that the governing equations of a system in equilibrium must necessarily fulfil this expression. This same conclusion was reached by Naumann and Balsara during their study of phase equilibria within systems incorporating a gradient term [137]. Substituting this expression for f into the general free energy density functional, and that into Equation (3.30), Equation (3.32) is reached.

$$\begin{aligned}\beta\sigma = \int_I dz\left[\gamma_1\left(c_1 - c_1^I\right) + \gamma_0\left(c_0 - c_0^I\right)\right] + \int_{II} dz\left[\gamma_1\left(c_1 - c_1^{II}\right) + \gamma_0\left(c_0 - c_0^{II}\right)\right] \\ + \int dz\left[\kappa_{11}c_1'c_1' + 2\kappa_{10}c_1'c_0' + \kappa_{00}c_0'c_0'\right]\end{aligned} \tag{3.32}$$

This expression can be simplified further through a clever placement of the interface, chosen so that the area between the concentration profile of the heterogeneous system and the concentration of the two respective bulk phases is equal in magnitude, but of opposite sign, on either side of the interface. This implies that the addition of the first two terms in the RHS of Equation (3.32) will be zero. This concept is illustrated in Figure 3.3.

Lastly, considering that the system is incompressible and grouping the gradient coefficients into $\kappa = \kappa_{11} - 2\kappa_{10} + \kappa_{00}$, the final expression for the interfacial tension of a one-dimensional binary system is given in Equation (3.33).

$$\beta\sigma = \int \kappa(c_1')^2 dz \tag{3.33}$$

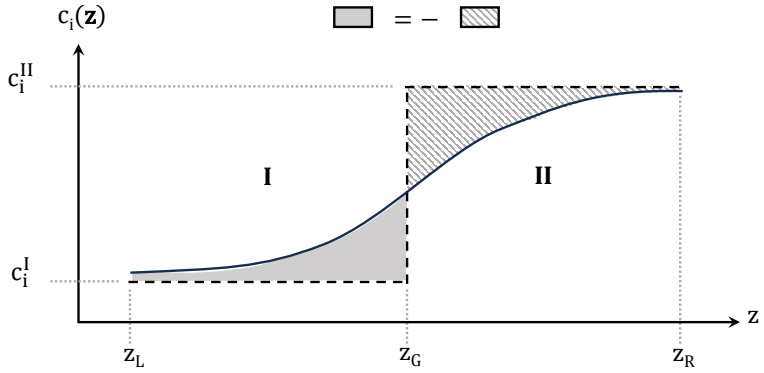


FIGURE 3.3: Diagram of the heterogeneous system in equilibrium. The continuous black line depicts its concentration profile, whereas the dashed lines correspond with the concentration of the individual, unconnected bulk phases: c^I and c^{II}. The location of the interface, z_G, is chosen so that the shaded grey and striped areas are equal in magnitude but of opposite sign.

where c_1' corresponds with the equilibrium composition profile of species 1.

The nondimensionalisation of this expression is shown in Equation (3.34). Since $\beta\sigma$ has units of $[1/L^2]$, it can be nondimensionalised through $\widetilde{\sigma} = \beta\sigma c^{-2/3}$. As for κ, it has units of $[L^5]$ and can be nondimensionalised through $\tilde{\kappa} = \kappa c^{5/3}$.

$$\widetilde{\sigma} = \int \tilde{\kappa}(x_1')^2 d\tilde{z} \tag{3.34}$$

It is clear that the interfacial tension is directly proportional to the gradient coefficient, and therefore the value of this coefficient for a specific system can be determined from experimental interfacial tension measurements. Physically this was expected, since κ controls the width of the interface by raising the free energy penalty associated with having compositional gradients in the system. This results in an increased energetic cost for the interface, which is an equivalent concept to raising the interfacial tension. This dependency also explains why a free energy model without a gradient term is not capable of simulating LLPS, and fails when in the spinodal: neglecting this term is equivalent to defining the interfacial tension as zero.

Hence, increasing or decreasing the value of κ in the simulations is equivalent to studying a system with a higher or lower interfacial tension, respectively. Their relationship is shown for $A = 3$ in Figure 3.4(a), where a concave curve dominates the trend at lower values, gradually approaching a more linear correlation as $\tilde{\kappa}$ increases. The interfacial tension also depends on the bulk thermodynamics of the system, which in this work are controlled by A. Since the Margules parameter determines the coexistence compositions, as illustrated in Figure 3.1, it directly affects the shape of the equilibrium composition profile within Equation (3.33). Consequently, Figure 3.4(b) depicts the evolution of the interfacial tension with this parameter when keeping $\tilde{\kappa}$ at a constant value of 0.05.

It becomes clear that the dependency between the interfacial tension and the Margules parameter is linear for most values of A in the studied range, albeit the trend becomes more curved in the vicinity of $A = 2$. Below this threshold the interfacial tension disappears, since the free

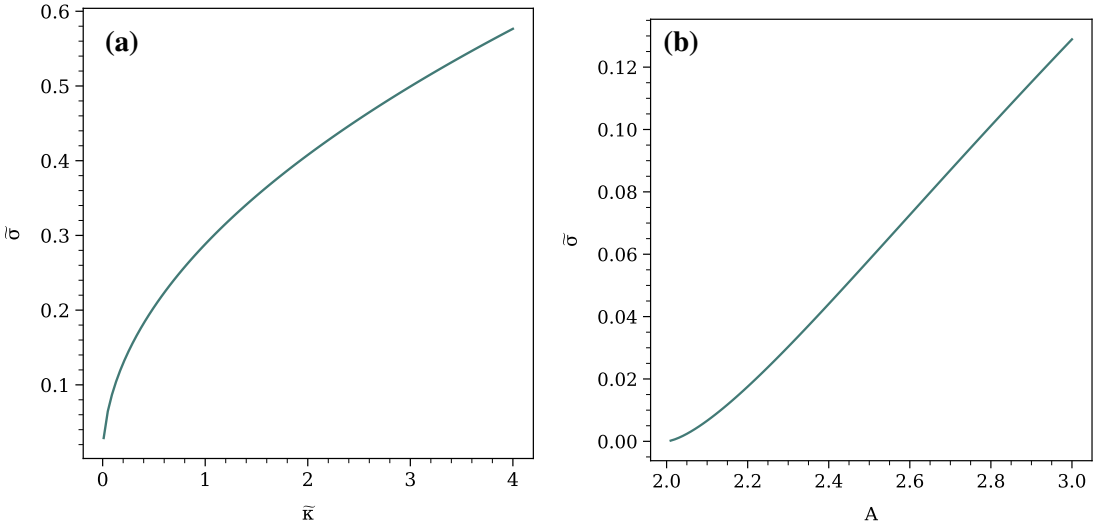


FIGURE 3.4: Evolution of the non-dimensional interfacial tension with respect to (a) the non-dimensional interfacial free energy coefficient $\tilde{\kappa}$, with a fixed $A = 3$, and (b) with respect to the Margules parameter A, with a fixed $\tilde{\kappa} = 0.2$.

energy density of the system becomes a single well, as depicted in Figure 3.1(a), and the mixing process results in only one final homogeneous phase. Moreover, since the gap between the equilibrium compositions of both phases widens as A increases, and so does the free energy of the compositions in-between, it was expected to observe a positive correlation between the interfacial tension and this parameter.

Equilibrium composition profiles

Now that the physical meaning of κ and its relation with the interfacial tension has been discussed, this section focuses on determining how its magnitude impacts the equilibrium composition profiles. Given the physical activity model incorporated in this work, these profiles must be calculated numerically, with the equilibrium condition derived in Equation (3.31) as the starting point.

Rewriting this expression for an incompressible system, Equation (3.35) is reached. For the sake of readability, Equations (3.36) and (3.37) define the chemical potentials of both species in equilibrium. The local Helmholtz free energy density of the system, f, was defined in Equation (3.14).

$$\frac{\kappa c^2}{2}(x_1')^2 = f - c_1\gamma_1 - c_0\gamma_0 + \beta p_0 \tag{3.35}$$

$$\gamma_1 = \beta\mu_1^\circ(T,p_0) + \ln x_1^I + A\left(1-x_1^I\right)^2 = \beta\mu_1^\circ(T,p_0) + \ln x_1^{II} + A\left(1-x_1^{II}\right)^2 \tag{3.36}$$

$$\gamma_0 = \beta\mu_0^\circ(T,p_0) + \ln\left(1-x_1^I\right) + A\left(x_1^I\right)^2 = \beta\mu_0^\circ(T,p_0) + \ln\left(1-x_1^{II}\right) + A\left(x_1^{II}\right)^2 \tag{3.37}$$

The entirety of the RHS in Equation (3.35) can be grouped into a known variable, Δf. Since the equilibrium chemical potentials are constant, the equilibrium compositions used to define γ_1 and γ_0 can correspond to either phase. Thus, the substitution of both leads to two analogous

forms of Δf, presented in Equations (3.38) and (3.39).

$$\Delta f = c x_1 \ln \frac{x_1}{x_1^I} + c(1-x_1)\ln \frac{1-x_1}{1-x_1^I} - Ac\left(x_1 - x_1^I\right)^2 \tag{3.38}$$

$$\Delta f = c x_1 \ln \frac{x_1}{x_1^{II}} + c(1-x_1)\ln \frac{1-x_1}{1-x_1^{II}} - Ac\left(x_1 - x_1^{II}\right)^2 \tag{3.39}$$

With this, every piece needed to calculate the equilibrium composition profile is known. Applying the time and length nondimensionalisations discussed above, Equation (3.40) presents the final expression used to calculate these profiles.

$$\frac{dx_1}{d\tilde{z}} = \left[\frac{2}{\tilde{\kappa}}\right]^{1/2}\left[\frac{\Delta f}{c}\right]^{1/2} \tag{3.40}$$

This way, Figure 3.5 describes the effect of the gradient coefficient (a) and the Margules parameter (b) on the equilibrium composition profile of species 1. Focusing first on the effect of $\tilde{\kappa}$ presented in Figure 3.5(a), it is clear that a higher value of this gradient coefficient leads to a wider interface. This is due to an increased penalisation of composition gradients and thus results in a more diffuse interface.

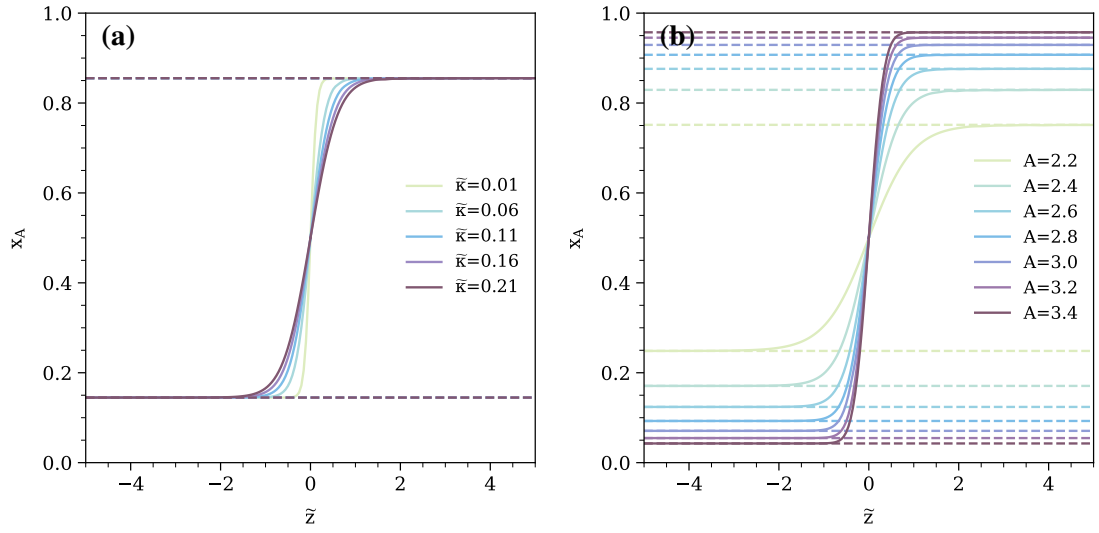


FIGURE 3.5: Equilibrium composition profiles at different conditions (solid lines) and their respective bulk equilibrium compositions (dashed lines). (a) Equilibrium behaviour at $A = 2.5$ and different values of $\tilde{\kappa}$. (b) Equilibrium behaviour for $\tilde{\kappa} = 0.2$ and different values of the Margules parameter.

As for the effect of the Margules parameter A, there are two main trends observed in Figure 3.5(b). Firstly, it is clear that a higher degree of incompatibility between the two species pushes the equilibrium compositions further apart, as expected from the discussion in Section 3.2.2. Secondly, the interface widens with lower values of A, which was not expected given that the value of $\tilde{\kappa}$ was kept constant for this study. Attending to Figure 3.1(a), the higher the A, the larger the drive to phase-separate is in the system, and thus the higher the energetic penalty

becomes for compositions in-between the coexistence values. Therefore, at constant κ, larger values of A will lead to increasingly sharper interfaces.

Solubility and supersaturation as functions of the chemical potential

The apparition of gradient terms within the chemical potential will unequivocally change the definition of key variables in the crystallisation process, one of which is the supersaturation, which is the driving force for crystallisation. Thus, supersaturation will dictate the times and regions where a system may form solid nuclei, making it one of the most important parameters in a crystallisation system. An accurate supersaturation definition will lead to a better prediction of the nucleation rate and in turn of the probability of nucleation, both key variables in crystallisation models such as PBM or the PRISMS framework [136].

The physical reason why crystallisation occurs is because the chemical potential of a system containing a mixture of solid and dissolved API is lower than the chemical potential of a system where all of the API is dissolved, making the first system more stable in comparison. Therefore, the system will be saturated when these two chemical potentials are equal: $\beta\mu_1^{(L)} = \beta\mu_1^{(S)}$.

The chemical potential of all species in the system has been given in Equations (3.21)– (3.24); these expressions are valid for both the solid and liquid phase. Focusing on species 1, its chemical potential in the solid phase can be considerably simplified by assuming that the formed nuclei are completely pure: $x_1^{(s)} = 1$. All contributions but that of the pure species vanish, since $\ln(1) = 0$, $A(1-1)^2 = 0$, and $\nabla(1) = 0$. Therefore, $\beta\mu_1^{(s)} = \beta\mu_1^{\circ,(s)}$.

Substituting this into the equilibrium condition, we find that $\beta\mu_1^{\circ,(S)} = \beta\mu_1^{(L)}$. Regarding the chemical potential of the liquid phase, $\beta\mu_1^{(L)}$, it is important to specify that it is tracked during the diffusion process as $\beta\mu_1^{(L)} - \beta\mu_1^{\circ,(L)}$. The contribution of the pure species to $\beta\mu_1$ has been not been considered, since it bears no impact on the driving force for mass transfer—the gradient of a constant is zero—nor on the evolution of the chemical potential with time. Thus, subtracting it to both sides in the equilibrium condition, Equation (3.41) is reached.

$$\beta\mu_1^{(L)} - \beta\mu_1^{\circ,(L)} = \beta\mu_1^{\circ,(S)} - \beta\mu_1^{\circ,(L)} \tag{3.41}$$

This expression denotes the solubility of the pure solid phase in the liquid solution. The LHS corresponds with the chemical potential tracked during the mass transfer study. As for the RHS, the value of $\beta\mu_1^{\circ,(S)} - \beta\mu_1^{\circ,(L)}$ is intrinsic to the physical system being studied, since it depends only on the solid and liquid properties of the chosen solute. Thus, this variable defines the solubility of the system, leading to the definition of supersaturation (s) and of the supersaturation ratio (S) in Equations (3.42) and (3.43), respectively.

$$s = \left(\beta\mu_1^{(L)} - \beta\mu_1^{\circ,(L)}\right) - \left(\beta\mu_1^{\circ,(S)} - \beta\mu_1^{\circ,(L)}\right) \tag{3.42}$$

$$S = \frac{\left(\beta\mu_1^{(L)} - \beta\mu_1^{\circ,(L)}\right)}{\left(\beta\mu_1^{\circ,(S)} - \beta\mu_1^{\circ,(L)}\right)} \tag{3.43}$$

While the supersaturation does not have any impact on the mass transfer dynamics presented in this work, it does help interpret its results from a crystallisation perspective. A system that favours crystallisation will present a positive value for s, as this means that species 1 has a lower chemical potential as a solid than in the solution. Similarly, such a system will have a value of S larger than 1. Thus, a system is supersaturated when $s > 0$ and $S > 1$; undersaturated when $s < 0$ and $S < 1$, and at equilibrium when $s = 0$ and $S = 1$.

3.2.3 Diffusion dynamics

Now that the thermodynamics of the proposed model have been detailed and explored, this section focuses on outlining the main considerations to be made regarding mass transfer dynamics.

The model chosen to describe diffusive dynamics is Maxwell-Stefan diffusion, presented in equations (3.44) and (3.45) for a binary system. It was developed with gradients of chemical potentials as the driving force for diffusion [11, 138], and thus it provides a suitable framework in which to cast our proposed free energy model.

$$\mathbf{J_1} = -Đ_{10} c_1 \nabla \beta\mu_1 \tag{3.44}$$

$$\frac{\partial c_1}{\partial t} = \nabla \cdot \left(Đ_{10} c_1 \nabla \beta\mu_1 \right) \tag{3.45}$$

where $Đ_{10}$ corresponds with the Maxwell-Stefan diffusion coefficient.

In this work, the driving force for mass transfer has been written as a difference of chemical potentials, as detailed in Equation (3.48). This approach, seen in Petrischeva and Abart [121], helped increase the convergence of the governing equations when solved numerically. Moreover, it indirectly makes the framework more robust, by building in compliance with the Gibbs-Duhem equation, shown in Equation (3.46) for a binary isothermal and isochoric system, into the driving force.

$$c_0 \nabla \beta\mu_0 + c_1 \nabla \beta\mu_1 = 0 \tag{3.46}$$

$$\nabla \beta\mu_1 = \nabla \beta\mu_1 - x_0 \nabla \beta\mu_0 - x_1 \nabla \beta\mu_1 \tag{3.47}$$

$$= x_0 \nabla \left(\beta\mu_1 - \beta\mu_0 \right) \tag{3.48}$$

The sum of the diffusive fluxes across all species in the system must be zero. The Maxwell-Stefan formulation, given in Equation (3.44), complies with this when the gradient term is not included, which can be proven by substituting Equations (3.23) and (3.24) into Equation (3.49). Note that the RHS of this expression corresponds with the Gibbs-Duhem equation (3.46).

$$\mathbf{J_0} + \mathbf{J_1} = c_0 \nabla \beta\mu_0 + c_1 \nabla \beta\mu_1 \tag{3.49}$$

This way, the reformulation of the driving force as a difference in chemical potentials enforcing compliance with Gibbs-Duhem indirectly enforces the condition that the sum of all diffusive fluxes must amount to zero. This can be seen by substituting Equation (3.48) into Equation (3.44),

and then working through $J_1 + J_0$. The updated version of the diffusive flux is given in Equation (3.50).

$$\mathbf{J_1} = -Đcx_1x_0\nabla\left(\beta\mu_1 - \beta\mu_0\right) \tag{3.50}$$

The system will thus reach dynamic equilibrium when $\nabla(\beta\mu_1 - \beta\mu_0) = 0$, which, attending to Equation (3.19), corresponds with $\nabla(\delta F/\delta x_1) = 0$. This is not a tight enough constraint to ensure chemical equilibrium [137], which is defined through $\nabla\beta\mu = 0$; nonetheless, the correct definition of the chemical potential will fulfil both constraints. A more careful look at Equation (3.21) reveals that whether a definition of the chemical potential is correct or not will depend entirely on choosing an adequate form for the composition dependence of κ. Thus, the dynamics and thermodynamics of the diffusion process have been successfully decoupled, since to ensure a correct mass transfer prediction it is only necessary to correctly define $\nabla(\beta\mu_1 - \beta\mu_0)$. A more detailed insight of the consequences this has upon the thermodynamics of the system is provided in Section 3.4.1.

Considering the definition of both chemical potentials given in equations (3.21)–(3.24), and specialising to the case in which κ_{ij} is a constant, the gradient of the difference in chemical potentials is given in Equation (3.51).

$$\nabla\left(\beta\mu_1 - \beta\mu_0\right) = \left[\frac{1}{x_1} + \frac{1}{x_0} - 2A\right]\nabla x_1 - \nabla\left[\kappa\nabla^2 c_1\right] \tag{3.51}$$

where $\kappa = \kappa_{11} - 2\kappa_{10} + \kappa_{00}$.

Substituting Equations (3.50) and (3.51) into the continuity equation, its final form for species 1 is reached in Equation (3.52). Equation (3.53) corresponds with its nondimensional formulation. This model has been named "CaHiMaS" in this work, blending the name of its two main inspirations: Maxwell-Stefan diffusion and the Cahn-Hilliard phase-field model, from which the idea for the gradient term came from.

$$\frac{\partial x_1}{\partial t} = Đ\nabla^2 x_1 - 2AĐ\nabla\cdot\left[x_1x_0\nabla x_1\right] - Đ\nabla\cdot\left[x_1x_0\nabla\left[c\kappa\nabla^2 x_1\right]\right] \tag{3.52}$$

$$\frac{\partial x_1}{\partial \tilde{t}} = \tilde{\nabla}^2 x_1 - 2A\tilde{\nabla}\cdot\left[x_1x_0\tilde{\nabla}x_1\right] - \tilde{\nabla}\cdot\left[x_1x_0\tilde{\nabla}\left[\tilde{\kappa}\tilde{\nabla}^2 x_1\right]\right] \tag{3.53}$$

where $\tilde{\nabla}$ corresponds with the nondimensional gradient of a variable in space, in this case evaluated in 1D.

3.3 Simulation methodology

The simulations presented in this work focus on a 1D spatial system, a schematic diagram of which is shown in Figure A. The continuity equation (3.53) was solved by applying finite volume discretisation. This method is particularly suitable for mass transfer problems, as it enforces mass conservation over the domain [139]. In particular, the simulation was implemented within the FiPy [140] library in Python.

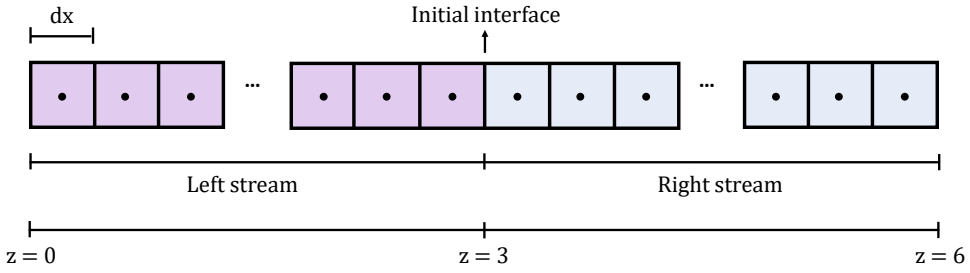


FIGURE 3.6: Schematic diagram of the discretised one-dimensional system. A two-layered initial configuration is depicted, indicating the position of the interface and what in this work have been sometimes referred to as left and right streams.

The fourth-order term within the continuity equation was discretised through a coupled system of equations, presented in Equation (3.54), with x_1 and ψ as the main variables. This was needed in order to avoid numerical instabilities, and to cast the system into FiPy's framework. This way, the main outputs of the system are the evolution of x_1 and ψ with time.

$$\begin{cases} \frac{\partial x_1}{\partial \tilde{t}} = \tilde{\nabla}^2 x_1 - \tilde{\nabla} \cdot \left[2A x_1 (1 - x_1) \tilde{\nabla} x_1 \right] - \tilde{\nabla} \cdot \left[x_1 (1 - x_1) \tilde{\nabla} \psi \right] \\ \psi = \tilde{\kappa} \tilde{\nabla}^2 x_1 \end{cases} \tag{3.54}$$

The main shared parameters of all simulations are detailed in Table 3.1(left), and the studied parameter combinations have been summarised in Table 3.1(right). All studies employed SciPy's `scipy.sparse.linalg.splu` [141] solver, as well as Neumann boundary conditions, which are suited to reproduce diffusion in a closed system with no flow across the boundaries. Figure 3.7 summarises the two different types of initial conditions studied in this work.

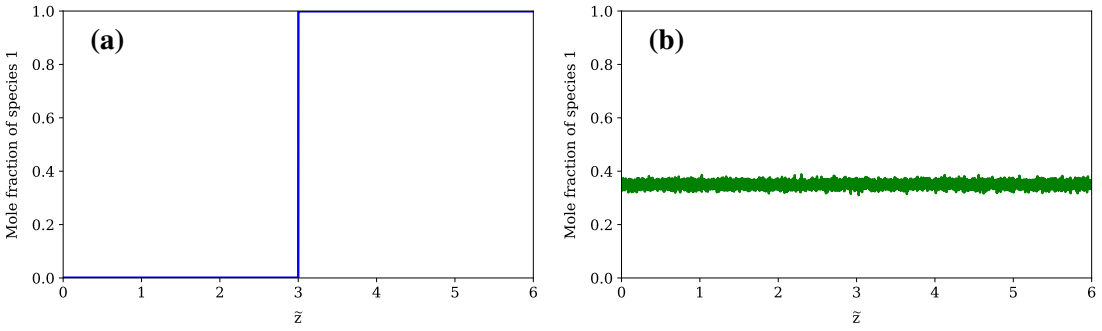


FIGURE 3.7: Diagram of the two different initial conditions employed within this work. (a) Step-like, aiming to reproduce two streams put in contact with each other. (b) Gaussian noise, randomly sampled from a distribution with $\overline{x}_1 = 0.35$ and $\sigma^2 = 10^{-4}$.

Four different studies were run as part of this work in binary mixing. Firstly, the definition of the gradient coefficient, κ, was addressed. As detailed in Section 3.4.1, this work found that the formulation of its composition dependence is nontrivial, since not all of them fulfil the condition of chemical equilibrium, that is, a constant value of $\beta\mu$ in space. This work explores the three

TABLE 3.1: Selected simulation parameters. Left: parameters shared between all performed simulations. Right: variable set of studied conditions. Attending to the left, `nx` and `dx` correspond with the number of volume elements in the discretised system and their width, respectively; `res tol` with the tolerance allowed within the residual step of the solver; `stag tol` with the tolerance considered to decide whether the minimum possible residual has been reached, or the solver has stagnated; `save freq` with the frequency with which a timestep was saved; lastly, `dt fcn` is the function used to define timestepping, and `dt` and `n` are its variables. Attending to the right, ICs corresponds with initial conditions; **G** to the group of studies those simulations belong to; the three functions tested as part of group 1 have been detailed in Section 3.4.1; GN stands for Gaussian noise, defined through mean ($\overline{x}_1$) and variance (σ^2); and, lastly, $\tilde{\kappa}$ and A correspond with the nondimensionalised gradient coefficient and Margules parameter, respectively.

Property	**Value**	**G**	$\tilde{\kappa}$	**A**	**ICs**	**Duration**
`nx`	$12 \cdot 10^3$	1	$\kappa = f_I(c)$	3	Step, 50%, 0.999-0.001	400
`dx`	$5 \cdot 10^{-4}$	1	$\kappa = f_{II}(c)$	3	Step, 50%, 0.999-0.001	400
`res tol`	10^{-5}	1	$\kappa = f_{III}(c)$	3	Step, 50%, 0.999-0.001	400
`dt fcn`	$e^{dt+n\cdot i}$	2	0	0	Step, 50%, 0.999-0.001	400
`dt`	-7	2	0	1	Step, 50%, 0.999-0.001	400
`n`	10^{-4}	2	0.2	1	Step, 50%, 0.999-0.001	400
`stag tol`	10^{-14}	3	0, 0.1, 0.2	0	Step, 50%, 0.999-0.001	400
`save freq`	15	3	0.025, 0.1, 0.2	3	Step, 50%, 0.999-0.001	400
		4	0.025, 0.2	3	GN, $\overline{x}_1 = 0.35, \sigma^2 = 10^{-4}$	600

most natural choices, first considering no composition dependence at all (f_I), then the chemical potential form presented by Petrischeva and Abart [121] (f_{II}), and lastly, a custom composition dependence proposed by the author (f_{III}). The specific equation for each form is given in Section 3.4.1. Note that this study had to be performed for a system in which phase separation would take place, that is, $A > 2$, since a homogeneous final composition would necessarily return a flat chemical potential profile.

The second study sought to compare the effect of the gradient term on a standard diffusion problem without phase separation, with regards to the two most widely applied diffusion models: Fick's law and Maxwell-Stefan. The benchmark for this test was considered to be a system that exhibited a degree of non-ideality between the two liquids equivalent to $A = 1$. Note that, as explained in Section 3.2.3, considering no gradient term immediately returns the diffusion dynamics of the proposed model to Maxwell-Stefan, and considering ideal behaviour on top of this returns Fickian diffusion. This way, Fick's law was recovered by considering $A = 0$ and $\tilde{\kappa} = 0$; Maxwell-Stefan diffusion, through $A = 1$ and $\tilde{\kappa} = 0$, and CaHiMaS, modelled via $A = 1$ and $\tilde{\kappa} = 0.2$.

The third study sought to understand the effect of the magnitude gradient coefficient alone on an ideal system and on a system where phase separation would occur. These two cases, in combination with those explored in the second study mentioned above, cover all the potential scenarios allowed by CaHiMaS diffusion during the diffusion of the two streams.

Lastly, the fourth study conducted as part of this work aimed to prove the application of the proposed model for a nearly-homogeneous system undergoing a sudden temperature decrease, also called crash-cooling. Although the effect of temperature is not explicitly included in the

proposed model, the nondimensional Margules parameter is an inverse function of temperature, as explained in Section 3.2.2, and thus increasing its value is equivalent to decreasing the latter. This way, a high-enough temperature to maintain the system as a homogeneous mixture would correspond with $A < 2$, and a sudden decrease in temperature would entail a sudden change to $A > 2$. This is the reason why the proposed simulation considers a nearly-homogeneous initial conditions and that $A = 3$. Note that the duration of this study had to be longer due to the system starting further away from equilibrium.

The timestep evolution was selected to follow an exponential trend due to the nature of this physical problem: it is fast-paced in early times, requiring very small steps, but as it approaches equilibrium more, the changes take longer to be perceivable [142]. In fact, too small a timestep at this stage can cause the solution to become stagnant across iterations. While it is complicated to find a combination of parameters that can succeed in both regimes, it is not entirely necessary. The solution stagnating in a particular timestep only entails the solution vector remaining the same as for the previous one, meaning that these timesteps are completely inert. Eventually, the time increase becomes large enough for the solution to continue moving forward. Hence, the approach followed in this work was primarily concerned with an adequate simulation of the early times, and the inert iterations were filtered out during the data postprocessing. Note that the output of an iteration was only saved as part of the output dataset every 15 timesteps, given the large volume of data generated by each simulation—around 4500 output files after postprocessing, and after the implementation of this measure.

The value of all non-dimensionalised parameters within the system can be related with their dimensional counterparts by assuming a value of the diffusion coefficient and concentration. Thus, the real time can be determined from these quantities, and the real length, from the concentration value. To determine a realistic value for the nondimensional gradient coefficient, a value for the surface tension must be defined as well. Then, $\tilde{\sigma}$ can be calculated, and the value of $\tilde{\kappa}$ can then be read from Figure 3.4. As an example, a surface tension of $25\,\mathrm{mN\,m^{-1}}$ and a concentration of $55\,\mathrm{mol\,L^{-1}}$ gives $\tilde{\sigma} = 0.59$; for $A = 3$, this corresponds to $\tilde{\kappa} \approxeq 4$.

While the range of values studied for $\tilde{\kappa}$ is an order of magnitude smaller than that established above, increasing the value of this parameter would require substantially increasing the size of the system and therefore the duration of each simulation. Since the aim of this work is to study the effect of the interfacial term on mixing and supersaturation, going to this length was not needed, as the chosen values still allow to study the qualitative effect of this term. Thus, the incorporation of more realistic values of $\tilde{\kappa}$ remains a challenge to be addressed in the future.

3.4 Results and discussion

This section is organised as follows. First, the interfacial free energy coefficient κ is considered. Some of the explored alternatives were found to misbehave when it came to chemical equilibrium, and therefore this section is focused on reaching a form of κ that is consistent with it. Then, its impact on mass transfer in comparison with Fickian and Maxwell-Stefan diffusion is explored, in the absence of a gradient term. This was followed by a study on the effect that the

value of κ has on liquid demixing dynamics. Lastly, the impact of this term on the study of a crash-cooling crystallisation system is explored.

3.4.1 Definition of the gradient coefficient

The mass transfer dynamics presented in Section 3.2.3 consider an alternative form of the diffusion driving force. As shown in Equations (3.47) and (3.48), it is rewritten in terms of the gradient of chemical potential differences, and not the chemical potentials of the pure species themselves. These two shapes follow from simple algebraic transformations and thus are completely interchangeable. As explained in Section 3.2.1, this change usefully decouples the mass transfer dynamics from its intrinsic thermodynamics, since diffusion will stop when the difference between chemical potentials is constant, not when the individual chemical potentials are. While a well-posed definition of the chemical potential will fulfil this condition when in equilibrium, there could be incorrect forms of the chemical potential that also satisfy this condition. Whether the chemical potential is correctly defined or not completely hinges on choosing an appropriate form of the composition dependency for the gradient coefficient. In this context, this section explores the suitability of three different definitions of this coefficient. For readability, these have been summarised in Table 3.2, albeit each expression is also individually discussed in its relevant section.

TABLE 3.2: Summary of all forms of composition dependence for κ_{ij} tried in this work and their resulting chemical potential. To calculate that of form I, it was assumed that $(\tilde{\kappa}_{11} - \tilde{\kappa}_{10}) = 0.5\tilde{\kappa}$.

Form	**κ definition**	**Chemical potential**
I	$(\kappa_{11}, \kappa_{10}, \kappa_{00}) \neq f(c)$	$\beta\mu_1 = {}^{\partial f}/_{\partial c_1} - \left(\tilde{\kappa}_{11} - \tilde{\kappa}_{10}\right) \nabla^2 x_1$
II	$(\kappa_{11}, \kappa_{10}, \kappa_{00}) = ({}^{k_p c_0^2}/_{c^3}, {}^{-k_p c_1 c_0}/_{c^3}, {}^{k_p c_1^2}/_{c^3})$	$\beta\mu_1 = {}^{\partial f}/_{\partial c_1} + {}^1/_2\tilde{k}_p\left(\tilde{\nabla} x_1\right)^2 - x_0\tilde{k}_p\tilde{\nabla}^2 x_1$
III	$(\kappa_{11}, \kappa_{10}, \kappa_{00}) = ({}^{k_u c_0^2}/_{c^5}, {}^{-k_u c_1 c_0}/_{c^5}, {}^{k_u c_1^2}/_{c^5})$	$\beta\mu_1 = {}^{\partial f}/_{\partial c_1} - {}^1/_2\tilde{k}_u\left(\tilde{\nabla} x_1\right)^2 - x_0\tilde{k}_u\tilde{\nabla}^2 x_1$

As discussed in Section 3.2.2, previous literature [122, 123] argues that the exact value of this parameter is exclusively dependent on the activity model, and that it can be considered constant if entropic contributions are disregarded. Focusing on the latter option, the chemical potential of species 1 would take on the shape presented in Equation (3.55); this form is hereinafter referred to as form (I). For its calculation, it was assumed that $(\tilde{\kappa}_{11} - \tilde{\kappa}_{10}) = 0.5\tilde{\kappa}$.

$$\beta\mu_1 = \frac{\partial f}{\partial c_1} - \left(\tilde{\kappa}_{11} - \tilde{\kappa}_{10}\right) \nabla^2 x_1 \tag{3.55}$$

Petrischeva and Abart [121], in their study of binary systems, considered a chemical potential which shape can be recovered by considering the interfacial free energy coefficient to be a function of composition through equations (3.56)–(3.58). Note that this is not an original assumption made by the authors, who did not explicitly consider any composition dependencies within the gradient coefficient. This way, the composition dependencies presented here are merely a form in which, from our formulation of the theory, we are able to recover a nondimensional expression of the chemical potential equal to theirs. Substituting these into Equation (3.21), the final form

of this chemical potential, referred to as form (II), is reached in Equation (3.59).

$$\kappa_{11} = k_p c_0^2 / c^3 \tag{3.56}$$

$$\kappa_{10} = -k_p c_1 c_0 / c^3 \tag{3.57}$$

$$\kappa_{00} = k_p c_1^2 / c^3 \tag{3.58}$$

$$\beta\mu_1 = \frac{\partial f}{\partial c_1} + \frac{1}{2}\tilde{k}_p\left(\tilde{\nabla}x_1\right)^2 - x_0\tilde{k}_p\tilde{\nabla}^2 x_1 \tag{3.59}$$

where $\tilde{k}_p$ is a constant with respect to composition.

The last definition of the gradient coefficient was chosen to fulfil Equation (3.31). Section 3.2.2 stipulated that this expression can only be satisfied if the chemical potentials of all species in the system are constant at equilibrium; hence, any form of the chemical potential that complies with equilibrium thermodynamics must satisfy this expression. This was studied in detail by Naumann and Balsara [137], who also correctly stipulated that not all solutions that recover a constant $\gamma_i - \gamma_j$ will constitute a solution of Equation (3.31). Forms (I) and (II) cannot satisfy it, since the former does not result in a first-order term, and the latter carries a positive sign in the coefficient of its first-order term. While this sign follows naturally from the variational derivative performed to obtain the most general expression for the chemical potential, presented in Equation (3.51), it prevents Equation (3.31) from being satisfied. As a solution, this work proposes the application of a third alternative chemical potential definition, which composition dependence for the interfacial free energy coefficient is outlined in equations (3.60)–(3.62). The resulting non-dimensional chemical potential, Equation (3.63), will be referred to as form (III).

$$\kappa_{11} = k_u c_0^2 / c^5 \tag{3.60}$$

$$\kappa_{10} = -k_u c_1 c_0 / c^5 \tag{3.61}$$

$$\kappa_{00} = k_u c_1^2 / c^5 \tag{3.62}$$

$$\beta\mu_1 = \frac{\partial f}{\partial c_1} - \frac{1}{2}\tilde{k}_u\left(\tilde{\nabla}x_1\right)^2 - x_0\tilde{k}_u\tilde{\nabla}^2 x_1 \tag{3.63}$$

where $\tilde{k}_u$ is a constant with respect to composition, with units of $[L]^{-5}$ and which nondimensionalisation corresponds with $\tilde{k}_u = k_u c^{-5/3}$. Note that, while κ and the k_p and k_u parameters proposed in forms II and III, respectively, all have different units, their nondimensional value is always the same: $\tilde{\kappa} = \tilde{k}_u = \tilde{k}_p$.

As mentioned, since the dynamics of the system are dependent on chemical potential differences, rather than their absolute values, this distinction in the definition of κ does not affect the development of the simulation itself or the observed evolution of the composition profiles. It only influences the posterior interpretation of the chemical potential profiles. This way, the non-dimensional continuity equation of the system, Equation (3.53), does not change when applying this composition dependence. The gradient energy coefficient $\tilde{\kappa}$ is just substituted by $\tilde{k}_u$ or $\tilde{k}_p$. Moreover, considering that $\kappa = k_u c^{-3}$, it should be possible to determine the value of this newly introduced parameter from the value of κ_{ij}, which in turn can be determined through the

activity model of the system, as described by Inguva *et al.* [123]. Lastly, it is important to note that this might not be the only choice of composition dependency in the interfacial free energy coefficient capable of fulfilling Equation (3.31), but merely one that does.

Figure 3.8 presents the evolution in time of the composition and chemical potential profiles achieved with these three forms for a non-ideal system reaching a final mixed state, in which $A = 1$ (Figure 3.8a, c), and for a non-ideal system undergoing phase separation, with $A = 3$ (Figure 3.8b, d). In both cases, the initial conditions correspond with Figure 3.7(a), and the value of $\tilde{\kappa}$ was 0.2. It is important to note again that in this model the evolution of the composition is completely separate from the evolution of the chemical potential, since the driving force for mass transfer has been rewritten as $\nabla(\beta\mu_1 - \beta\mu_0)$. This way, since $\tilde{\kappa} = \tilde{k_p} = \tilde{k_u}$, these case studies shared the same mole fraction profile evolution with time, given by Equation (3.54), and differ only in the posterior interpretation of the chemical potential.

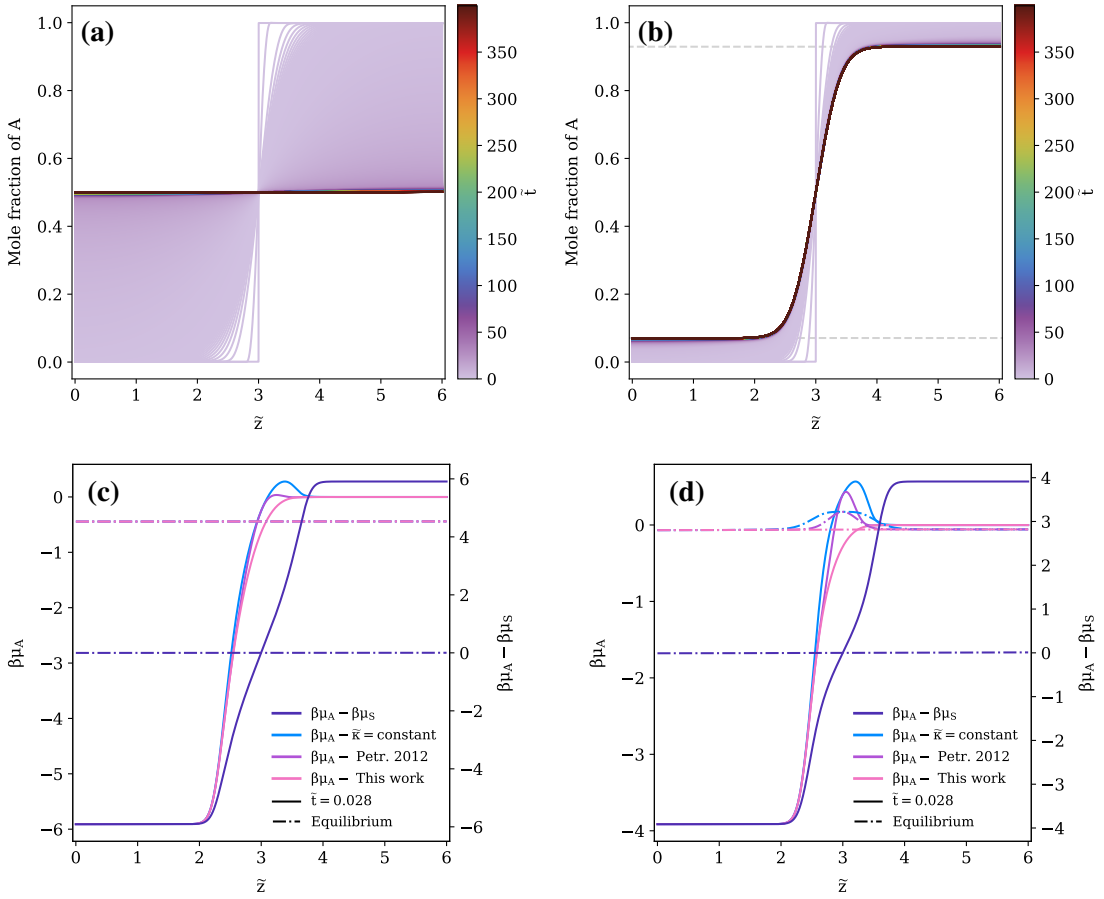


FIGURE 3.8: Evolution with time of the mole fraction and chemical potential profile of species 1, for three different definitions of κ: (I) constant, (II) $\kappa \propto c^{-3}$ and (III) $\kappa \propto c^{-5}$. Note that these three definitions yield the same nondimensional mass transfer equation, and thus the diffusion dynamics presented in the mole fraction profiles are the same in all three cases. The value of the nondimensional gradient energy parameter used in the equation dynamics was kept at 0.2, and two values of A have been evaluated: $A = 1$ (a, c) and $A = 3$ (b, d). The dashed lines in (d) correspond with the coexistence compositions. The equilibrium composition profile has been considered to be the last saved value of each simulation. In (a), the equilibrium chemical potential profiles overlap.

The results shown in Figure 3.8 confirm the behaviour expected from the three forms of

κ_{ij} tested. It is clear that both the mixed and phase-split systems exhausted their driving force for mass transfer, $\nabla\left(\beta\mu_1 - \beta\mu_0\right)$, since in equilibrium this difference is constant throughout the system in both cases. This is manifested within the composition profiles by reaching a constant value in Figure 3.8(a) and the coexistence compositions in Figure 3.8(b), for A less and greater than 2, respectively.

In Figure 3.8(c) the three forms of $\beta\mu_1$ produce the same constant final value as well, since the constant equilibrium profile means that there is no gradient contribution to this chemical potential. However, this is not true for the phase-separated system, as shown in Figure 3.8(d). In this case, forms I and II fail to remain constant around the interface, violating the condition for thermodynamic equilibrium. The reason why this was not observed in the fully mixed system is that, when the final composition profile is flat, all gradient terms are necessarily zero, allowing $\beta\mu_1$ to remain flat at equilibrium and hiding any errors associated with its formulation. On the other hand, form III is able to reach a constant final profile for $\beta\mu_1$ in both cases, indicating this composition dependence for κ_{ij} leads to a more thermodynamically robust definition of the chemical potential.

Moreover, attending to the early times presented in Figure 3.8(c) and (d) for both the mixed and demixed systems, forms I and II result in significant overshoots of the chemical potential, whereas the evolution of form III does not present these. Considering the proven ill-posedness of the former two formulations, these overshoots are most likely unphysical. Since supersaturation directly depends on the chemical potential of the species, following Equations (3.42) and (3.43), and local supersaturation spikes are linked with a higher probability of primary nucleation occurring, it is clear that an inadequate formulation of the gradient term can lead to erroneous predictions regarding the time and location at which supersaturation, and thus nucleation, could be observed in the system.

Phase-field models have been traditionally employed to study microstructure evolution within metallic systems, and in such studies the dynamics of the system may be of more concern than the evolution of the chemical potential. This could explain why this field focuses more on achieving an adequate description of the difference between chemical potentials, as these have been cast as the driving force for mass transfer. This is not discussed either in any studies that apply PFM to the problematic of oiling out within antisolvent crystallisation, which, to the author's knowledge, only extends to the work of Tsugawa *et al.* [10]. While this gap has been addressed in the past more generally, with Naumann and Balsara [137] also reaching Equation (3.31), this knowledge does not seem to be easily accessible in literature.

As a final observation regarding these trends, the chain rule expansions of the chemical potential given in equations (3.17) and (3.19) indicate that for the equilibrium chemical potential to be flat, Equation (3.65) must be fulfilled. Section 3.2.1 explained that rewriting the driving force as $\mathbb{d}_i = -\nabla_{T,V}(\mu_i - \mu_j)$ meant shifting the equilibrium condition followed by the dynamics to $\nabla(\delta F/\delta x_1) = 0$. Applying a gradient to the chain rule expansion of $\beta\mu_1$, as given in Equation (3.64), quickly reveals this conclusion: if the final gradient of chemical potential is not zero,

Equation (3.65) will necessarily remain unfulfilled in equilibrium.

$$\nabla\frac{\delta F}{\delta c_1} = \nabla\frac{\delta F}{\delta c} + \frac{\delta F}{\delta x_1}\nabla\frac{(1-x_1)}{c} + \frac{(1-x_1)}{c}\nabla\frac{\delta F}{\delta x_1} \tag{3.64}$$

$$c\nabla\frac{\delta F}{\delta c} - \frac{\delta F}{\delta x_1}\nabla x_1 = 0 \tag{3.65}$$

While it is not straightforward to obtain analytical expressions for the derivatives within Equation (3.65), this can be regarded as an additional numerical equilibrium condition. Interestingly, it corresponds with $c\nabla\beta\mu_0 = 0$, which is also the outcome of expanding the Gibbs-Duhem expression on this system, as shown in Equation (3.66).

$$\sum_{i=0}^{n} c_i \boldsymbol{\nabla}\frac{\delta F}{\delta c_i} = c\boldsymbol{\nabla}\frac{\delta F}{\delta c} - \frac{\delta F}{\delta x_1}\boldsymbol{\nabla}x_1 \tag{3.66}$$

Therefore, if the chemical potential of the system in equilibrium is not constant, it is possible that the composition dependence of the gradient coefficient, or something else in the system, is forcing the equations to violate Gibbs-Duhem.

3.4.2 Differences between mass transfer models

Now that a definition of the chemical potential consistent with equilibrium thermodynamics has been reached, this section compares the performance between Fickian and Maxwell-Stefan mass transfer and the model proposed in this work, CaHiMaS. Fick's law was replicated by considering $A = 0$ and $\tilde{\kappa} = 0$, and Maxwell-Stefan, $A = 1$ and $\tilde{\kappa} = 0$. While these two frameworks have been previously compared in literature [11, 95], the incorporation of an interfacial free energy term to the system dynamics has not been previously explored in detail in the context of antisolvent crystallisation. To the author's knowledge, there is only one study, by Tsugawa *et al.* [10] approaching this topic in this way. Thus, the comparison of the dynamics of this model to other diffusion frameworks has not been done before in this context.

The system selected for this study is formed by two pure streams put in contact without flow, with these initial conditions described in Figure 3.7(a). It was assumed that the degree of non-ideality of the real system corresponds with $A = 1$, and thus no demixing is expected to occur. While both Maxwell-Stefan and CaHiMaS are able to reproduce this non-ideality, this is not the case for Fick's law. Figure 3.9 summarises the evolution of the composition (a) and chemical potential (b) across the two mixing streams towards equilibrium.

The evolution of the two mole fractions presented in Figure 3.9(a) shows that, while all systems reach the expected homogeneous final state, the times at which this occurs are different for each model. It is also clear that at early times, e.g. $\tilde{t} = 0.6$, Fickian diffusion presents the fastest mass transfer, followed by CaHiMaS and Maxwell-Stefan. As the simulation progresses towards equilibrium, the difference between the latter becomes less obvious.

This is a consequence of the assumptions made in each model. Fick's law imposes ideal behaviour, whereas both Maxwell-Stefan and CaHiMaS are able to consider incompatibilities between species. These non-idealities imply the two species are more reluctant to mix, and thus

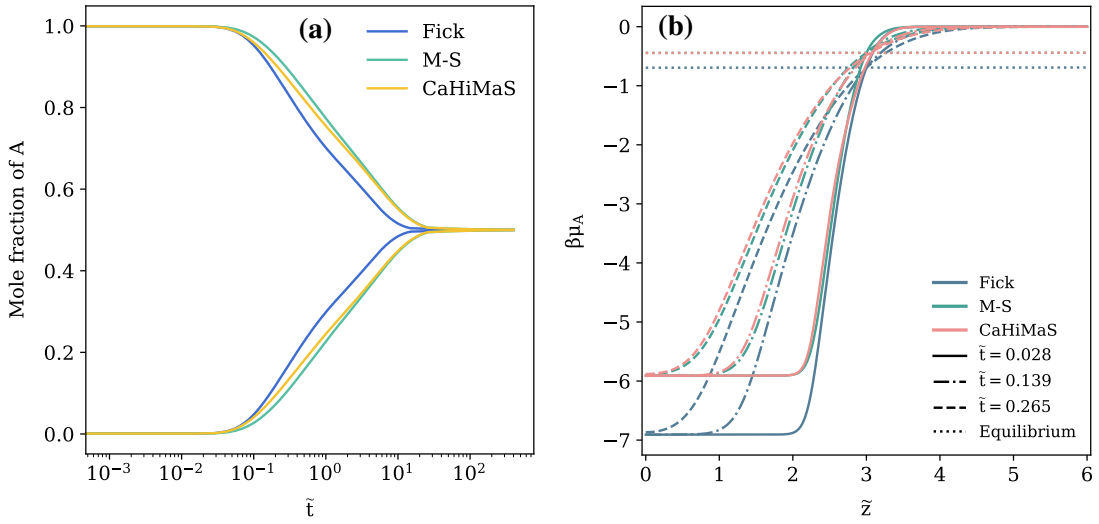


FIGURE 3.9: Mass transfer performance for Fickian ($A = 0$, $\tilde{\kappa} = 0$), Maxwell-Stefan ($A = 1$, $\tilde{\kappa} = 0$), and CaHiMaS ($A = 1$, $\tilde{\kappa} = 0.2$) diffusion. (a) Evolution with time of the mole fraction at two points in the system, located at $z = 2.25$ (bottom) and 3.75 (top). (b) Chemical potential profiles across the system throughout the simulation, where the equilibrium composition profile has been considered to be the last saved value of each simulation. Note that the Maxwell-Stefan and CaHiMaS equilibrium chemical potential profiles overlap, since there is no gradient contribution when the composition profile is flat.

the rate of mass transfer decreases in comparison with Fick. Moreover, the difference in dynamics between Maxwell-Stefan and CaHiMaS are a consequence of the interfacial free energy term in the latter. This term penalises composition nonuniformities, which leads to an increase in the driving force for mass transfer, and thus the rate of mass transfer, at earlier times. As the composition becomes more homogeneous, the value of this term decays, bringing closer the two models. Hence, the activity model and the interfacial free energy are proven to have opposite effects. This shows the importance of accounting for the interfacial free energy within the formulation of the mass transfer model even for systems that do not undergo phase separation, as its presence impacts the dynamics of mass transfer.

Figure 3.9(b) presents the chemical potentials of species 1 across the system throughout the simulation. Attending to the initial profile ($\tilde{t} = 0.028$), there are several trends standing out. Firstly, the Fickian $\beta\mu_1$ on the bulk left-hand side of the system shows a lower value than that recovered through Maxwell-Stefan and CaHiMaS, which is a consequence of ignoring the non-idealities in the Fickian case. Moreover, in the bulk phases, Maxwell-Stefan and CaHiMaS present exactly the same chemical potential. This is due to the composition profile being still flat in most of this region at this time, causing the gradient in composition and thus the interfacial free energy term to drop to zero. These same arguments explain why, in equilibrium, the Fickian model reaches a lower final value, and the other two models show no variation among theirs. As for the bulk right-hand side of the system, where the mole fraction of species 1 is around 1, the chemical potential drops to zero for all models; this is a consequence of the chosen form for the activity model, and immediately follows from substituting $x_1 \approx 1$ into Equation (3.23).

Furthermore, all iterations show that the Fickian chemical potential is lower than the other two at all points except when converging around 0 in the right-hand side bulk phase. Since mass

transfer takes place from regions of high to low chemical potential, this indicates a higher driving force for mass transfer, supporting the observed trend within the composition profiles, where Fick's law presented the fastest diffusion. In contrast, the profiles corresponding to Maxwell-Stefan and CaHiMaS intersect each other, with the latter showing lower $\beta\mu_1$ values around the interfacial region, located at $\tilde{z} = 3$. This is most likely caused by the second-order term in the driving force expression, Equation (3.51). The second spatial derivative of the composition is related to its curvature over the simulation domain, and thus this term is likely seeking to minimise this curvature. This implies that the bulk of the gradient effect will be seen in the shoulders of the composition profile, the area of transition from the bulk phases towards the interface. The CaHiMaS and Maxwell-Stefan chemical potentials intersect around this area, supporting this idea.

3.4.3 Effect of the interfacial free energy on mixed and demixed systems

This section aims to understand how the interfacial free energy term affects the diffusion between two streams, which can follow an ideal mixing behaviour ($A = 0$) or be partially immiscible ($A > 2$). This way, the initial conditions employed in this study are consistent with those used when testing the evolution of different mass transfer models, and described in Figure 3.7(a). These outcomes, in combination with the results of the previous section for $A = 1$, cover the entire range of potential behaviours that the two mixing liquids could exhibit.

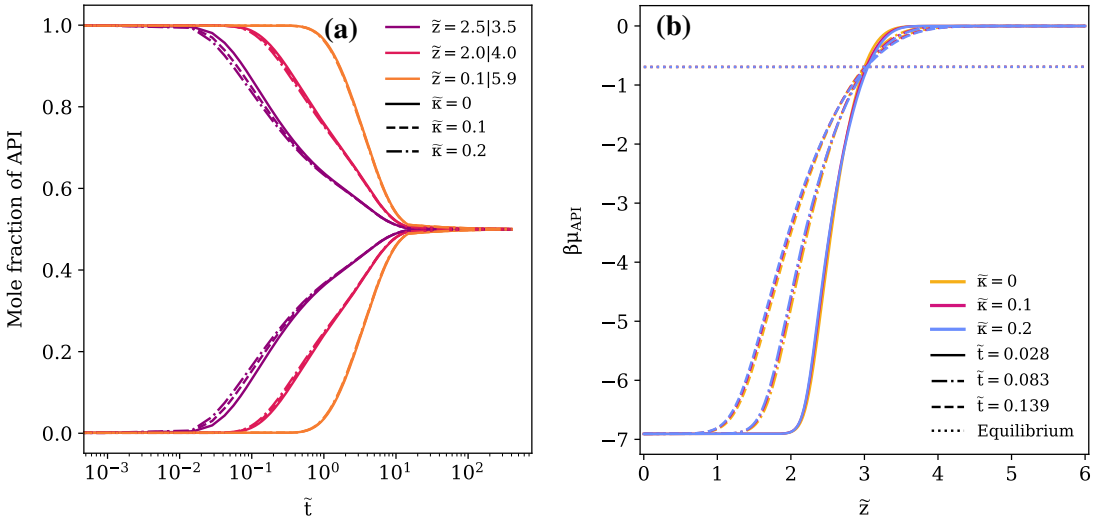


FIGURE 3.10: Mass transfer performance for an ideal system ($A = 0$) combined with different magnitudes of the interfacial free energy coefficient. (a) Evolution with time of the mole fraction for two points symmetric with respect to the original interface, and located at $z = 2.5|3.5$, $2|4$ and $0.1|5.9$. In all cases, the first number corresponds to the bottom trend, and the second, to the top. (b) Chemical potential profiles across the system throughout the simulation, where the equilibrium composition profile has been considered to be the last saved value of each simulation. Note that the equilibrium chemical potential profiles for all $\tilde{\kappa}$ overlap, in this case because there is no gradient contribution when the composition profile is flat.

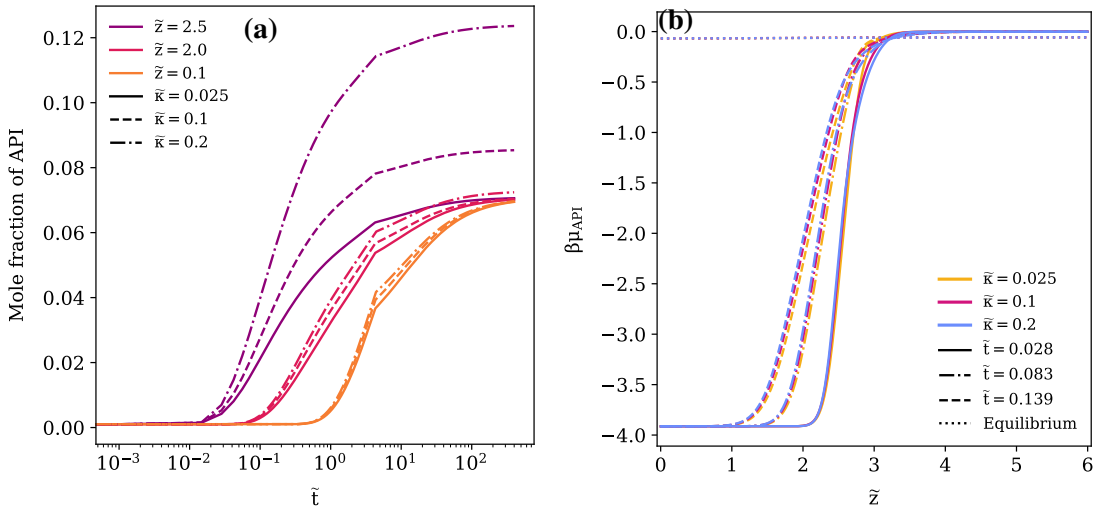


FIGURE 3.11: Mass transfer performance for a system undergoing phase separation ($A = 3$) combined with different magnitudes of the interfacial free energy coefficient. (a) Evolution with time of the mole fraction at several points, located at $z = 0.1$, 2.0 and 2.5. (b) Chemical potential profiles across the system throughout the simulation, where the equilibrium composition profile has been considered to be the last saved value of each simulation. Note that the equilibrium chemical potential profiles for all $\tilde{\kappa}$ overlap.

Figure 3.10 summarises the dynamic and thermodynamic results for the ideal solution case, and Figure 3.11 presents those corresponding to the demixing system. In both cases, the evolution of the mole fraction and the chemical potential reinforce the intuition presented from comparing the performance of CaHiMaS and Maxwell-Stefan diffusion in the previous section. Higher values of $\tilde{\kappa}$ lead to a faster mass transfer due to a stronger penalisation of nonuniformities within the system, thus generating a larger driving force for diffusion. Focusing on the different positions depicted in Figure 3.11(a), it is clear that the effect of $\tilde{\kappa}$ becomes more prominent when approaching the interface; this trend is also observed in Figure 3.10(a). This is consequence of the gradient term becoming more prominent closer to the interface, whereas in the boundaries of the system ($\tilde{z} = 0$ and $\tilde{z} = 6$) the composition profile remains mostly flat, even when evolving towards the coexistence composition. This trend was captured in Figure 3.8(b). Thus, the gradient contribution is much lower than at the interfacial region, tampering down the effect of any differences in the value of $\tilde{\kappa}$. Moreover, near the boundaries of the system, $\tilde{\kappa}$ does not have a strong effect on the final equilibrium composition, whereas at $\tilde{z} = 2.5$ the equilibrium compositions vary more significantly. Since a larger value of $\tilde{\kappa}$ leads to a stronger gradient penalty, it was expected for positions close to the interface to show compositions closer to 0.5 as this parameter increased, signalling the widening of the interface.

Interestingly, the ideal system seems to reach equilibrium noticeably faster than the demixing system does. This could be due to these initial conditions being closer in composition to the equilibrium state of the latter, which is translated into a smaller gradient in chemical potential between the left and right phases. For this system in particular, attending to the Y axis of Figures 3.10(b) and 3.11(b), $\beta\mu_1^R - \beta\mu_1^L \approx -7$ and -4, respectively.

Overall, the impact that the degree of non-ideality and the value of the gradient coefficient have on the velocity of mass transfer is not straightforward, since this is also affected by the initial

conditions of the system, and whether it wants to phase-separate. In a system with no demixing and step-like initial conditions, such as Figure 3.7(a), a larger A will slow the diffusion, since the incompatibility between species is higher. In contrast, a larger $\tilde{\kappa}$ will accelerate it, since this term seeks to reduce compositional inhomogeneities. This was observed in Figure 3.9(a). However, if the same system wanted to phase-separate, the effect would be the opposite: a larger A would promote this, and a larger $\tilde{\kappa}$ would hinder it.

3.4.4 Phase behaviour under crash-cooling conditions

This section aims to prove the application of the method developed in this work for a system undergoing sudden temperature decrease, or crash-cooling. While temperature effects were not explicitly part of the equations considered in the CaHiMaS model, it is possible to mimic such a crash-cooling process by controlling the nondimensional Margules parameter, which is inversely related to temperature. Starting from a homogeneous system ($A < 2$), this process would be simulated by observing the evolution of the system when A is suddenly set to a value greater than 2.

Figure 3.12 summarises the composition and chemical potential profiles obtained from this study. The initial conditions of the system, depicted in Figure 3.7(b), represent a liquid mixture with a composition close to homogeneity but exhibiting some noise. In particular, Gaussian noise was chosen, with $\overline{x}_1 = 0.35$ and variance $\sigma^2 = 10^{-4}$, and in which the Margules parameter is set to $A = 3$. Different values of $\tilde{\kappa}$ were tested, which is equivalent to the systems presenting different interfacial tensions: $\tilde{\kappa} = 0.025$ in Figures 3.12(a), (c), (e) and (f), and $\tilde{\kappa} = 0.2$ in Figures 3.12(b) and (d). In particular, Figures 3.12(a) and (b) present the evolution of the composition profile with time; Figures 3.12(c) and (d), the evolution of the chemical potential profile; and Figures 3.12(e) and (f) present the composition and chemical potential profiles at a subset of times, for which phase coalescence is observed.

Moreover, Figures 3.13(a) and (b) present the evolution of the total free energy, which was scaled by deducting its equilibrium value, taken to be that at the end of the simulation. Similarly, all separate contributions to the free energy are presented, namely, that of ideal mixing, non-ideal mixing, and the gradient term. They were also scaled by subtracting to it their respective values at equilibrium.

The composition profiles in Figures 3.12(a) and (b) show three distinct stages. First, the initial noise is quietened, and the system becomes close to fully homogeneous. This can be observed particularly well in (b), where the initial profile is lavender, and the blue profiles corresponding to a later time are observed to be quite horizontal. The initial noise causes compositional gradients to appear across the entire system, which could result in a large free energy due to the contribution of the gradient term, which would punish the inhomogeneities caused by this noise. While this is not visible in the free energy trends presented in Figure 3.13, this large free energy may have been resolved in the first 15 iterations of the solver, which as explained in Section 3.3 is the saving frequency used in this work. As for the chemical potential, the flattening of the composition profile causes it to evolve into an almost uniform value.

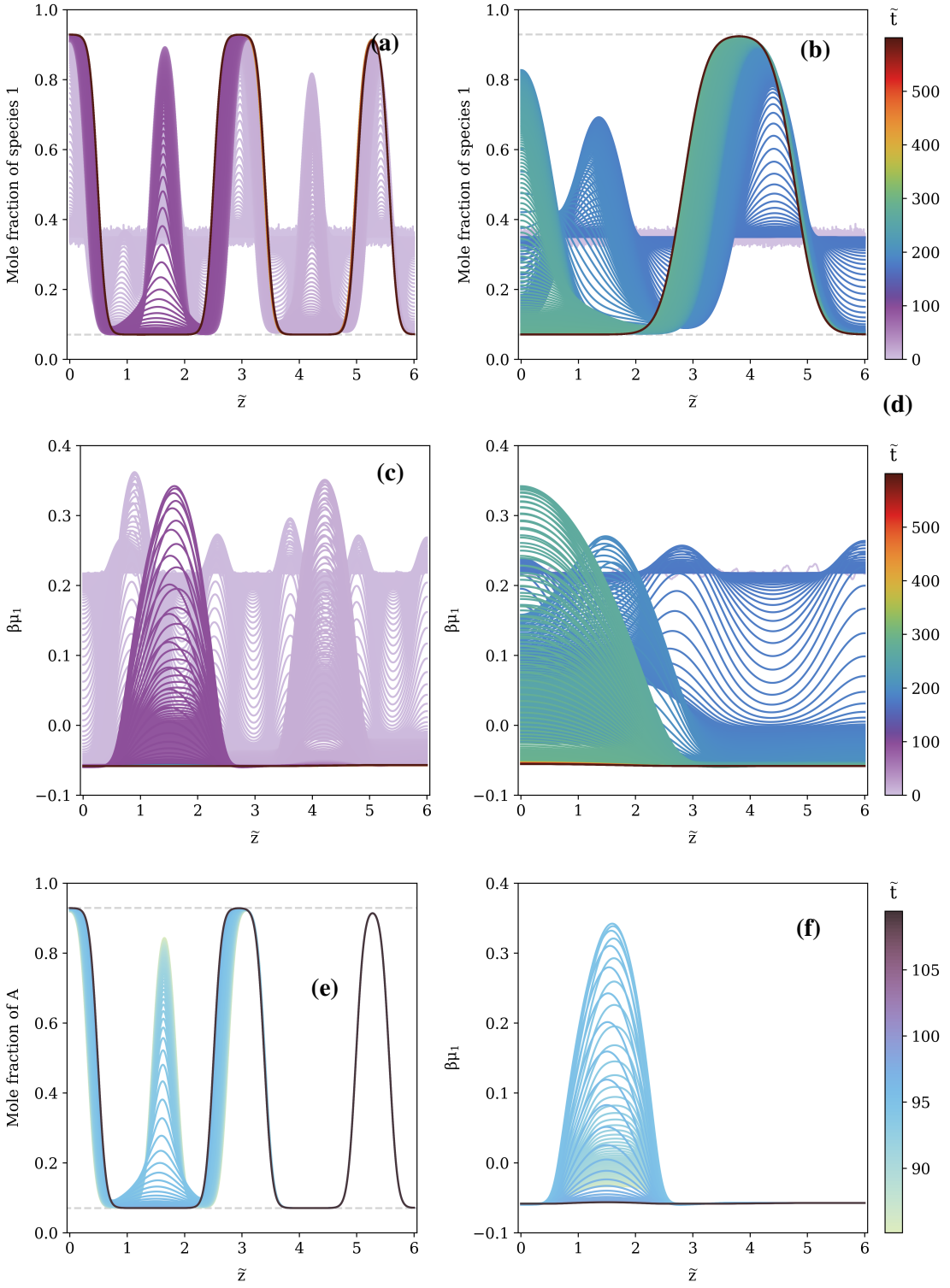


FIGURE 3.12: Crash-cooling of a binary system, modelled with $A = 3$ and $\tilde{\kappa} = 0.025$ for (a), (c), (e) and (f), and with $\tilde{\kappa} = 0.2$ for (b) and (d). (a-b) Mole fraction evolution with time; same colorbar applies to both cases. The grey dashed lines correspond with the coexistence compositions for the studied conditions. (c-d) Chemical potential profile evolution with time; same colorbar applies to both cases. (e-f) Cmposition and chemical potential profiles, respectively, for selected times showing phase coalescence, within the $\tilde{\kappa} = 0.025$ study. Same colorbar applies to both cases.

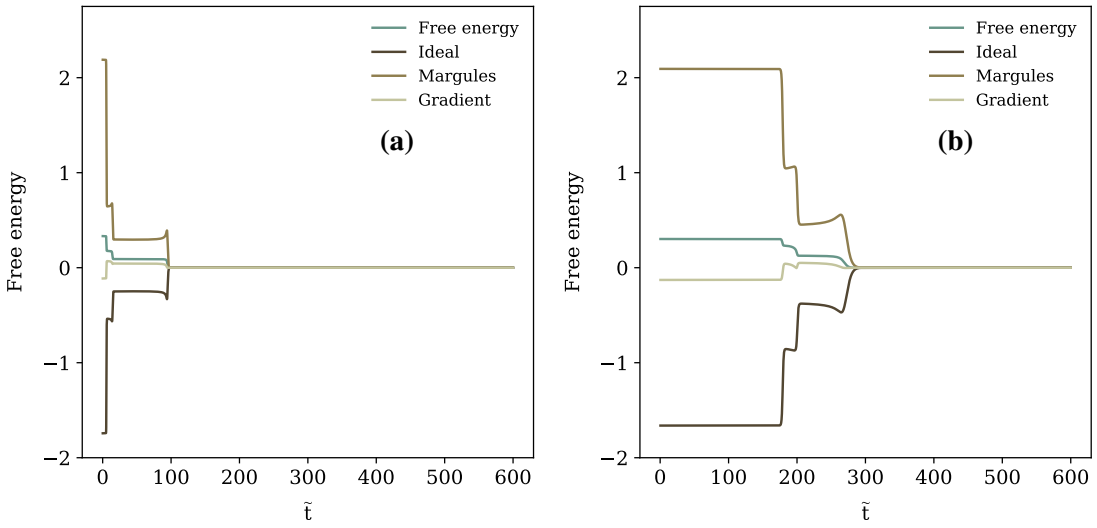


FIGURE 3.13: Free energy evolution in the crash-cooling of a binary system, modelled with $A = 3$ and $\tilde{\kappa} = 0.025$ and 0.2 for (a) and (b), respectively. Both the total free energy and the individual contribution of the ideal, non-ideal (Margules) and interfacial (gradient) terms are included. They have each been scaled by deducting their value in equilibrium, taken to be that at the end of the simulation.

The second stage corresponds with a relatively rapid phase separation, growing the small local composition gradients into different phases; note that this outcome could have not been predicted by any mass transfer models neglecting the gradient term contribution. This formation of two different phases causes the system to undergo uphill diffusion, that is, the diffusion of a species against its composition gradient. The effect of $\tilde{\kappa}$ is quite noticeable at this stage: the smaller value corresponds with a larger tolerance for compositional inhomogeneities and a smaller surface tension, and thus allows the presence of more interfaces, as can be seen comparing Figures 3.12(a) and (b). Additionally, the system with the larger $\tilde{\kappa}$ is slower to reach this demixing stage. At this stage, the chemical potential profile begins oscillating as the phases start to separate, presenting several overshoots. once the initial phases have been formed, the chemical potential profile becomes almost, albeit not fully, flat, as portrayed in the initial times presented in Figure 3.12(f). The presence of these overshoots in chemical potential is interesting, since they will clearly lead to matching peaks in supersaturation–see Equations (3.42) and (3.43). These supersaturation spikes could lead to crystal nucleation at their location, with the resulting crystal form dictated by the local composition at this region and its placement on the phase diagram.

Interestingly, a third stage in the evolution of the composition profiles could be defined, characterised by the coalescence of some of the initially formed phases. Attending to the $\tilde{\kappa} = 0.025$ case, this takes place two times: in the ranges $\tilde{t} = 10$–20 and $\tilde{t} = 85$–110, with the composition and chemical potential evolutions of the latter case presented in Figures 3.12(e) and (f), respectively. In the case of $\tilde{\kappa} = 0.2$, the merging of phases can be observed between $\tilde{t} = 183$–205 and $\tilde{t} = 230$–295. This behaviour, also reported by Nauman and He [143], is reminiscent of Ostwald ripening, highlighting the potential that phase-field models would have for the description of this process. This was emphasised by Tsugawa *et. al* [10], who established that the growth dynamics observed in phase-field models during phase coalescence correspond with those of Ostwald

ripening when close to the spinodal boundary.

During this coalescence the composition trend exhibits uphill diffusion again, in the regions rich in species 1 that become wider as a result; a good example of this is observed in Figure 3.12(e). The phase coalescence is also reflected in the free energy and the chemical potential. When this occurs, the chemical potential in the region rapidly grows from a very slight bump into a sharp peak, and, as the phases finish merging, this overshoot dies down and this profile returns back to an almost fully flat state, as depicted in Figure 3.12(f). Again, these spikes will translate directly into supersaturation spikes, which could cause crystal nucleation to occur at this time and in this region. These overshoots in chemical potential could be caused by the compositions in this region of the system temporarily travelling through mid-range values, around 0.5, where the energetic penalisation from the activity model is the largest. The non-ideal contribution to the free energy clearly spikes at this time before sharply decreasing, supporting this idea. Moreover, the total free energy presents a step-like evolution, decreasing to a lower level every time a phase coalesces.

It is interesting to note that the gradient contribution evolves following the same qualitative trend as the total free energy at the phase coalescence stage, but when the initial phase separation occurs in the second stage, the gradient trend increases, since before that the system was almost homogeneous. The ideal and non-ideal contributions to the free energy show qualitative opposite trends, following the idea that the first aims to keep the system homogeneous at its mixing point, whereas the second aims to push the system towards the binodal coexistence compositions.

Lastly, it is possible that the compositional configurations observed in-between phase coalescence events correspond with metastable states. The free energy can remain nearly constant for long stretches of time, until the fluctuations grow enough to trigger the merging of phases. In combination with the chemical potential profile being almost uniform before and after coalescence, this suggests these configurations may constitute metastable states of the system. The most stable configuration would be the presence of two phases at the coexistence compositions joined by a smooth interface, as observed in Figure 3.5 and Figure 3.8(b). However, the value of $\tilde{\kappa}$ may be too low to drive the system to transition to this more stable state; and even if this were not the case, it is not possible to predict how long this transition would take. Considering this evidence, the final states presented in Figures 3.12(a) and (b) can be classified as metastable.

3.5 Conclusions

The aim of this work was to incorporate an interfacial free energy term to the driving force for mass transfer within a diffusion model, and to examine its effect upon mixing outcomes in a binary system. The shape of this term was based on that proposed by Cahn and Hilliard [14], and it is based on the idea that the driving force should depend not only on the compositions themselves, but also on their surrounding environment, taken into account through their spatial gradient. This study proved that this model allows the modelling of the dynamics of liquid-liquid phase separation, which had not been previously achieved for a binary system within a crystallisation context. This phenomenon, albeit mostly undesired, plays an important role in

pharmaceutical processes such as antisolvent crystallisation. Moreover, a novel form for the composition dependency within the interfacial free energy coefficient was proposed, which allowed to recover the conditions for thermodynamic equilibrium. It was observed that other invalid forms led to the prediction of erroneous chemical potential overshoots, which could result in misleading conclusions regarding the times and locations where crystals may nucleate in the system. The results of the liquid-liquid mixing study indicate that neglecting the effect of the interfacial term in a mass transfer model can lead to inaccuracies in the estimation of diffusion timescales, especially in the early stages of the mixing process and at locations near the interface, since this term contributes positively to the diffusive driving force. Lastly, the results of the crash-cooling study, which could not have been conducted were the interfacial term not present, confirmed the adequacy of this model for predicting the apparition of chemical potential and supersaturation overshoots. These indicate potential times and regions where crystal nucleation could be observed and control the corresponding nucleation rates. Moreover, phase coalescence and the existence of potential metastable states were observed in this study. Overall, these results highlight the great potential that incorporating an interfacial term holds when it comes to understanding mass transfer in the context of crystallisation. The importance of this contribution will only increase as the system of study becomes more complex; this way, the next chapter aims to study the evolution of mass transfer in a ternary antisolvent crystallisation system.

Chapter 4

Diffusion and phase behaviour in antisolvent crystallisation

The previous chapter proposed the addition of a nonlocal gradient term to the free energy formulation of a diffusion model, which incorporated the contribution of interfaces in the system to its thermodynamics. The proposed model was capable of simulating spinodal decomposition, one of the mechanisms through which oiling out can occur, thus proving the great potential that this framework holds for the study of this phenomenon. Moreover, by focusing on a binary system, it helped build intuition towards the expected behaviour of the model under different conditions, and the theory behind it. The stage is now set for the current study, which applies the same framework to a ternary system, representative of an antisolvent crystallisation process. This work is comprised of three main parts: (1) the analysis of the model behaviour under different initial conditions, spanning across the entire phase diagram; (2) a study of its behaviour in equilibrium across the miscibility gap; and (3) a study on the effect that the value of the diffusion coefficients and the degree of nonideality have upon the outcomes a set process.

4.1 Introduction

Antisolvent crystallisation is a widely used purification method in the pharmaceutical industry, which exploits the difference in solubility of a solute in two miscible liquids: a solvent and an antisolvent [144]. In this process, the local values of the supersaturation are dictated by the local compositions; during the mixing of the solvent and antisolvent-rich streams, local regions of vastly different compositions will come into contact, leading to the formation of temporal interfaces and to local regions of higher supersaturation than expected for the fully mixed system. Variations in the supersaturation can greatly affect the properties of the final crystalline product, and, consequently, mixing plays a major role in these processes. Unfortunately, mass transfer is not well understood in these systems, often leading to the formation of unwanted crystal phases or to undesired phenomena such as oiling out, also called liquid-liquid phase separation (LLPS) (i.e. the separation of the solute via the formation of a secondary liquid phase).

Traditionally, mixing at the microscale has been described through Fick's law, which considers composition gradients to be the driving force for mass transfer, instead of the thermodynamically accurate chemical potential gradients. This significant limitation prevents this model from correctly describing more nuanced aspects of mass transport, such as "uphill diffusion" [11]—the

diffusion of species against its concentration gradient—which are important in antisolvent crystallisation. Recent studies [9, 95] focus on the application of the less commonly used Maxwell-Stefan diffusion model [12, 13], which is based on chemical potential gradients and thus constitutes a more realistic description of diffusive mass transfer.

The key challenge is now reaching an accurate portrayal of the thermodynamics of the ternary system, in order to obtain a chemical potential capable of describing the phenomena relevant to mixing. So far, mixing studies in the context of antisolvent crystallisation have only included local mixing terms in their free energy, corresponding with that of the pure species, ideal, and non-ideal interactions. On its own, this cannot adequately describe antisolvent crystallisation, since it does not consider the contribution of potential interfaces within a system to the free energy, and, thus, to the species chemical potentials and mass transfer. These interfaces, inevitable due to the inherent multiphase nature of antisolvent crystallisation [145], can appear when new phases nucleate. LLPS is an example of this, which can arise as non-idealities in the system lead it towards unexpected regions of the phase diagram.

Moreover, the ability of models based only on these thermodynamic contributions to accurately predict the mixing trajectories of the system across the phase diagram is compromised as the process approaches the spinodal region, given their inability to deal with phase transformations. While a previous study [9] harnessed this limitation to predict when LLPS may happen by monitoring when the model failed, it is possible that estimated times and regions where the system entered the spinodal were less accurate than those made with a more complete thermodynamic model.

Additionally, some studies [6, 72] mention the potential of LLPS as a tool to be deployed, highlighting potential advantages such as inducing the formation of certain polymorphs [74], aiding in the control of crystal size and aspect ratio [75, 76], and promoting the sphericity of the product [73]. In fact, Gong *et al.* [146] deployed this technique experimentally to enhance the sphericity of vanillin crystals, known to favour needle-like shapes. With this in mind, only identifying the potential for LLPS does not provide sufficient insight to increase our understanding of this phenomenon for it to become an aid to the design of antisolvent crystallisation process.

For these reasons, these models clearly do not suffice when it comes to the description of the dynamics of microscale mass transfer in antisolvent crystallisation, which inherently involves multiphase phenomena.

LLPS can occur in both the binodal and spinodal regions, albeit following nucleation and growth dynamics in the first case, and spinodal decomposition in the second. Their main difference is that binodal LLPS will need to overcome an energy barrier to occur, whereas the liquid-liquid demixing that takes place in the spinodal is completely spontaneous. While the modelling of this phenomenon is still new to the pharmaceutical crystallisation community, there is a vast amount of research done on phase transformations in the context of physical metallurgy [147–149] and polymer science [115, 123, 150], which has remained largely untapped. This work leverages this knowledge and proposes the incorporation of an additional square-gradient term to the free energy model, designed to enable the modelling of LLPS through spinodal decomposition. This addition is rooted in the work of Cahn and Hilliard [14]; mainly included within

Phase-Field Models (PFM), other names for it being the Gradient Theory and Density Functional Theory.

The application of PFM in the context of pharmaceutical crystallisation is starting to gain attention from the scientific community, albeit, to the author's knowledge, only one peer-reviewed study has been published so far in this context. Tsugawa *et al.* [10] assessed the performance of a 2D Cahn-Hilliard-like PFM on the modelling of LLPS in a water/ethanol/butylparabene system. Among its interesting findings, the compliance of the model with Ostwald-ripening dynamics when in the relevant region of the spinodal stands out. Nonetheless, the authors highlight the need for further research regarding the compositional behaviour of these models when in equilibrium within the spinodal; additionally, the theory remains obscure, with the physical meaning of the gradient term and its coefficients unclear.

Overall, the most recent work performed towards the understanding of LLPS in pharmaceutical crystallisation highlights the need to accurately predict the trajectories of the system within the ternary phase diagram during the mass transfer process. This is because it is their deviation towards unexpected regions the diagram that leads to unexpected outcomes, such as different polymorphs or LLPS. Moreover, there is interest in developing the ability to predict and also understand these phenomena, in the first case to prevent it, and in the second, to help harness it. Phase-field models hold great potential for this purpose, and it is the aim of this work to both increase our understanding of diffusion in antisolvent crystallisation, and serve as a guide for those seeking to apply PFM within this context.

4.2 Theoretical background

This work considers a ternary system which species are the API, solvent and antisolvent (1, 2 and 0, respectively), in which the antisolvent is selected as the dependent species. This means that the continuity equations solved were that of the API and the solvent, and the antisolvent composition was calculated through $1 - x_1 - x_2$. Similarly to Chapter 3, the system is closed and isothermal, with mass transfer occurring exclusively via diffusion.

This section aims to provide the bases of the mass transfer model applied in this work, considering the physical meaning of its constituent terms and their relation with known variables and phase transformation behaviours. A detailed introduction to the theory was already provided in Section 3.2 for the case of a binary mixture; while the equations now will incorporate an additional component, most arguments will remain unchanged. This section will focus on providing the generalisation of all relevant equations to the multicomponent case—with n species—accompanied by key reduced explanations.

As mentioned previously, diffusive mixing in antisolvent crystallisation has traditionally been described by Fickian diffusion, which considers the driving force for mass transfer to be the gradient in concentration of each species: $\mathbb{d}_i^{Fick} = -\nabla_{T,V} c_i$. Under this definition, the only possible mass transfer outcome is a homogeneous system; while sufficient for the modelling of ideal

systems, this is not capable of describing the complex mass transfer phenomena inherent to antisolvent crystallisation, such as uphill diffusion and oiling out. The correct thermodynamic definition of the driving force for diffusion is the gradient in chemical potential: $\mathbb{d}_i^{Fick} = -\nabla_{T,V}\mu_i$, with mixing studies in the context of antisolvent crystallisation postulating this definition as the clearly superior choice [11, 95, 151].

The square-gradient theory applied is based on the work of Petrischeva and Abart [121], more recently implemented by Inguva *et al.* [123], who also refer to Nauman and He [122] as a source, to study polymer blends. The resulting governing equations maintain the same modular nature observed in Chapter 3 for binary systems, separating the diffusion dynamics from the thermodynamics of the process. This way, the main difference between this formulation and that devised for binary systems is that the employed diffusive fluxes were not formulated following Maxwell-Stefan diffusion, but nonetheless constructed to be linear with respect to the gradient of chemical potential, and preserving all the necessary physics. More detail is provided in Section 4.2.2, although interested readers are directed to explore Petrischeva and Abart's work directly [121].

4.2.1 General thermodynamic framework

It is clear that an accurate diffusion model hinges on reaching an accurate description of the chemical potentials within the system. This necessarily implies redefining its free energy, since the chemical potential of a species i is calculated from its derivative, as shown in Equation (4.1).

$$\beta\mu_i = \left.\frac{\partial F}{\partial n_i}\right|_{T,V,n_{j\neq i}} \tag{4.1}$$

Most applications in literature are limited to the contribution of local terms, that is, those that within a discretised system depend exclusively on the composition at a specific location: $F[c_i(\mathbf{r}),\dots,c_n(\mathbf{r})]$. These are restricted to the first three RHS terms of Equation (3.6), and in turn can only represent the contributions of (1) the pure species, (2) ideal interactions, and (3) non-ideal interactions.

The main limitation of this approach is that, in focusing only on compositions at a discrete point, it completely ignores the effect that formations such as temporary interfaces—prone to arise during mixing—have upon the free energy landscape. This work aims to bridge this shortcoming by including a fourth term in the definition of the chemical potential which accounts for non-local contributions by considering that the free energy is not only a function of composition, but also of its gradient: $F[c_i(\mathbf{r}),\dots,c_n(\mathbf{r}),\nabla c_i(\mathbf{r}),\dots,\nabla c_n(\mathbf{r})]$. As explained in Section 3.2, this makes the free energy a functional of composition, and redefines the chemical potential into the variational derivative presented in Equation (4.2).

$$\beta\mu_i = \left.\frac{\delta F}{\delta n_i}\right|_{T,V,n_{j\neq i}} \tag{4.2}$$

The theory proposed in this work has been formulated in terms of the Helmholtz free energy, following the example set by Chapter 3. The remainder of this section briefly describes the physical meaning of the local and non-local contributions in the context of a multicomponent system.

Free energy due to mixing non-idealities

The local free energy density of a multicomponent system is given in Equation (4.3), where the one-parameter Margules activity model has been employed to describe the non-ideality in the interactions between species. In accordance with the framework for binary mixtures presented in Chapter 3, the contributions to the free energy are modular, making this activity model easily replaceable with any other alternatives. The interested reader is encouraged to read the work of Inguva *et al.* [123], who performed a detailed study of the effect of different activity models in the field of polymer blends.

Formulating the model in the Helmholtz framework requires taking into account the variation with pressure of the parameters that are pressure-dependent within Equation (4.3), which in this case are the chemical potential of the pure species, $\beta\mu_i^\circ(T,p)$, and the Margules parameters, $A_{ij}(T,p)$. This was done through a first-order Taylor series, the details of which are given in Appendix B. Through suitable algebraic manipulation, it was possible to reduce these parameters in the final free energy density to depend exclusively on p_0, a constant reference pressure of the system. This way, following the definition given in Equation (4.1), Equation (4.4) provides the general chemical potential of a species in the system.

$$f(c_0,\dots,c_n) = \sum_{i=0}^{n} c_i\left[\beta\mu_i^\circ(T,p_0)+\ln x_i\right] + c\sum_{j>i}^{n}\sum_{i=0}^{n-1} A_{ij}(T,p_0)x_i x_j - \beta p_0 \tag{4.3}$$

$$\beta\mu_1 = \beta\mu_1^\circ(T,p_0)+\ln x_1 + \sum_{i=0}^{n} A_{1i}x_i - \sum_{j>i}^{n}\sum_{i=0}^{n-1} A_{ij}(T,p_0)x_i x_j \tag{4.4}$$

In this work, the interactions between the API and the antisolvent were considered to be non-ideal, while, for simplicity, API-solvent and solvent-antisolvent interactions remained ideal ($A_{12} = A_{20} = 0$). This allows to simplify the free energy density and the chemical potential as given in Equations (4.5) and (4.6), considering that $A = A_{10}$.

$$f(c_1,c_2,c_0) = \sum_{i=0}^{2} c_i\beta\mu_i^\circ(T,p_0) + \beta p_0 + \sum_{i=0}^{2} c_i\ln x_i + cA(T,p_0)x_1x_0 \tag{4.5}$$

$$\beta\mu_1 = \beta\mu_1^\circ(T,p_0)+\ln x_1 + A(1-x_1)x_0 \tag{4.6}$$

Since both the free energy density and the chemical potential are defined up to an additive constant, the two first terms of the RHS of Equation (4.5) can be obviated, as well as the first term of the RHS of Equation (4.6). Therefore, it is possible to calculate the free energy density without considering these terms, through $f - \sum_i c_i\beta\mu_i^\circ - \beta p_0$. Similarly, the chemical potential can be calculated through $\beta\mu_i - \beta\mu_i^\circ$.

Figure 4.1(a) displays the resulting free energy landscape projected onto the ternary diagram, where the degree of non-ideality between API and antisolvent has been fixed at $A = 3$. For clarity, Figure 4.1(b) presents the matching free energy curves for each binary pair, which correspond with the profiles along all axes within the ternary diagram in Figure 4.1(a). As expected, API-solvent and solvent-antisolvent interactions return a single well, whereas the API-antisolvent pair features a double well. The most prominent trend in the free energy landscape is the global minimum around the centre and just above the miscibility gap. From there, the free energy progressively increases along the direction perpendicular to the API-AS axis, as the solvent content decreases, and also as it increases, following the opposite direction. While the solvent content is below the critical point, the lowest free energy values found along a constant solvent line will be located on the binodal curve.

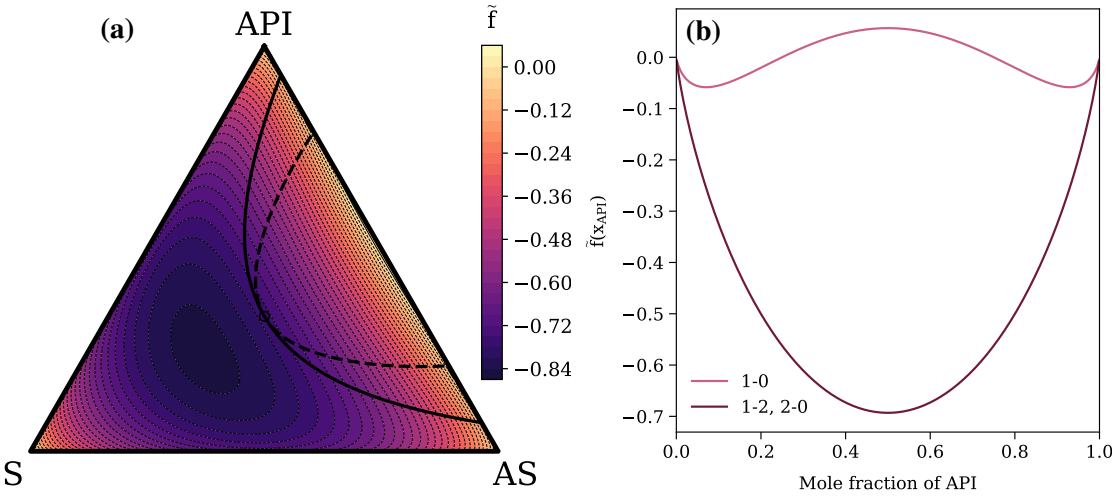


FIGURE 4.1: Local nondimensional free energy density contributions, where $\tilde{f} = f/c = \sum_{i=0}^{2} x_i \ln x_i + A x_1 x_0$. (a) Free energy landscape across the ternary diagram for a system with $A = 3$ (non-ideality in the API-antisolvent pair) and ideal interactions between API-solvent and solvent-antisolvent. The continuous and dashed black lines correspond with the binodal and spinodal curves, respectively; the black circle marks the critical point. (b) Nondimensional free energy density for all binary pairs within the system; the profiles correspond to those found along the triangle axes in (a).

In the context of antisolvent crystallisation, the solid-liquid solubility of a species in the system is determined by the local thermodynamics, and is defined through $\beta\mu_i^{(S)} = \beta\mu_i^{(L)}$. Thus, attending to Equation (4.6) and considering that the solid species is pure, and therefore only $\beta\mu_1^{\circ,(S)}$ contributes to its chemical potential, the solubility condition can be written as in Equations (4.7) and (4.8) for a multicomponent and ternary system, respectively.

$$\beta\mu_1^{\circ,(S)} - \beta\mu_1^{\circ,(L)} = \ln x_1 + \sum_{i=0}^{n} A_{1i} x_i - \sum_{j>i}^{n} \sum_{i=0}^{n-1} A_{ij} x_i x_j \tag{4.7}$$

$$\beta\mu_1^{\circ,(S)} - \beta\mu_1^{\circ,(L)} = \ln x_1 + A(1 - x_1) x_0 \tag{4.8}$$

These evidence that calculating the solubility only requires prior knowledge of the the degree of non-ideality between species, A, and the chemical potentials of the pure species in the solid

and liquid state. The last two can be combined into a parameter $\beta\mu_i^{\circ,(S)} - \beta\mu_i^{\circ,(L)}$, which defines the solubility curve of the system. The exact steps to take to obtain this curve from Equation (4.8) have been laid out in Appendix E, together with a more detailed derivation of Equation (4.8).

The effects of A and of this solubility parameter on the ternary diagram have been summarised in Figure 4.2. The value of A controls the properties of the miscibility gap between API and antisolvent, such as the location of the critical point and the binodal and spinodal curves. A smaller value indicates a lower degree of non-ideality, and thus will reduce the total area of the miscibility gap, as well as the distance between the coexistence binodal compositions. The only other thermodynamic feature within the ternary diagram considered in this work is the solid-liquid solubility curve. Analogously to its effect in the binary system in Chapter 3, this curve does not affect the dynamics of the diffusion process, and serves instead as a means to interpret the results of the model in terms of supersaturation and, therefore, explain them in the context of crystallisation. The solubility curve is affected by both the solubility coefficient and A, given the positive contribution that the latter exerts over the chemical potential of the API in the liquid phase. This can be observed in the trends depicted in Figure 4.2, where while the curve is clearly more affected by the solubility parameter, a higher value of A also visibly lowers it at all points except the API-solvent axis, since at this point there is no antisolvent in the system.

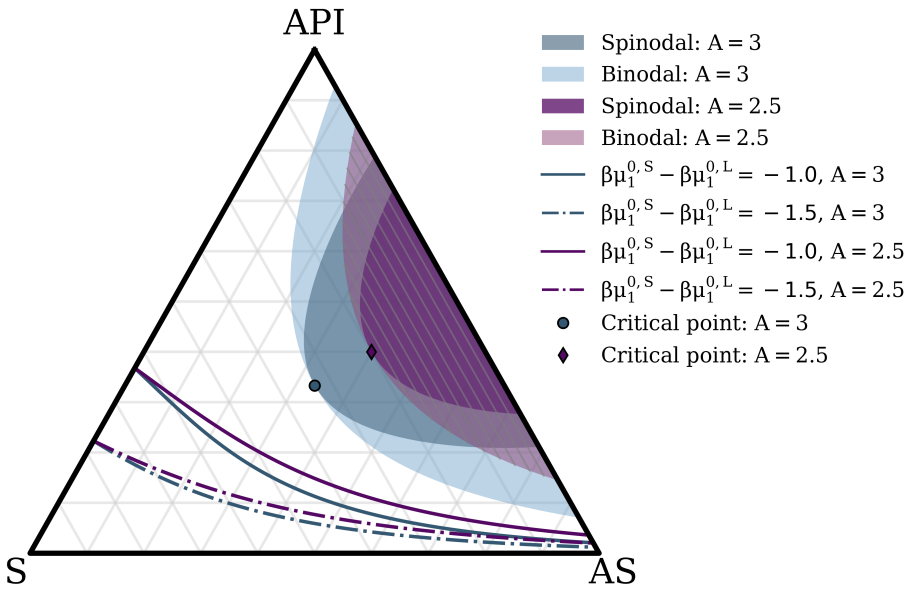


FIGURE 4.2: Effect of A and of the solubility parameter $\beta\mu_1^{\circ,(S)} - \beta\mu_1^{\circ,(L)}$ on the shape of the miscibility gap, affected only by the former, and the solubility curve, affected by both.

Non-locality in the free energy functional

This work studies the addition of a non-local gradient term to the free energy definition, based on Cahn and Hilliard's formulation [14], which exerts an energetic penalty upon compositional inhomogeneities within the system, and thus accounts for the presence of interfaces. As described in Section 3.2.2, this redefines the free energy as a functional, given in Equation (4.9) for the

multicomponent case at hand.

$$F\left[c_i(\mathbf{r}), \nabla c_i(\mathbf{r})\right] = \int f\left[c_i(\mathbf{r})\right] d\mathbf{r} + \int \left[\frac{1}{2}\sum_{ij=0}^{n} \kappa_{ij} \nabla c_i(\mathbf{r}) \cdot \nabla c_j(\mathbf{r})\right] d\mathbf{r} \tag{4.9}$$

where κ_{ij}, referred to as the gradient coefficient, gradient free energy coefficient and interfacial free energy coefficient throughout this thesis, has dimensions of L^5.

The transformation of the free energy into a functional implies that the chemical potential of a species must now be calculated through a variational derivative, as defined in Equation (3.16). The result of this derivative for species 1 is given in Equation (4.10).

$$\beta\mu_1 = \frac{\delta F}{\delta c_1} = \frac{\partial f}{\partial c_1} - \sum_{i=0}^{n} \nabla \cdot [\kappa_{1i} \nabla c_i(\mathbf{r})] + \frac{1}{2}\sum_{ij}^{n} \frac{\partial \kappa_{ij}}{\partial c_1} \nabla c_i(\mathbf{r}) \cdot \nabla c_j(\mathbf{r}) \tag{4.10}$$

This definition of the chemical potential assumes that the independent variables of the system are the concentrations of the species in the system, $(c_0, \ldots, c_n)$. An alternative choice is to pick the total concentration and the mole fractions of all independent species $(c, x_1, \ldots, x_n)$ for this purpose. To calculate the chemical potential in terms of these variables, its definition, given in Equation (3.16), can be rewritten accordingly through a chain rule, as shown in Equations (4.11) and (4.12) for a ternary system, and Equation (4.13) for a general multicomponent case.

$$\beta\mu_1 = \frac{\delta F}{\delta c_1} = \frac{\partial c}{\partial c_1}\frac{\delta F}{\delta c} + \frac{\partial x_1}{\partial c_1}\frac{\delta F}{\delta x_1} + \frac{\partial x_2}{\partial c_1}\frac{\delta F}{\delta x_2} \tag{4.11}$$

$$\beta\mu_1 = \frac{\delta F}{\delta c_1} = \frac{\delta F}{\delta c} + \frac{1 - x_1}{c}\frac{\delta F}{\delta x_1} - \frac{x_2}{c}\frac{\delta F}{\delta x_2} \tag{4.12}$$

$$\beta\mu_1 = \frac{\delta F}{\delta c_1} = \frac{\delta F}{\delta c} + \frac{1}{c}\frac{\delta F}{\delta x_1} - \sum_{i>0}^{n} \frac{x_i}{c}\frac{\delta F}{\delta x_i} \tag{4.13}$$

The resulting expression shows that the formulation of the chemical potential through these variables becomes a sum of the contributions of compositional variations, $\delta F/\delta x_i$, and changes in the bulk phase, $\delta F/\delta c$. Thus, the latter will be a contribution common to the chemical potential of all the species. Since in this work the driving force for mass transfer has been cast in terms of the differences in chemical potential between species (see Section 4.2.2), this implies that the $\delta F/\delta c$ contribution will cancel out when calculating this difference.

Furthermore, the subsequent chain rule expansions presented in Equations (4.14) and (4.15) reveal that $\delta F/\delta x_i$ corresponds with the difference in chemical potentials between species i and 0, the latter being the dependent one, and thus are directly related to the driving force.

$$\frac{\delta F}{\delta x_i} = \sum_{j=0}^{n} \frac{\delta F}{\delta c_j}\frac{\partial c_j}{\partial x_i} \tag{4.14}$$

$$\frac{\delta F}{\delta x_i} = c(\beta\mu_i - \beta\mu_0) \tag{4.15}$$

Therefore, the formulation of the chemical potential through Equation (4.12) is more convenient for the purpose of this work, and it has henceforth been considered. Assuming that the system is incompressible, the derivations needed to calculate it for any given species through the chain rule expansion of Equation (4.13) are given in Equations (4.16) and (4.17). Note that f corresponds with the local free energy contributions, given in Equations (4.3) and (4.5) for a multicomponent and a ternary system, respectively.

$$\frac{\delta F}{\delta c} = \frac{\partial f}{\partial c} + \frac{c}{2}\sum_{ij}^{n}\frac{\partial \kappa_{ij}}{\partial c}\nabla x_i \cdot \nabla x_j + \sum_{ij}^{n}\kappa_{ij}\nabla x_i \cdot \nabla x_j \tag{4.16}$$

$$\frac{\delta F}{\delta x_1} = \frac{\partial f}{\partial x_1} + \frac{c^2}{2}\sum_{ij}^{n}\frac{\partial \kappa_{ij}}{\partial x_1}\nabla x_i \cdot \nabla x_j - c^2\sum_{i}^{n}\nabla \cdot (\kappa_{1i} - \kappa_{0i})\nabla x_i \tag{4.17}$$

where to retrieve $\delta F/\delta x_2$ it is only needed to substitute 2 in place of 1 in the second expression.

Adaptability of the phase-field method to diffusion, nucleation and growth

The incorporation of this gradient term to the free energy enables the modelling of more accurate diffusion dynamics and of liquid-liquid phase separation when occurring inside the spinodal region. That is because, by construction, the free energy functional in Equation (4.9) can only evolve downhill with time, meaning that the free energy can only decrease. For a detailed derivation proving this, the interested reader is directed to read Petrsicheva and Abart's [121] work directly.

In contrast, phase transformations that follow nucleation and growth dynamics must overcome an initial free energy barrier before the free energy starts evolving exclusively downhill, making it impossible for this model to simulate them. Nonetheless, by monitoring supersaturation, the model is able to predict the times and locations where nucleation could occur, as well as potential nucleation rates. Moreover, the model's ability to handle spinodal decomposition will help reach a more accurate description of diffusion in the vicinity of this region, without the simulation failing if the system wandered into it.

The problem of nucleation has been extensively studied in the metallurgy and polymer fields, where this limitation is bridged through two main alternatives. The first one consists on the addition of a noise term to the governing equations, eventually resulting in the apparition of nuclei in a process that mimics the stochastic nature of nucleation [133–135]. The second one consists on the artificial insertion of nuclei within the simulation domain if certain criteria are met. One example would be the nucleation probability, calculated from the nucleation rate and the local supersaturation, crossing over a certain threshold [136]. Lastly, it is worth mentioning that the limitation of the model only extends to nucleation, and that it is fully capable of describing nuclei growth (or dissolution), since this process does not require the free energy to travel uphill at any point in the evolution.

Nondimensionalisation of the governing equations

The governing equations have been nondimensionalised following a characteristic time and length of $\tau = L^2/D_{10}$ and $L = c^{-1/3}$, respectively, where c has dimensions of particles per volume ($1/L^3$). This choice of characteristic length scale permits to recast the equations solely in terms of the length scale introduced by the gradient term ($\kappa_{ij}^{1/5}$), which is related to the range of interaction between molecules and the interface thickness. Considering this, the gradient coefficients can be rewritten in dimensionless form as $\tilde{\kappa}_{ij} = \kappa_{ij} c^{5/3}$.

The effect of κ_{ij} on the interfacial tension and the equilibrium composition profiles

The positive contribution of the gradient term to the free energy serves as a penalisation for compositional inhomogeneities, which has the effect of controlling interface formation within the system. Hence, it is expected to bear a relation with known physical interfacial properties. Its link with the interfacial tension is given in Equation (4.18), in the context of a multicomponent incompressible system of infinite length with two distinct phases divided by a planar interface. A comprehensive review of the algebra involved can be found in Appendix C.

$$\beta\sigma = \int dz \sum_{ij}^{n} \kappa_{ij} c_i' c_j' \tag{4.18}$$

where c_i' and c_j' correspond, respectively, with the derivative of the one-dimensional equilibrium composition profiles of the species pair being added. Note that these can be integrated to yield the equilibrium composition profiles. Moreover, $\beta\sigma$ can be nondimensionalised through $\widetilde{\sigma} = \beta\sigma c^{-2/3}$.

This shows a direct relationship between the interfacial tension and the gradient coefficients of the different pairs, indicating that neglecting the gradient term in the free energy formulation is equivalent to setting the interfacial tension of the system to zero. Similarly, a larger κ_{ij} implies a higher interfacial tension, and this higher energetic cost for compositional inhomogeneities is finally translated into a smoother, wider interface. Lastly, it is worth noting that the interfacial tension is also affected by the degree of non-ideality between the species in the system through the impact of this parameter on their equilibrium composition profiles.

Analogously to the binary case, the calculation of the total equilibrium free energy density in the system—needed to derive the relationship between the interfacial tension and the gradient term—leads to the expressions needed to solve for the equilibrium composition profiles, Equations (4.19) and (4.20). These clearly show the influence that both κ_{ij} and A exert on the final profile, and thus on σ. The interested reader is directed to the work of Naumann and He [143],

who present and analyse these equilibrium spatial composition profiles.

$$\frac{c}{2}\sum_{ij}^{n}\kappa_{ij}x_i'x_j' = \frac{\Delta f}{c} \tag{4.19}$$

$$\frac{\Delta f}{c} = \sum_{i=0}^{n} x_i \ln\frac{x_i}{x_i^{eq}} + \sum_{j>i}^{n}\sum_{i=0}^{n} A_{ij}x_i x_j - \sum_{k=0}^{n} x_k\left[\sum_{i=0}^{n} A_{ki}x_i^{eq}\right] - \sum_{k=0}^{n} x_k\left[\sum_{j>i}^{n}\sum_{i=0}^{n-1} A_{ij}x_i^{eq}x_j^{eq}\right] \tag{4.20}$$

where the superindex *eq* indicates equilibrium compositions which can refer to either bulk phase; thus, $\Delta f/c$ can be defined through two different expressions.

Defining supersaturation through the model dynamics

In this chapter the spatial and temporal supersaturation (S) definition has been based on the composition evolution predicted by the model. Its calculation entails recasting the solubility curve, collected with (x_1^*, x_2^*, x_0^*) coordinates, into X-Y composition measurements of API (Y) vs the antisolvent/solvent ratio (Y), calculated as $x_0^*/(x_2^* + x_0^*)$. This allows to retrieve the value of x_1^* at the solvent/antisolvent ratio pertaining to a particular point and time. Thus, the supersaturation can be defined through Equation (4.21).

$$S(\tilde{t}_i, \tilde{z}_i) = \frac{x_1(\tilde{t}_i, \tilde{z}_i)}{x_1^*(\tilde{z}_i)} \tag{4.21}$$

This definition of the supersaturation is consistent with the one normally used in antisolvent crystallisation studies [145, 152], allowing a more direct translation of the results of this work.

On the individual chemical potential profiles

In this work, it was considered that the gradient coefficients had a linear dependence with the total concentration: $\kappa_{ij} \equiv c\kappa_{ij}$. Attending to equations (4.16) and (4.17), this choice of composition dependence allows to recover the same form of $\delta F/\delta x_i$ as given by Petrischeva and Abart [121], which in turn allows to recover their final continuity equations for both independent species. These dynamics were also recently applied by Inguva *et al.* [123] for binary mixtures, and thus it was considered best to reproduce them.

While this composition dependency does not yield the same form of $\delta F/\delta c$ given by Petrischeva and Abart, this is not necessarily problematic. Firstly, as discussed above, $\delta F/\delta c$ does not contribute to the diffusion dynamics, since it is added to the chemical potentials of all species and thus disappears when casting the driving force as the difference in chemical potentials, $\mathbb{d}_i = -\nabla_{T,V}(\mu_i - \mu_j)$. Thus, recovering a different expression for $\delta F/\delta c$ does not compromise in any way the accuracy of the mass transfer predictions of the model.

Secondly, the form of $\delta F/\delta c$ given by Petrischeva and Abart is not thermodynamically accurate, failing to recover a flat chemical potential profile in equilibrium when the system undergoes phase separation. The proposed composition dependence results in a form of $\delta F/\delta c$ that is also unable to do so, and, due to time constraints, it was not possible to investigate this further to reach

a more accurate definition. Nonetheless, this does not compromise the ability of the model to predict mass transfer. This is not only because of the irrelevance of $\delta F/\delta c$ on the driving force, but also because the length scale employed for the nondimensionalisaton in this work ensures that the nondimensional equivalent of a composition dependence that complies with this condition will be equal to the nondimensional κ_{ij}, as seen in Chapter 3. The current thoughts of the author on the topic of the individual chemical potentials have been summarised in Appendix F.

4.2.2 Diffusion dynamics

This work has considered the formulation of the diffusive flux posed by Petrischeva and Abart [121], shown in Equation (4.22), instead of the Maxwell-Stefan equations, which have so far been the primary choice for describing this flux in the studies of diffusive mixing in antisolvent crystallisation [9, 95]. The reason for this choice was simplicity: the Maxwell-Stefan formulation of the diffusive flux is considerably more convoluted for systems with more than two species [8]. The addition of the gradient term already increases significantly the complexity of the governing equations, and thus it was considered best to employ the simplest physically adequate model for the diffusive flux.

$$\mathbf{J_i} = -\sum_{j=0}^{n} L_{ij} \nabla \mu_j \tag{4.22}$$

where L_{ij} is the mobility of the system.

The driving force considered within these fluxes is correctly defined as $\mathbb{d}_i = -\nabla_{T,V}\mu_i$, as reflected in Equation (4.22). This can be expressed as the gradient of a difference between chemical potentials, $\mathbb{d}_i = -\nabla_{T,V}(\mu_i - \mu_j)$. For details on this transformation, the reader is directed to read Petrischeva and Abart's work [121].

The mobility can be related with the diffusivity between species, D_{ij}, through $L_{ij} = -D_{ij} c x_i x_j$. Incorporating this mobility definition into $\mathbf{J_i}$ leads to the final formulation of this diffusive flux and of the continuity equation used in this work, shown respectively in equations (4.23) and (4.24).

$$\mathbf{J_i} = -\sum_{j=0}^{n} D_{ij} c x_i x_j \nabla \left(\beta\mu_i - \beta\mu_j\right) \tag{4.23}$$

$$\frac{\partial x_i}{\partial t} = -\frac{1}{c}\nabla \cdot \mathbf{J_i} = \nabla \cdot \left[\sum_{j=0}^{n} D_{ij} x_i x_j \nabla \left(\beta\mu_i - \beta\mu_j\right)\right] \tag{4.24}$$

To conclude this section, Equations (4.25) and (4.26) provide the differences in chemical potentials, as obtained when specialising for a ternary system, between the two independent species (API and solvent, referred to as 1 and 2) and the dependent composition (antisolvent, 0). These have been obtained through the combination of Equations (4.15) and (4.17), and their

subsequent simplification by considering a lineal composition dependence in the gradient coefficients: $\kappa_{ij} \equiv c\kappa_{ij}$.

$$\beta\mu_a = \beta\mu_1 - \beta\mu_0 = \frac{1}{c}\frac{\partial f}{\partial x_1} - \tilde{\kappa}_{aa}\widetilde{\nabla}^2 x_1 - \tilde{\kappa}_{ab}\widetilde{\nabla}^2 x_2 \tag{4.25}$$

$$\beta\mu_b = \beta\mu_2 - \beta\mu_0 = \frac{1}{c}\frac{\partial f}{\partial x_2} - \tilde{\kappa}_{ab}\widetilde{\nabla}^2 x_1 - \tilde{\kappa}_{bb}\widetilde{\nabla}^2 x_2 \tag{4.26}$$

where $\tilde{\kappa}_{aa} = \tilde{\kappa}_{11} - 2\tilde{\kappa}_{10} + \tilde{\kappa}_{00}$; $\tilde{\kappa}_{bb} = \tilde{\kappa}_{22} - 2\tilde{\kappa}_{20} + \tilde{\kappa}_{00}$; and $\tilde{\kappa}_{ab} = \tilde{\kappa}_{12} - \tilde{\kappa}_{10} - \tilde{\kappa}_{20} + \tilde{\kappa}_{00}$.

Similarly, equations (4.27) and (4.28) present the nondimensional continuity equations for the API and solvent.

$$\frac{\partial x_1}{\partial \tilde{t}} = \tilde{\nabla} \cdot \left[\tilde{D}_{12} x_1 x_2 \tilde{\nabla}\left(\beta\mu_a - \beta\mu_b\right) + \tilde{D}_{10} x_1 x_0 \tilde{\nabla}\beta\mu_a\right] \tag{4.27}$$

$$\frac{\partial x_2}{\partial \tilde{t}} = \tilde{\nabla} \cdot \left[\tilde{D}_{12} x_1 x_2 \tilde{\nabla}\left(\beta\mu_b - \beta\mu_a\right) + \tilde{D}_{20} x_2 x_0 \tilde{\nabla}\beta\mu_b\right] \tag{4.28}$$

4.3 Methodology

This work considers the diffusive mixing of two streams, one a solution of API and solvent, and the other an antisolvent-rich solution, in a one-dimensional system. The simulations presented follow this system from the moment the two streams are put in contact until the time they reach equilibrium, and analyses their evolution in terms of mass transfer and supersaturation. These simulations have been conducted using the FiPy [140] library in Python, which is based on Finite Volume (FVM) discretisation. This method is particularly suitable for mass transfer problems, as it enforces mass conservation over the domain [139]. To comply with FiPy's framework, the equations governing this process had to be divided into a system of six coupled equations ((4.29)–(4.34)), comprising the two continuity equations for the two independent components and two gradient term definitions for each of the diffusive fluxes. Note that these equations can be obtained by substituting and expanding Equations (4.25) and (4.26) into Equations (4.27)

and (4.28).

$$\begin{aligned}\frac{\partial x_1}{\partial \tilde{t}} = &\widetilde{\nabla}\left[\widetilde{D}_{12}x_2\widetilde{\nabla}x_1\right] - \widetilde{\nabla}\left[\widetilde{D}_{12}x_1\widetilde{\nabla}x_2\right] - \widetilde{\nabla}\left[A\widetilde{D}_{12}x_1x_2\widetilde{\nabla}x_1\right] - \widetilde{\nabla}\left[A\widetilde{D}_{12}x_1x_2\widetilde{\nabla}x_2\right] \\ &- \widetilde{\nabla}\left[\widetilde{D}_{12}x_1x_2\widetilde{\nabla}\psi_{aa,1}\right] - \widetilde{\nabla}\left[\widetilde{D}_{12}x_1x_2\widetilde{\nabla}\psi_{ab,2}\right] + \widetilde{\nabla}\left[\widetilde{D}_{12}x_1x_2\widetilde{\nabla}\psi_{ab,1}\right] + \widetilde{\nabla}\left[\widetilde{D}_{12}x_1x_2\widetilde{\nabla}\psi_{bb,2}\right] \\ &+ \widetilde{\nabla}\left[\widetilde{D}_{10}(1-x_2)\widetilde{\nabla}x_1\right] + \widetilde{\nabla}\left[\widetilde{D}_{10}x_1\widetilde{\nabla}x_2\right] - \widetilde{\nabla}\left[2A\widetilde{D}_{10}x_1x_0\widetilde{\nabla}x_1\right] - \widetilde{\nabla}\left[A\widetilde{D}_{10}x_1x_0\widetilde{\nabla}x_2\right] \\ &- \widetilde{\nabla}\left[\widetilde{D}_{10}x_1x_0\widetilde{\nabla}\psi_{aa,1}\right] - \widetilde{\nabla}\left[\widetilde{D}_{10}x_1x_0\widetilde{\nabla}\psi_{ab,2}\right]\end{aligned} \tag{4.29}$$

$$\begin{aligned}\frac{\partial x_2}{\partial \tilde{t}} = &-\widetilde{\nabla}\left[\widetilde{D}_{12}x_2\widetilde{\nabla}x_1\right] + \widetilde{\nabla}\left[\widetilde{D}_{12}x_1\widetilde{\nabla}x_2\right] + \widetilde{\nabla}\left[\widetilde{D}_{12}Ax_1x_2\widetilde{\nabla}x_1\right] + \widetilde{\nabla}\left[\widetilde{D}_{12}Ax_1x_2\widetilde{\nabla}x_2\right] \\ &+ \widetilde{\nabla}\left[\widetilde{D}_{12}x_1x_2\widetilde{\nabla}\psi_{aa,1}\right] + \widetilde{\nabla}\left[\widetilde{D}_{12}x_1x_2\widetilde{\nabla}\psi_{ab,2}\right] - \widetilde{\nabla}\left[\widetilde{D}_{12}x_1x_2\widetilde{\nabla}\psi_{ab,1}\right] - \widetilde{\nabla}\left[\widetilde{D}_{12}x_1x_2\widetilde{\nabla}\psi_{bb,2}\right] \\ &+ \widetilde{\nabla}\left[\widetilde{D}_{20}x_2\widetilde{\nabla}x_1\right] + \widetilde{\nabla}\left[\widetilde{D}_{20}(1-x_1)\widetilde{\nabla}x_2\right] - \widetilde{\nabla}\left[A\widetilde{D}_{20}x_2x_0\widetilde{\nabla}x_1\right] \\ &- \widetilde{\nabla}\left[\widetilde{D}_{20}x_2x_0\widetilde{\nabla}\psi_{ab,1}\right] - \widetilde{\nabla}\left[\widetilde{D}_{20}x_2x_0\widetilde{\nabla}\psi_{bb,2}\right]\end{aligned} \tag{4.30}$$

$$\psi_{aa,1} = \widetilde{\nabla}\left[\tilde{\kappa}_{aa}\widetilde{\nabla}x_1\right] \tag{4.31}$$

$$\psi_{ab,2} = \widetilde{\nabla}\left[\tilde{\kappa}_{ab}\widetilde{\nabla}x_2\right] \tag{4.32}$$

$$\psi_{ab,1} = \widetilde{\nabla}\left[\tilde{\kappa}_{ab}\widetilde{\nabla}x_1\right] \tag{4.33}$$

$$\psi_{bb,2} = \widetilde{\nabla}\left[\tilde{\kappa}_{bb}\widetilde{\nabla}x_2\right] \tag{4.34}$$

4.3.1 Selection of initial conditions

The effect of the interfacial tension on mass transfer dynamics could have been approached in many ways, since almost all scenarios across the entirety of the ternary phase diagram would be novel in nature. It was decided to approach it from three perspectives, all of them summarised in Table 4.1.

Firstly, the physical properties (solubility and degree of non-ideality between API and antisolvent) of the system were fixed, and the behaviour of different initial conditions was analysed. The aim behind the initial conditions selected was to study diffusion in the main regions of the ternary phase diagram—one phase, binodal and spinodal region—and to test the reduction of antisolvent purity as a means of preventing liquid-liquid phase separation. Predicting how diffusion may evolve in these regions is not straightforward, both experimentally and from a phase-field model perspective. This way, the four initial conditions pertaining to this case have been summarised in Figure 4.3(a).

The set of conditions (1) observes the mixing of a 25% API and 75% solvent solution mixed with pure antisolvent, as per experiments 1 and 2 in Table 4.1. It represents conditions typical from an antisolvent crystallisation process, and has been used to determine the effect of the interfacial free energy term on diffusion and supersaturation in this context. Set (2) comprises

TABLE 4.1: Summary of conditions studied in this work. The composition indicated in the top and bottom streams is in the form (x_{API}, x_S, x_{AS}). The abbreviations employed in the diffusion coefficients correspond with 1 for API, 2 for solvent and 0 for antisolvent.

ID	Composition		$\widetilde{\mathbf{D}}_{10}$	$\widetilde{\mathbf{D}}_{20}$	$\widetilde{\mathbf{D}}_{12}$	A	$\tilde{\kappa}_{\mathbf{aa}}$	$\tilde{\kappa}_{\mathbf{ab}}$	$\tilde{\kappa}_{\mathbf{bb}}$
1	Right stream Left stream	$(0.24995, 0.74995, 10^{-4})$ $(10^{-4}, 10^{-4}, 0.9998)$	0.5	1	1	3	0	0	0
2	Right stream Left stream	$(0.24995, 0.74995, 10^{-4})$ $(10^{-4}, 10^{-4}, 0.9998)$	0.5	1	1	3	0.05	0.016	0.05
3	Right stream Left stream	$(0.44995, 0.54995, 10^{-4})$ $(10^{-4}, 10^{-4}, 0.9998)$	0.5	1	1	3	0.025	0.008	0.025
4	Right stream Left stream	$(0.44995, 0.54995, 10^{-4})$ $(10^{-4}, 10^{-4}, 0.9998)$	0.5	1	1	3	0.1	0.032	0.1
5	Right stream Left stream	$(0.54995, 0.44995, 10^{-4})$ $(10^{-4}, 10^{-4}, 0.9998)$	0.5	1	1	3	0.025	0.008	0.025
6	Right stream Left stream	$(0.44995, 0.54995, 10^{-4})$ $(10^{-4}, 0.19995, 0.79995)$	0.5	1	1	3	0.025	0.008	0.025
7	Right stream Left stream	$(0.8999, 0.1, 10^{-4})$ $(10^{-4}, 0.1, 0.8999)$	0.5	1	1	3	0.025	0.008	0.025
8	Right stream Left stream	$(0.7999, 0.2, 10^{-4})$ $(10^{-4}, 0.2, 0.7999)$	0.5	1	1	3	0.025	0.008	0.025
9	Right stream Left stream	$(0.6999, 0.3, 10^{-4})$ $(10^{-4}, 0.3, 0.6999)$	0.5	1	1	3	0.025	0.008	0.025
10	Right stream Left stream	$(0.24995, 0.74995, 10^{-4})$ $(10^{-4}, 10^{-4}, 0.9998)$	0.1	1	1	3	0.025	0.008	0.025
11	Right stream Left stream	$(0.24995, 0.74995, 10^{-4})$ $(10^{-4}, 10^{-4}, 0.9998)$	0.5	1	1	3	0.025	0.008	0.025
12	Right stream Left stream	$(0.24995, 0.74995, 10^{-4})$ $(10^{-4}, 10^{-4}, 0.9998)$	0.1	0.1	1	3	0.025	0.008	0.025
13	Right stream Left stream	$(0.24995, 0.74995, 10^{-4})$ $(10^{-4}, 10^{-4}, 0.9998)$	0.5	1	1	3.75	0.025	0.008	0.025

a stream of 45% API and 55% solvent stream mixed with pure antisolvent, in order to study diffusion in a system which mixing point lays within the binodal region. It corresponds with experiments 3 and 4 in Table 4.1. Set (3), corresponding with experiment 5 in Table 4.1, constitutes a system in which the mixing point lays within the spinodal region, and is formed by a 55% API and 45% solvent solution mixed with pure antisolvent. Together with set (2), its purpose is to help esclaresce the behaviour of the system inside the binodal and spinodal regions. Lastly, set (4), corresponding with experiment 6 in Table 4.1, comprises a 45% API and 55% solvent stream mixed with 80% antisolvent and 20% solvent, accounting for a mixing point close to the miscibility gap, but outside it. Its purpose is to determine whether cutting the purity of the antisolvent stream can be an effective strategy for avoiding LLPS.

This way, the outcomes observed in this section of the results will help increase our understanding regarding the behaviour of experimental systems, and will also prove useful for those seeking to employ phase-field models as a tool to simulate LLPS [10].

Secondly, a study of diffusion across the miscibility gap was performed, which initial conditions are visualised in Figure 4.3(b) and correspond with experiments 7–9 in Table 4.1. Matsushima *et al.* [153] identified the need to conduct more research regarding the equilibrium phase

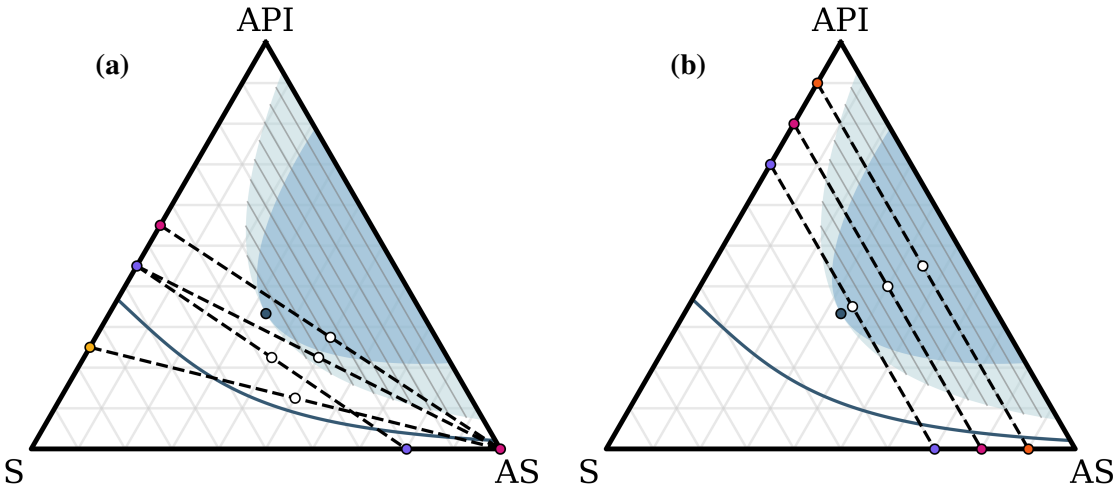


FIGURE 4.3: Projection on the ternary diagram of the initial conditions studied on the first (a) and second (b) subset of results, which respectively correspond with a study of mass transfer and phase behaviour under different regions of the ternary diagram, and with a study of mass transfer across the miscibility gap. These initial conditions are step-like, and the points located in the API-S and S-AS axis indicate the compositions of the two streams being put in contact. The same colors belong to the same experiment. Moreover, these two compositions are joint by a dashed line that indicates the pathway that a linear mass transfer process would follow. The white circle located on each respective line indicates the mixing point between the two streams, would the system evolve towards a homogeneous final state.

behaviour across the miscibility gap in order to better understand localised LLPS. Phase-field models are starting to emerge as a tool for modelling this phenomenon [10], since, besides their contribution to the general description of diffusion via the interfacial term they are capable of simulating spinodal decomposition. However, some details of the behaviour of the different species in equilibrium within this region remain unexplored in this context. By studying the equilibrium behaviour across the miscibility gap, this section aims to help cover these two research gaps.

Thirdly, the initial conditions and solid-liquid solubility of the system were fixed, and the diffusion coefficients between the API and the two solvents was varied, as well as the non-ideality between API and antisolvent, according to experiments 10–12 and 13 in Table 4.1, respectively. The reason why the effect of solubility was not isolated and studied on its own is because this variable does not affect the mass transfer dynamics on their own within the context of this model. Was crystal nucleation incorporated, solubility would impact mass transfer through the depletion of supersaturation to form the solid nuclei. However, in this model, its impact is reserved for the posterior supersaturation analysis. Therefore, its value does not determine whether a supersaturation overshoot occurs, but only whether this overshoot is large enough to make the system supersaturated. Since the value of this variable depends exclusively of the physical system being studied, this assumption implies that the solubility of the API at different solvent/antisolvent ratios is constant for all the studies considered in this work.

This model presents a great number of tunable parameters, considering there are three diffusion coefficients in the system ($\widetilde{D}_{12}$, $\widetilde{D}_{10}$, $\widetilde{D}_{20}$), three grouped interfacial free energy coefficients

($\tilde{\kappa}_{aa}$, $\tilde{\kappa}_{ab}$, $\tilde{\kappa}_{bb}$), the Margules interaction parameter between API and AS (A), the initial compositions of the two streams, the boundary conditions with which the system is evaluated, and the solubility of the API in the solution, albeit, as established above, this does not affect the mass transfer dynamics. It would not be practical to study these parameters by varying them individually, and thus there are some constraints that have been applied to the values tested. The diffusion coefficient between solvent and antisolvent ($\widetilde{D}_{12}$) has been kept constant, whereas certain studies (experiments 10–12) have been devoted to understanding the effect of different API diffusivities with both solvent and antisolvent on the diffusion process. Since the diffusion coefficients can be interpreted as the inverse of drag coefficients [11], their variation can lead to an alteration of the mass transfer pathway through the ternary diagram. Regarding the interfacial free energy coefficients, Petrischeva *et al.* [121] state their value must obey $\kappa_{ab}^2 < \kappa_{aa}\kappa_{bb}$. Thus, it was decided to maintain $\tilde{\kappa}_{aa} = \tilde{\kappa}_{bb}$ in all studies and apply $\tilde{\kappa}_{ab} = \sqrt{\tilde{\kappa}_{aa}\tilde{\kappa}_{bb}/10}$, since the effect of one species upon another is not expected to have as strong an effect as upon itself. However, a future more thorough study of the effect of these values would be beneficial, in order to determine how larger or lower values may impact mass transfer trends. The degree of non-ideality remained at $A = 3$ in all studies except experiment 13, which explores the effect that a different antisolvent may have. The solubility variable $\beta\mu_{API}^{\circ,(S)} - \beta\mu_{API}^{\circ,(L)}$ was kept as -1. Lastly, only Neumann boundary conditions [154] have been presented, which enforce no-flow across the boundaries. It would be beneficial to investigate diffusion in the context of a bulk mixing regime in a future study, which in some cases could potentially be replicated by applying periodic boundary conditions.

4.3.2 Computational details

The one-dimensional system of study was discretised into `nx` = 1200 points spaced `dx` = 0.005 each, making the total length of the domain $\tilde{z} = 6$. A schematic diagram of the discretised system can be found in Figure 3.6. Adaptive time-stepping was incorporated, since it was observed that the conservative timestep values required at the start of the simulation resulted in the solver facing numerical challenges with the negligible change at later times. This resulted in inert timesteps, that is, timesteps for which the solution did not change. While this did not cause the simulation to crash and did not constitute a major problem, it could cause a mismatch between time labels and the profile stored under them. As a solution, the adaptive time-stepping algorithm detailed in Figure 4.4 was applied. The two different methods of adapting the value were chosen to avoid an excessive growth of `dt` destabilising the simulation. While the second criterion (adding 0.005 to the existing `dt`) was slightly conservative, leading to some inert iterations, this never occurred more than 15 times in a row, ensuring that the next profile saved was never identical to the previous one. As a final comment on the timestep, it is worth mentioning that this algorithm was found to be more computationally efficient than the exponential time-stepping employed in Chapter 3, and thus its implementation is also recommended for any future studies on binary systems.

Figure 4.4 also showcases the conditions used to determine whether a time-stepping iteration had finished correctly or not. There were two main aspects to take into account. A decreasing residual is a sign of sweeping leading to convergence, but the lowest possible residual value

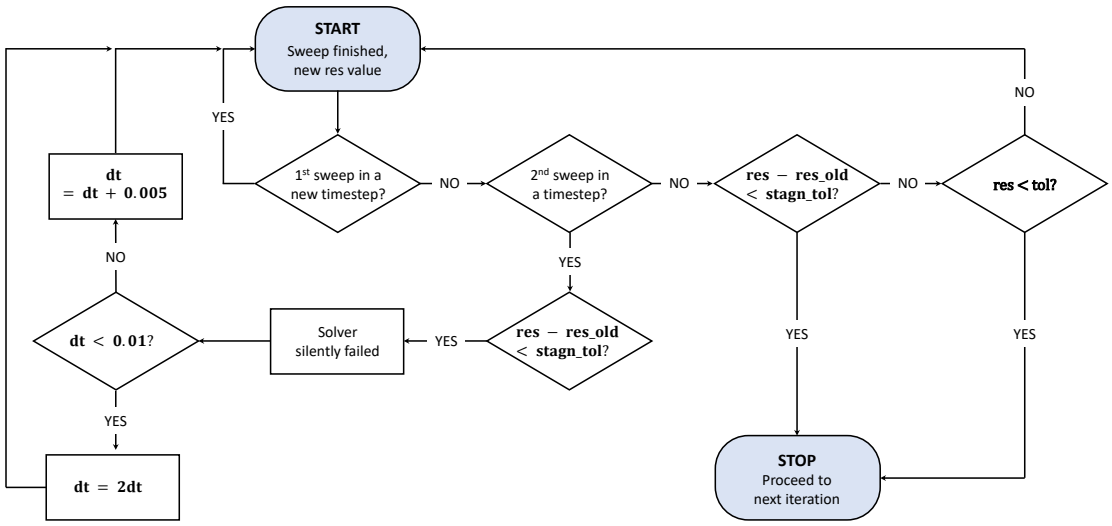


FIGURE 4.4: Adaptive time-stepping algorithm and tolerance threshold applied during the simulations. The tolerance value (`tol`) depended on what iteration the simulation was at, with the first four getting gradually decreasing values fine-tuned for each case study. After this, all simulations maintained `tol` = $2 \cdot 10^{-6}$. The tolerance value used to check for stagnation/equality between residual values, `stagn_tol`, had a value of $1 \cdot 10^{-14}$.

that can be obtained is system-dependent, with parameters such as grid size, resolution and the choice of initial and boundary conditions influencing it. Note that, in FiPy, sweeping is used to reach a solution that satisfies the nonlinear form of the equation as much as the discretised, linear one, which is passed to the solver. This way, sweeping corresponds with a fixed-point iteration, occurring within each timestep, and the residual, different to the solver tolerance, indicates how well the current solution satisfies the nonlinear equation. Thus, in early iterations (approx. $\tilde{t} < 5$) the residual limit might be higher than the general specified tolerance; this does not mean that the solution is ill-formed, but rather that the system has hit its limit. The algorithm was designed to check for this occurrence and accept it as a good solution, since the alternative (setting a tolerance high enough to also work with iterations at the start of the simulation) resulted in too loose a criterion at later stages.

The residual tolerance employed as a threshold to determine the successful end of an iteration had to be fine-tuned for the first four iterations in a given simulation, after which point they all had the same value. This is consequence of the chosen initial conditions: the step profiles show a discontinuity at the interface, which causes the gradient term in that vicinity to reach abnormally large values that can be hard to work with numerically. This way, the potential solutions reached by the solver must be herded towards reasonable values, sacrificing accuracy in the first 1–4 iterations for the sake of convergence. Acknowledging this and deciding to err on the side of caution, the first saved iteration, which corresponds to the 15^{th} timestep, was excluded from all presented results. Table 4.2 summarises the initial residual tolerances applied for every study.

When it comes to the postprocessing of results, the adaptive timestep algorithm applied ensured that only token changes were required. When presenting profiles at specific times, be it of

TABLE 4.2: Tolerance thresholds accepted in the solver residual for the first four time iterations. The compositions indicated in both streams are in the form (x_{API}, x_S, x_{AS}).

ID	Right stream	Left stream	`tol0`	`tol1`	`tol2`	`tol3`
1	$(0.24995, 0.74995, 10^{-4})$	$(10^{-4}, 10^{-4}, 0.9998)$	1.2	0.5	0.1	0.05
2	$(0.24995, 0.74995, 10^{-4})$	$(10^{-4}, 10^{-4}, 0.9998)$	1.2	0.5	0.1	0.05
3	$(0.44995, 0.54995, 10^{-4})$	$(10^{-4}, 10^{-4}, 0.9998)$	2.5	0.5	0.3	0.1
4	$(0.44995, 0.54995, 10^{-4})$	$(10^{-4}, 10^{-4}, 0.9998)$	2.5	0.5	0.3	0.1
5	$(0.54995, 0.44995, 10^{-4})$	$(10^{-4}, 10^{-4}, 0.9998)$	2	0.5	0.1	0.05
6	$(0.44995, 0.54995, 10^{-4})$	$(10^{-4}, 0.19995, 0.79995)$	2	1.5	0.3	0.05
7	$(0.8999, 0.1, 10^{-4})$	$(10^{-4}, 0.1, 0.8999)$	2	0.5	0.3	0.05
8	$(0.7999, 0.2, 10^{-4})$	$(10^{-4}, 0.2, 0.7999)$	2	0.5	0.3	0.05
9	$(0.6999, 0.3, 10^{-4})$	$(10^{-4}, 0.3, 0.6999)$	2	0.5	0.3	0.05
10	$(0.24995, 0.74995, 10^{-4})$	$(10^{-4}, 10^{-4}, 0.9998)$	x			
11	$(0.24995, 0.74995, 10^{-4})$	$(10^{-4}, 10^{-4}, 0.9998)$	2.6	1.3	0.5	0.1
12	$(0.24995, 0.74995, 10^{-4})$	$(10^{-4}, 10^{-4}, 0.9998)$	2.6	1.3	0.5	0.1
13	$(0.24995, 0.74995, 10^{-4})$	$(10^{-4}, 10^{-4}, 0.9998)$	2.75	1.5	0.5	0.1

composition or supersaturation, the profiles have been linearly interpolated between the two simulation times closest to the specified times. The `scipy.interpolate.interp1d` function from the SciPy library [141] was used for this. Given the high resolution of saved timesteps, this had minimal impact on the plotted profile, but was done for the sake of visualisation.

It is worth noting that, while the main features of the computational model have been discussed in this text, the complete code can be found in the supplementary information in case of doubt.

4.4 Results and discussion

This section presents the outcomes of the diffusion studies described above and examines their implications in the context of antisolvent crystallisation. Particular attention is given to the trajectories followed by the system across the ternary phase diagram, the phase behaviour caused by these pathways, and the evolution of supersaturation. Through their analysis, this model provides insight into how different systems may evolve, why LLPS or undesired CQAs may unexpectedly occur, and identifies the times and regions where solid-liquid nucleation becomes possible.

When interpreting these results in the context of experimental antisolvent crystallisation systems, it is important to consider the scope of the model. As discussed by Petrischeva and Abart [121] through a monotonicity analysis, this model can only evolve downhill in the free energy landscape. Hence, while it is fully capable of simulating LLPS within the spinodal region, it is unable to simulate nucleation, since this phenomenon requires the overcoming of an energy barrier to take place. This way, trajectories entering the binodal region may correlate experimentally to the formation of solid or liquid nuclei, whereas the simulated system will continue to diffuse. Despite this, the model can predict the times and regions in which the system becomes supersaturated and thus where nucleation could be observed experimentally.

4.4.1 Phase behaviour under different regions of the diagram

This section seeks to explore the diffusion and phase behaviour of the system under different initial stream compositions, spanning across the three main regions of the phase diagram. To isolate this effect, the physical characteristics of the system were fixed: (1) the Margules interaction parameter, $A = 3$, which describes the degree of non-ideality between the API and antisolvent; (2) the solubility parameter, $\beta\mu_1^{\circ,(S)} - \beta\mu_1^{\circ,(L)} = -1$; and (c) the diffusion coefficients between all species in the system, set to $D_{12} = D_{20} = 1$, and $D_{10} = 0.5$. The lower value of diffusion coefficient between API and antisolvent aimed to replicate a system where the diffusion of API is more challenging in the antisolvent than in the solvent. Moreover, the molar ratio between the streams was maintained constant at 50/50.

Mixing in the one-phase region: 25% **API,** 75% **solvent mixed with pure antisolvent**

This study focuses on reproducing the conditions of a typical antisolvent crystallisation system, with the compositions of both streams in the undersaturated region and their mixing point slightly above it, in what could possibly be considered the metastable region had this model incorporated nucleation. This way, a stream of pure antisolvent is mixed with a solution of 25% API. The effect of the gradient coefficient within this setup has also been studied, with two cases presented: $\tilde{\kappa}_{aa} = \tilde{\kappa}_{bb} = \tilde{\kappa}_{ab} = 0$ and $(\tilde{\kappa}_{aa}, \tilde{\kappa}_{ab}, \tilde{\kappa}_{bb}) = (0.05, 0.016, 0.05)$. These correspond respectively with experiments 1 and 2 in Tables 4.1 and 4.2.

Figure 4.5 presents the trajectories throughout the phase diagram (a-d) and the spatial composition profiles (e, f) of these two studies. In particular, experiment 1 is presented in Figure 4.5(a, c, e), and experiment 2, in Figure 4.5(b, d, f).

The compositional pathways in Figure 4.5(a) and (b) correspond with a subset of the studied times, whereas the complete temporal evolution is presented in Figure 4.5(c) and (d). Since the diagram represents composition space only, not all profiles will span across its width. In fact, the profiles become shorter as diffusion advances, until homogeneous mixing is achieved and the compositions across the system overlap on the same point. It should also be emphasised that the non-ideal interactions between API and antisolvent do not, by themselves, guarantee liquid-liquid phase separation, even if $A > 2$. Rather, they give rise to a miscibility gap within which LLPS is possible. If the compositional trajectories do not enter this region, as is the case in the present study, diffusion ultimately leads to homogeneous mixing.

The most prominent trend observed in these pathways is their significant non-linearity, which contrasts with the current general understanding of the scientific community on how diffusion occurs in antisolvent crystallisation. A linear evolution is generally assumed, with the compositions of both inlet streams travelling along a straight line in the ternary diagram until they reach the mixing point. However, both with (Figure 4.5b and d) and without (Figure 4.5a and c) considering an interfacial free energy term, the trajectories recovered by the proposed model are very distinctly nonlinear.

This deviation from the expected linear pathways can significantly affect the outcome of the crystallisation process. The curved trajectories could be veering outside of the design envelope,

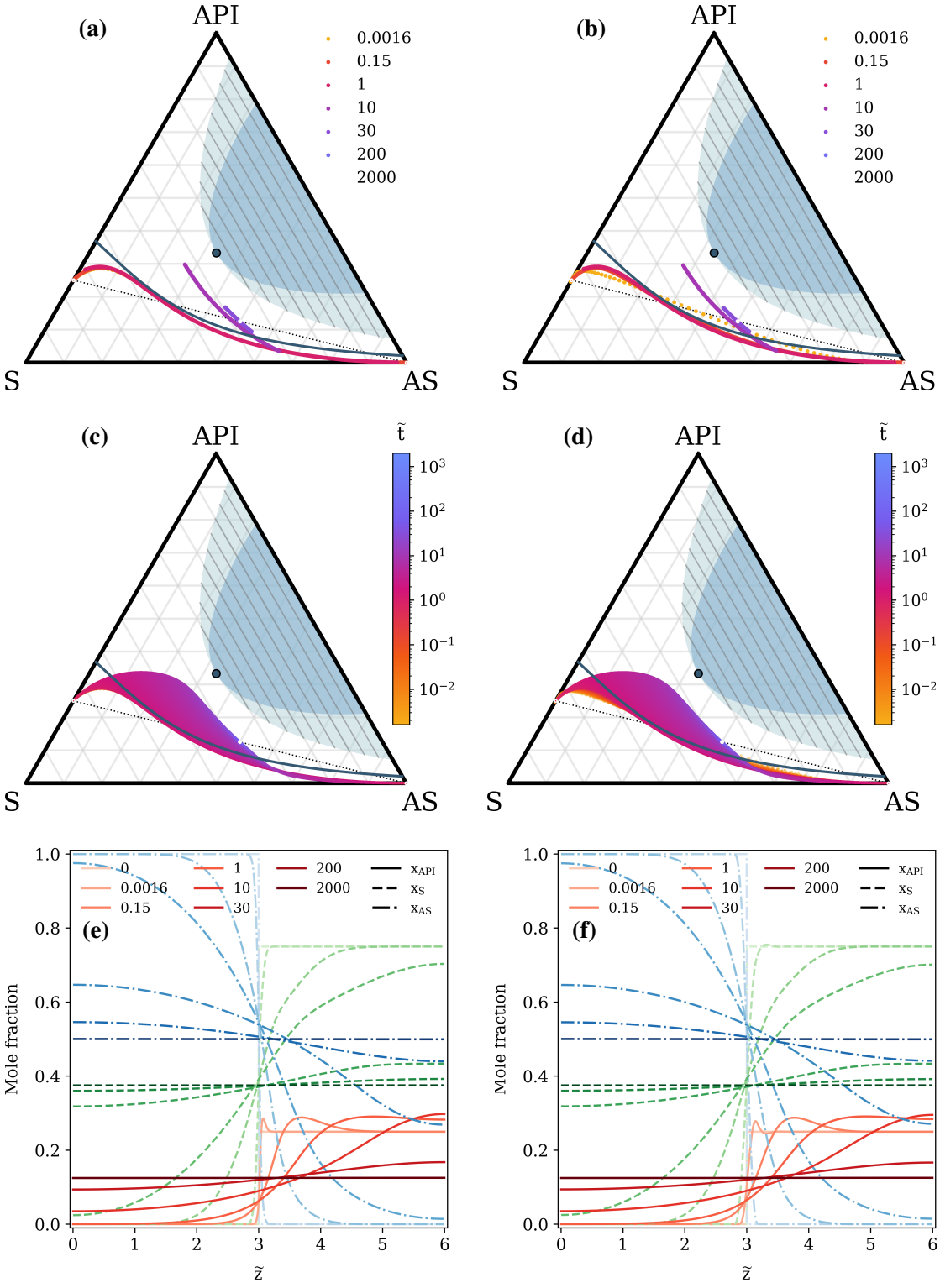


FIGURE 4.5: Evolution of the composition with time in a system mixing pure antisolvent with a 25% API solution, considering that $A = 3$ and $\beta\mu_1^{\circ,(S)} - \beta\mu_1^{\circ,(L)} = -1$. The gradient coefficient values are (a, c, e) $\tilde{\kappa}_{aa} = \tilde{\kappa}_{bb} = \tilde{\kappa}_{ab} = 0$ and (b, d, f) $(\tilde{\kappa}_{aa}, \tilde{\kappa}_{ab}, \tilde{\kappa}_{bb}) = (0.05, 0.016, 0.05)$. In particular, the compositional pathways through the ternary diagram are depicted in (a-d), with (a, b) presenting a subset of times, as per the legend, and (c, d) showcasing the the entire evolutions. In them, the solid blue line corresponds with the solubility curve, and the dotted line joins the two initial compositions, marked by a white circle. The last recorded profile for the system has been plotted in white. Lastly, (e, f) present the spatial composition profiles at the same times showcased in (a, b), in this case indicated by the coloured legend.

the region of the ternary phase diagram that guarantees the desired CQAs in the final crystalline product. Hence, inadequately predicting the diffusion trajectories of the system could translate into crystallising an unexpected polymorphic form, or an undesired crystal shape.

Exploring these dynamics in more detail reveals that both the system with and without a gradient free energy term present the same general trend regarding the API evolution, which can be divided into three major stages. (1) Immediately after the streams are put in contact, the API experiences uphill diffusion, accumulating next to the interface ($\tilde{z} = 3$) on the solvent side. In Figure 4.5(e) and (f), this corresponds with $\tilde{t} = 0.0016$. This is due to the non-ideal interactions between API and antisolvent causing a spike in the chemical potential at the point of contact between streams, as shown in Figure 4.6(a) for the case in which $\tilde{\kappa}_{aa} = \tilde{\kappa}_{bb} = \tilde{\kappa}_{ab} = 0$. Since the API-solvent interactions are ideal, this provokes the API to diffuse uphill into the solvent. (2) After this, and at still very early times, the wave of API continues to travel further into the solvent side, with the peak widening, growing and smoothing. Eventually, a maximum accumulation is reached at the boundary of this region ($\tilde{z} = 6$). In Figure 4.5(e) and (f), this stage corresponds with $\tilde{t} = 0.15$–10. The retreat of the API further into the solvent-rich region is a response to the mixing of solvent and antisolvent, which, due to their ideal interactions and larger interdiffusion coefficient, is more favoured than the diffusion of API into the antisolvent stream. This way, this trend can also be explained by considering the API chemical potential and diffusive flux profiles, presented for two consecutive times in Figure 4.6(b) together with the API composition profile. Since mass transfer occurs from regions of high to low chemical potential, the driving force will seek to smooth out the initial spike formed in the chemical potential profile. The reason why doing so by diffusing uphill towards the right region is favoured over diffusing downhill towards the left is because the non-ideality between API and antisolvent, as well as the near-zero API and solvent compositions on the left, make the diffusive flux stronger towards the right side. This is clearly visible in Figure 4.6(b), where the diffusive flux $\widetilde{J}_1$ has a larger absolute value on the positive peak at the right side of the interface, indicating a faster rate of mass transfer towards the solvent-rich side of the system. (3) After the wave of API reaches its maximum value at the right boundary, its diffusion continues exclusively downhill, which in Figure 4.5(e) and (f) can be observed at $\tilde{t} > 10$. From a driving force perspective, this occurs because the initial chemical potential spike has smoothed out towards the solvent-rich side to the point that its highest value is now at $\tilde{z} = 6$, leaving only a left-side gradient. Given the lower interdiffusion coefficient between API and antisolvent, and their non-ideal interactions, this downhill diffusion proceeds at a much slower rate, as the profiles in Figure 4.5(e) and (f) demonstrate.

The fact that these composition and chemical potential trends were observed both with and without an interfacial free energy confirms their physical validity. The same qualitative composition and chemical potential trends were obtained by Zhang [9] when studying oiling out in an antisolvent crystallisation system, further supporting this conclusion. Moreover, this also indicates that the curved composition pathways and API overshoots were primarily rooted in the non-idealities of the system [151], and thus can be described by considering a thermodynamically accurate driving force for diffusion. This perspective agrees with recent literature trends [9, 95], where the Maxwell-Stefan framework is identified as a more suitable alternative to Fickian

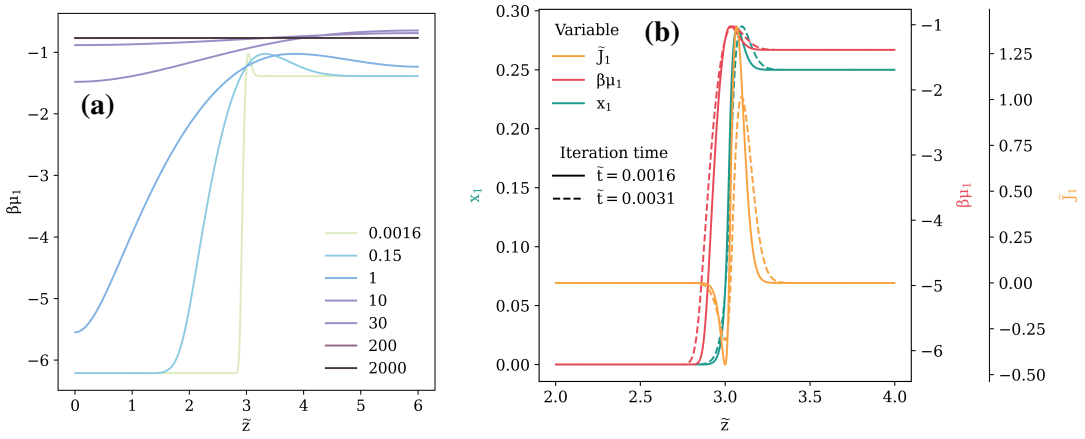


FIGURE 4.6: Chemical potential and diffusive flux exploration in a system mixing pure antisolvent with a 25% API solution, and considering that $\tilde{\kappa}_{aa} = \tilde{\kappa}_{bb} = \tilde{\kappa}_{ab} = 0$, $A = 3$ and $\beta\mu_1^{\circ,(S)} - \beta\mu_1^{\circ,(L)} = -1$. (a) Evolution of the chemical potential profiles with the times reported in the legend. (b) Chemical potential, mole fraction and diffusive flux of API for two consecutive saved iterations.

diffusion to describe the evolution of mass transfer in non-ideal systems. Lastly, it is worth mentioning that the three-stage cycle described above may be disrupted at any point if nucleation occurred. This would decrease the concentration of API in the solution, which would alter the trajectory through the phase diagram. Thus, the system may cross into different regions than those predicted by this model.

The agreement of these qualitative trends between the cases with and without an interfacial free energy should not be interpreted as evidence that this term does not bear an impact on systems outside of the miscibility gap. This is clearly proven by the supersaturation profiles presented in Figure 4.7, in which (a) corresponds with $\tilde{\kappa}_{aa} = \tilde{\kappa}_{bb} = \tilde{\kappa}_{ab} = 0$ and (b) with $(\tilde{\kappa}_{aa}, \tilde{\kappa}_{ab}, \tilde{\kappa}_{bb}) = (0.05, 0.016, 0.05)$. Incorporating the interfacial free energy term predicts supersaturation values greater than 1 near the interface at the start of the diffusion process, when the two streams are put in contact. To mitigate the sharpness of the initial composition gradient at the interface, the gradient term rapidly establishes a series of intermediate compositions, which trajectory corresponds with the yellow profile in Figure 4.5(b), at $\tilde{t} = 0.0016$. In contrast, the initial profiles of the system without interfacial free energy shown in Figure 4.5(a) follow a trajectory much more parallel to the solubility curve, and do not cross it at any point. After this initial supersaturation spike, the system returns to an undersaturated state, to later become supersaturated again at approximatedly $\tilde{t} = 2$, in a region of the phase diagram different to the one of the initial spike. In fact, the largest levels of supersaturation are found at this second stage ($\tilde{t} = 10$–100), away from the interface and deep into the solution side, as the uphill diffusion of the API comes to its end.

These results demonstrate how neglecting the contribution of the interfacial free energy to mass transfer can lead to erroneous predictions of the time, spatial location, and region of the phase diagram in which supersaturation occurs. If the system has long induction times at low

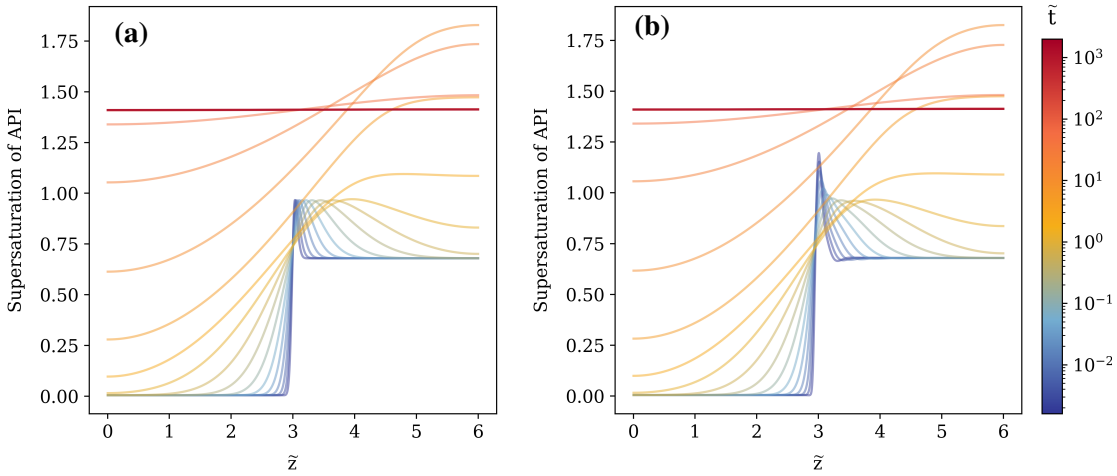


FIGURE 4.7: Evolution of the supersaturation profiles across the entire time range within a system of two mixing streams, one of pure antisolvent and another formed by 25% of API and 75% of solvent. It is considered that $A = 3$ and $\beta\mu_1^{\circ,(S)} - \beta\mu_1^{\circ,(L)} = -1$. Two subsets of the interfacial free energy coefficient are presented: (a) $\tilde{\kappa}_{aa} = \tilde{\kappa}_{bb} = \tilde{\kappa}_{ab} = 0$, and (b) $(\tilde{\kappa}_{aa}, \tilde{\kappa}_{ab}, \tilde{\kappa}_{bb}) = (0.05, 0.016, 0.05)$.

levels of supersaturation, nucleation may not occur during the initial spike predicted in Figure 4.7(b). However, if induction times are short, crystal nucleation may occur during this period. In that case, since the system would be nucleating at a very different region of the phase diagram, the resulting product may have unexpected and undesired properties, such as a different crystal shape or polymorphic form.

Mixing point in the binodal region: 45% API, 55% solvent mixed with pure antisolvent

The second set of initial conditions was selected such that the presumed linear mixing pathway between the streams would lie within the binodal region, by mixing a stream composed of 45% API and 55% solvent with pure antisolvent. These correspond respectively with experiments 3 and 4 in Tables 4.1 and 4.2. Although this initial API solution is already supersaturated, the objective of this study is to understand the behaviour of the system in different regions of the phase diagram, rendering these initial conditions appropriate.

Figure 4.8 presents the ternary diagram trajectories (a, b) and composition profiles (c, d) obtained from this study. The effect of the interfacial free energy has been analysed, with Figures 4.8(a) and (c) corresponding to $(\tilde{\kappa}_{aa}, \tilde{\kappa}_{ab}, \tilde{\kappa}_{bb}) = (0.025, 0.008, 0.025)$ and Figures 4.8(b) and (d), to $(\tilde{\kappa}_{aa}, \tilde{\kappa}_{ab}, \tilde{\kappa}_{bb}) = (0.1, 0.032, 0.1)$.

This case study is of particular interest, since without the gradient term it would not have been possible to solve either of these simulations. The non-idealities between API and antisolvent have clearly driven the compositional pathways into the spinodal region, a possibility already observed and postulated in recent mixing studies [96, 151]. However, the results of this work seemingly indicate that whether it remains inside as a phase-separated system or not depends on the magnitude of the interfacial tension. The low interfacial free energy coefficient employed in Figures 4.8(a) and (c) shows the system becoming trapped within the spinodal region, undergoing liquid-liquid phase separation into two binodal coexistence compositions. In

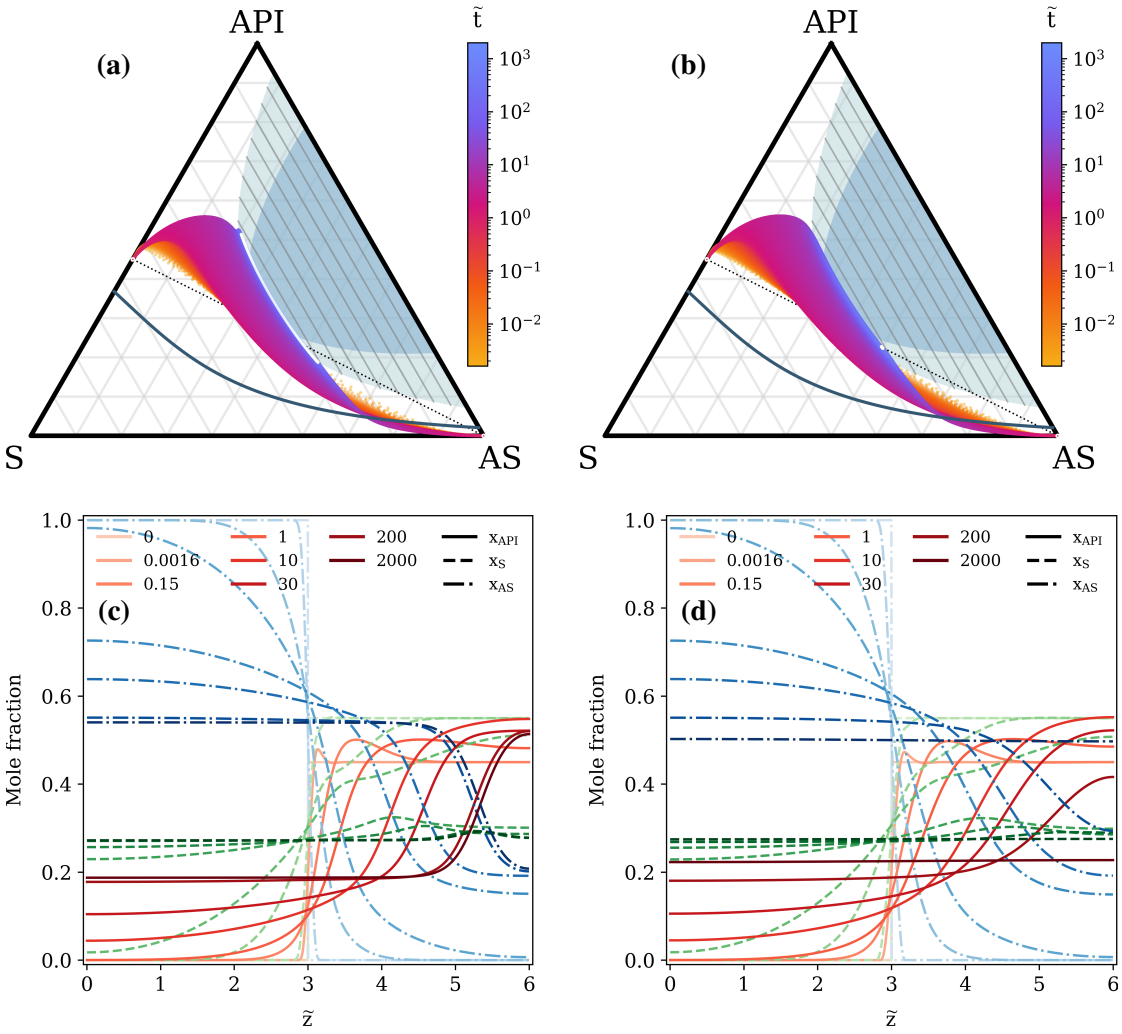


FIGURE 4.8: Evolution of the composition with time in a system mixing pure antisolvent with a 45% API solution, considering that $A = 3$ and $\beta\mu_1^{\circ,(S)} - \beta\mu_1^{\circ,(L)} = -1$. The gradient coefficient values are (a, c) $(\tilde{\kappa}_{aa}, \tilde{\kappa}_{ab}, \tilde{\kappa}_{bb}) = (0.025, 0.008, 0.025)$ and (b, d) $(\tilde{\kappa}_{aa}, \tilde{\kappa}_{ab}, \tilde{\kappa}_{bb}) = (0.1, 0.032, 0.1)$. In particular, (a, b) depict the compositional pathways through the ternary diagram. The blue line in them is the solubility curve, and the dotted line joins the two initial compositions, marked by a white circle. To ease visualisation, the last recorded profile has been plotted in white. (c, d) present the spatial composition profiles at the times indicated by the coloured legend.

contrast, the larger coefficient considered in Figures 4.8(b) and (d) enables the system to leave the spinodal region and reach a fully mixed final state, the composition of which corresponds with the expected mixing point. This agrees with the previously discussed impact of κ_{ij}: a larger gradient coefficient implies a larger interfacial free energy, and thus imposes a greater energetic penalty compositional heterogeneities within the system.

The spatial composition profiles presented in Figures 4.8(c) and (d) help explain why one system remained phase-separated while the other one evolved towards homogeneity. Figure 4.8(c) shows that, in the final configuration, the interface is located considerably close to the right-hand boundary of the system ($\tilde{z} = 6$). This is most likely because the uphill diffusion of the API drove

that region of the system to compositions very close to the binodal boundary. Shortly after downhill diffusion began, this region settled on the binodal curve, while the remainder of the system approached the corresponding coexistence composition on the opposite side of the miscibility gap. Interestingly, the curved pathway characteristic of this diffusion behaviour altered its course after reaching the coexistence composition on the solvent-rich region, with none of the intermediate interfacial compositions venturing further into the spinodal region than required by the equilibrium profile. It is also interesting to note that the final profile does not follow a straight line, as would be expected through the tie lines, but a curved one, as shown in Figure 4.8(a). This behaviour is discussed more in depth when discussing the next set of experiments, and in Section 4.11; it is consequence of solvent enrichment at the interface, and it is physical and characteristic of equilibrium in a phase-separated system [143].

Close examination of the final configuration depicted in Figures 4.8(a) and (c) reveals that the bulk phase near $\tilde{z} = 6$ does not actually sit on the binodal curve, but slightly inside the binodal region. This behaviour is most likely a consequence of the gradient term. As observed in Section 3.4.3, the system is sufficiently large for the contribution of the gradient term to vanish at the boundaries when the interface is located at $\tilde{z} = 3$. However, when the interface is positioned as close to the boundary as in Figure 4.8(c), this assumption no longer holds. Consequently, the composition near $\tilde{z} = 6$ does not sit exactly on the binodal curve because the gradient term is strong enough to penalise compositional inhomogeneities in this region, thereby shifting the composition slightly away from the coexistence value.

This argument can also explain why the system reaches homogeneous mixing in Figures 4.8(b) and (d). In this case, the gradient coefficient is larger, implying a larger interfacial tension and, consequently, a stronger energetic penalty for compositional inhomogeneities. It is possible that this penalty becomes large enough that, despite the system wanting to phase-separate when crossing the spinodal boundary, the system is driven towards complete mixing, aided in this by the Neumann boundary conditions used in these simulations.

The observed trends indicate that simply increasing the size of the simulation domain would not alter this outcome. As explained above, the reason the system approaches the binodal region so close to the solvent-rich boundary is that the uphill diffusion of the API drives it there. Uphill diffusion only ceases because the wave-like profile exhibited by the API composition reaches the boundary of the domain, which then becomes the location of maximum chemical potential, leaving downhill diffusion towards the left-hand side as the only possible next pathway. Therefore, a larger system would be expected to exhibit the same trends observed in Figure 4.8. A more accurate assessment is that this behaviour arises from the finite nature of the system.

The available evidence therefore suggests that the fully mixed results obtained for $(\tilde{\kappa}_{aa}, \tilde{\kappa}_{ab}, \tilde{\kappa}_{bb}) = (0.1, 0.032, 0.1)$ may be representative of the behaviour of a physical system in which the interface ultimately interacts closely with the boundaries of the domain, as may occur, for example, in a microfluidic device. Were this not the case, the physical system would be expected to undergo phase separation after the uphill diffusion of the API.

Despite this challenge, it is important to emphasise that this model can still successfully simulate liquid-liquid phase separation, as Figures 4.8(a) and (c) demonstrate. According to Fickian

diffusion, a system with these characteristics would never undergo spinodal decomposition, since the model cannot predict the system departing from a linear composition pathway. Although the Maxwell-Stefan framework can predict non-linearities in the mass transfer evolution, it is unable to capture spinodal dynamics and would therefore fail for both of the case studies presented in this section. Incorporating the interfacial term into the diffusion model overcomes this limitation, as shown in Figures 4.8(a) and (c).

Mixing point in the spinodal region: 55% API, 45% solvent mixed with pure antisolvent

This set of initial conditions was selected to allow the presumed linear mixing pathway between streams and the mixing point of the homogeneous system to lay inside the spinodal region. Thus, a stream of pure antisolvent is mixed with a solution formed by 55% API and 45% solvent. The binary interaction parameter between API and antisolvent is maintained at $A = 3$, and the interfacial free energy coefficients, set to $(\tilde{\kappa}_{aa}, \tilde{\kappa}_{ab}, \tilde{\kappa}_{bb}) = (0.025, 0.008, 0.025)$. This corresponds with experiment 5 in Tables 4.1 and 4.2.

The composition evolution during its diffusion process has been summarised in Figure 4.9. At a glance, the compositional pathways follow a very similar trend to those in the previous two case studies, with initial uphill diffusion occurring on the API-rich stream causing an API composition overshoot on the vicinity of the interface, and with the system eventually reaching equilibrium in a phase-split configuration. In addition to this, two prominent trends are worth noting.

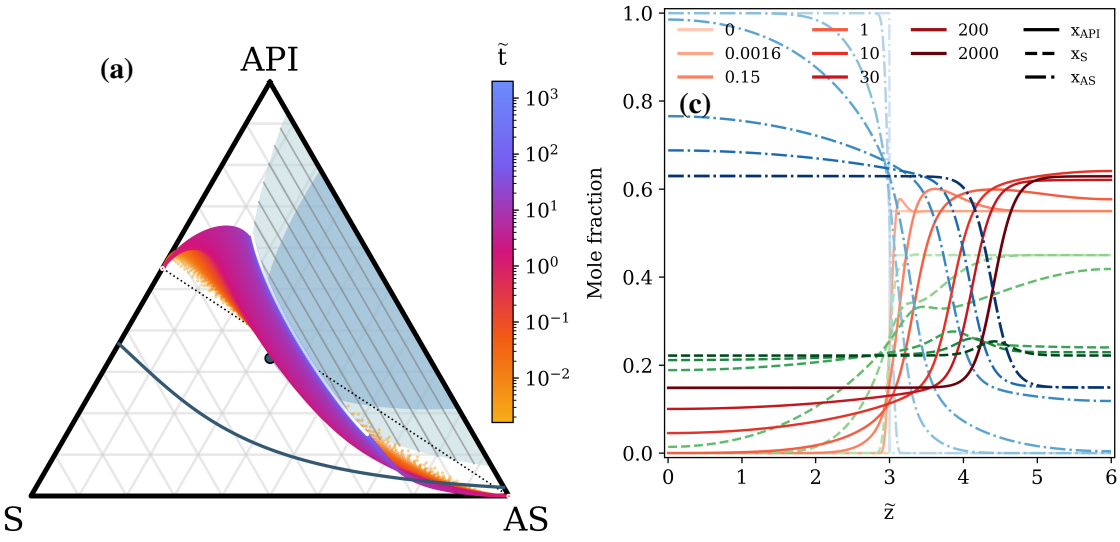


FIGURE 4.9: Mass transfer evolution across the ternary phase diagram (a) and as composition profiles (b) within a system of two mixing streams, one of pure antisolvent and another formed by 55% of API and 45% of solvent. It is considered that $A = 3$ and $\beta\mu_1^{\circ,(S)} - \beta\mu_1^{\circ,(L)} = -1$. The interfacial free energy coefficients are set to $(\tilde{\kappa}_{aa}, \tilde{\kappa}_{ab}, \tilde{\kappa}_{bb}) = (0.025, 0.008, 0.025)$. (a) The solid blue line corresponds with the solubility curve, and the dotted line joins the two initial compositions, which have been marked by a white circle. The last recorded profile for the system has also been plotted as a series of white markers. (b) The coloured legend corresponds with the presented times, which are shown for all three species.

Firstly, the equilibrium composition profiles were expected to follow a linear trend, completely parallel to the tie lines, when represented on the ternary diagram. However, this is not so for the presented case, or for any other values of the gradient coefficient tested, which can be found in Appendix F. While the compositions of the two bulk phases are symmetrical with respect to the critical point, laying across a tie line and located on the binodal curve, the interfacial compositions present a slight curvature, which maximum occurs on the critical point axis. This curvature is caused by an accumulation of solvent at the interface, clearly identifiable in the composition profiles in Figure 4.9(b). Interestingly, this phenomenon was also observed in the previous case study in Figure 4.8(a). This phenomenon has been reported in literature as characteristic of the equilibrium composition profile in a ternary system undergoing spinodal decomposition [143], and was also reported by Petrischeva and Abart [121]. From a physical perspective, the solvent may be accumulating at the interface because doing so decreases the total free energy of the system. The non-ideality between API and antisolvent causes mixtures with compositions that lay inside the spinodal to have a much higher free energy than mixtures at the coexistence compositions. However, since passing through these intermediate values is needed to form the interface, the system decreases the free energy at this location by trapping solvent at the interface, which Figure 4.1 shows leads to a more energetically favourable profile. The fact that the free energy trend supports the accumulation of solvent at the interface indicates that this behaviour is physical. In Section 4.4.2, the question of whether this behaviour is maintained across the entire miscibility gap is addressed.

The second trend of interest is the apparent existence of two different compositional regimes, one observed at very early times ($\tilde{t} = 10^{-3}$–10^{-1}), and the other developed at later stages of the simulation ($\tilde{t} = 1$–2000). In Figure 4.9(a), the yellow and orange trends belong to the first regime, and the magenta and purple regions correspond with the second one. It is worth mentioning that this trend could also be observed in the two previous case studies. In particular, in Figure 4.5 it can be observed that when the interfacial free energy term is omitted, only the second compositional regime is visible. In Figure 4.9, for the current case study, the higher value of the interfacial free energy coefficient yields a denser region for the first regime. This evidence indicates that the first regime is related to the interfacial term, and the latter, to the more general bulk diffusion terms. The step configuration of the initial conditions possesses a discontinuity at the interface, which in the discretised system is translated into an extremely large composition gradient at early stages of the simulation. Thus, the value of the interfacial free energy is also incredibly large, overpowering the other terms and forcing the system to quickly establish an interface to relax the value of the gradients. This is the phenomenon observed in the first compositional regime. After the initial interfacial response is sufficiently neutralised, the system progresses with bulk diffusion, which occurs at a considerably slower pace.

Reduction of the S/AS ratio as a means of avoiding spontaneous LLPS

The last set of initial conditions was designed to establish the reduction of the solvent/antisolvent ratio as an effective strategy for the control of oiling out. Previous work in this area [96] has established the ratio of solvent to antisolvent as a critical parameter to control the occurrence of

oiling out, with antisolvent streams closer to purity being reported as having a higher chance of LLPS [9]. Observing the phase diagram, it is clear that this is caused by the higher proximity of any potential diffusion pathways to the miscibility gap. Regardless of the degree of nonlinearity, positioning the system closer to the boundaries of the miscibility gap will clearly increase the probability of veering into the binodal or spinodal regions, potentially causing oiling out. By cutting the pure antisolvent with some solvent, which is equivalent to decreasing the ratio between the two, the initial composition of the antisolvent-rich stream is brought to a point in the phase diagram much less enclosed by the miscibility gap. Thus, it will be less probable to observe LLPS.

This is confirmed by the results summarised in Figure 4.10, where the evolution of the system with interfacial coefficients of $(\tilde{\kappa}_{aa}, \tilde{\kappa}_{ab}, \tilde{\kappa}_{bb}) = (0.025, 0.008, 0.025)$, corresponding with experiment 6 in Tables 4.1 and 4.2, is presented. In particular, Figure 4.10(a) follows the compositional pathways throughout the ternary diagram, and Figure 4.10(b) showcases certain composition profiles at selected times.

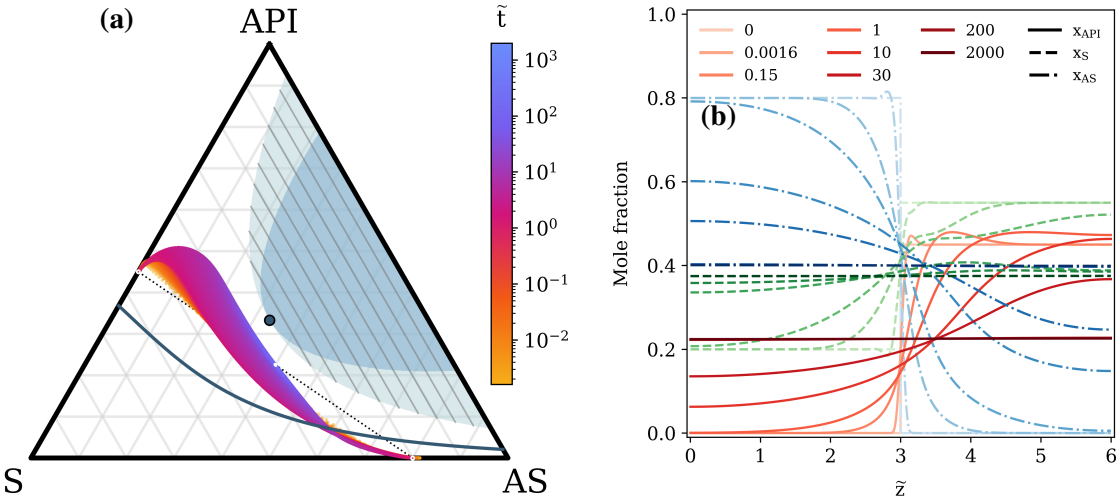


FIGURE 4.10: Mass transfer evolution across the ternary phase diagram within a system of two mixing streams, one formed by 45% of API and 55% of solvent, and the other, by 80% antisolvent and 20% solvent. It is considered that $A = 3$ and $\beta\mu_1^{\circ,(S)} - \beta\mu_1^{\circ,(L)} = -1$. The interfacial free energy coefficients are $(\tilde{\kappa}_{aa}, \tilde{\kappa}_{ab}, \tilde{\kappa}_{bb}) = (0.025, 0.008, 0.025)$. (a) Composition evolution throughout the ternary phase diagram. The solid blue line corresponds with the solubility curve, and the dotted line joins the two initial compositions, which have been marked by a white circle. The last recorded profile for the system has also been plotted as a series of white markers. (b) Composition profiles of the three species at selected times. Note that the times have been represented through colours of increasing intensity, and they are the same for all three species.

The values of the interfacial free energy coefficients are the same as those explored in Figure 4.8, where a solution of the same composition was mixed with pure antisolvent, and for which an incursion into the spinodal region was observed. However, the current initial conditions managed to position the system sufficiently further away from the miscibility gap to avoid that the initial API composition spike on the solvent-rich side causes the diffusion pathway to cross the binodal or spinodal boundaries. Thus, this proves the effectiveness of diluting the antisolvent with solvent as a strategy to reduce the probability of observing oiling out. These

results were replicated for all tested values of the interfacial coefficients, ranging from 0 to $(\tilde{\kappa}_{aa}, \tilde{\kappa}_{ab}, \tilde{\kappa}_{bb}) = (0.1, 0.032, 0.1)$. They can be seen in Appendix F.

It is worth mentioning the spike that both API and antisolvent experience immediately after the two streams are put in contact, on their respective neighbouring regions to the interface, as observed in Figure 4.10(b). The antisolvent also experiences some initial uphill diffusion, albeit to a lower extent than the API and with the initial spike being smoothed out at later times. This can also be observed in Figure 4.10(a) where some yellow points move from the initial composition towards the pure antisolvent. This uphill diffusion is again due to the nonideality in the API-antisolvent interactions. The reason why in the previous case studies uphill diffusion was observed exclusively in the API trends is because the antisolvent stream was completely pure, thus preventing it from experiencing any composition increase.

4.4.2 Diffusion and equilibrium across the miscibility gap

Having established the behaviours expected in different regions of the phase diagram and the physical phenomena underpinning them, this section examines the diffusion dynamics within the spinodal region in more detail. This is a unique capability of the model proposed in this work, enabled by the incorporation of an interfacial term to the free energy. Although Tsugawa *et al.* [10] applied a ternary phase-field model to the study of diffusion dynamics within the spinodal region, their work focused on determining the potential configurations that the system could reach, and did not discuss the equilibrium compositions reached in each phase or at their interface. In fact, Matsushima *et al.* [153] recently identified the study of equilibrium phase behaviour as key for the understanding of localised oiling out. This way, this section provides a deeper insight into the diffusion and phase dynamics occurring inside the spinodal region, aiming to contribute to the understanding of LLPS.

For this purpose, three systems which mixing points lay within the spinodal decomposition region have been investigated, each containing a different initial solvent composition (10, 20 and 30%). The solvent composition was maintained constant across both initial streams in order to ensure the initial conditions remained parallel to the tie lines within the miscibility gap. These systems correspond with experiments 7–9 in Tables 4.1 and 4.2. In all cases, the degree of nonideality between API and antisolvent was fixed at $A = 3$, while the gradient coefficients were set to $(\tilde{\kappa}_{aa}, \tilde{\kappa}_{ab}, \tilde{\kappa}_{bb}) = (0.025, 0.008, 0.025)$.

Figure 4.11 presents the results of this study, focusing on the evolution of composition and free energy. In particular, Figure 4.11(a) depicts the evolution with time of their trajectories through the ternary diagram. A subset of composition pathways observed for the latter is presented in Figure 4.11(b); and Figure 4.11(c) showcases selected composition profiles from this case, which are representative of all three studies since their evolution follows the same qualitative steps. Lastly, Figure 4.11(d) presents the evolution with time of the unscaled total free energy in the three systems.

The mass transfer pathways across the ternary diagram presented in Figure 4.11(a) show

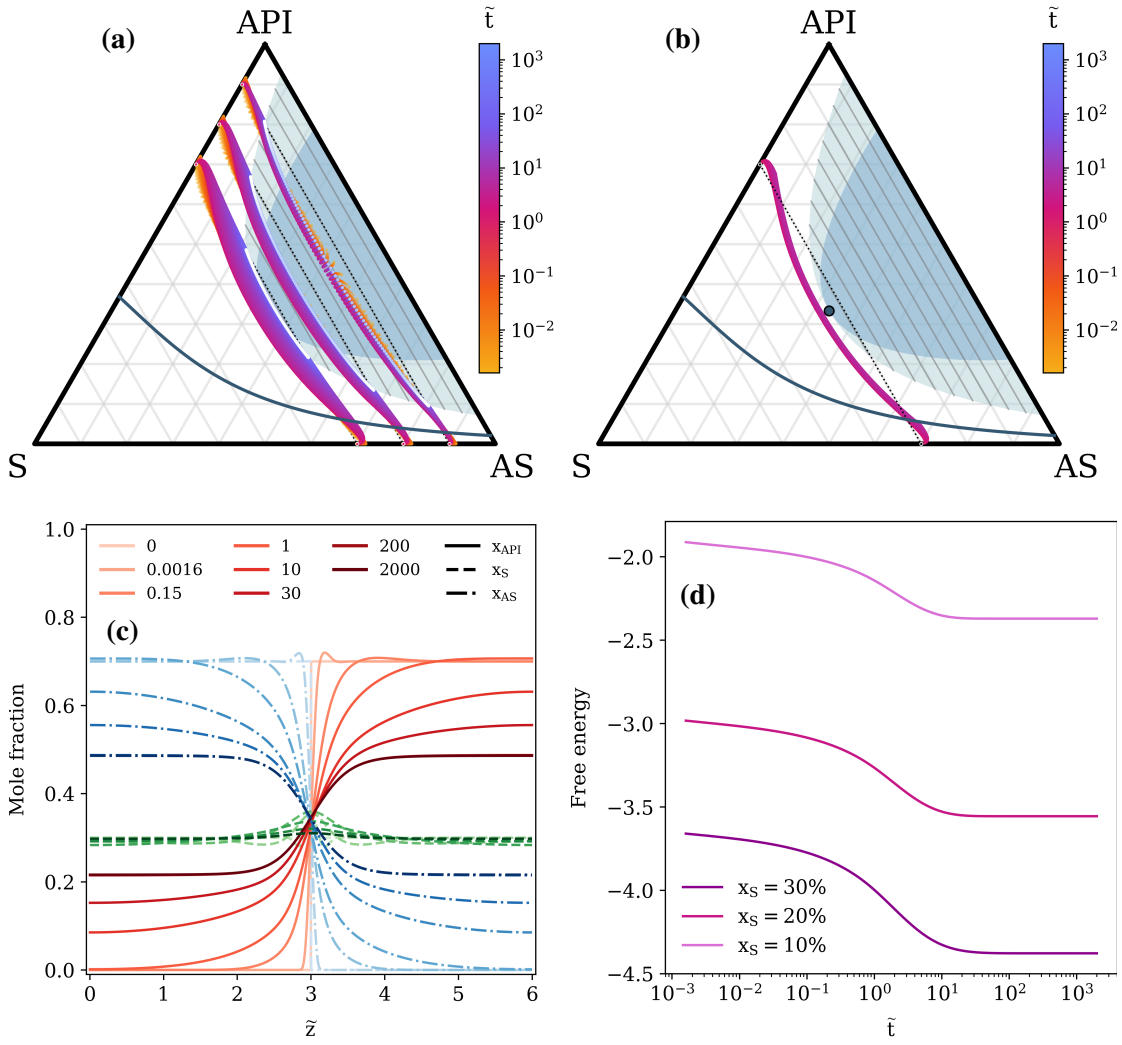


FIGURE 4.11: Summary of system evolution during diffusion for initial conditions positioned across the miscibility gap and parallel to tie lines; 10, 20 and 30% initial solvent composition in both streams were considered. The degree of non-ideality between API and antisolvent was fixed at $A = 3$; $\beta\mu_1^{\circ,(S)} - \beta\mu_1^{\circ,(L)} = -1$; and the interfacial free energy coefficients were $(\tilde{\kappa}_{aa}, \tilde{\kappa}_{ab}, \tilde{\kappa}_{bb}) = (0.025, 0.008, 0.025)$. (a) Mass transfer pathways across the ternary diagram, with the last recorded profile plotted as a series of white markers. (b) Subset of times, from $\tilde{t} = 1$–5, for the $x_S = 30\%$ case. (c) Composition profiles at selected times for the $x_S = 30\%$ case. The times have been represented through colours of increasing intensity, and they are the same for all three species. (d) Total unscaled nondimensional free energy in all three systems with time.

the same accumulation of solvent at the interface observed in Section 4.4.1. Although this prevents the final profile from following the tie lines, the equilibrium compositions of the two separated phases still correspond with the expected coexistence compositions, located symmetrically across the miscibility gap. The temporal free energy evolutions shown in Figure 4.11(d) show that this behaviour is physical, since the free energy only ever decreases or remains constant. Moreover, as mentioned in Section 4.4.1, this phenomenon has been previously reported in literature, and is characteristic of the equilibrium composition profiles in a phase-split system [143]. As Figures 4.12(a) and (b) demonstrate, from the critical point until the API–AS axis, the free

energy increases as the solvent content decreases. Therefore, trapping solute at the interface allows the system to reach a more energetically favourable composition profile in this region.

Interestingly, the curvature of the interfacial region arising from solvent accumulation becomes increasingly pronounced as the total solvent content decreases. The free energy curves shown in Figure 4.12(b) prove that the penalty between the double well becomes increasingly shallower when approaching the critical point. Therefore, at $x_S = 30\%$ the bulk phases and interfacial region maintain a much more similar free energy level. As a result, less solvent accumulation is required for stability than in the $x_S = 10\%$ system, in which the free energy penalty between the wells is much steeper.

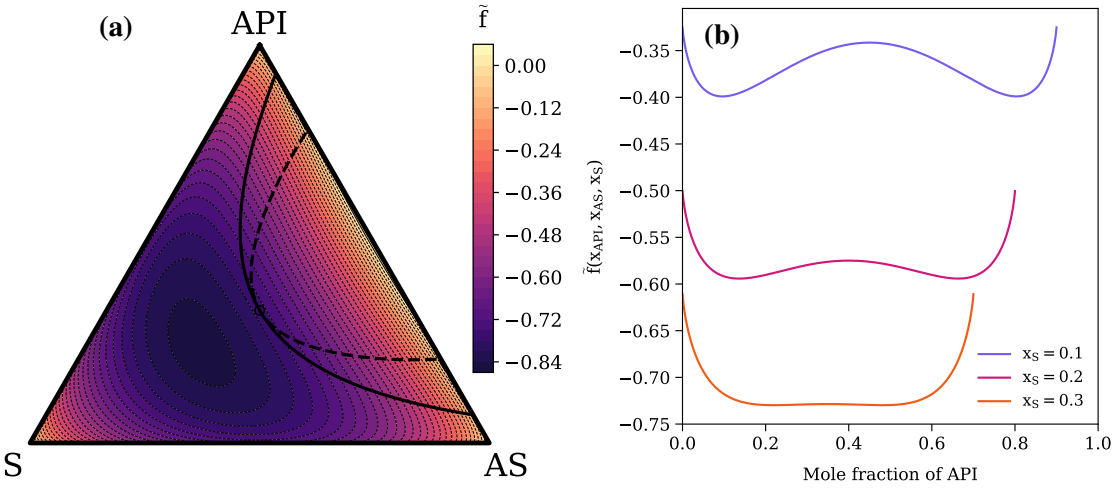


FIGURE 4.12: Free energy landscape of a system in which $A = 3$ and $\beta\mu_1^{\circ,(S)} - \beta\mu_1^{\circ,(L)} = -1$, without considering the gradient term. (a) Unscaled free energy across the ternary phase diagram. (b) Unscaled free energy profiles for the three fixed solvent contents explored in this study: 10, 20 and 30%.

Figure 4.11(b) presents a subset of the spatial composition profiles observed during the diffusion of the $x_S = 30\%$ case at the onset of the second diffusion regime, which are particularly noteworthy. Whereas the equilibrium profile in this case shows the smallest accumulation of solvent at the interface, the range of compositions covered by the system during this diffusion process is the widest. This indicates the accumulation of a larger relative solvent content in the interfacial region during the diffusion, which eventually smooths out. Notably, the concentration of solvent at the presented subset of times (before the phase separation stage occurs) is high enough to push the system entirely out into the one-phase region, bending it away from the miscibility gap. The system later returned to the miscibility gap rather than homogenising in the one-phase region because its mixing point lies within the spinodal region. Therefore, the system cannot maintain a homogeneous composition outside the miscibility gap, as there is insufficient material available to do so. The system also cannot remain phase-separated outside of the miscibility gap because there is no thermodynamic driving force for phase separation in this region. Consequently, the composition pathway had to return to the spinodal region.

Lastly, the composition profiles showcased in Figure 4.11(c) reveal the same spikes of API and antisolvent that were observed in Section 4.4.1. While their locations are maintained, appearing on their respective vicinities to the interface, in this case the antisolvent peak is much more

pronounced. Interestingly, accommodating the excess material in these two regions requires a local decrease in solvent composition, with the displaced material potentially accumulating at the interface.

Together with the other spatial composition profiles presented so far, this observation suggests that the behaviour of the solvent is partly governed by the non-ideality between API and antisolvent. The accumulation of solvent at the interface in order to support a more energetically stable composition profile through this region supports this idea, as well as the mentioned dip of the solvent composition at the sides of the interface to accommodate the uphill diffusion of the other two species. Similarly, in Figure 4.10(b), the shape of the solvent composition profile on the API-rich side at $\tilde{t} = 0.15$ and 1 presents kinks uncharacteristic of natural bulk diffusion. This could be because the solvent amount is adjusting to the spike of API and the gradual diffusion of antisolvent into this region. This behaviour is most likely a consequence of the solvent presenting the same affinity for the API as for the antisolvent, since the binary interaction parameters of these pairs were zero, indicating thermodynamically ideal interactions.

4.4.3 Study on the effect of different antisolvents

The last section of this study aims to understand how different solvent-antisolvent pairs could be investigated within this modelling framework, and their potential impact on the outcomes of both crystal nucleation and LLPS in the antisolvent crystallisation process.

The three main variables that the proposed model offers when it comes to species customisation are (1) the solubility of the API in the liquid matrix, which in this work is determined by $\beta\mu_1^{\circ,(S)} - \beta\mu_1^{\circ,(L)}$; (2) the diffusivities between species, and (3) the activity model used, which, for the chosen one-parameter Margules model in this work, corresponds with the value of the binary interaction parameters.

With this in mind, this section presents first the impact of changing the diffusion coefficient ratios as per experiments 10–12 in Tables 4.1 and 4.2. Afterwards, the effect of increasing the value of A is analysed, this study corresponding to experiment 13 in Tables 4.1 and 4.2. The reason why it was decided not to perform a dedicated solubility study is that this parameter does not have an impact on the diffusion dynamics. Changing its value would not alter the composition trajectories in the ternary diagram, it would only alter the supersaturation profiles, behaving as a threshold change.

Diffusion coefficients between species

This section explores the effect of different diffusivity combinations on the mass transfer and supersaturation dynamics of a system in which a stream of pure antisolvent mixes with a 25% API solution. The degree of nonideality corresponds with $A = 3$, and the interfacial free energy coefficients are fixed at $(\tilde{\kappa}_{aa}, \tilde{\kappa}_{ab}, \tilde{\kappa}_{bb}) = (0.025, 0.008, 0.025)$. Three different case studies are considered: (1) a reproduction of the values used in all previous studies, $(\widetilde{D}_{10}, \widetilde{D}_{20}, \widetilde{D}_{12}) = (0.5, 1, 1)$; (2) a reduction of only the API-antisolvent diffusivity (D_{10}) to 0.1; and (3) a reduction of the diffusion of the API in both solvents ($\widetilde{D}_{10} = \widetilde{D}_{20} = 0.1$).

Figure 4.13 summarises the outcomes of the first two studies. In particular, Figures 4.13(a, b) and (e, f) show their trajectory across the ternary phase diagram, while Figures 4.13(c) and (d) compare their spatial composition and supersaturation profiles, respectively.

The spatial composition profiles presented in Figure 4.13(c) show that a smaller diffusivity between the API and the antisolvent leads to slower overall mass transfer. However, this is not the only difference between the two cases. The lower $\widetilde{D}_{10}$ results in more pronounced uphill diffusion at the first presented time and, consequently, as shown in Figures 4.13(a) and (b), a wider region of the phase diagram is explored during the system's evolution towards equilibrium.

Since the degree of non-idelality between the API and the antisolvent is identical in both cases, the more pronounced uphill diffusion observed at lower $\widetilde{D}_{10}$ must originate from the difference in diffusivity itself. Inspection of the spatial composition profiles presented for the previous case studies—Figures 4.5(e, f), for example—shows that, although the primary response of the API upon contact with the antisolvent stream is uphill diffusion, a small fraction of it simultaneously diffuses downhill, albeit to a much smaller extent. Comparison with Figure 4.13(c) indicates that this downhill diffusion is further reduced at a given time because the decrease in API-antisolvent diffusivity increases the time required for these species to mix. As a result, a larger amount of API may remain at the interfacial region at a given time, making it available for uphill diffusion and thus promoting the observed behaviour.

Interpreting the diffusion coefficient as the inverse of a drag coefficient also supports this behaviour. A decrease in the diffusivity between the API and the antisolvent implies a larger drag coefficient between them. Consequently, while the time required for the mixing of these species increases, the time required for them to separate also does. Since the solvent and antisolvent exhibit ideal interactions and possess a substantially larger diffusivity, it is possible that the antisolvent diffusing into the solvent-rich stream drags the API with it, thus enhancing the uphill diffusion response.

Interestingly, although the smaller diffusivity results in a higher composition spike at the presented time, the corresponding supersaturation spike is slightly lower, as shown in Figure 4.13(d). This contradicts the expectation that a sharper peak in the API composition would necessarily correspond to a state further above the solubility threshold and therefore produce a larger supersaturation. While this interpretation holds for a binary system, in a ternary system a change in the API composition implies a change in the solvent/antisolvent ratio and, consequently, the solubility threshold. Therefore, this behaviour must be interpreted through its representation in the ternary diagram.

The first point to note is that the supersaturation spike does not occur at the spatial location of the maximum uphill-diffusion peak, but slightly to its left, within the interfacial region. Examination of the subset of early times presented in Figures 4.13(e) and (f) for $\widetilde{D}_{10} = 0.1$ and 0.5, respectively, shows that the enhanced uphill diffusion of the API, in combination with the lower diffusivity of API into the antisolvent-rich side, forces the composition profile in the interfacial region to align more parallelly to the solubility curve. Consequently, the profile crosses the curve more shallowly, resulting in a lower supersaturation.

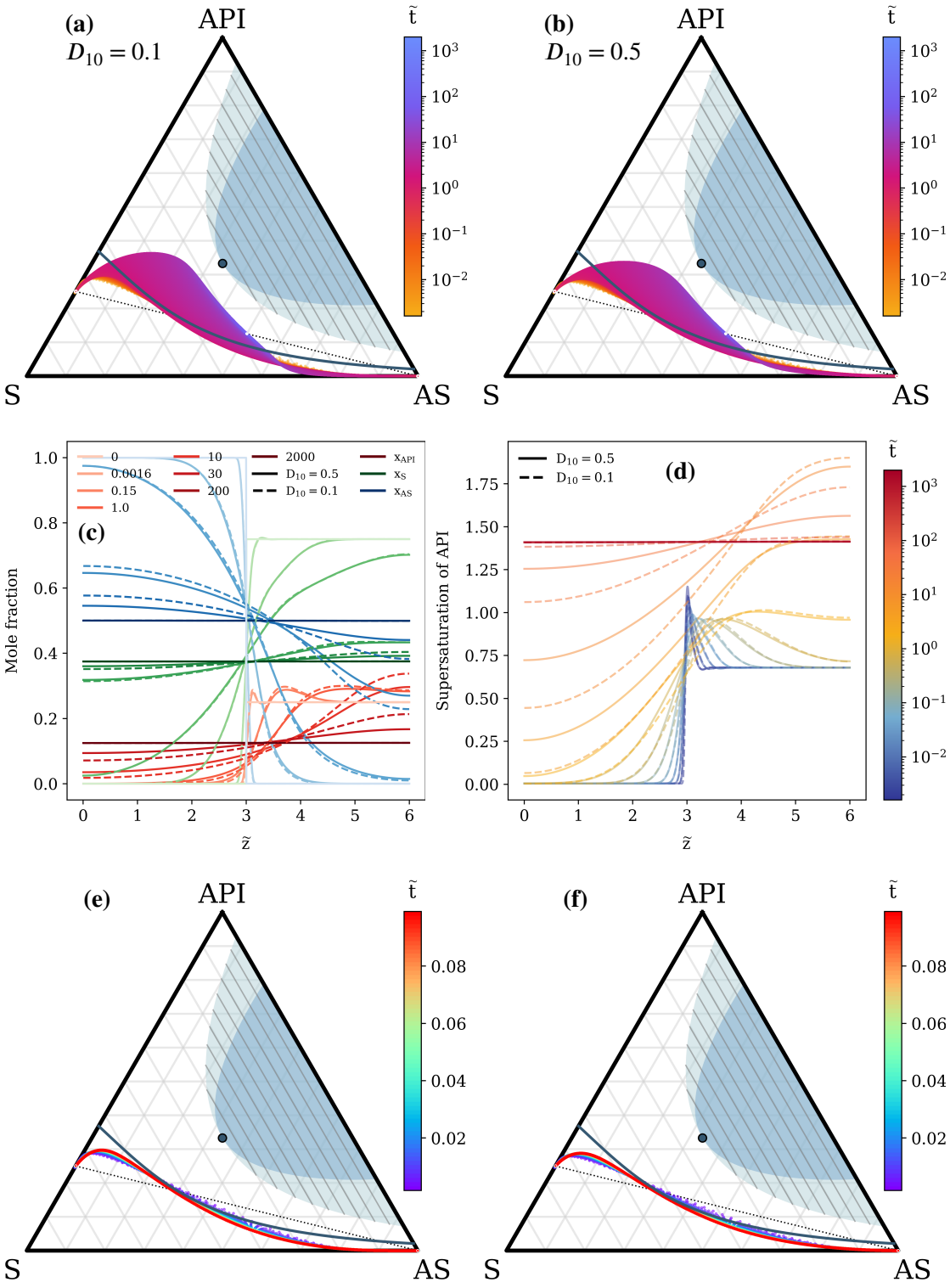


FIGURE 4.13: Evolution of the composition and supersaturation with time in a system mixing a stream of pure antisolvent with a 25% API solution. The Margules parameter between API and AS was fixed at $A = 3$; $\beta\mu_1^{\circ,(S)} - \beta\mu_1^{\circ,(L)} = -1$; and the interfacial free energy coefficients, at $(\tilde{\kappa}_{aa}, \tilde{\kappa}_{ab}, \tilde{\kappa}_{bb}) = (0.025, 0.008, 0.025)$. (a, b) Composition trajectories across the ternary phase diagram for $\widetilde{D}_{10} = 0.1$ and 0.5, respectively. Note that the last profile was plotted in white to aid its visualisation. (c, d) Comparison of their spatial composition and supersaturation profiles, respectively. (e, f) Trajectories across the ternary phase diagram for $\tilde{t} = 0.0016$–0.1, for $\widetilde{D}_{10} = 0.1$ and 0.5, respectively.

To conclude the diffusivity study, Figure 4.14 presents the results obtained when the diffusivities of the API with both solvents ($\widetilde{D}_{10}$ and $\widetilde{D}_{20}$) are reduced to 0.1. In particular, Figures 4.14(a) and (b) show the corresponding composition profiles across the phase diagram, with Figure 4.14(b) presenting a sparse subset of times to aid in the visualisation of the overall trend. Figure 4.14(c) presents the spatial supersaturation profiles observed in this study and compares them with those obtained for $(\widetilde{D}_{10}, \widetilde{D}_{20}, \widetilde{D}_{12}) = (0.5, 1, 1)$.

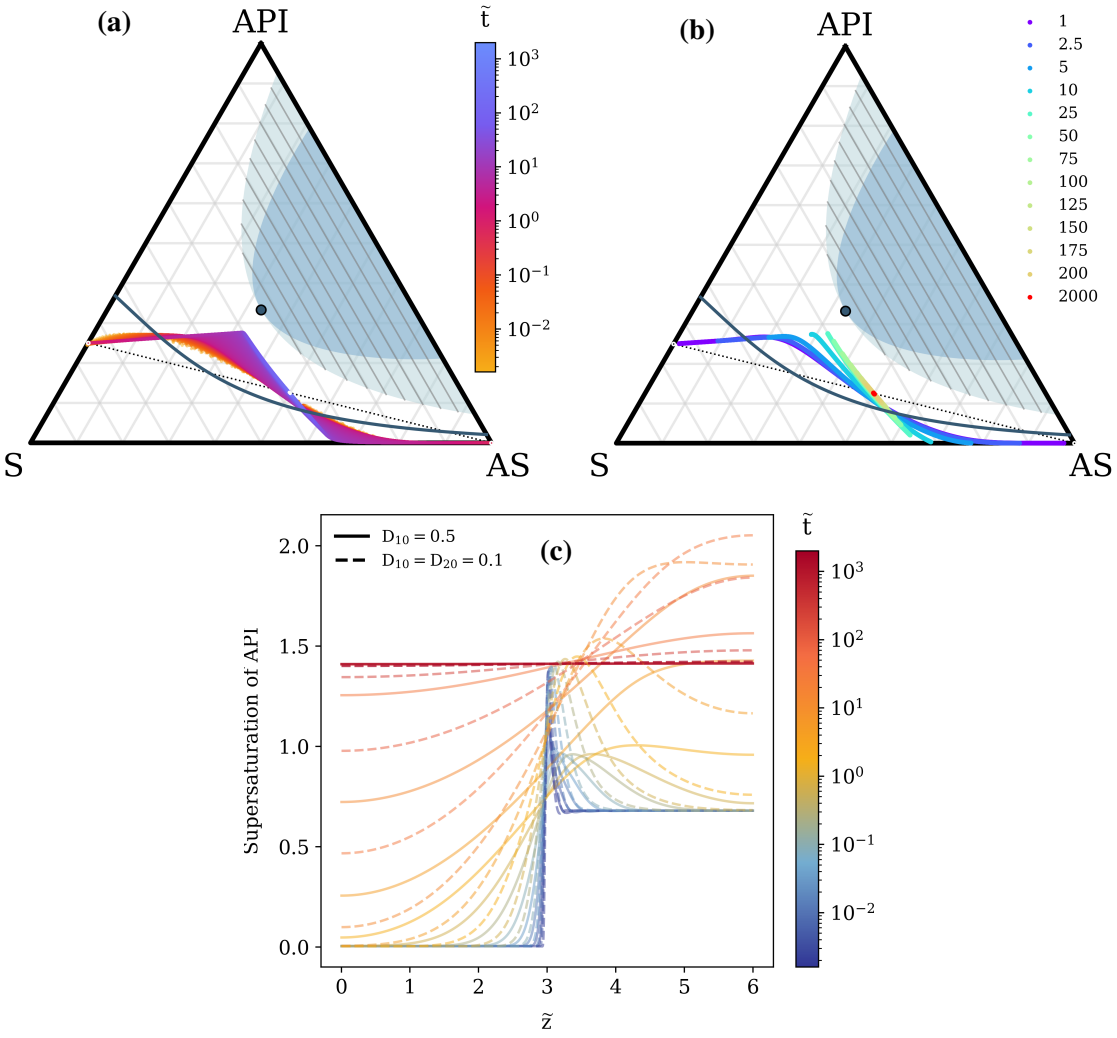


FIGURE 4.14: Evolution of the composition and supersaturation with time in a system mixing a stream of pure antisolvent with a 25% API solution. The diffusion coefficients were fixed at $(\widetilde{D}_{10}, \widetilde{D}_{20}, \widetilde{D}_{12}) = (0.1, 0.1, 1)$. The Margules parameter between API and AS was fixed at $A = 3$; $\beta\mu_1^{\circ,(S)} - \beta\mu_1^{\circ,(L)} = -1$; and the interfacial free energy coefficients, at $(\tilde{\kappa}_{aa}, \tilde{\kappa}_{ab}, \tilde{\kappa}_{bb}) = (0.025, 0.008, 0.025)$. (a, b) Composition pathways throughout the ternary diagram. (a) The last composition profile has been plotted in white, to aid in its visualisation. (b) comprises a smaller subset of times to help in their visualisation. (c) Spatial supersaturation profiles. Note that the profiles of the $(\widetilde{D}_{10}, \widetilde{D}_{20}, \widetilde{D}_{12}) = (0.5, 1, 1)$ case were included for comparison purposes.

The composition evolution through the ternary diagram seen in Figure 4.14(a) and (b) deviates from the curved trajectories observed in previous studies, exhibiting instead a sigmoid shape. Although the API still undergoes uphill diffusion, the effect is considerably weaker than

in the previous cases. The nearly-horizontal trajectories forming the lag and plateau segments of the sigmoid indicate that, during the initial stages of mixing ($\tilde{t} = 0$–10), the amount of API in both bulk phases remains almost constant while the solvent and antisolvent interdiffuse. These pathways suggest that the increase in the drag coefficient between the API and the antisolvent and between the API and the solvent, resulting from the reduced diffusivity of these pairs, limits the ability of the API to separate from either species. This indicates that, in this case, the observed uphill diffusion for the API may be driven only by the non-ideal API–antisolvent interactions. Following this initial mixing stage, once the solvent profile becomes nearly spatially uniform, the API and antisolvent continue to diffuse into one another at a substantially lower rate.

Interestingly, the weaker uphill diffusion causes the initial interfacial compositions to cross the solubility curve at a shallower point, resulting in a considerably larger initial supersaturation than in the $(\widetilde{D}_{10}, \widetilde{D}_{20}, \widetilde{D}_{12}) = (0.5, 1, 1)$ case. Therefore, the present system has a greater probability of overshooting past the metastable zone boundary, potentially leading to reduced control over solid–liquid nucleation and the resulting crystalline product properties.

Non-ideality between API and antisolvent

To conclude the diffusion studies presented in this work, this section explores the effect that different degrees of non-ideality between the API and the antisolvent have on the composition and supersaturation mass transfer trends. The system selected for this study mixes a stream of 25% API and 75% solvent with pure antisolvent, increasing the binary interaction parameter to $A = 3.75$ and maintaining $(\tilde{\kappa}_{aa}, \tilde{\kappa}_{ab}, \tilde{\kappa}_{bb}) = (0.025, 0.008, 0.025)$. A further case study considering $A = 2.5$ has been included in Appendix F, as the qualitative evolution of its mass transfer trends matches the behaviour observed for $A = 3$, which was discussed in Figure 4.5 within Section 4.4.1. Decreasing the value of the interaction parameter reduces the non-ideality between API and antisolvent, thus decreasing the miscibility gap. Since this system already started at a considerable distance from the miscibility gap when $A = 3$, no significant changes in the diffusion trends were expected.

The mass transfer dynamics and thermodynamics results for $A = 3.75$ have been summarised in Figure 4.15. In particular, Figure 4.15(a) and (c) present the evolution of the compositional pathways throughout the entire simulation time in the ternary diagram and in space, respectively. Similarly, Figure 4.15(b) depicts the same trends over a subset of times, from $\tilde{t} = 4$ to 200, to aid in the interpretation of the observed behaviour, while Figure 4.15(d) shows the spatial evolution of the supersaturation profiles. In Figure 4.15(c) and (d), the composition and supersaturation profiles of this case study are presented alongside those corresponding to the same system, but with $A = 3$, to facilitate comparison.

The system exhibits a fully mixed final state, contrary to the expectations generated by Figure 4.8(a), which corresponds to a system with identical interfacial free energy coefficients and comparable initial conditions. In that case, the final mixing point also fell within the binodal region, and the antisolvent stream was likewise completely pure. However, in Figure 4.8(a), the selected values of $\tilde{\kappa}_{aa}$, $\tilde{\kappa}_{ab}$ and $\tilde{\kappa}_{bb}$ allowed the existence of a phase-separated equilibrium state.

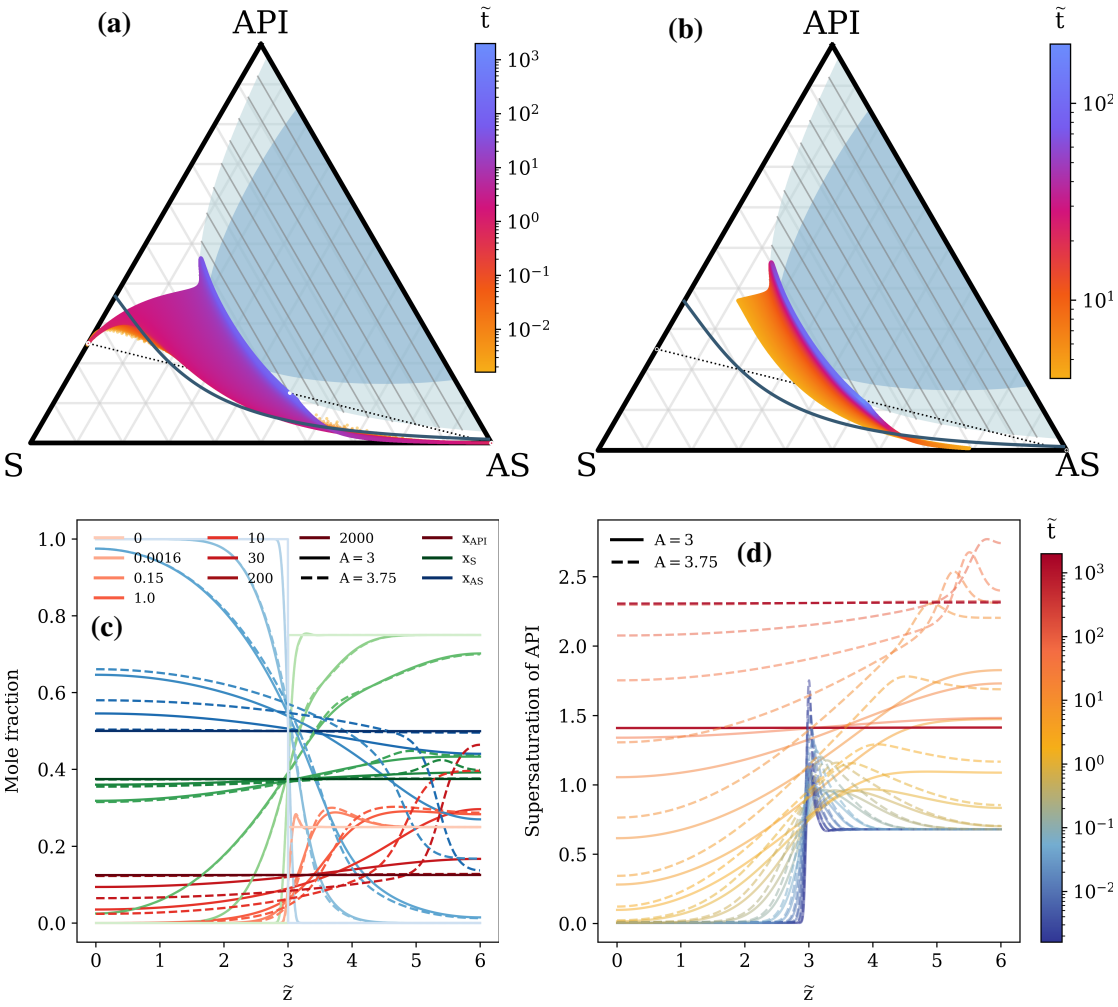


FIGURE 4.15: Evolution of the composition and supersaturation with time in a system mixing pure antisolvent with a 25% API solution, considering that $A = 3.75$, $\beta\mu_1^{\circ,(S)} - \beta\mu_1^{\circ,(L)} = -1$, and that the interfacial free energy coefficients had values of $(\tilde{\kappa}_{aa}, \tilde{\kappa}_{ab}, \tilde{\kappa}_{bb}) = (0.025, 0.008, 0.025)$. (a, b) Evolution across the entire simulation time and from $\tilde{t} = 4$–200, respectively, across the ternary phase diagram. (c, d) Selected spatial mole fraction and supersaturation profiles, respectively, throughout the entire simulation time. Note that in these, the solid lines correspond with the evolutions of the same system but considering $A = 3$, included for comparison purposes.

This behaviour can be explained by considering that the present system seeks to phase-separate at a section of the miscibility gap much closer to the critical point than in Figure 4.8(a). As discussed in Section 4.4.2, and illustrated in Figure 4.12(b), the double well in the free energy curve becomes increasingly shallow as the critical point is approached. It is possible that this reduction in the energetic penalty between wells was sufficient for the gradient term to dominate, despite its low coefficients, driving the system towards complete homogeneity through the same process observed in Figure 4.8(b). Therefore, a physical system with a lower interfacial tension than that corresponding to the gradient coefficients studied here may remain phase-separated, whereas a physical system with a larger interfacial tension may become homogeneous.

Before reaching equilibrium, Figure 4.15(a) shows part of the system on the solvent-rich

side evolving down the binodal curve; this behaviour can be appreciated more clearly in Figure 4.15(b). This may occur because the diffusion trajectories intersect the miscibility gap before the chemical potential gradient towards the right-hand side of the system has been levelled. Consequently, the system still seeks to diffuse uphill and, because the binodal curve constitutes the most energetically favoured trajectory, it evolves along this boundary. To a lesser extent, this behaviour is also seen in Figure 4.9(a). In contrast, the cases presented in Figure 4.8 intersected with the miscibility gap only after having started the downhill diffusion stage.

The qualitative trends of the composition profiles presented in Figure 4.15(c) remain consistent with those analysed in Figure 4.5. However, the uphill diffusion of the API is considerably more pronounced than in the $A = 3$ case, most likely because the stronger repulsive interactions between API and antisolvent generate a larger initial chemical potential spike. This implies a steeper gradient relative to the solvent-rich bulk phase, enabling the uphill diffusion of substantially more API. The times associated with the different profiles are consistent with this interpretation, with uphill diffusion ceasing much sooner for $A = 3$.

Similarly, the qualitative supersaturation trends presented in Figure 4.15(d) are consistent with those observed in Section 4.4.1 for a lower degree of non-ideality, summarised in Figure 4.7. However, the greater non-ideality between API and antisolvent leads to the prediction of a significantly larger supersaturation spike upon the initial contact of the two streams than that observed for the $A = 3$ case. This results from the effect of non-ideality on both the solubility curve and the mass transfer dynamics. As shown in Figure 4.2 and Equation (4.8), increasing the parameter A lowers the solubility curve in the phase diagram and therefore reduces the supersaturation threshold. While this alone would lead to a greater supersaturation response, even if the initial chemical potential spike remained unchanged, the composition profiles in Figure 4.15(c) also suggest a larger initial chemical potential overshoot, as evidenced by the much more pronounced uphill diffusion of the API. This pushes the system further above the solubility limit, resulting in larger supersaturation. Interestingly, whereas the damping of the initial supersaturation overshoot causes the $A = 3$ system to return to an undersaturated state, the larger supersaturation predicted for $A = 3.75$ is sufficient for the system to remain supersaturated throughout the simulation.

From a crystal nucleation perspective, these results suggest that higher levels of non-ideality between API and antisolvent increase the probability of nucleation at the start of the antisolvent crystallisation process. If nucleation did occur, the pathways predicted by this model would differ from those of the physical system, as crystal formation would deplete both the API concentration and the supersaturation, thus altering the trajectory of the uphill diffusion front. Should the system cross into the binodal region, there would be a competition between solid and liquid nucleation, with the possibility of solid nuclei subsequently forming within the liquid droplets. If the system also entered the spinodal region, spontaneous liquid-liquid demixing would occur. In this scenario, any formed liquid nuclei would most likely coalesce into the larger bulk phases characteristic of this mechanism. In contrast, the very high supersaturation found in this region may promote the rapid growth of the solid nuclei.

4.5 Conclusions

This work explored, in the context of an antisolvent crystallisation system, the effect of incorporating a gradient term into the free energy formulation of a diffusion model on the mass transfer dynamics and, consequently, on the API supersaturation profiles. The effects were explored from three different perspectives: (1) investigating how mixing develops in the different regions of the phase diagram, (2) exploring the behaviour of the system within the miscibility gap, and (3) mimicking the testing of different solute-antisolvent pairs by varying their physical properties.

The diffusion trajectories across the phase diagram were found to be highly nonlinear. This arose from the uphill diffusion experienced by the API, which was found to be primarily affected by the degree of non-ideality between API and antisolvent, and by the ratio of the diffusion coefficients between different species. The influence of these parameters tended to become more significant at later stages in the simulation ($\tilde{t} = 10$–100), whereas the effect of the gradient coefficient was primarily observed during the initial stages ($\tilde{t} < 0.5$), effectively dividing the diffusion process into two distinct regimes.

Furthermore, the nonlinearity of the trajectories occasionally caused the systems to enter the miscibility gap, and modelling such behaviour was only possible because of the incorporation of the gradient term proposed in this work. However, in some cases, the coexistent phases formed very close to the boundaries of the system, which could result in the gradient term driving the system to homogeneity. This was consequence of the finite nature of the mesh and could be representative of a physical system in which these conditions are replicated, such as in a microfluidic device. Systems entering the miscibility gap through regions close to the critical point were found to be more susceptible to this behaviour, as the free energy barrier between the wells becomes shallower.

In addition, reducing the amount of antisolvent within the antisolvent stream was found to be effective in helping to avoid oiling out. This was because it positioned the initial composition profile within a less enclosed region of the phase diagram, reducing the likelihood of the composition pathways entering the miscibility gap.

When studying LLPS within the miscibility gap, the solvent was observed to accumulate at the interface at equilibrium, providing valuable insight into the equilibrium phase behaviour predicted by these models.

With respect to the supersaturation, neglecting the gradient term in a system representative of a typical antisolvent crystallisation process was found to cause an underestimation of the supersaturation attained when bringing the two streams into contact. In this case, the model without the gradient term predicted that the system would remain undersaturated, whereas the model with the gradient term predicted the occurrence of local supersaturation. Thus, neglecting the contributions of the gradient term can lead to erroneous conclusions regarding the time and location at which crystal nucleation may occur. Furthermore, the supersaturation response was found to be highly dependent on the region of the ternary diagram where the system crossed the solubility line, as well as on the composition trajectory followed while doing so.

Overall, these results prove the great potential of this model for the qualitative modelling

and interpretation of antisolvent crystallisation processes, and for increasing the understanding of less well-characterised phenomena such as oiling out. The more accurate supersaturation predictions provided by the model can contribute to more representative estimates of nucleation and growth rates and similarly help inform other modelling approaches. Future research should focus on determining a composition-dependent form of the gradient terms capable of producing a flat equilibrium chemical potential profile, incorporating non-ideality in the API-solvent and solvent-antisolvent interactions, and, if investigating a physical system, adopting a more suitable activity model.

Chapter 5

Generating diffusive mixing fingerprints via Raman microscopy

This chapter is focused on the development of an experimental setup isolating diffusion as the dominant mass transfer mechanism, providing a platform from which the predictions of the models developed in Chapters 3 and 4 can be qualitatively assessed. The combination of a microfluidic device with Raman microscopy is proposed, leveraging this quantitative PAT to also enable the generation of rich data that can be used to benchmark mass transfer models. While similar setups have been previously applied to the measurement of diffusive mixing, these studies have primarily focused on the determination of the Fickian diffusion coefficients as the only output. At present, there is not any experimental data available in organic systems that can adequately validate, qualitatively or quantitatively, the predictions of a model incorporating interfacial contributions. This way, this work aims to provide the groundwork required to address this gap by establishing an experimental platform capable of generating spatially resolved concentration measurements under diffusion-controlled conditions. The setup was developed and tested in a binary ethanol–water system, and, as proof of concept, used to inform a Fickian diffusion model. The overall procedure is summarised in Figure 5.1.

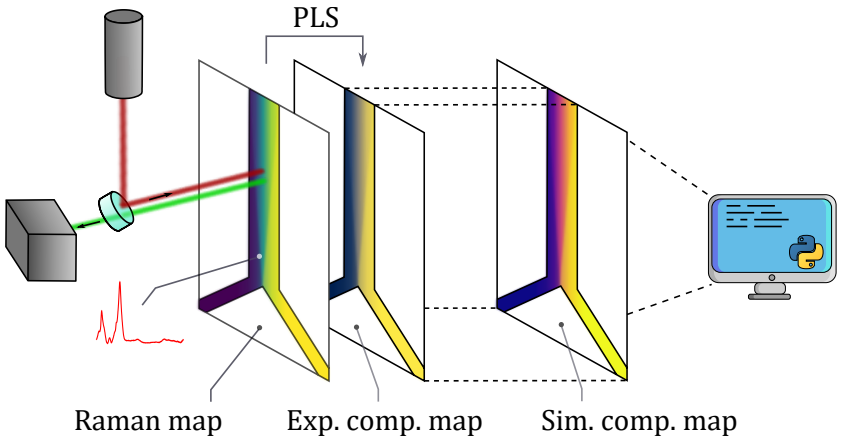


FIGURE 5.1: Diagram summarising the experimental and in-silico methodology built to extract the value of the benchmark parameters in a mass transfer model. The spectral maps collected via Raman microscopy are translated into composition maps using a PLS model. In turn, these are used as the ground truth for an optimisation loop to parameterise the models.

5.1 Introduction

The popularity of microfluidic devices has increased in recent years. They are associated with reduced experimental times due to their high-throughput nature, and with lower material consumption, leading to an overall lower cost than traditional laboratory-scale setups. Numerous applications for microfluidic devices can be found within life sciences, and within the pharmaceutical field in particular, such as drug screening, drug metabolism or pharmacokinetics; these have been reviewed by Cui and Wang [155].

The geometry of microfluidic devices is of particular interest for the purpose of this work, since they favour Peclet numbers—which indicates the ratio between convective and diffusive mixing, leaning towards the former if greater than one—significantly lower than the unity [8]. This enables the control of mass transfer exclusively through diffusion, making them an excellent medium in which to conduct studies able to qualitatively validate the mass transfer models proposed in Chapters 3 and 4, which describe diffusion-driven composition evolution.

The coupling of these devices with Process Analytical Technologies (PATs) is especially powerful, and their combination with Raman spectroscopy in particular shows significant promise. This particular PAT has several advantages over other techniques, the most important being that it does not require fluorescence to detect a species, and thus it does not have to rely on tracers or dyes [156]. This is particularly advantageous when studying chemical reactions, mixing, and phase transformations [157]. It is non-invasive, and it can detect the presence and concentration of several species at once, provided they have a non-overlapping Raman signal. Hence, Raman spectroscopy remains a popular choice which application is well supported within the literature [158].

Rinke *et al.* [159] applied Raman imaging with light sheets to capture concentration maps during the evolution of a mixing process of water and ethanol. In this study, fluids passed through several microchannels disposed in a grid-like fashion and feeding into a cuvette, being there where the concentration evolution was monitored. The system was kept under laminar conditions, but the flowrates used were 1.2 and $12\,\mathrm{L\,h^{-1}}$, several orders of magnitude larger than those used in this work. They compared their experimental results with computational fluid dynamics modelling, finding them in good agreement. From the same group, Wellhausen *et al.* [160] applied this Raman imaging technique to water–ethanol and water–methanol systems in the same setup, with a flowrate of $1.6\,\mathrm{L\,h^{-1}}$ per component. They combined these experiments with Particle Image Velocimetry (PIV) to measure the velocity field of the system. Roetmann *et al.* [157] used 2D molecular tagging velocimetry and μPIV, and planar spontaneous Raman scattering, to measure the velocity and concentration fields in a water–ethanol system in the same setup, respectively, flowing at $500\,\mathrm{mL\,h^{-1}}$ per fluid. None of these studies extracted the values of any mass transfer descriptors from their concentration monitoring results. Similarly, Schafer *et al.* [161] applied coherent anti-Stokes Raman scattering to the monitoring of concentration in a 20 wt% ethanol–water solution, for two different microfluidic setups. They fitted the evolution of a cross-sectional composition profile, fixing the Fickian diffusion coefficient (D) to the value reported on literature, in order to calculate the velocity profile of the system.

When it comes to reporting mass transfer descriptors, the most popular option being the Fickian diffusion coefficient, there have been several studies exploiting the combination of Raman and microfluidics. Bouchaudy *et al.* [162] reported the interdiffusion coefficient of a water–glycerol system over the whole concentration range. Flow was induced via pervaporation, the velocity profile was measured by PIV, and 1D composition measurements were conducted via Raman confocal spectroscopy. Peters *et al.* [126] demonstrated the feasibility of measuring the Fickian diffusion coefficient in a similar manner, for both binary and ternary systems, cyclohexane–toluene and 1-propanol–1-chlorobutane–heptane, respectively. They repeated this proof of concept with a quaternary system in their posterior work [127]. They assumed cross-sectional variation in velocity, but a constant velocity profile along the channel; as for the composition, they took four discrete samples along their microchannel, extracting the Fickian diffusion coefficient from their evolution, assuming that the system stayed in steady state. Their results are in good agreement with literature values. Finally, Salmon *et al.* [163] used confocal Raman imaging to map the composition evolution of a chloroform and methylene chloride system in 2D along a microchannel. The mean velocities in the channel were fitted from these maps, and the values of the Fickian diffusion coefficient were preliminarily obtained from the slope of the line relating the width of the diffusion zone along the channel with different x values.

While this shows that the understanding of diffusive mass transfer is a well-studied field, there is a gap when it comes to combining the different techniques and approaches used by all the different studies. In general, those in which the diffusion coefficient is reported only focus on 1D measurements, while those where a 2D map was collected do not report the value of any characteristic mass transfer parameters. The exception to this is the work by Salmon *et al.* [163], but nevertheless there are three main differences between this work and the present one. Firstly, different chemical systems were studied. Secondly, the method in which the data is fitted to obtain Fick's diffusion coefficient is different, since this work makes a direct comparison between experimental maps and maps obtained from solving a Fickian diffusion model. Finally, the greater aim of this work is to provide the basis through which the predictions of the more complex CaHiMaS model presented in Chapter 3 can be qualitatively assessed.

To this end, the work conducted in this study aims to provide an environment in which the predictions of the model can be qualitatively assessed. While the spatial resolution of Raman microscopy is insufficient to directly resolve the nanoscale interfacial structures predicted by CaHiMaS, the developed platform provides diffusion-controlled composition measurements that can be compared with model predictions. Therefore, it establishes the experimental basis required for future validation of models incorporating interfacial contributions, through the comparison of predicted and measured composition pathways, or of other qualitative outcomes, an example being the CQAs of the recovered crystalline product or the formation of secondary liquid phases.

5.2 Materials and methods

This section provides information on the materials used to carry out this study, as well as on the devised experimental setup and the processing of experimental data. The optimisation routine

developed for extracting information out of the collected maps is also described.

5.2.1 Materials

The binary mixing study comprised of ethanol absolute ($\geq$ 99.85%v/v), purchased from VWR, and deionised water obtained through purification with a Milli-Q IQ 7003/05/10/15 unit, acquired from Merck. When stored, the ethanol bottle was sealed with parafilm to minimise potential water contamination, given its hygroscopicity [164].

5.2.2 Raman spectroscopy: working principle

Raman spectroscopy is a form of vibrational spectroscopy in which monochromatic light is shone onto a sample. The incident photons are momentarily absorbed into the sample molecules, inducing a dipole moment in their electron cloud and thus raising them to an unstable virtual state of higher energy. This instability causes photons to be rapidly scattered back, lowering the molecule into a more stable energy state. Depending on the relative configuration of the original and final energy states, as illustrated in Figure 5.2, this phenomenon will be classified into three categories: Rayleigh, Stokes and anti-Stokes scattering, of which the last two are considered Raman scattering [165].

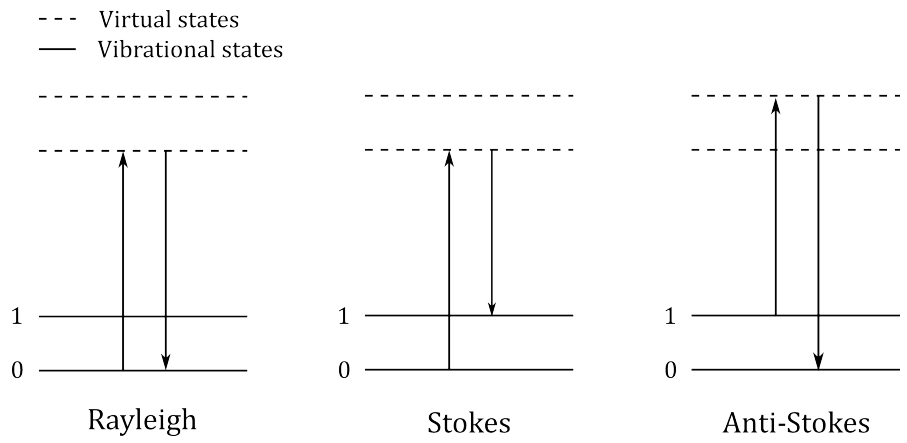


FIGURE 5.2: Energy diagrams depicting the different types of scattering present when performing Raman spectroscopy.

Rayleigh scattering is of a completely elastic nature, since the molecule starts from, and returns to, the ground state after absorbing and releasing the incident photon. This is the most probable and thus most frequent outcome. Stokes scattering takes place when a molecule in the ground state prior to the scattering event finishes in a vibrationally excited level, with higher energy. Conversely, in anti-Stokes scattering a molecule starting from a vibrationally excited state finishes in the ground level. The low probability of a molecule being in an excited state at room temperature makes anti-Stokes the most infrequent scattering event. Both Stokes and anti-Stokes constitute inelastic scattering, since in them the energy of the original molecule and of the absorbed photon change after the event [166].

In this work, Stokes scattering was measured by a confocal Raman microscope. In this type of equipment, the laser is reflected and focused onto the sample by a beam splitter and an objective lens, respectively, with both the Raman and Rayleigh scattering being collected. The latter is filtered out and the former is focused by a pinhole, which allows only scattering from the focal plane to pass through and be sent to the spectrograph. The sample is placed on a stage with the ability to move in the XYZ directions, thus allowing for spatially-resolved collection of Raman spectra in the 3D space [167].

One of the problems encountered during the collection of the spectra was the apparition of cosmic rays. These are spectral artifacts caused by particles of high energy colliding with the spectrometer detector at an arbitrary time and position. This creates very sharp spikes in the spectra, which must be filtered out [168].

5.2.3 Experimental setup

The microfluidic setup used in this work is depicted in Figure 5.4 and 5.5(a). It was formed by a Harvard Apparatus PHD ULTRA^{TM} 4400 remote syringe pump, used to infuse liquid from two Hamilton Gastight 1/4-28 UNF glass syringes, acquired from Darwin Microfluidics. The two syringes were connected via PTFE tubing (1/16 inch OD, 1/32 inch ID) to a hydrophilic glass Y-junction chip from Dolomite Microfluidics (part number: 3200008), of which a picture is provided in Figure 5.3. This material was chosen for the chip in order to achieve a strong Raman signal. The volume and length of the channel are 0.2 µL and 12.5 mm, and its depth and height are 100 µm×205 µm, respectively.



FIGURE 5.3: Y-junction microfluidic chip from Dolomite Microfluidics, fabricated with hydrophilic glass. Taken from [169].

The shape of its cross-sectional area is illustrated in Figure 5.5 (c); Figure 5.5 (b) provides the definitions of terms used along this chapter, such as "column" and "channel length". The chip was set up within a H interface, and connected to tubing at both ends through a 4-way linear connector, both purchased from Dolomite Microfluidics. A plastic support for the chip was 3D printed, which allowed for better adjustment and positioning on the microscope stages.

The spectra for the quantitative Raman analysis were captured using the Horiba XploRA PLUS confocal Raman microscope, which spot size is quoted as 0.5 µm [170]. A 532 nm laser was used, paired with a 1200 grating and a 50x objective. The spectra acquisition time was 3 s, with an accumulation time of 1 s. The slit and hole were set to 200 and 500 µm, respectively, and

the studied wavenumber range was 400 – 4000 cm^{-1}, in order to capture all the relevant ethanol and water Raman peaks.

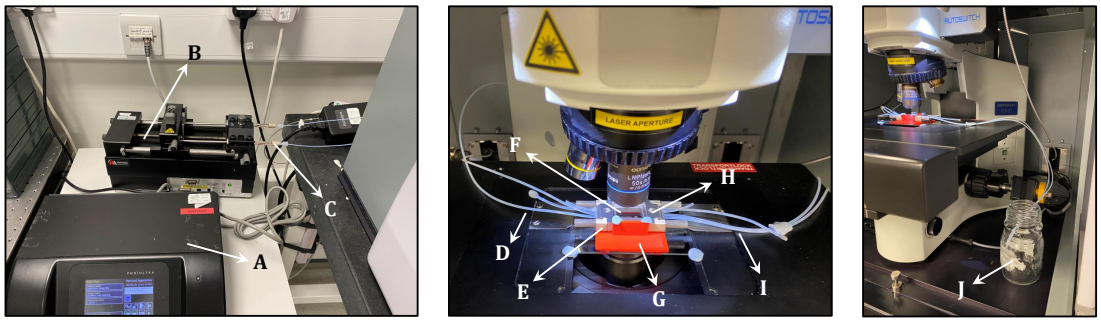


FIGURE 5.4: Experimental setup used for the collection of the microfluidic maps. The different pieces are labelled as follows: (A) and (B) conform the syringe pump, with (A) being the remote control unit and (B) the pushing block; (C) microfluidic syringe; (D) inlet tubing; (E) 4-way linear connector; (F) microfluidic chip; (G) 3D printed plastic support; (H) H interface; (I) outlet tubing; and (J) waste disposal.

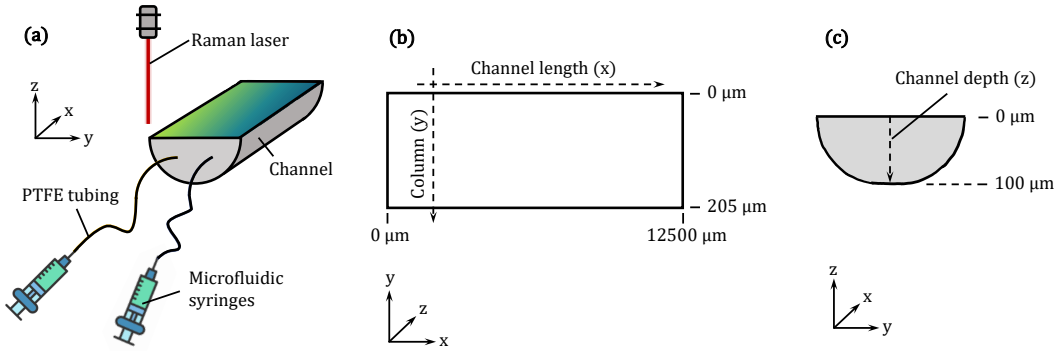


FIGURE 5.5: Experimental setup used for the collection of the microfluidic mixing maps (not to scale). (a) Two syringes pumping the different solvents into a microfluidic channel, where their mixing is mapped by collecting Raman measurements in columns along this channel. (b) Depiction of the meaning given to the terms "columns" and "measurements along the channel" in this work; the columns also correspond with the channel height. (c) Channel cross-sectional profile adapted from the manual, depicting the meaning given to depth, also called z measurements, in this work.

5.2.4 Experimental procedure

The collection procedure consisted of three main steps: (1) setting up the microfluidic syringes and channel, (2) preparing the microscope, and (3) the data collection itself. The general procedure, including the main components of each step, is outlined in Figure 5.6.

The experimental collection began by filling the syringes and tubing by capillary action, in order to minimise the presence of air bubbles inside of the system. To minimise any potential contamination during this step due to ethanol's hygroscopic nature, the opening of the vessel was sealed with parafilm, and a razor was used to make a thin cut through which to introduce the tubing. This process is summarised in Figure 5.7. Once full, the tubing was reattached to the microfluidic channel, which was then fixed to the Raman stage. With the system connected and

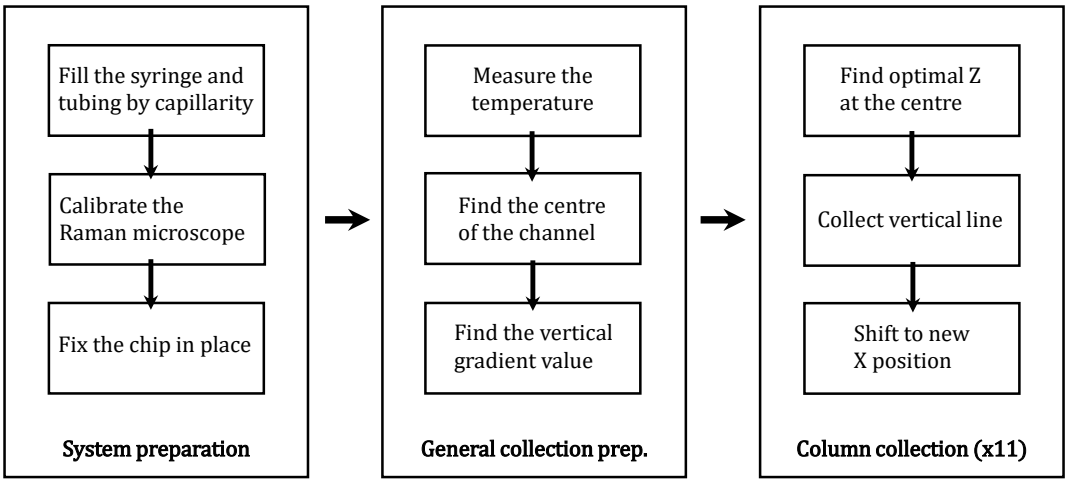


FIGURE 5.6: Diagram of the experimental procedure followed during the collection of the Raman microscopy maps. There were 11 columns collected in each system, and thus the last block was repeated 11 times.

loaded, the Raman microscope, which had already been calibrated with a standard silica sample, was prepared for the data collection process.

This process began by correcting for two particularities of the experimental setup. Firstly, a misalignment was detected in the microscope between the true position of the laser beam and the position indicated in the software. This meant that the true y coordinate of the beam could not be accurately determined through the software. Secondly, there was a slight tilt along the length of the channel. Thus, before starting to gather the measurements, the relative position of the centre of the channel with respect to the collection line was determined, and, to make the collection path as perpendicular to the channel length as possible, it was attempted to correct for the tilt in its specified coordinates. While an experimental error was incurred in at this step, it resulted in less than 1 µm of deviation in the verticality of the columns. Finally, the temperature in the vicinity of the microfluidic channel was measured with a thermocouple (YCT YC–747UD).

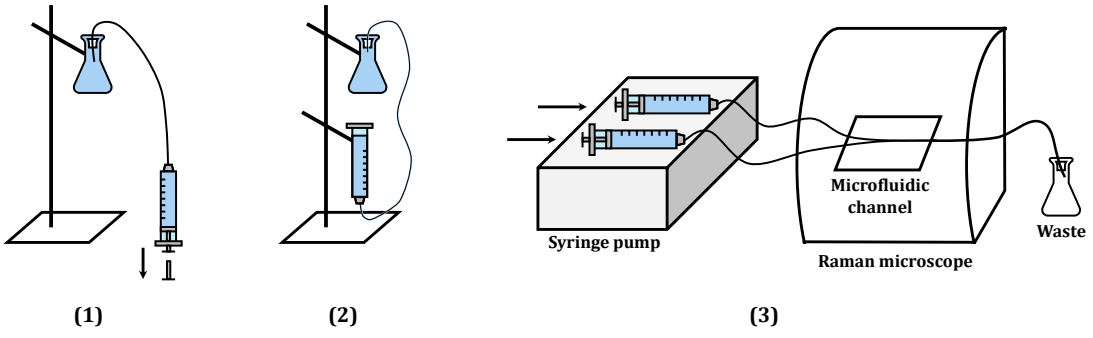


FIGURE 5.7: Diagram outlining the steps involved in preparing the system for data collection. The system is first filled up through capillarity by holding the syringe under the vessel with solution, in order to minimise the presence of air bubbles (1-2), and then fixed onto the stage of the Raman microscope (3). To minimise any potential contamination in steps (1-2) due to ethanol's hygroscopic nature, the opening of the vessel was sealed with parafilm, and a razor was used to make a thin cut through which to introduce the tubing.

The collection process of a particular column consisted in, firstly, determining the optimal z position for the microscope stage by comparing the ethanol signal in the centre of the channel at different depths. Then, with the stage correctly positioned in that direction, the measurements could be collected.

2D Raman maps were made of 11 columns, each consisting of data points measured every 5 µm on the Y direction. Measurements along the X direction were taken in 1250 µm intervals, with the exception of the last column. This was always collected before the 12 500 µm mark, to avoid any inaccuracies coming from the outer Y-junction.

Initially, a calibration dataset was gathered for ethanol (EtOH)–water (H_2O) mixtures across the whole mass fraction range to translate the Raman signal into compositions, as detailed in Table 5.1; for this dataset, each column measurement was repeated three times.

TABLE 5.1: Weights and ethanol mass percentages of the solutions used within the calibration dataset, and temperatures at which each calibration measurement was performed.

EtOH (g)	**H_2O (g)**	**C (wt%)**	**T (°C)**	**EtOH (g)**	**H_2O (g)**	**C (wt%)**	**T (°C)**
-	50.0	0	22.7–23.1	29.99	20.00	60.0	20.6–20.9
5.04	45.01	10.1	20.8–20.9	35.02	15.03	70.0	22.2–22.5
10.01	40.03	20.0	20.8–21.0	40.03	10.00	80.0	21.0–21.5
15.01	35.03	30.0	21.8–22.0	45.00	4.99	90.0	21.0–21.2
20.01	30.03	40.0	21.7–21.9	50.0	-	100	22.8–23.3
25.00	25.02	50.0	21.7–22.5	-	-	-	-

Table 5.2 provides a summary of the conditions studied during the mixing experiments. The inlet compositions of the two streams were chosen to cover the entire mass fraction range, and the flowrates were chosen in order to ensure a good degree of diffusion was achieved at the channel outlet.

TABLE 5.2: List of experiments performed for the spectroscopical analysis of the EtOH–H_2O system, and the room temperatures at which they were performed. C_1 and C_2 correspond to the ethanol mass percentages of the two solutions used and Q corresponds with the total flowrate, reported in µL min^{-1}.

ID	**C_1 (wt%)**	**C_2 (wt%)**	**Q**	**T (°C)**	**ID**	**C_1 (wt%)**	**C_2 (wt%)**	**Q**	**T (°C)**
1	100	0	2.0	20.6–20.7	8	100	24.96	3.0	20.7–21.1
2	100	0	2.0	22.3–23.0	9	100	49.93	3.0	20.5–20.8
3	100	0	2.0	21.8–22.3	10	100	74.98	3.0	20.7–21.0
4	100	0	3.0	19.9–20.1	11	0	24.95	3.0	20.9–21.1
5	100	0	3.0	22.5–23.0	12	0	49.98	3.0	19.3–19.6
6	100	0	3.0	23.4–23.6	13	0	75.00	3.0	19.3–19.5
7	100	0	4.0	20.9–21.4	-	-	-	-	-

5.2.5 Raman spectra preprocessing

The data processing had to be carefully tailored to the specific problems encountered throughout the experimentation. The procedures applied to the raw data are detailed and justified in this

section. They are classified into those based on the characteristics of a specific spectrum, and those relative to an experiment or set of spectra as a whole. As a reference, Figure 5.8 describes the basic steps followed depending on whether the data processed was that of a calibration file or of a mixing experiment.

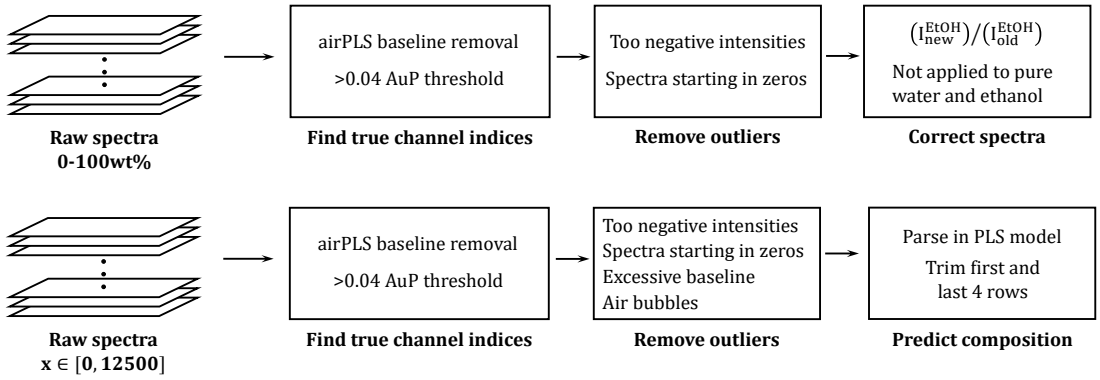


FIGURE 5.8: Top: Step by step description of the data processing followed for calibration runs. Note that 0–100wt% corresponds with the mass percentage of ethanol. The spectra correction step is further described in Section 5.2.6. Bottom: Step by step description of the data processing followed in the case of mixing experiments.

Spectra-specific preprocessing

The three main preprocessing steps applied to each spectrum were the removal of baseline, the filtering of cosmic rays, and the correction of two types of outliers: those in which the spectra showed negative intensities, and those in which the first few recorded intensities are zero.

The baseline removal algorithm chosen to treat the data was adaptive iteratively reweighted penalised least squares (airPLS) [171], as applied in [172]. The parameter λ can take values between 1 and 10^9 and controls the smoothness of the background vector, with larger values leading to larger penalties for roughness and consequently resulting in little change of the actual spectrum. This is because the spectrum is corrected according to $S_{corrected} = S_{original} - S_{bckgr}$, and since a smoother background vector would be closer to zero, its subtraction from the original spectrum would have little effect. A value of 100 was chosen for this work, as it allows to completely remove the baseline in most cases, without distorting the peaks present in the spectra; further discussion on this is provided in Section 5.3.2. First-order difference penalties were applied, as they allowed to achieve the desired outcome. Figure 5.9 shows how this method allows for adequate baseline removal across the whole composition range.

The cosmic rays present within the spectra were identified by applying the `scipy.signal.find_peaks` function from the SciPy library [141]. The selected threshold defines the difference in intensity that two adjacent points must have in order for one to be considered a cosmic ray. A value of 650 A.U. was selected, as a lower value compromises the signal of pure ethanol. As demonstrated in Figure 5.10, this value allowed to detect all of the present rays in most spectra, without mistakenly selecting any of the spectral peaks. This function returned an array of 5 wavenumbers, with the location of the detected spike, which

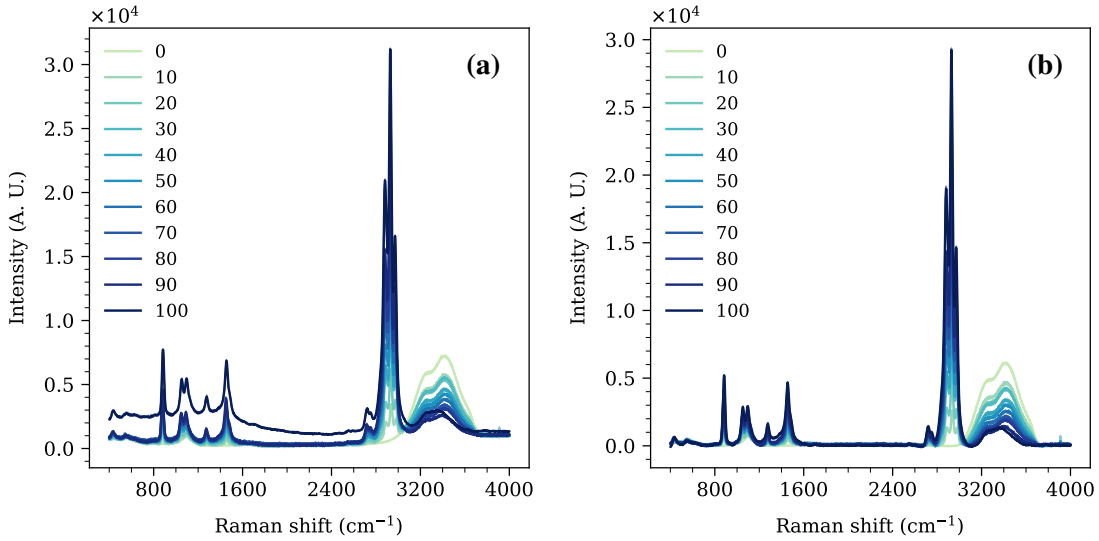


FIGURE 5.9: Example of how the airPLS baseline removal method, with $\lambda = 100$ and first-order difference penalties, affects spectra across the whole range of mass compositions (wt%) for the ethanol-water system. (a) Raw spectra. (b) Same spectra, after baseline removal.

we will call i, being in the middle. To correct for the spike, a line was fitted using six points, three on each side of this group: $[i-4, i-3, i-2, i+2, i+3, i+4]$. This line was then used to interpolate the intensities of the cosmic ray location and its two adjacent points, $i-1$ and $i+1$.

Finally, when it comes to the handling of outliers, two specific cases could be detected by observing spectra in isolation: those in which the spectra showed negative intensities, and those in which the first few intensities recorded in the spectra were zero. In order to avoid unnecessary inaccuracies in the collated results, it is important to identify and deal with both. Negative intensities, which can sometimes appear due to instrumental error, will result in inaccurate composition readings. Thus, all spectra showing intensities below 150 A.U., which was the threshold distinguishing noise from outlier, were discarded and their predicted composition replaced by a `NaN`. Similarly, a spectrum starting in zeros will react inadequately to the baseline removal algorithm and result in a distorted trend. The handling of this scenario was different for the calibration measurements and for the experiments, given that in the former each measurement was repeated three times, and in the latter this was not possible. Thus, spectra with these characteristics found within a mixing experiment were discarded, and their predicted composition was replaced with a `NaN`. As for the calibration dataset, the affected intensities were replaced with the average of the intensities from the two additional repetitions at these points, as depicted in Figure 5.11.

Dataset-wide postprocessing

Two processing routines needed to be computed across the whole dataset: (1) the detection and discarding of spectra showing a disproportionately large baseline, and (2) the identification of what measurements actually belong within the microfluidic channel.

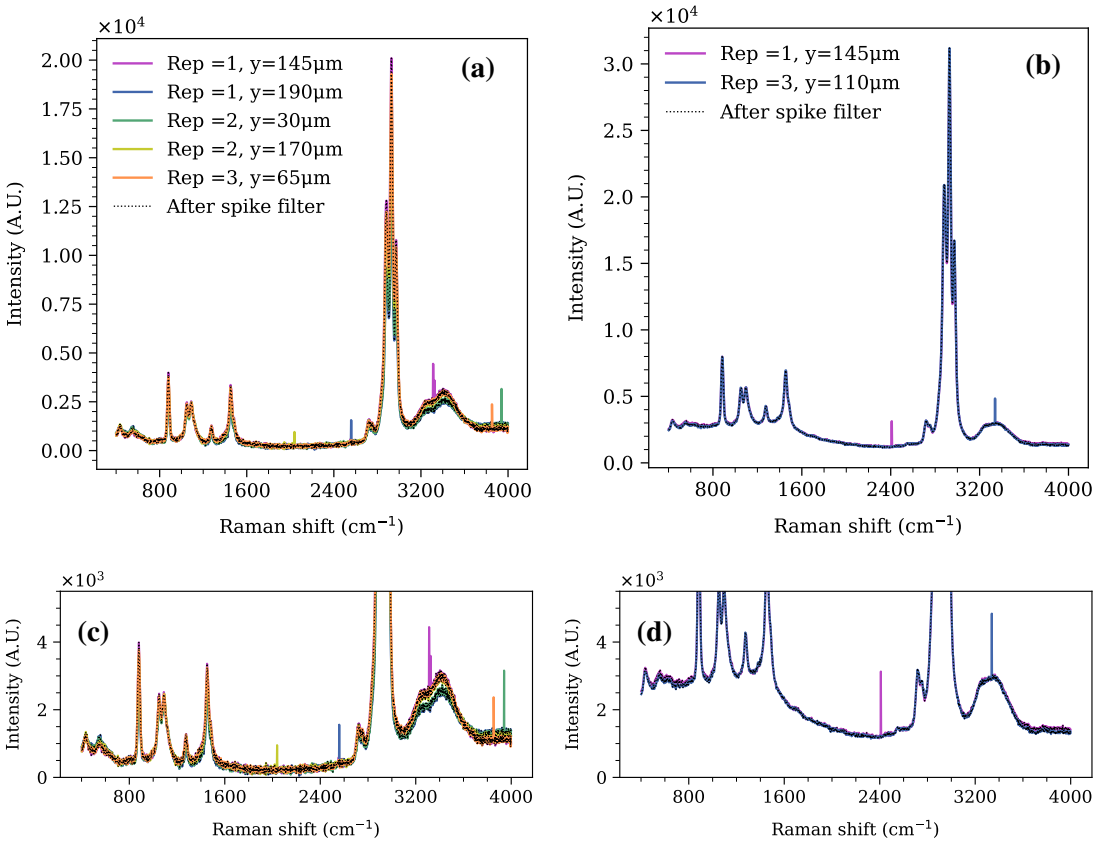


FIGURE 5.10: Example of how the cosmic rays in spectra are filtered without compromising the ethanol signal. (a, b) Complete spectra. (c, d) Zoom into the relevant intensity range for enhanced visibility. (a, c) Spectra for an ethanol mass fraction of 0.8. (b, d) Spectra for an ethanol mass fraction of 1. Both (a, c) and (b, d) share the legend, where y and *Rep* indicate, respectively, at what Y position and in what repetition (1, 2 or 3) the spectra was found on. There are multiple repetitions because the spectra shown in these examples is part of the calibration dataset, for which each measurement was repeated three times.

Firstly, spectra showing excessively large baselines were detected by computing their z-score, which indicates how many standard deviations away from the mean a data point is located [173]; for this work, a threshold of ± 3.5 was selected. The area under the spectra in the range 400 – 2500 cm^{-1} was computed, after which the z-score of each element within this distribution of areas was calculated using the `scipy.stats.zscore` function from the SciPy library [141]. Figure 5.12 shows an example of an outlier that would be discarded through this method.

Lastly, the measurements that did not fall inside the microfluidic channel were identified. The top and bottom edges of the channel, $y = 0$ and $y = 205$, respectively, were considered to be the first points at which any ethanol signal was detected within the spectra. To quantify this signal, the area under the most prominent ethanol peak, 2800 – 3040 cm^{-1}, was calculated, prior normalisation of the spectra. The only exception was the pure water spectra within the calibration dataset, for which the water peak between 3060 – 3690 cm^{-1} was used. These peaks correspond with the CH and OH stretching modes, respectively [159]. The selected threshold value for this area was 0.04, with the first Y position which spectrum showed an area under the peak higher than this value being considered the edge of the channel. This value, as shown in Figure 5.13,

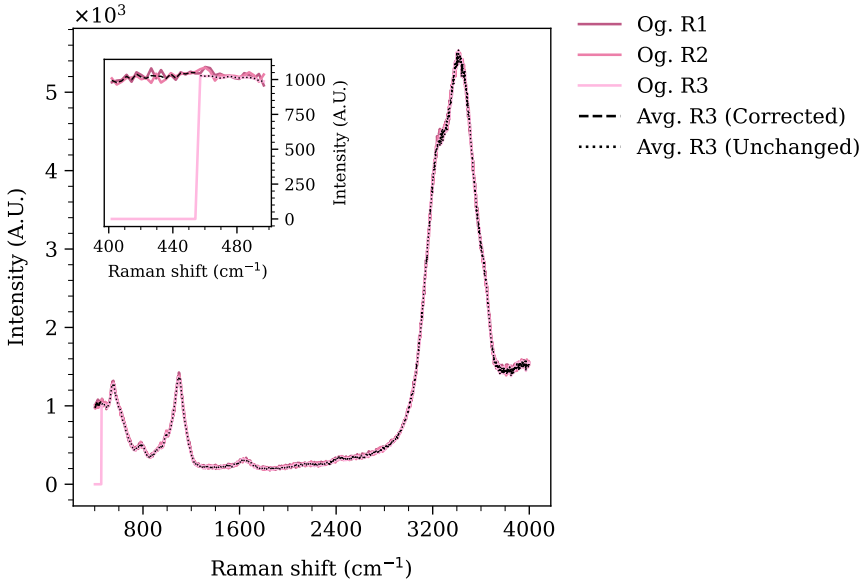


FIGURE 5.11: Example of how the intensities marked as zero in some spectra within the calibration dataset have been corrected by replacing these with the average of the other two repetitions. The labels *Og. R1*, *Og. R2* and *Og. R3* denote the original raw spectra, while the labels *Avg. R3 (corrected)* and *Avg. R3 (Unchanged)* refer to the two parts of the modified spectra: the corrected, averaged intensities from the beginning, and the unchanged intensities across the rest of the wavenumber range. The spectra shown in this example correspond to a pure water measurement.

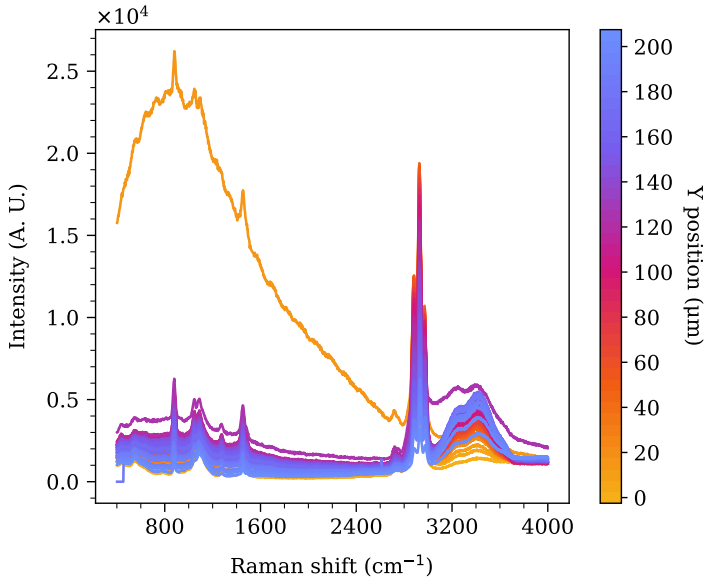


FIGURE 5.12: Example of a spectra showing a disproportionately large baseline in comparison to other measurements in the same column, resulting in the deformation of the spectral shape. Note that each *Y* position in the legend corresponds with a discrete colour, with 0 and 205 being the top and bottom of the channel, respectively.

allows to distinguish between noise in the signal and the start of a peak, even for the systems with lower concentrations. After the edge had been identified, the next 41 points were considered to comprise the entirety of the channel, given its height of 205 µm and the 5 µm increments used

between Y measurements.

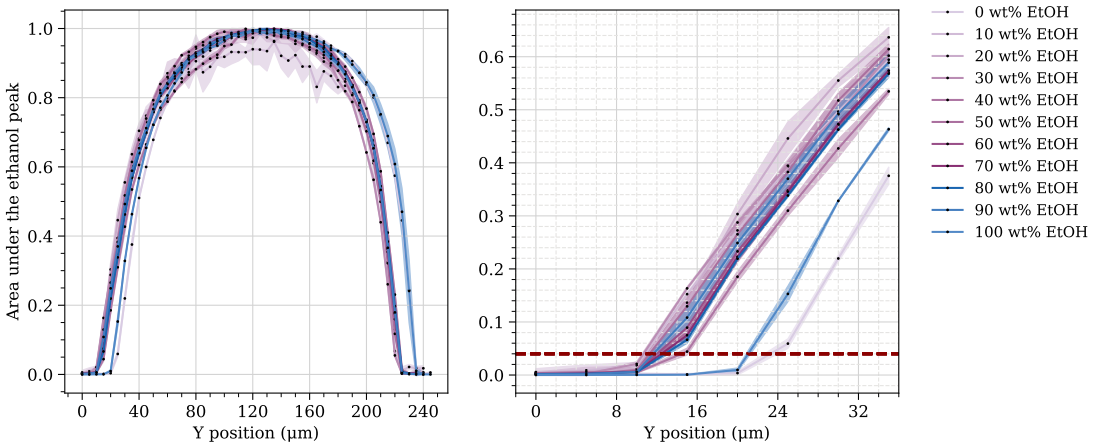


FIGURE 5.13: Average normalised area under the signal peak, as used to determine the borders of the channel. The shadowed area corresponds with the standard deviation of each average. In all cases except pure water, the 2800 – 3040 cm^{-1} ethanol peak was used; the former considered instead the 3060 – 3690 cm^{-1} water peak. A close-up of this figure is displayed on the right to showcase the adequacy of the selected threshold value, 0.04, indicated by the red dashed line.

Note that the curved trend observed in Figure 5.13(a) is a consequence of the cross-sectional shape of the microfluidic channel, shown in Figure 5.5. The implications of this artificially reduced signal towards the channel edges will be discussed in Section 5.3.2.

For the calibration measurements, the indices belonging inside the channel were checked from both top and bottom, and in both cases and for all concentrations the results were the same. As for the mixing measurements, the indices were gathered from the side from which the solution with the highest ethanol concentration was flowing. When the experiment consisted of mixtures and pure ethanol, the indices were determined starting from the bottom, as that is where the pure ethanol was introduced. When they consisted of mixtures and pure water, the indices were detected from the top. Thus, the error in this process could be slightly higher for the latter type, as the ethanol signal used to detect the start of the channel would have been less intense.

5.2.6 Transforming spectra into compositions

The next main step in the processing of the data was to transform the clean Raman spectra into compositions, for which it was decided to employ a PLS model, as defined in [174], trained on the calibration dataset detailed in Table 5.1. Moreover, to maintain accuracy across the whole y position range, the variation in Raman signal intensity caused by the transverse shape of the channel had to be taken into account. This shape is described in Figure 5.5, and its effect on the signal is visible in Figure 5.13. Hence, it was decided to train one PLS model for each y position measured along a column. Figure 5.14 presents (a) the different spectra and (b) the highest ethanol peak intensities for each concentration studied, at $y = 100\,\mu m$.

Two different pure ethanol measurements have been included in Figure 5.14(b). Collected at different dates, they are represented by a pink and a black marker, respectively, with the latter being the most recent one. This is also the one included in the final calibration dataset, since

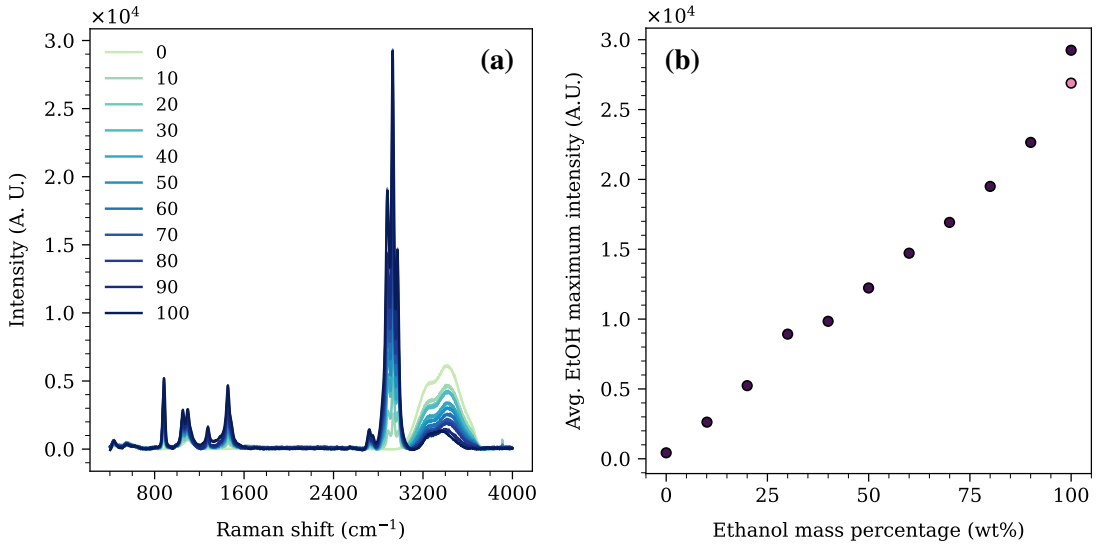


FIGURE 5.14: (a) Average Raman spectra for each concentration in the calibration dataset, after baseline removal; the shadowed area corresponds with the standard deviation. (b) Average and standard deviation of the highest ethanol intensity for each composition of the calibration dataset. Two values for the pure ethanol value were presented, collected at different times; the earlier one corresponds with the pink marker. Note that the error bars showcasing the standard deviation may be too small in comparison to the marker size to be appreciated.

it is more representative of the measurements obtained when collecting the mixing maps. The earlier measurement has been included for comparison purposes.

The data presented in Figure 5.14(b) overall follows the expected linear trend [175], albeit a slight deviation is observed at 30 wt% and a more pronounced one at 100 wt% when compared with the more recent pure ethanol measurement. The 10–90 wt% EtOH measurements were acquired on the same date as the earlier pure ethanol measurement, while the 0 and 100 wt% EtOH measurements were acquired on a posterior date. Therefore, the deviation from linearity could have been due to a number of reasons. The ethanol used for the more recent measurement belonged to a freshly opened bottle, and thus may have been less contaminated with water; moreover, the microscope may have been slightly better focused. Figure 5.15(a) shows the difference in signal intensity from the two pure ethanol measurements.

It is likely that the measurements in the 10–90 wt% range were affected by the same systematic differences between acquisition dates. To account for this, these spectra were multiplied by a correction factor, SF, depicted in Figure 5.15(b). For each Y position, SF was calculated as the quotient between the average maximum ethanol intensity recorded in both dates, as presented in Equation (5.1). Its magnitude is overall close to 1, even though the positions closer to the edges of the channel show a much higher deviation. While this could lead to an excessive correction at those points, this was not a matter of concern in this work, since the measurements of the first and last 4 y positions have been excluded from the final composition map, due to an excessive error in the PLS model at those positions; this is explained in Section 5.3.2.

$$SF = \frac{\max(I_y^{new})}{\max(I_y^{old})} \tag{5.1}$$

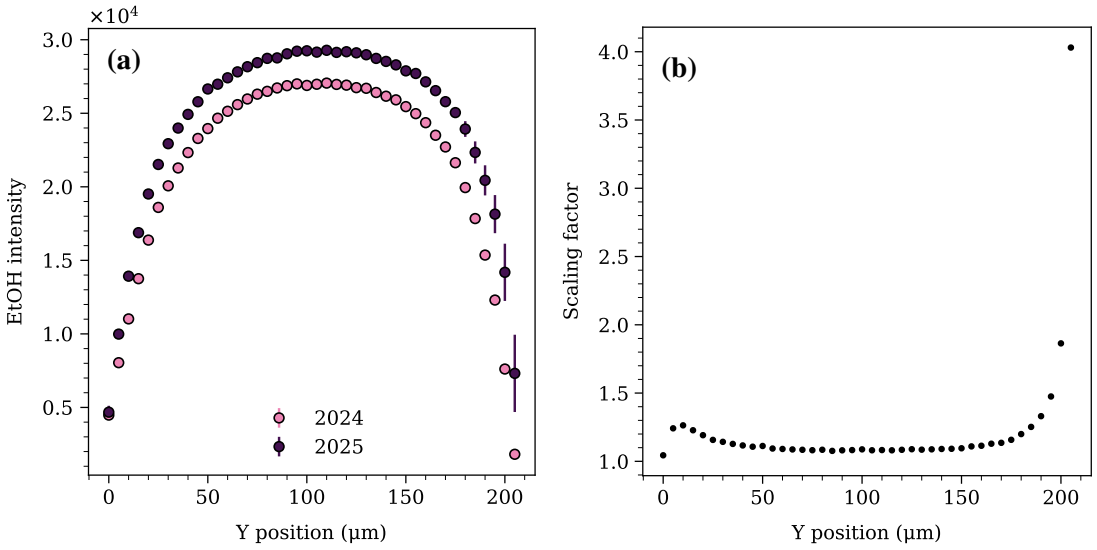


FIGURE 5.15: (a) Average ethanol intensity across the entire channel height for the two calibration measurements of pure ethanol, labelled by the date they were acquired. The error bars correspond with the standard deviation between repetitions. (b) Value of the calculated scaling factor for each y position along the channel height.

Figure 5.16(a) compares the spectra for 90 wt% before and after the correction was applied, making clear that the overall intensity of the signal is being corrected without incurring in an increase of noise or a deformation of the spectral shape. Figure 5.16(b) shows the difference in trend of the maximum ethanol intensity with and without this correction, as well as the linear fit of both datasets; the proposed correction increases the R^2 of this fit from 0.977 to 0.991.

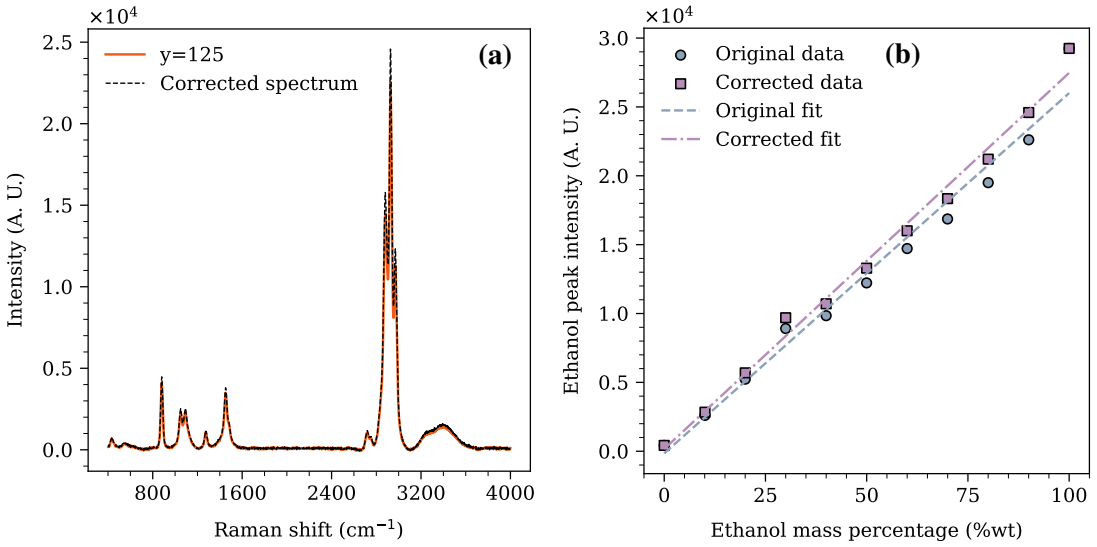


FIGURE 5.16: (a) Spectra from the 90 wt% calibration measurement at $y = 125$, before (solid line) and after (dashed line) correction. (b) Original and corrected average and standard deviation of the ethanol signal for each calibration composition, and their linear fit.

The PLS models trained on these corrected data were used to translate the spectrum at their corresponding y position into a composition value. During the training of these models, the

measured mass composition of each solution, displayed in Table 5.1, was considered as its ground truth. Their performance was quantified using the leave-one-group-out cross-validation (LOGO-CV) method, as applied in [174]. Each group was comprised of a single composition, and was iteratively used as the test set, while the remaining compositions constituted the training set. This way, each of these iterations yielded an error value, which corresponded to the Root Mean Square Error (RMSE) (5.2). To condense this into a single error value for each PLS, the resulting RMSE was averaged across all iterations, excluding those in which 0 or 100 wt% ethanol was the test set. This is because in them, the model was asked to extrapolate, leading to falsely high RMSE values that would skew the overall average. The final PLS models used to generate the raw composition maps were trained in all the available groups, without leaving out any data.

$$RMSE = \sqrt{\frac{1}{n}\sum_{i=0}^{n-1}\left(w^i_P - w^i_{GT}\right)} \tag{5.2}$$

where n is the total number of samples in the test set, and w^i_P and w^i_{GT} correspond with the predicted and ground truth mass fraction values, respectively.

Finally, two postprocessing steps were applied to the raw 2D composition maps. Firstly, as will be explained in more depth in Section 5.3.2, the overall error of the models at the top and bottom edges of the channel was excessively high, and much larger than the error found around the middle section. Therefore, it was decided to discard the first and last four rows of the maps. Lastly, the points where air bubbles had interfered with the signal were discarded. These were identified by checking the evolution of the area under the ethanol peak with each y position for sudden dips in the signal strength. Figure 5.17 provides an example of these trends, as found in an experiment with a 50 wt% mixture in one inlet and a pure water stream in the other. In this particular case it was decided to exclude the points $(3750, 90)$ and $(11250, 105)$.

5.2.7 Extraction of mass transfer model parameters

As stated in Chapter 1, the main significance of the proposed experiments revolves around their ability to accurately reflect the behaviour of the physical system in microfluidic devices. Consequently, the goal is to produce composition maps of mixing processes that can inform mass transfer models, initially for binary systems, and that can help qualitatively ascertain the predictions of the models developed in Chapters 3 and 4. The computational results of this chapter develop the workflow needed for this purpose; as an example of this, the gathered 2D composition maps have been used to inform a Fickian diffusion model for mixing in a binary system. Moreover, a velocity sensitivity study was performed so as to understand the impact that variations of the velocity profile could have on the recovered Fickian diffusion coefficient. This section details the modifications made to the model, and the characteristics of the optimisation algorithm developed to fit the model to the experimental data.

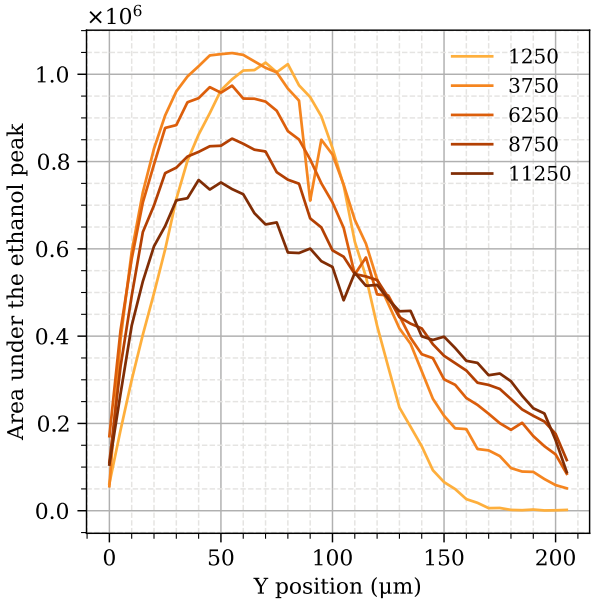


FIGURE 5.17: Area under the ethanol peak across the height of the channel for selected x positions recorded in the experiment 50–0 wt%. The (x, y) coordinates of the points that were identified as air bubbles and subsequently eliminated are $(3750, 90)$ and $(11250, 105)$.

Incorporating convection into the models

The mass transfer models presented in Chapters 3 and 4 were developed under stop-flow conditions; however, in order to reproduce the behaviour of this experimental microfluidic system, it is necessary to incorporate a convection term into the continuity equation (5.3).

$$\frac{\partial \varphi_A}{\partial t} + \nabla \cdot (\varphi_A \mathbf{v}) = -\nabla \cdot \mathbf{J_A} \tag{5.3}$$

where φ_A corresponds with the volume fraction of component A. This formulation assumes that the molar volumes of both species remain constant in space and time throughout the system.

To represent the fluid flow along the channel with higher accuracy, the Navier-Stokes equations would need to be solved. However, this is beyond the scope of this work, since the aim of this section is to provide an example of how the collected data can be used to inform and validate a mass transfer model. Since the simplest way of achieving this is by considering a constant velocity profile, a convection term was defined with these conditions: no convection along the Y axis, and constant velocity along the X axis, with a value equal to the average velocity inside the channel, given by Q/A. In this case, A corresponds with the cross-sectional area of the channel, calculated by dividing its total volume, 0.2 µL by its length, 12.5 mm.

Moreover, since ethanol and water have very different molar volumes, 58.4 and 18 mL mol^{-1} respectively, the molar flowrate of each species entering through the top and bottom streams is very disparate, despite them having an equal volumetric flowrate. To correct for this behaviour, the variable in Equation (5.3) was considered to be the volume fraction of ethanol, φ_{EtOH}. Hence, the in-silico composition maps obtained from solving this expression are comprised of volume fractions. These can afterwards be related to the molar fraction of ethanol,

x_{EtOH}, following Equations (5.4), (5.5) and (5.6).

$$x_{EtOH}^{z_i} = \left(\varphi_{EtOH}^{z_i}/V_m^{EtOH}\right)/\left(\varphi_{EtOH}^{z_i}/V_m^{EtOH} + (1-\varphi_{EtOH}^{z_i})/V_m^{H_2O}\right) \tag{5.4}$$

$$V_m^{EtOH} = MW_{EtOH}/\rho_{EtOH} \tag{5.5}$$

$$V_m^{H_2O} = MW_{H_2O}/\rho_{H_2O} \tag{5.6}$$

where $x_{EtOH}^{z_i}$ and $\varphi_{EtOH}^{z_i}$ correspond with the mole and volume fractions at a specific point in space, and V_m^i, MW_i and ρ_i correspond with the molar volume, molecular weight and density, respectively. The molecular weights of ethanol and water were taken as, respectively, 46.07 and 18.015 $\mathrm{g\,mol^{-1}}$.

The densities needed to obtain the molar volumes of the pure components were interpolated based on composition and temperature from the data given in [176], with the temperature considered for each experiment being the average of the range borders given in Table 5.2. Table 5.3 summarises the value of these parameters for each experiment.

TABLE 5.3: Properties of the system studied in each experiment. Left to right: experiment identification number; average temperature $\overline{T}$ (°C); ethanol mole fractions of the inlet streams; and molar volumes ($\mathrm{cm^3\,mol^{-1}}$) of ethanol and water at that average temperature. Note that the mole fractions correspond with the theoretical composition of each stream, not with measured values.

ID	$\overline{T}$	x_{top}	x_{bot}	V_m^{EtOH}	$V_m^{H_2O}$	ID	$\overline{T}$	x_{top}	x_{bot}	V_m^{EtOH}	$V_m^{H_2O}$
1	20.65	1	0	58.403	18.049	8	20.90	0.115	1	58.419	18.050
2	22.65	1	0	58.530	18.058	9	20.65	0.281	1	58.403	18.049
3	22.05	1	0	58.492	18.055	10	20.85	0.540	1	58.416	18.050
4	20.00	1	0	58.362	18.047	11	21.00	0.115	0	58.425	18.051
5	22.75	1	0	58.537	18.058	12	19.45	0.281	0	58.327	18.045
6	23.50	1	0	58.584	18.061	13	19.40	0.540	0	58.324	18.045
7	21.15	1	0	58.435	18.052	-	-	-	-	-	

Algorithm for informing mass transfer models

One of the main applications of experimental data gathered through this setup is their ability to inform mass transfer models, helping determine the values of their characteristic parameters. To illustrate this, an optimisation to a Fickian diffusion model was performed. While this model was chosen for the sake of simplicity and due to the wealth of literature data available with which the results can be compared, the same procedure could be applied to a more complex model, such as Maxwell-Stefan or CaHiMaS, if focusing on the diffusion coefficient.

The optimisation algorithm developed for this purpose, which steps are summarised in Figure 5.18, relies on the minimisation of the difference between the experimental 2D composition maps and maps generated in-silico following Equation (5.3). For the purpose of this optimisation, the volume fractions of the simulated map and the mass fractions of the experimental map are converted to mole fractions, which is the form in which the optimisation occurs.

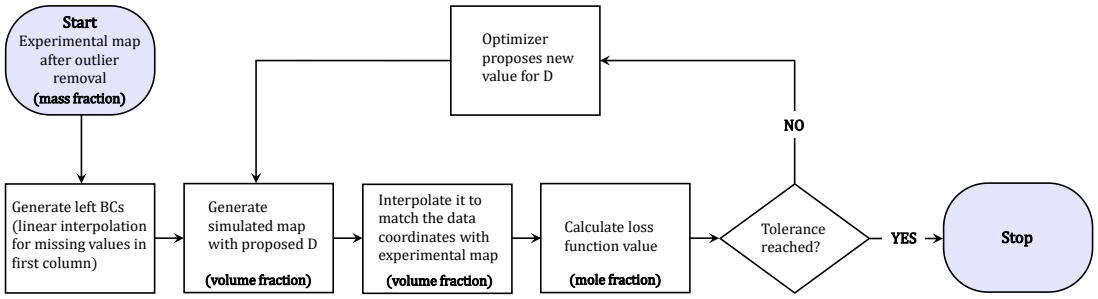


FIGURE 5.18: Step-by-step flowchart for the optimisation process. For clarity, it has been indicated what form of composition each step was conducted in. The results of the first interpolation, labelled as "Generate left BCs", are only used to define the left boundary conditions of the simulation, but the interpolated missing values are not considered when evaluating the error function.

The employed simulation grid had the same dimensions as the microfluidic channel, 12 500 µm × 205 µm, with 2500 and 82 nodes in x and y, respectively, and thus 2.5 and 5 µm increments in these two directions. A timestep of 0.04 sec was employed. A two-layered configuration was chosen for the initial conditions, given its resemblance with the experimental flow before any diffusive mixing takes place, whereas the boundary conditions differ depending on location.

Zero-flow was maintained at the top and bottom of the channel, given that the fluid is constrained by the solid channel wall. Neumann boundary conditions were used at the outlet (right), following the recommendation given in [177] for this type of problem. These dictate that the gradient in composition is zero at the outlet, i.e., the composition of the last cell and the cell that would be immediately after in the x direction are the same. Hence, the diffusive flux at that point is zero. Finally, Dirichlet boundary conditions were used at the inlet (left), consisting of two-layered fixed composition values taken from the first column of the experimental map that the model is being validated against. Since the simulation grid was finer than the experimental grid, intermediate values were obtained through linear interpolation using the `numpy.interp` Python library [178]; additionally, the values missing due to discarding the top and bottom four rows of the experimental map were filled with the highest and lowest recorded compositions in that particular column. Moreover, in a few cases, this first column presented values that had been eliminated as outliers during the data preprocessing. As a workaround, these values were linearly interpolated for the purpose of defining this boundary condition, using the `pandas.series.interpolate` function in the Python library [179, 180]. Figure 5.19 presents two examples of this interpolation, showing that the overall trend was mostly unaffected by this treatment.

Before the experimental and simulated maps could be compared, the simulated map had to be interpolated to match the grid coordinates of the experimental one; this was done via `scipy.interpolate.RectBivariateSpline()` [141], with `order=1`. There were two reasons for this: not only was the resolution of the simulation grid finer along the y axis, but also the coordinates of the final simulation do not match precisely those of the experiment. This is because the equations are solved in the centres of each cell, and thus, while the experimental

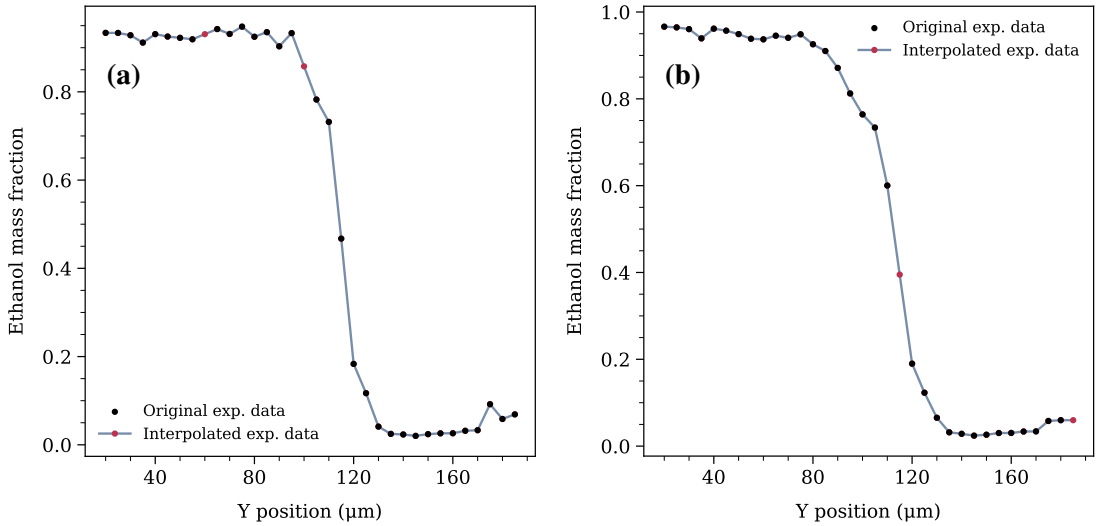


FIGURE 5.19: Depiction of how the linear interpolation of missing datapoints within the first column of experiments 4 (a) and 5 (b) affects the overall trend. In both cases, the original trend is preserved, including when estimating an end value, as seen in (b).

data are collected at discrete points from 0 to 205, the values returned by the simulation would be displaced from those coordinates by 1.25. This is illustrated in Figure 5.20.

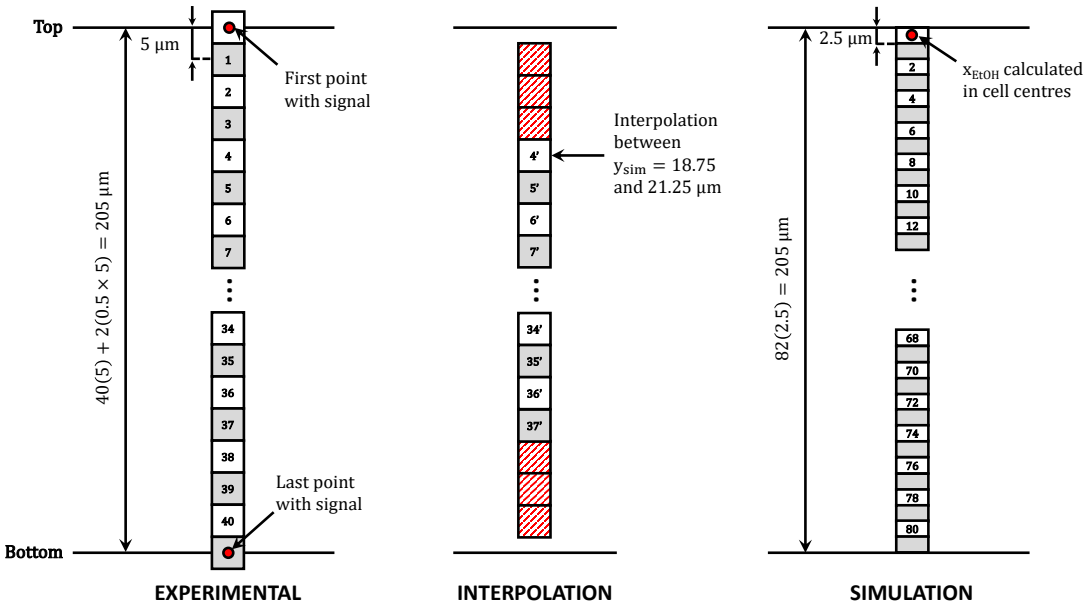


FIGURE 5.20: Coordinates at which the data in the experimental and simulated maps are located. Since the simulation mesh is finer across the y axis, with the equations solved at the centre of each cell, an interpolation of this map onto the experimental grid was required, as illustrated in the middle map. The red-shaded cells indicate the points trimmed out of this interpolated map to match the number of discarded rows in the experimental maps.

Regarding the optimiser itself, the Nelder–Mead [181] method was selected, as implemented in `scipy.optimize.minimize()` [141], with a tolerance of $1\,\mu m^2\,s^{-1}$ for the diffusion coefficient, and of 10^{-5} for the loss function value. The chosen loss function was the Mean

Squared Error (MSE) (5.7). An initial guess for D of 800 $\mu m^2 s^{-1}$ was used in all cases.

$$MSE = \frac{1}{n}\sum_{i=1}^{n}\left(\varphi_i^E - \varphi_i^S\right)^2 \tag{5.7}$$

where φ_i^S and φ_i^E correspond with the simulation and experimental ethanol volume fractions for each node in the composition map, respectively, and n corresponds with the total number of cell centres present.

Velocity profile sensitivity analysis

To test the extent to which the velocity of the streams inside the channel affected the predicted value of the diffusion coefficient, a velocity sensitivity analysis has been conducted for experiment 7, following Table 5.2 notation. This study consists on the scaling of the entire velocity profile through its multiplication by a certain factor. Four different scaling factors were included in this analysis: 0.25, 0.75, 1.25, 1.75. Velocity variations of this nature would have most likely been caused by changes in the flowrate of either stream. Some possible causes for these potential variations will be discussed in Section 5.3.2.

5.3 Experimental results

This section presents and discusses the results obtained throughout the experimental study of this system. It first presents the outcome of an initial qualitative study of the system, comprising of optical microscopy images captured at different conditions, with the aim to build an intuition of what the system looks like. The Raman microscopy results are discussed afterwards, divided in two main parts: (1) the results of the parameter search and optimisation carried out for the PLS model, and (2) the measured spectra and calculated 2D composition mixing maps.

5.3.1 Optical microscopy

A manual Leica M165 C optical microscope was used to perform this qualitative exploration of the system. Figure 5.21 summarises the results of this study, focusing on two aspects, namely, the behaviour of the system when under different flowrates, and when under different inlet compositions. The main element to observe is the interface that forms between the two miscible liquids, which corresponds with the laminar flow diffusion interface. This is commonly observed between co-flowing liquids in microfluidic systems, and is a consequence of the difference in viscosity among both fluids when co-flowing in a laminar regime [182].

From Figure 5.21(a) it is clear that, when pure water and ethanol streams are mixed, the length of the interface formed between both liquids increases with increasing flow rates. Since a higher velocity means a lower contact time for diffusive mixing, this behaviour was expected. Figure 5.21(b) shows that the intensity and length of the interface increase with increasing composition differences between the two streams, while when the same solution was introduced at

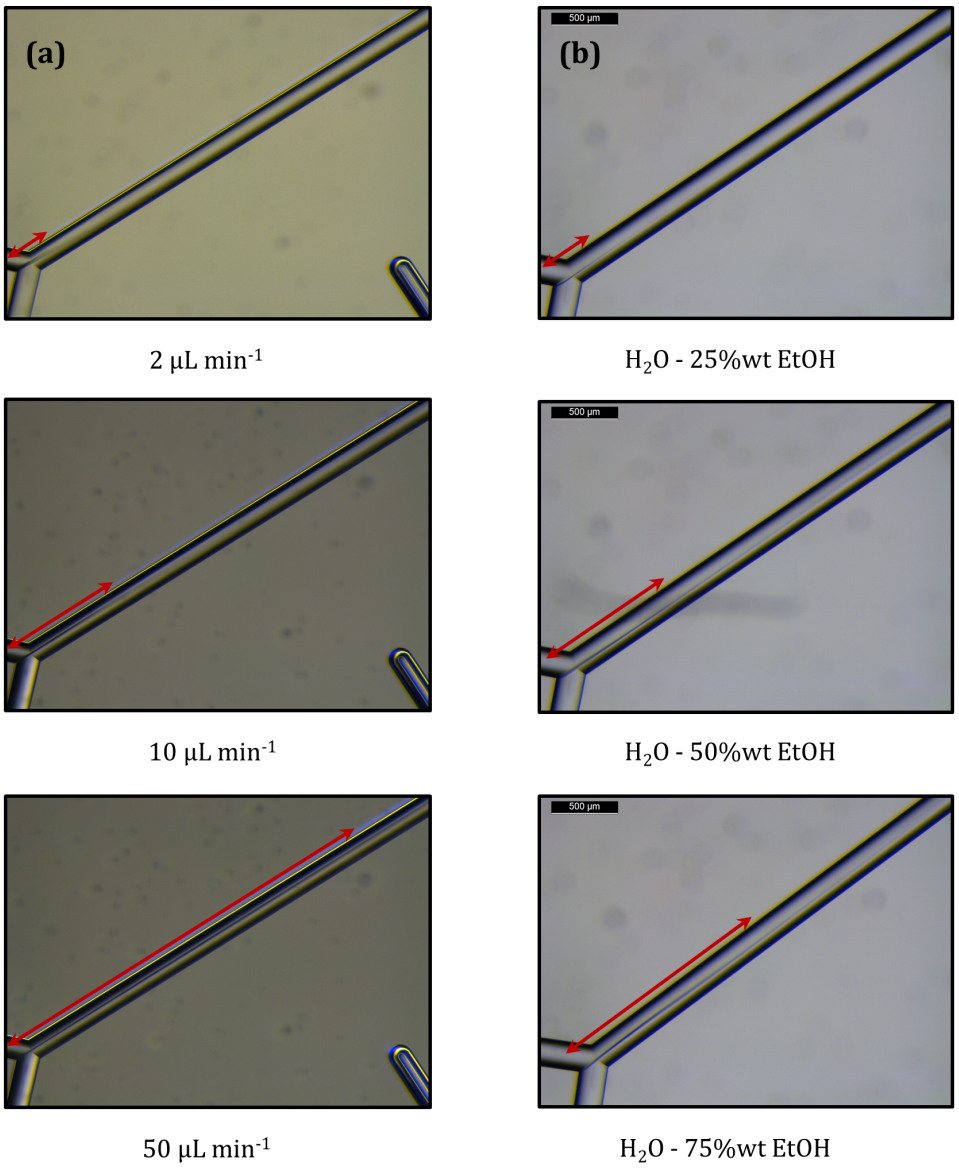


FIGURE 5.21: Mixing of water–ethanol solutions as observed with the Leica M165 C optical microscope: (a) Mixing of pure ethanol and pure water streams under increasing flow rates (top to bottom). (b) Mixing of a pure water stream with a water–ethanol solution of increasing ethanol composition (top to bottom) at $10\,\mu L\,min^{-1}$. The red arrows are a guide to the eye.

both inlets, no interface was formed. This was also expected since, as the difference in properties between the two streams increases, more contact time is required for both fluids to fully mix.

5.3.2 Raman microscopy

Optimisation of the PLS model configuration

As explained in Section 5.2.6, the Raman spectra was transformed into compositions using a PLS model. In order to discover the features of this model that would minimise the prediction error, a hyperparameter search was performed, exploring the impact of the number of latent variables,

the baseline method applied to the spectra and the scaling of the data. Table 5.4 summarises these parameters and the alternatives studied for each of them.

TABLE 5.4: Hyperparameters analysed during the optimisation of the features of the PLS model, and the different values tested for each of them. Note that the combined baseline removal method consists of applying first airPLS to the spectra and then a Savitzky-Golay filter, with parameters $(9, 2, 1)$ for window length, polynomial order and derivative order, respectively.

Hyperparameter	**Range of study**
Data scaling	True, False
Latent variables	2, 3, 4, 5
Baseline removal	airPLS, Savitzky-Golay filter, combined
λ	75, 100, 125, 150, 250, 500, 1000

While λ can vary between 1 and 10^9 [171], the studied range aimed to cover the subset of all potential values that could yield a satisfactory baseline removal, since very large λ values were found to not have any impact on the spectrum. When the combined baseline removal approach was taken, airPLS was applied to the spectra first, followed by a Savitzky-Golay (SGS) filter from the Python library [141]. The parameters of the latter were fixed at $(9, 2, 1)$ for the window length, polynomial order and derivative order, respectively. It is worth mentioning that this hyperparameter search was carried out by testing all the possible combinations, although the value of λ will not impact the performance outcome of the first derivative baseline removal method.

Figure 5.9 depicts the effect of the airPLS baseline removal method, and its comparison to the raw spectra. Similarly, Figure 5.22(a) shows the effect of the SGS filter on this same spectra, and Figure 5.22(b), the effect of the combined method, which results in very similar spectra.

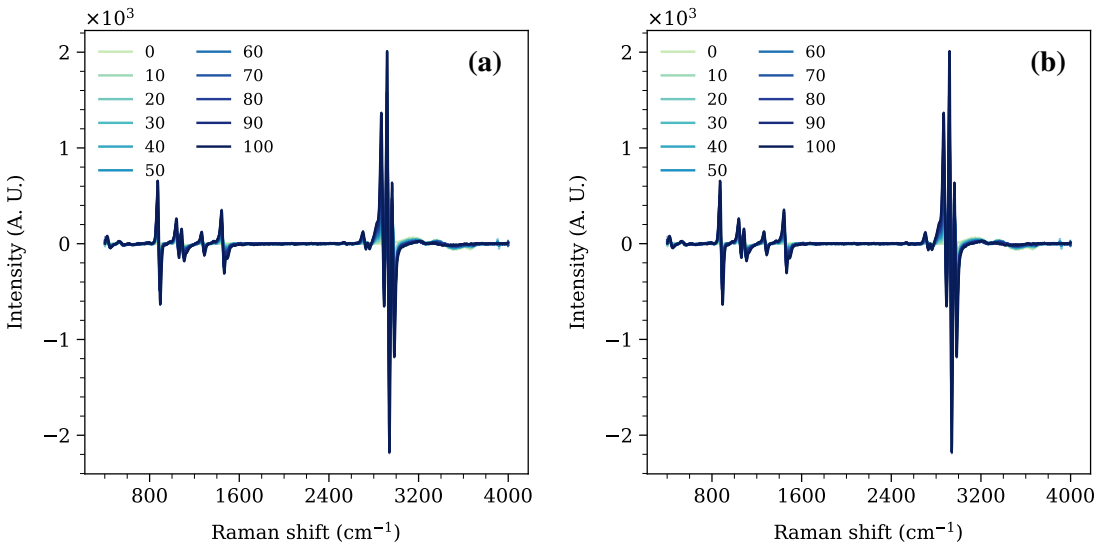


FIGURE 5.22: Example of the effect that the SGS filter (a) and combined (b) baseline removal methods have on the calibration dataset, at $y = 100\,\mu$m. Note that the combined methodology consists on applying airPLS baseline removal first, followed by a SGS filter.

Figure 5.23(a) shows the average RMSE, calculated as described in Section 5.2.6, across all the tested number of latent variables and for both scaled and unscaled data, when employing airPLS baseline removal in combination with $\lambda = 100$; Figures 5.23(b) and (c) show the same information for the SGS filter and combined baseline removal methods, respectively. Several trends can be observed. Firstly, the number of latent variables seems to not have much of an effect on scaled data, with the average RMSE and magnitude of the error bars not changing significantly across the studied range. On the contrary, when the data is not scaled, the performance of the model tends to improve as the size of the PLS model increases.

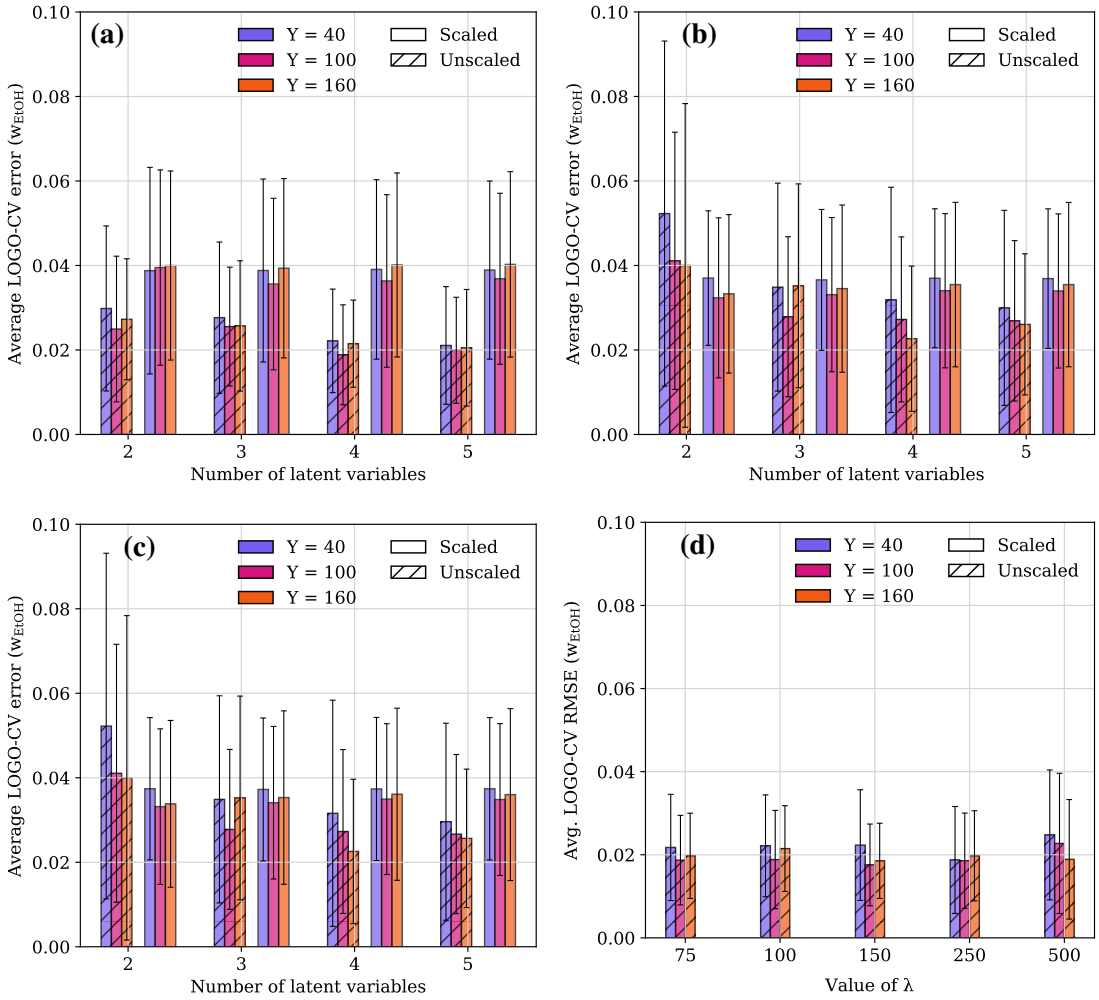


FIGURE 5.23: Performance of PLS models at different channel y positions trained under different combinations of number of latent variables, scaling of the data and baseline removal methods: (a) airPLS; (b) SGS filter; (c) combined (airPLS + SGS filter). The λ value was kept constant at 100 for these studies (a-c). Finally, (d) presents the performance of PLS models with 4 latent variables at different channel y positions, trained on unscaled data which baseline was removed through airPLS, but at different values of λ. The performance was quantified following the average RMSE calculated from the LOGO-CV process, as well as its standard deviation.

As for the effect of the baseline removal method, there is not much difference between the SGS filter and combined approaches, which was expected, given how similar the spectra returned

from both approaches are, as can be appreciated in Figure 5.22. For scaled data, these two methods lead to better performance, while airPLS does better when the data is not scaled. Overall, the combination leading to the lowest error and error bars is airPLS without scaling the data; since both 4 and 5 latent variables perform similarly, 4 were selected, in order to reduce the risk of overfitting, which would be higher with a larger model.

Regarding the effect of λ, Figure 5.23(d) presents the results obtained with a model with 4 latent variables and trained on unscaled data processed through airPLS. The value of this parameter seems to have little effect on the model performance under these conditions, until $\lambda = 500$ is reached, in which case the standard deviation is noticeably higher. In the end, $\lambda = 100$ was selected for the final model, since, when tested on experiment spectra, it provided a good balance between not interfering with broader peaks and still removing the spectral baseline in most cases. Smaller values distorted the former, and larger values were not sufficiently effective in removing the baseline. This way, the final configuration selected for the PLS model was airPLS baseline removal with $\lambda = 100$, no data scaling and 4 latent variables.

Finally, Figure 5.24(a) shows the average RMSE for the chosen set of hyperparameters across the entire height of the microfluidic channel, as well as, in Figure 5.24(b), an example of one iteration of the LOGO-CV process for one position along this height. Looking at Figure 5.24(a), it is clear that the PLS models corresponding to the top and bottom y positions of the channel present an excessive error. This explains the decision to discard four rows of data from either end, as mentioned in Section 5.2.6. The reason for this excessive error is most likely rooted in how the channel edges had to be identified: as explained in Section 5.2.5, the first position belonging to the channel was recognised as the first position at which signal was detected. However, the amount of solution passing through near the top and bottom edges was very small, due to the curved cross-sectional area of the channel shown in Figure 5.5(c). This could mean that a certain y position could be inside the channel in reality, but due to the small flow of solution in that point, the captured signal was not strong enough to pass the selected threshold. This would introduce an unavoidable uncertainty in the system, which would in turn be translated into the produced experimental maps.

Spectral results

This section provides an example of the Raman spectra measured during a typical mixing experiment, which constitutes the data afterwards translated into composition maps. The system selected, which corresponds with experiment 7 in Table 5.2, is formed by pure ethanol–water system flowing at $4\,\mu L\,min^{-1}$. Its spectral evolution is given in Figure 5.25, both along the y direction at $x = 3750\,\mu m$ in Figure 5.25(a), and along the x direction at $y = 30\,\mu m$ in Figure 5.25(b).

Figure 5.25(a) clearly shows how the ethanol and water peaks decrease and increase, respectively, when travelling down the channel height. This was expected, given that pure water was passing through the bottom stream ($y = 205\,\mu m$) in this experiment. Moreover, the evolution of intensities also shows that the highest ethanol signal is located at $y = 45\,\mu m$. This can be explained considering the effect of the cross-sectional area of the channel in the signal intensity, observed in Figure 5.13: the lower amount of liquid flowing near the channel edges results in

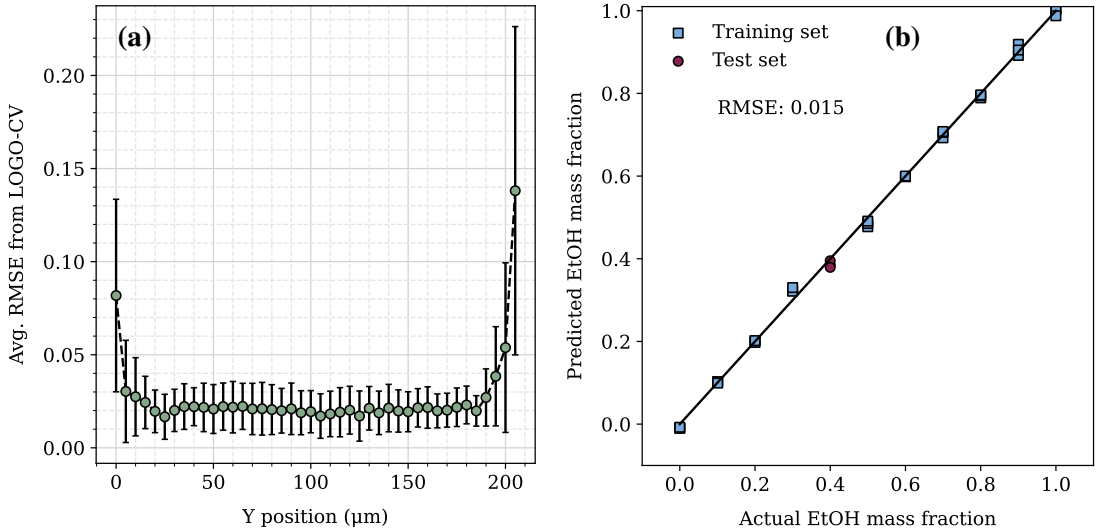


FIGURE 5.24: Overview of the performance of the final PLS model configuration. (a) Average RMSE across all LOGO-CV iterations, except for those in which 0 and 100 wt% were used as the test set. (b) Example of prediction plot for one of the LOGO-CV iterations of the 105 µm model.

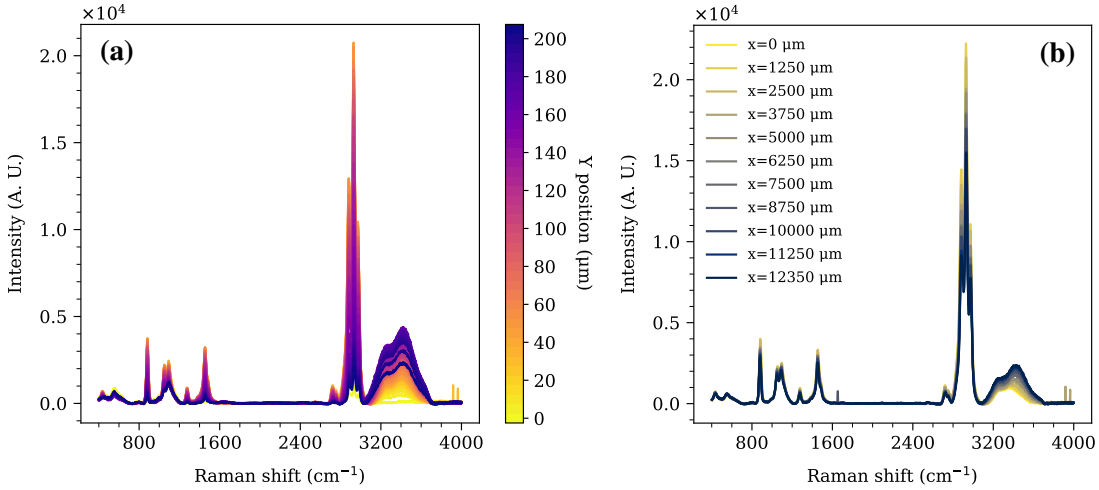


FIGURE 5.25: Evolution of the Raman spectra captured during the study of the pure EtOH-H_2O system flowing at 4 µL min^{-1}, without applying any baseline correction. Note that $y = 0$ corresponds with the top edge of the channel where ethanol was introduced. (a) At x =3750 µm, along the y axis, and (b) at y =30 µm, along the x direction.

a lower signal intensity. Since ethanol was flowing in this experiment through the top stream, finding the highest ethanol signal in the upper quarter of the channel height is consistent with the expected behaviour. Interestingly, the location of the maximum intensity at a specific channel length is found slightly above the channel centre when at the inlet (y =60 µm, in particular). As the mixing evolves, the effect of the cross-sectional area becomes more dominant.

Figure 5.25(b) shows how the ethanol and water content are progressively decreasing and increasing, respectively, as the signal travels further away from the channel inlet. Since y =30 µm is located on the top of the channel, through which pure ethanol was flowing, this signals diffusive mixing taking place.

2D composition mixing maps

There are two main factors contributing to the mixing evolution in this setup: the residence time, controlled by the flowrate magnitude, and the driving force for mass transfer, which in this case is directly related to the difference in composition of the two inlet streams. So as to analyse their effect, these two factors have been isolated, with the main findings summarised in Figures 5.26, 5.28 and 5.27. The reproducibility of these experiments is explored in Figures 5.29 and 5.30.

Note that compositions in these experimental maps are given as mass fractions. For the sake of clarity, the discussion in this section is focused on the comparison of experiment outputs with one another and the analysis of the arising trends; however, a more detailed discussion on the composition maps recorded in each experiment will be provided in Section 5.4, when comparing these to the simulation outputs, as it is only in light of this comparison that certain points become relevant.

Figure 5.26 explores the effect of the flowrate in the mixing evolution by maintaining constant the composition of the inlet streams, which are pure ethanol and pure water. In particular, Figures 5.26(a-c) present the composition maps corresponding to 2, 3 and 4 $\mu L\,min^{-1}$, respectively; these correspond with experiments 1, 4 and 7 in Table 5.2. Figure 5.26(d) shows a comparison of their composition profiles at $x = 0$ and 11 250 µm.

Overall, these composition maps clearly show a conical evolution in the mixing, which was expected of a system in the laminar regime in which mass transfer takes place exclusively through diffusion. This conical profile becomes wider as the flowrate decreases, due to the increase in residence time: at the same x, the two streams will have been in contact for longer the lower the flowrate is, thus allowing diffusion to have progressed further. This is supported by Figure 5.26(d), in which the slope of the composition profile towards the end of the channel clearly increases as the flowrate decreases despite the very similar inlet profiles, indicating a more homogeneous final composition and thus a higher degree of mixing achieved.

The x =5000 µm column in Figure 5.26(b) exhibits notably lower compositions than its neighbours, which is probably consequence of an experimental error when adjusting the equipment focus in z. As explained in Section 5.2.4, this focus was adjusted for every measured column, and an error when detecting its optimal value would lead to capturing a lower intensity, as seen in this case. Due to this potential error, this unfocused column was disregarded when compiling the dataset for the estimation of the diffusion coefficient in Section 5.4.

The effect of the driving force for mass transfer is presented in Figures 5.27 and 5.28, in which the composition mixing maps of six different systems flowing at 3 $\mu L\,min^{-1}$, and a selection of their composition profiles, are presented. In particular, Figure 5.27 considers ethanol mixtures of 25, 50, and 75 wt% with pure ethanol as the bottom stream, while Figure 5.28 comprises mixtures of these same compositions with pure water flowing through the bottom. These correspond, respectively, with experiments 8–10 and 11–13 in Table 5.2.

All the composition maps presented in Figures 5.27 and 5.28(a-c) overall follow the expected conical evolution, although this trend is more easily identified in the systems with a higher composition difference between the two streams. These results also present a certain amount of

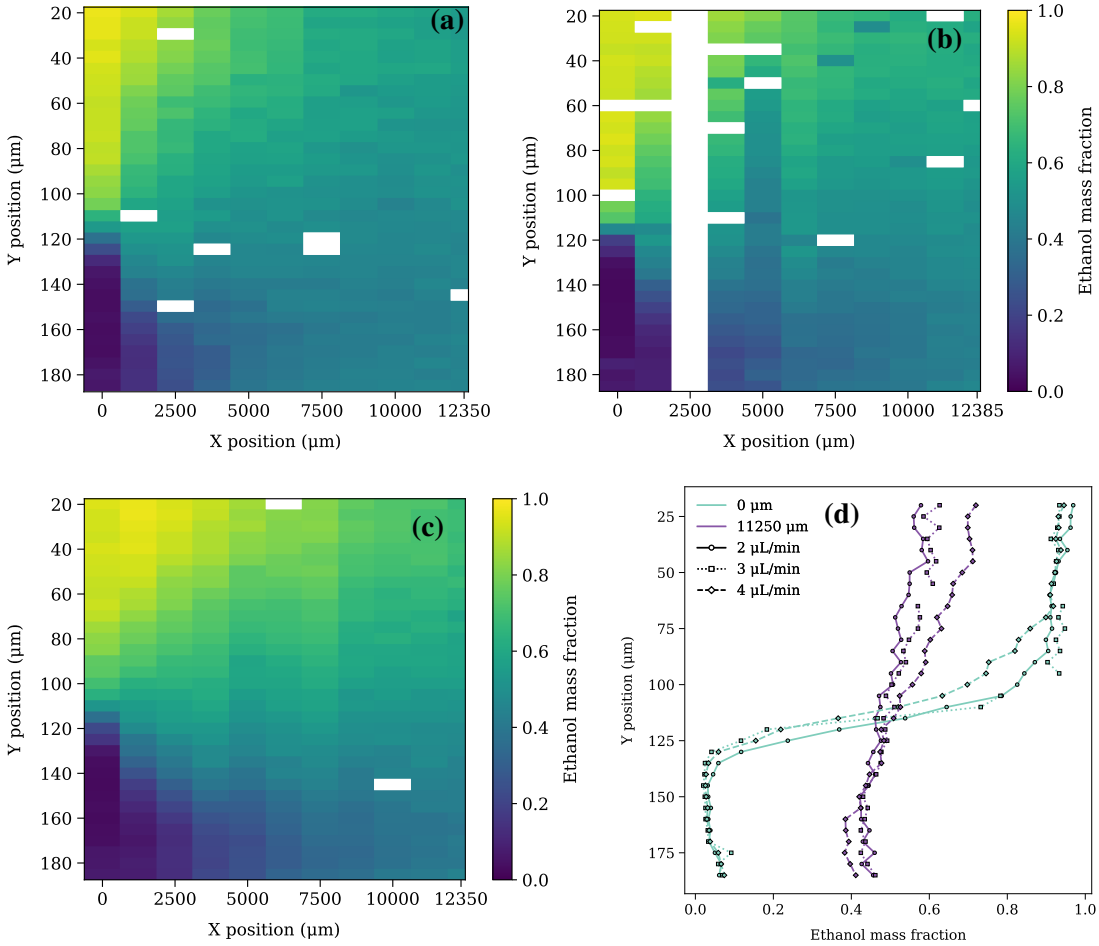


FIGURE 5.26: Raman composition mixing maps for a pure water–ethanol system studied at different flowrates: (a) $2\,\mu L\,min^{-1}$; (b) $3\,\mu L\,min^{-1}$; and (c) $4\,\mu L\,min^{-1}$; these correspond with experiments 1, 4 and 7 in Table 5.2, respectively. Composition is given as the ethanol mass fraction; the white squares represent eliminated outliers, and the white column indicates a missed collection point in the x axis. (d) Selected composition profiles extracted from these mixing maps at two x positions: the channel inlet, and 11 250 µm. Those points at which the trendline breaks correspond to discarded outliers. The larger pixels in the second and third columns in (b) are due to the $x = 2500\,\mu m$ column being missing in this map.

noise and artifacts. As noteworthy mentions, the maps in Figure 5.27(b) and Figure 5.28(c) both feature columns in which the depth focus of the microscope was not optimal. Therefore, the compositions at these locations were not part of the dataset employed for the estimation of the diffusion coefficient in Section 5.4. Moreover, the maps in Figure 5.27(a) and Figure 5.28(b) show some deviation in the interface location on the first column in comparison to the rest of the map. This was most likely caused by the rocking motion of the interface, which is discussed more in depth in Section 5.3.2.

Comparing the maps presented across these two figures, the width of the conical profile seems to be largely unaffected by the composition variations in the inlet, with all the composition maps across these two figures showing a very similar evolution. This means that the higher the compositional gradient, the faster the mixing is occurring. This observation is supported by the mass fraction profiles seen in Figures 5.27 and 5.28(d). Their value at $x = 11\,250\,\mu m$

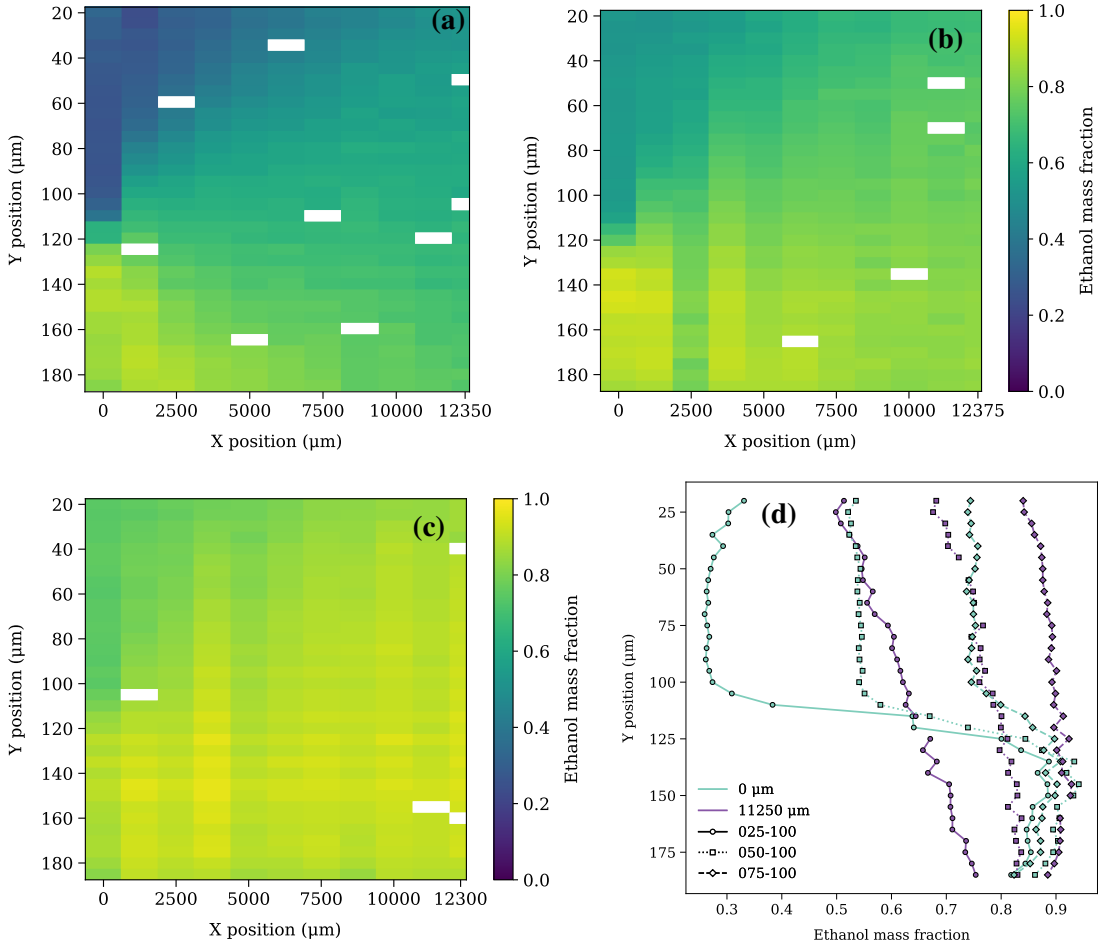


FIGURE 5.27: Raman composition mixing maps for a system at $3\,\mu L\,min^{-1}$. (a) 25–100 wt% EtOH; (b) 50–100 wt% EtOH; (c) 75–100 wt% EtOH. These correspond, respectively, with experiments 8–10 in Table 5.2. Composition is given as the ethanol mass fraction; the white squares represent eliminated outliers. (d) Composition profiles at $x = 0$ and 11 250 µm for the three systems. Those points at which the trendline breaks correspond to discarded outliers.

shows that the closer the experiment started to equilibrium, which, in an ethanol–water system, is a homogeneous solution, the more homogeneous its final composition profile is, becoming increasingly more vertical. However, when comparing the difference between the top and bottom compositions at both inlet and outlet, it is clear that the experiments with higher initial composition disparity between the streams are changing more rapidly, and thus experiencing mixing at a much faster rate. This can be explained by considering the thermodynamic behaviour of this system. Since the driving force for mass transfer between two phases is proportional to the gradient in chemical potential, and for ethanol and water this is proportional to the gradient of composition, the larger the compositional gap is at the inlet, the larger the chemical potential difference will be, and thus the faster mass transfer will occur.

Lastly, it is worth mentioning that the highest mass fraction recorded for the pure ethanol stream in Figure 5.27(d) is only slightly above 0.9, which could be due to the contamination of the ethanol with water despite the efforts taken to prevent this during its storage.

As for the reproducibility of these experimental results, this has been studied by performing

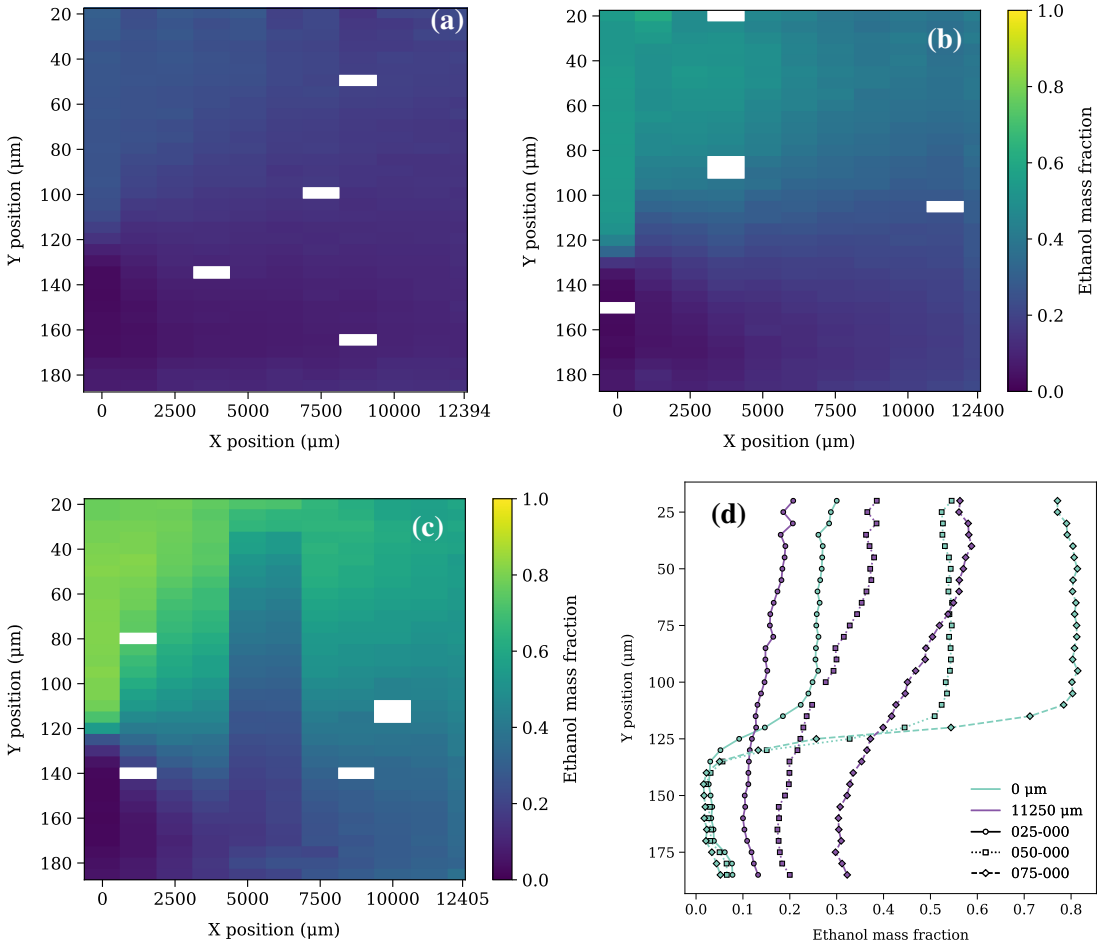


FIGURE 5.28: Raman composition mixing maps for a system at $3\,\mu L\,min^{-1}$. (a) 25 wt% EtOH–H_2O; (b) 50 wt% EtOH–H_2O; (c) 75 wt% EtOH–H_2O. These correspond, respectively, with experiments 11–13 in Table 5.2. Composition is given as the ethanol mass fraction; the white squares represent eliminated outliers. (d) Composition profiles at $x = 0$ and 11 250 µm for the three systems. Those points at which the trendline breaks correspond to discarded outliers.

two repetitions of two of the experiments conducted: pure ethanol and pure water flowing at 2 and $3\,\mu L\,min^{-1}$. Unfortunately, the considerable length of each experiment (7–12 h) impeded the collection of more repetitions. The results of this study are summarised in Figures 5.29 and 5.30, with the former presenting the composition maps for both cases, and the latter showing a comparison of some of their composition profiles.

Focusing first on the mixing maps presented in Figure 5.29, they present the expected conical evolution. In particular, the maps captured at a lower flowrate, given in Figure 5.29(a) and (b), exhibit a larger width in this conical profile; this agrees with the trend observed in Figure 5.26. A noticeable trend is the increase in the number of outliers within Figures 5.29(a), (b) and (d). This is suspected to be a consequence of an equipment malfunction, which will be treated in more detail when discussing the experimental sources of uncertainty in the next section.

Regarding the composition profiles depicted in Figure 5.30, it is worth noting that the error in these figures must be read horizontally, as the degree of variation in the composition that a particular y position could have. Considering this, these profiles show an overall good agreement

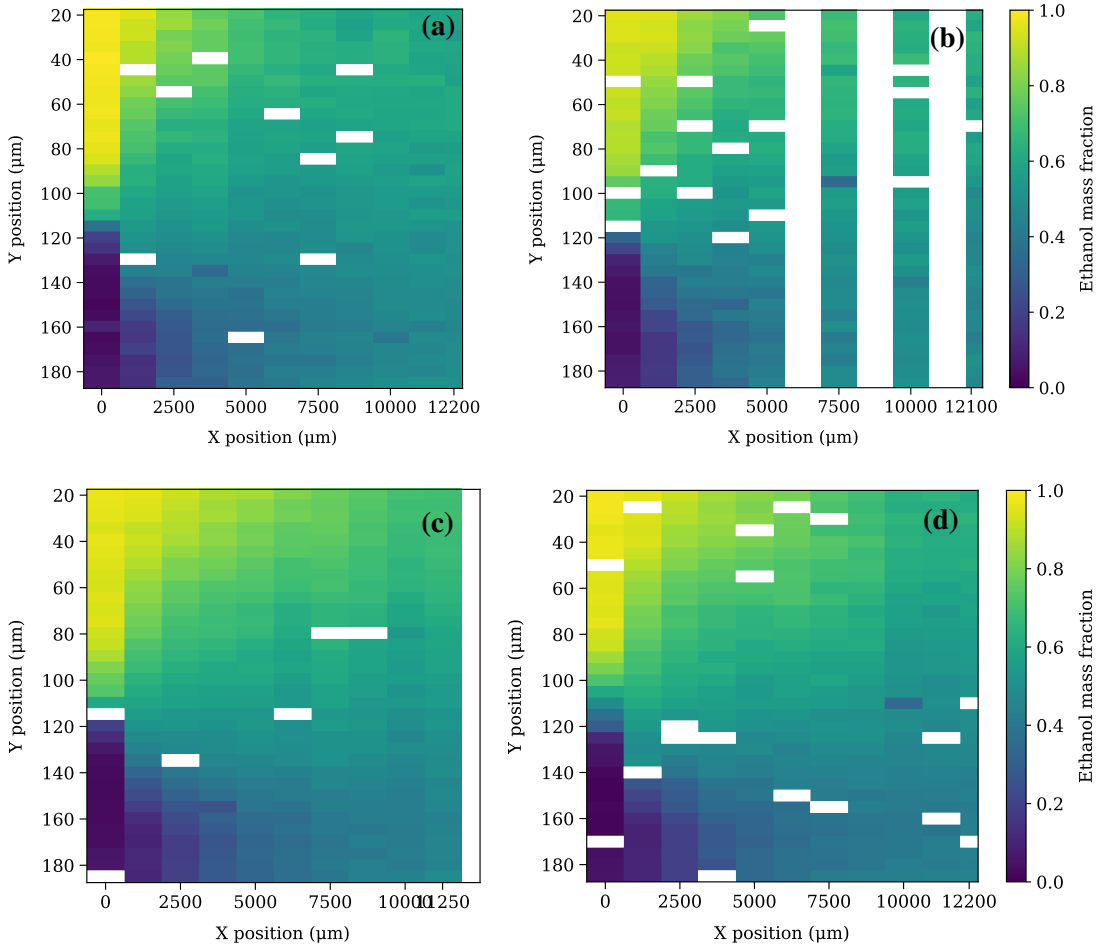


FIGURE 5.29: Repeated Raman composition mixing maps for pure ethanol–water flowing at $2\,\mu L\,min^{-1}$ (a, b), and $3\,\mu L\,min^{-1}$ (c, d). In particular, the maps correspond with experiments 2 (a), 3 (b), 5 (c) and 6 (d), as per Table 5.2. Composition is given as the ethanol mass fraction; the white squares represent eliminated outliers, and a white column indicates a missed collection point in the x axis.

between repetitions. While the difference among repetitions varies slightly between columns, the system flowing at $3\,\mu L\,min^{-1}$, shown in Figure 5.30(b), displays perhaps a smaller disparity. Moreover, the discrepancy among repetitions seems to be roughly constant across the y axis for all columns except the inlet, in which the top and bottom sections of the channel show a much higher consistency than the interface region towards the middle. The higher variability in this region is a consequence of operating at such small flowrates. The gear in the syringe pump could not maintain a continuous rotation when operating in this range, and had instead to alternate rotating with completely stopping. This led to a vertical rocking motion at the channel inlet, affecting mostly the interface location in the y direction. This will be further discussed below, in the experimental uncertainty section.

Lastly, there are certain specific points at which these profiles show a considerable deviation from the trend, with the first repetition at x =3750 µm of Figure 5.30(b) being the most prominent example. These points, which in the mentioned case most likely corresponds with an undetected air bubble, are clear outliers that managed to bypass the prior screening. Hence, they should not

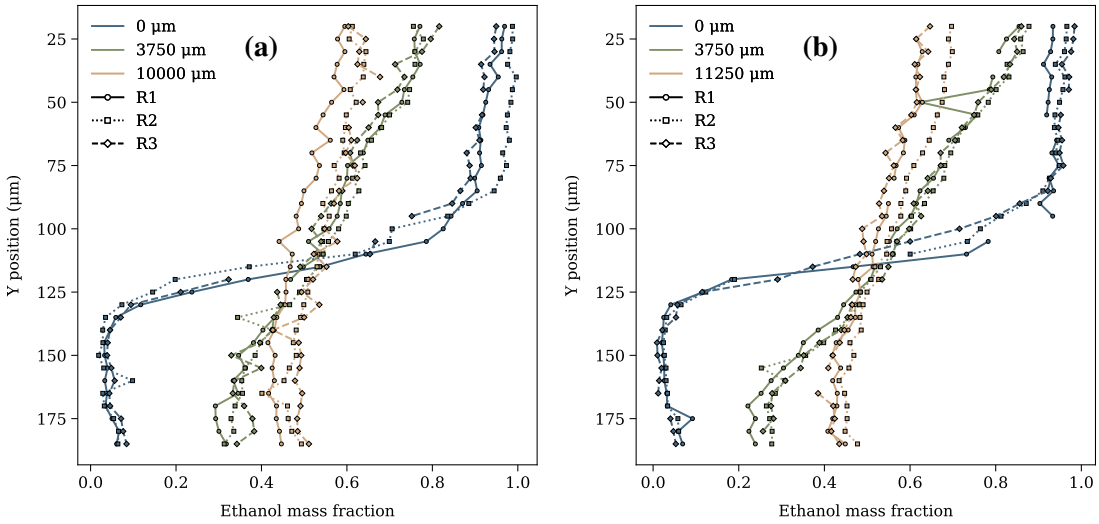


FIGURE 5.30: Composition profiles for pure ethanol–water flowing at (a) $2\,\mu L\,min^{-1}$, and (b) $3\,\mu L\,min^{-1}$ at different x positions along the channel. R1, R2 and R3 correspond respectively with experiments 1–3 in (a) and 4–6 in (b), as per Table 5.2. The points at which the trendline breaks correspond to discarded outliers.

be taken into account when interpreting the overall variability from one repetition to another.

Experimental sources of uncertainty

Now that the experimental results and their collection method have been presented and analysed, this subsection examines the different areas within the experimental procedure from which uncertainty may arise, and aims to provide a more complete understanding of the challenges faced during the experimental collection stage.

Firstly, there was probably an accumulation of uncertainty from small experimental sources, such as the microfluidic syringes having one end open to the environment when being filled up; this could have caused the ethanol concentration to decrease, given its hygroscopic nature. During several experiments there were works being carried out inside the laboratory, which could have impacted the stability of the interface. Moreover, during the collection of experiments 2, 3, 5 and 6 the Raman microscope was showing signs of malfunction, leading to a much larger amount of outliers in these.

Another source of error to consider is the need to identify which spectra belong inside the channel through an inspection of its ethanol or water signal, which was a consequence of the misalignment in the Raman microscope. Had the cross-sectional area of the channel been rectangular, this would not have led to further issues. However, as explained in the PLS results segment within Section 5.3.2, the cross-sectional area of the channel is curved. This imposes increasingly small amounts of material towards the top and bottom borders, resulting in a progressively weaker Raman signal and, potentially, in y positions that do belong within the channel being overlooked. Incurring in an error of this nature when processing a calibration file would impact all further data processing: the PLS model would incorrectly learn that the signal at the channel borders is higher/lower than it actually should be, and thus it will return an artificially

low/high composition when processing the experimental data. This would lead to an increased uncertainty in this region of the channel, which is clearly observed in Figure 5.24(a). This is the reason why four rows of data are discarded from both the top and the bottom of the channel in all experiments. Similarly, if this error occurred when determining the start of a column in a mixing map, it would displace the entire column, impacting the conical profile expected in the mixing process. To minimise the probability of such an error, the threshold was chosen with the utmost care, selected to work with both pure water and the whole ethanol composition range, as explained in Section 5.2.5.

Another issue that can contribute to the uncertainty in the experimental measurements is the up-and-down oscillation of the interface near the channel inlet, consequence of the low flowrates the pump had to operate at. This oscillation led to a higher discrepancy between repetitions in this region, as discussed in the experimental sources of uncertainty segment within Section 5.3.2. To test the extent to which this uncertainty would decrease if repeating the measurement enough times, a column at $x = 0\,\mu m$ was measured 17 times in a pure ethanol–water system. Figure 5.31(a) depicts the average and standard deviation of the spectra gathered at $y = 120\,\mu m$, and Figure 5.31(b) shows the evolution of the ethanol signal intensity across the whole channel height.

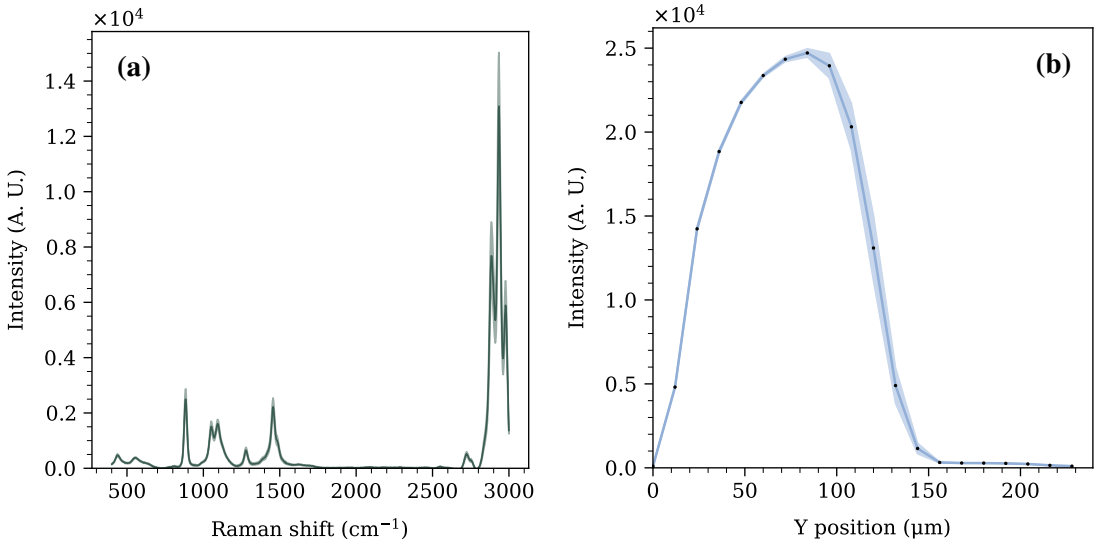


FIGURE 5.31: Uncertainty test performed in a pure ethanol–water system, consisting on measuring the column at the channel inlet 17 times. (a) Average and standard deviation of the spectra located at $y = 120\,\mu m$. (b) Averaged ethanol signal across the y axis, and its standard deviation. In both cases, the standard deviation is presented as a shadowed area.

Figure 5.31(b) clearly shows that the standard deviation in the ethanol signal is negligible towards the top and bottom of the channel, but that its value increases significantly when in the interfacial region. Nonetheless, its value is still reasonably small, with the 2800–3040 cm^{-1} ethanol peak in Figure 5.31(a) showing an intensity of approximately $1.3\ 10^4 \pm 2\ 10^3$ A.U. at its highest value. Therefore, despite the low flowrates causing uncertainty around the interface in the channel inlet, its impact could be minimised by sampling enough times.

Another point of consideration is the presence of a slight horizontal gradient along the x axis of the channel. In an effort to make the column collection path as perpendicular as possible to the channel border, their start and end coordinates took the effect of this gradient into account. While a small experimental error was incurred in at this step, it resulted in less than 1 µm of deviation in the verticality of the columns, and thus is considered to have had a negligible effect in the final result.

Finally, some unexpected formations were observed during the experimental work, with some examples displayed in Figure 5.32. After a few hours of flow through the microchannel, what seemed to be pockets of air appeared in the channel, as seen in Figure 5.32(a), as well as a fine trail of dot-like bubbles, shown in Figures 5.32(b) and (c), and, in some cases, air bubbles that seemed to grow attached to the channel wall, as shown in Figure 5.32(d), and exit only after certain size had been reached. These were observed in experiments 2, 3, 5, 6, and 10–13. None of these formations seemed to give any Raman signal, supporting the hypothesis that they were air pockets. Contamination of the setup was considered as a possible source, since these formations seemed to disappear only when flushing the system with ethanol; however, this was tested and subsequently discarded. While the used microfluidic chips had been in storage for over a year when the experimentation was conducted, the inner channel did not have any coatings that could have degraded with time. Nonetheless, the most plausible explanation for this behaviour is a wetting problem in the channel walls.

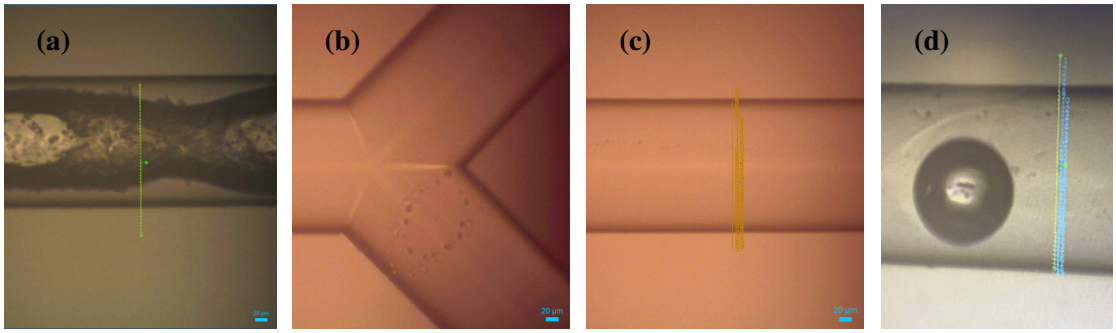


FIGURE 5.32: Unexpected formations observed during the gathering of the compositional maps. (a) Pocket of air located against the top wall of the channel; (b, c) trail of dot-like bubbles; (d) formation and growth of an air bubble against a channel wall. These formations did not show any Raman signal.

While these unexpected formations did not seem to bear any effect on the Raman spectra, it is highly probable that the velocity field inside the channel was affected by them. To minimise their impact, when one of these formations was identified, the flowrate was momentarily increased to fully expel it from the system, and then reduced to its original value, waiting for it to stabilise before taking the next measurement. Nonetheless, the velocity profile was most likely still affected, as air bubbles further along the channel or inside the tubing would not have been spotted, but still would affect the flowrate due to their compressible nature. This would result in uncertainty in the final composition maps, and, consequently, the diffusion coefficients obtained using these maps as the ground truth will also carry a certain error. The extent to which the predictions could be affected is discussed in the velocity sensitivity analysis presented in Section 5.4.3. This same analysis can be applied to the small air bubbles that sometimes seeped into

the system at the connections.

5.4 Computational results

This section illustrates how the compositional information provided by the collected mixing maps can be leveraged to inform mass transfer models. It focuses on the development of an optimisation platform through which parameters from a mass transfer model—the Fickian diffusion coefficient, in this case—may be estimated from these maps. As mentioned in Section 3.1, this diffusion model was chosen for the sake of simplicity, but the same procedure could be applied to estimate parameters of a more complex model, such as Maxwell-Stefan or CaHiMaS. Therefore, while the obtained composition maps are resolved at a coarser scale than that of the models studied in Chapters 3 and 4, they provide useful compositional information. This can be leveraged for the qualitative validation of the gradient coefficients in the CaHiMaS model, and enables the extraction of other mass transfer parameters.

For the sake of clarity, the reader is again directed towards Figure 5.18, which provides a schematic diagram of the developed optimisation platform. Particularly noteworthy is the fact that, while the experimental composition maps were collected as mass fractions, and the simulated map is solved for volume fractions, their comparison and the error minimisation step occurs between both maps converted to mole fractions.

This section is divided in three parts: the comparison between the experimental ground truth and the in-silico composition maps produced by the simulation; the comparison of the retrieved diffusion coefficients with literature values; and, lastly, the velocity sensitivity analysis.

5.4.1 Experimental vs simulated maps

The information algorithm was built on the minimisation of the MSE between the simulated and experimental molar fraction maps, and thus it is expected to lead to a simulation output as similar as possible to the provided experimental data. The quality of the fit can be qualitatively evaluated by comparing these two maps, as done in Figure 5.33 for experiment 7, following the notation presented in Table 5.2.

Regarding the evolution of the mass transfer and the final degree of mixing achieved, the simulated map in Figure 5.33(b) shows a remarkable resemblance to the experimental one, given in Figure 5.33(a), despite the slight experimental noise. This trend is overall maintained throughout all experiments. The first column of both maps match almost perfectly, including the small area around the channel centre in which the interface rocking, as explained in Section 5.3.2, caused a blurring of the interface. Recalling, from Section 5.2.7, this is because the values of the inlet column in the experimental map were used to define the left boundary conditions of the simulation. Hence, this high level of similitude indicates that this design choice is mitigating the impact of the interface rocking in the simulation, as desired. It not only accounts for the width of this interface rocking area at the inlet region the simulation, but it also forces the conical mixing trend to adapt to it, leading to a more accurate result.

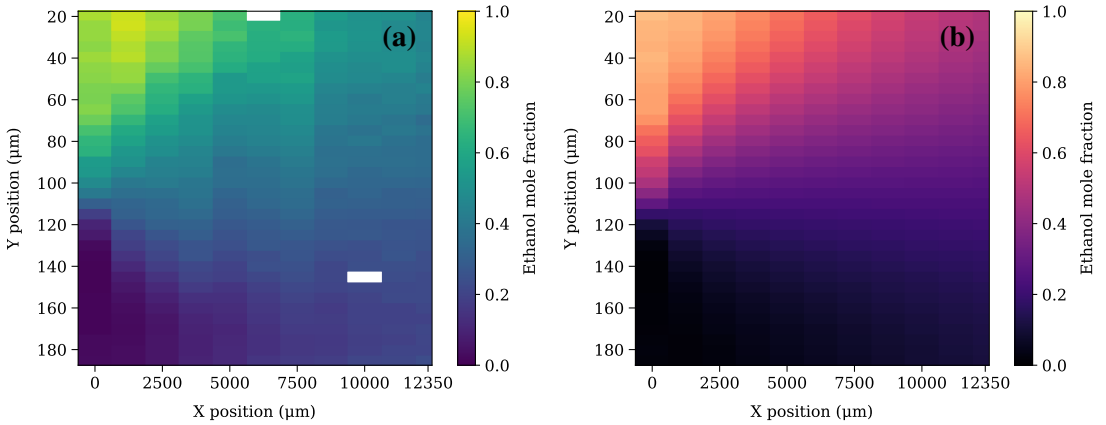


FIGURE 5.33: Experimental mole fraction map (a) and best-fit simulated map, given in mole fractions, (b) for experiment 7. The outliers present in (a) were not taken into account when evaluating the loss function, despite their corresponding cells being full in (b).

To facilitate the understanding of spatial composition trends, it is useful to consider what information can these trends provide in the context of the optimisation routine. A good agreement between experimental and simulated profiles indicates how well the algorithm has been able to match the experimental ground truth. However, this is not necessarily indicative on how close the diffusion coefficient it is to the real physical value. Each experiment has one optimal set of simulated composition profiles—namely, the set that minimises the loss function—which the optimisation algorithm seeks by varying the diffusion coefficient. Therefore, a poor agreement between the experimental and composition profiles can indicate whether the predicted mass transfer parameter is reliable. However, good agreement between these profiles does not necessarily imply a good prediction of this parameter.

Having outlined the context of these results, Figure 5.34 presents a comparison between the experimental composition profiles and those from the simulation best-fit of experiment 4, in Figure 5.34(a), and experiment 13, in Figure 5.34(b). These two experiments correspond, respectively, with a stream of pure water mixing with a stream of pure ethanol, and with a stream of pure water mixes with an ethanol–water solution of 75wt%. This comparison has been collected for all of the experiments within Appendix D.

The results are in good agreement in both cases, indicating that the algorithm was able to successfully minimise the loss function. The differences among both profiles are most likely consequence of an accumulation of one, or more, of the potential experimental sources of error discussed in Section 5.3.2. This similarity between experimental and simulated evolution of the ethanol mole fraction is maintained for most of the experiments (see Appendix D), indicating that the optimisation routine successfully captures the overall mixing behaviour across the studied range of conditions.

Only four cases show a stronger disparity between the experimental and simulated trends, two of which are presented in Figure 5.35. These have been analysed to demonstrate how the experimental uncertainties identified in Section 5.3.2 may affect the collected results.

Figure 5.35(a) corresponds with experiment 10, and presents the highest level of discrepancy

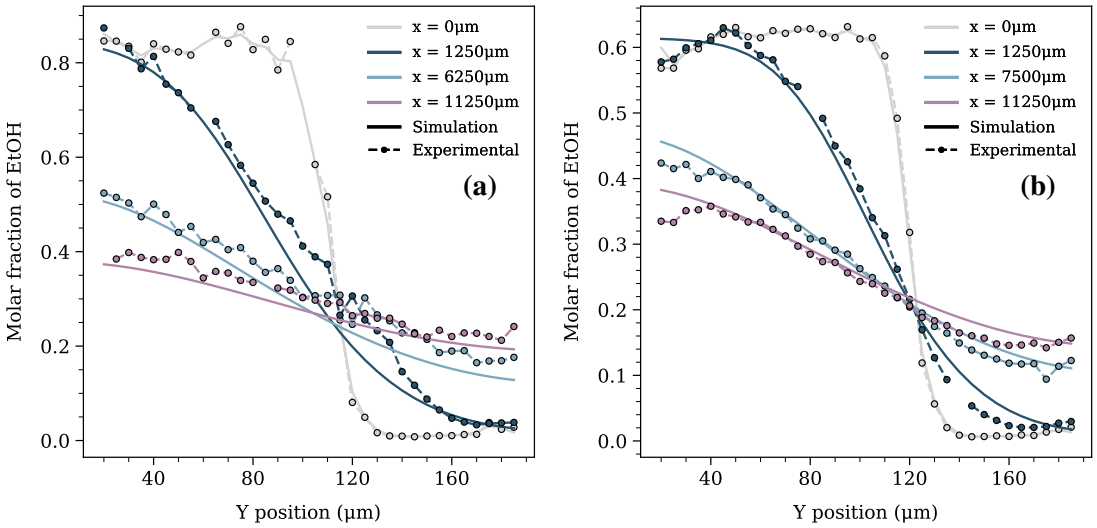


FIGURE 5.34: Comparison between experimental and simulation best-fit composition profiles for experiment 4 (a) and 13 (b), at different points along the channel length. The missing points on the trends reflect discarded outliers.

between both trends. There is a noticeable level of noise in the experimental profiles, which matches the trends observed in its 2D mixing map presented in Figure 5.27(c). Moreover, at all x positions except for the inlet the composition profiles show a considerable difference between experimental and simulation.

Another noticeable trend is that the experimental compositions recorded at the positions shown in Figure 5.35(a) along the channel for the bottom stream ($y = 102.5$–$205\,\mu m$) are higher than the inlet compositions, which is the opposite of the expected result. Figures 5.35(c) and (d) present the evolution of the spectra along the channel height for positions $x = 0$ and $1250\,\mu m$, respectively. The ethanol peak located between 2800 and 3040 cm^{-1} shows that the signal collected at the second position is higher, explaining the smaller compositions observed in the inlet profile. This behaviour is consistent with a focusing error affecting the first column, which would subsequently propagate into the simulation because the inlet compositions are used to define the left boundary conditions. This thus explains the difference between the simulated and experimental composition profiles.

Figure 5.35(b) shows the experimental and simulation composition profiles for experiment 12, in which pure water is mixed with a solution of 50wt% ethanol. The simulation profiles are observed to lay higher in composition than their experimental counterparts in all positions beyond the inlet. There are two prominent features that could be leading to this outcome. Firstly, the profile at $x = 0\,\mu m$ exhibits a large disparity in layer height between both inlet streams, which is not maintained in the profiles captured further along the channel. Moreover, the compositions recorded near the top edge ($y = 0\,\mu m$) of the channel at $x = 1250\,\mu m$ are subject to a considerable error, disrupting the trend followed by the rest of this profile and presenting values above those recorded at the inlet.

The presumably erroneous difference in layer heights at $x = 0\,\mu m$ could have skewed the model results because of these values specifying the left boundary conditions of the simulation.

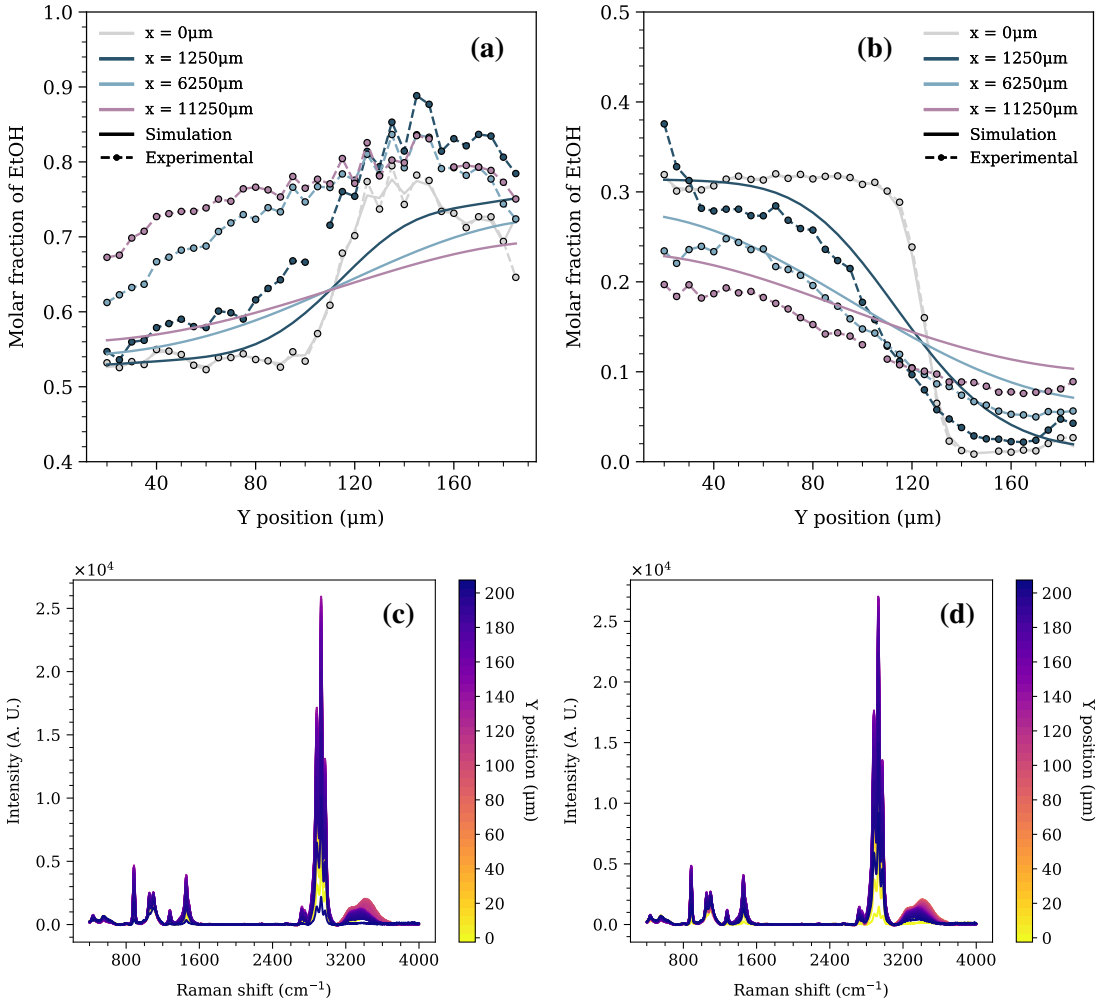


FIGURE 5.35: Comparison between experimental and simulation best-fit composition profiles for experiment 10 (a) and 12 (b) at different points along the channel length. The missing points on the trends reflect discarded outliers. Evolution along the y axis of the spectra captured for experiment 10 at $x = 0$ (c) and x =1250 µm (d).

Since the the ethanol-rich stream is favoured, this would explain why its profiles lie above all their experimental counterparts. In the case of x =1250 µm, this difference between the simulated and experimental profiles may have been exacerbated by the non-physical compositions recorded near its top edge.

These non-physical compositions are most likely a consequence of incorrect channel-edge detection. If the true edge of the channel is missed, the subsequent measurement point is incorrectly assigned as the boundary. Because this point lies further within the channel, it produces a stronger Raman signal than would normally be obtained at the edge due to the greater depth of the cross sectional profile and thus larger amount of liquid sampled at that point. The PLS model, having been trained on spectra acquired at the true channel boundary, may therefore interpret this increased signal intensity as a higher composition. Beyond the y =20 µm point, the gradient of the cross-sectional profile may have decreased enough for this effect to become unnoticeable.

The disparity in layer heights observed at $x = 0$ µm could have been caused by interface rocking, although this experiment was conducted at the same flowrate as many others, 3 µL min^{-1}, in which this behaviour was not observed. Since the wetting problems described in Section 5.3.2 were observed when performing this experiment, another reason could be the presence of entrapped air within the system leading to an inconsistent flowrate in one or both streams.

It is important to note that these are educated guesses of the causes behind the observed trends; the many variables simultaneously at play make it impossible to isolate them with certainty. Furthermore, despite the differences between simulated and experimental profiles being higher in these four instances, the rest of the experiments show good agreement between them. This indicates that the measured experimental maps evolve as expected, at least qualitatively, increasing the confidence in them.

5.4.2 Comparison with literature diffusion coefficients

As mentioned before, a high resemblance between composition profiles does not correlate with a good predicted diffusion coefficient. This section aims to understand the quality of these predictions by comparing them with the relevant literature data.

The interdiffusion coefficient, also referred to as the mutual diffusion coefficient, between water and ethanol has been measured through several experimental techniques, which can be broadly grouped into three categories. Hammond and Stokes [183] and Tyn and Calus [184] measured it using a diaphragm cell, whereas Pratt and Wakeham [185] and Harris *et al.* [186] employed Taylor dispersion. Although Pratt and Wakeham's later measurement of the water–1-propanol system was later proved inaccurate [186], their original ethanol–water measurements are consistent with the rest of the literature, and have therefore been included in the comparison. Finally, several authors [187–189] have measured the interdiffusion coefficient through thermodiffusion measurements, following the relaxation of Ludwig–Soret-induced concentration gradients.

Although the experimental techniques used in the literature to determine the interdiffusion coefficient differ substantially from the setup employed in this work, the reported measurements exhibit a consistent trend. Peters *et al.* [126], who used an experimental setup similar to that adopted here, obtained values that were in good agreement with literature data measured through a diaphragm cell. Consequently, the values recovered in the present work would be expected to fall within the range defined by the broader body of literature, which includes diaphragm-cell measurements.

Table 5.5 summarises the recovered values of the Fickian diffusion coefficient for each experiment, and Figure 5.36 presents their comparison with the summarised literature. The ethanol mole fraction chosen to represent each case corresponds with the theoretical final composition of the mixed streams. Additionally, the literature data for which different temperatures were available was taken at 25 °C.

Figure 5.36 shows that the interdiffusion coefficients recovered in this work are situated in the same order of magnitude as those reported in literature. In particular, experiments 8–12

TABLE 5.5: Interdiffusion coefficient values predicted by the optimisation algorithm after fitting Fickian diffusion to the experimentally measured composition mixing maps.

ID	x_{top}	x_{bot}	D ($\mu m^2 s^{-1}$)
1	1	0	1732
2	1	0	1835
3	1	0	1471
4	1	0	1864
5	1	0	1463
6	1	0	1618
7	1	0	1189
8	0.115	1	728
9	0.281	1	838
10	0.540	1	810
11	0.115	0	1471
12	0.281	0	1255
13	0.540	0	1309
-	-	-	-

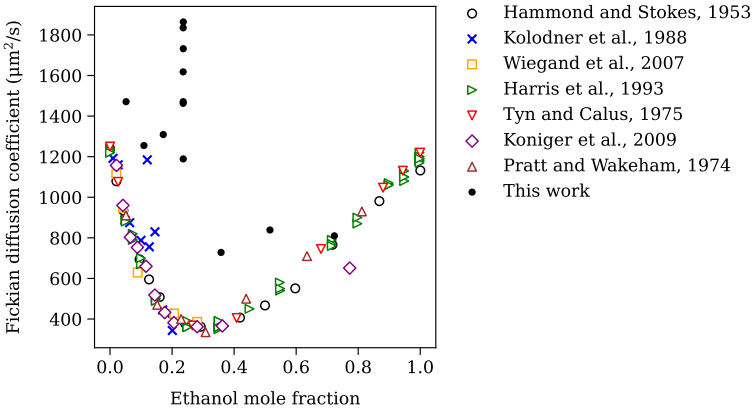


FIGURE 5.36: Comparison of the predicted interdiffusion coefficient values in this work with literature. Note that the compositions assigned to each of the values reported in this work corresponds with the theoretical final composition of the mixed streams. Literature data taken from [183], [187], [188], [186], [184], [189], [185]. Note that, as pointed out in [190], the value for D at an ethanol mass fraction of 0.8968 was erroneously listed as 2.51×10^{-10} $m^2 s^{-1}$ in Table 3 of [189]; however, the correct value of 6.51×10^{-10} $m^2 s^{-1}$ was displayed in Fig. 4. Therefore, it is this amended value that was included in this work.

differ from literature by a factor of approximately 2 or less, while for experiments 1–7 and 13 this factor ranges from, approximately, 2.5–4.6.

The error present was expected, given the experienced hurdles outlined in Section 5.3.2. Assigning the recovered values to the theoretical final composition of each experiment may be inadvertently contributing to this, since it assumes no water was absorbed by the ethanol in the solutions and the pure streams. If this was the case, as suggested by the composition profiles presented in Section 5.4.1, the real composition may be lower than reported. This could help explain the differences between experiments 1–3 and 4–6, which are repetitions of the same conditions, but in which experiments 1 and 4 were performed with a less fresh ethanol bottle.

Furthermore, there is a noticeable variation in the predicted values between experiments 1–7, which correspond with those in which pure ethanol and water mixed at different flowrates. This was not the expected behaviour, since the diffusion coefficient is only dependent on concentration and temperature. These differences are probably consequence of the obstacles encountered

during the experimental data collection, which were different for each case, explaining the inconsistency. Unfortunately, the high number of overlapping factors that impacted the data collection renders impossible finding a specific culprit for the error in each particular case.

The spread in the recovered value for the measurements at varying flowrate obscures the perception of the evolution of the predicted diffusion coefficient following the same trend seen in literature. Out of these, experiment 7 presents the least amount of inaccuracies, which was then translated to a considerably clean experimental composition map. Moreover, this experiment recovers the lowest prediction for the diffusion coefficient within the 1–7 experiment range. Thus, under the assumption that this value is the most accurate out of all of these, the predicted values do seem to mostly follow the same trend as literature data.

Overall, despite the presence of error and the obstacles outlined in Section 5.3.2, the recovered diffusion coefficients are relatively close to the expected values. While there is room for optimisation of the experimental setup, this proves the potential that this setup holds for the accurate estimation of diffusion coefficients. Moreover, it provides a data-rich composition map that could also serve as the ground truth from which to inform other mass transfer models.

5.4.3 Velocity scaling

To conclude this discussion, a sensitivity analysis studying the effect of variations in the velocity profile has been performed for experiment 7. Its results have been outlined in Figures 5.37(a) and (b), which respectively present a comparison between case studies of selected composition profiles and the evolution of their predicted diffusion coefficients with different scaling factors applied to the velocity.

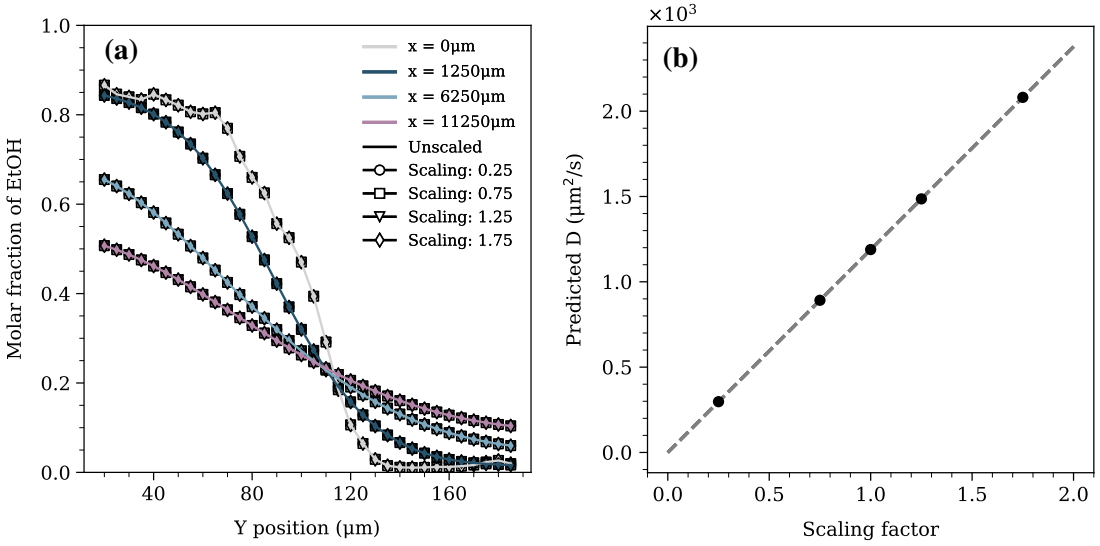


FIGURE 5.37: Results of the velocity sensitivity analysis conducted for experiment 7. (a) Selected composition profiles for all studied scaling factors. (b) Variation of the predicted diffusion coefficient based on the applied scaling factor.

The composition profiles of Figure 5.37(a) follow the expected trend, since, as explained before, there is only one set of profiles that minimise the loss function, and what varies is only the value of the diffusion coefficient required to achieve them.

As for Figure 5.37(b), the observed trend follows a perfect straight line, yielding a $R^2 = 1$. This was also expected, since including convection in the system allows it to become stationary, and therefore makes the temporal derivative of composition in the continuity equation drop to zero. This implies that the diffusive and convective fluxes are equal to each other, and thus that the diffusion coefficient will show a proportional change when scaling the entire velocity profile. The trendline itself is notably steep, indicating that a change in velocity of 10% could make the predicted diffusion coefficient change by approximately $150\,\mu m^2\,s^{-1}$. In order to recover the literature value for the diffusion coefficient, in this case the velocity needs to be a 35% of its true value; however, the difference will be significantly lower for experiments 8–12.

This analysis proves that having flowrate fluctuations in the system, which could be caused by air bubbles or by the wetting problems mentioned in Section 5.3.2, could have had a significant impact in the measurements. Moreover, a more refined approximation of the velocity profile may have increased the accuracy of the predicted diffusion coefficients.

5.5 Conclusions

This work proposed an experimental methodology capable of isolating diffusion as the dominant mechanism contributing to mass transfer. Based on the coupling of Raman microscopy and microfluidics, it allows to acquire mixing data capable of qualitatively validating the advanced mass transfer models proposed in Chapters 3 and 4. The captured data takes the form of composition mixing maps that, in principle, constitute an exact representation of the behaviour of the system. This methodology was applied to different ethanol–water binary systems, with the resulting mixing maps following the expected qualitative trends. Moreover, an in-silico optimisation framework was built, leveraging the experimental data to estimate the benchmark parameters of mass transfer models. In particular, it was validated through the estimation of Fickian diffusion coefficients in the studied ethanol–water system. These predicted coefficients remained within one order of magnitude of those reported in the literature using different methods, despite having to contend with the several inevitable sources of experimental inaccuracy. This, in combination with the successful isolation of diffusion as the mass transfer mechanism, indicates the great potential that this platform holds for, in the future, qualitatively and quantitatively validating the outcomes of the advanced mass transfer models developed in this thesis. Finally, to improve the accuracy of the experimental results, the best option would be to choose a rectangular cross-sectional profile for the microfluidic channel. This would eliminate the dependency of the signal intensity with the channel position, and thus reduce the uncertainty in the channel-edge detection process, as well as eliminate the need for a different PLS model at each y point of the channel. Other elements that could mitigate the identified uncertainty sources are the degassing the solutions prior to filling up the system to minimise entrapped gas; a more stable microfluidic setup; and a more appropriate microfluidic pump for the selected flowrate.

Chapter 6

Conclusions and future work

6.1 Conclusions

This thesis has explored the development of a diffusion model capable of simulating spontaneous LLPS through the incorporation of a non-local gradient term into the free energy formulation, and the development of an experimental platform through which to isolate diffusion as the dominant mass transfer mechanism. The main conclusions of this work are summarised here, in relation to the initial objectives mentioned in Section 1.1.

- **To study the effect of the non-local term on diffusion in a binary system.**

  The non-local gradient term was proven to successfully reproduce diffusive mixing in a homogeneous system and to enable the modelling of spontaneous LLPS in the system, which also takes place via diffusion. It therefore overcomes the limitations of previous models, such as Fick's law and Maxwell-Stefan, allowing the exploration of composition trajectories throughout the entire phase diagram. Upon further analysis of the effect of the gradient term at different locations in the system, it was established that it bears the greatest effect on the composition profiles at, and close to, the interfacial region, whereas the boundaries of the system barely changed their trajectory when increasing the value of the gradient coefficient. Moreover, during the development of this model, it was found that the chemical potential expression used in several relevant studies in literature did not comply with the condition for chemical equilibrium, not leading to flat chemical potential profiles for the final system. It was possible to define a composition dependence for the interfacial free energy coefficient that allowed to comply with this condition without modifying the nondimensional continuity equation, and thus not altering the mass transfer dynamics that had been developed and proved in the literature. It was found that other inaccurate definitions of this coefficient predicted a spike of chemical potential upon the two streams getting in contact, whereas this more accurate definition did not predict this feature. Thus, this highlights the importance of correctly describing the system to avoid reaching erroneous conclusions regarding the times and regions where nucleation may occur, as well as the corresponding nucleation and growth rates, which are dependent on supersaturation. Lastly, the developed model was used to simulate a system under crash-cooling conditions, leading to the observation of different metastable states and phase coalescence following the initial phase split. It was observed that the coalescence of a phase triggers a spike

in the chemical potential, and consequently, on the supersaturation of the system, which in certain physical systems could lead to crystal nucleation competing with the already occurring liquid-liquid phase separation.

- **To study the effect of the non-local term on diffusion in a ternary system, aimed towards antisolvent crystallisation.**

  The non-local interfacial term was proven to successfully enable the simulation of spontaneous liquid-liquid phase separation in a ternary antisolvent crystallisation system, thus allowing the description of the mass transfer pathways followed by the system across the entire ternary phase diagram. These pathways were found to be significantly nonlinear, with the evidence suggesting this is consequence of both the non-ideal API-antisolvent interactions causing the API to undergo uphill diffusion towards the solvent-rich bulk phase, as well as of the different diffusivity ratios between species. Additionally, these nonlinear trajectories were found to lead the system into the miscibility gap on occasion. This proves how neglecting them could lead to undesired LLPS or unexpected properties of the crystal product, due to the system crossing into unexpected regions of the ternary diagram. Upon entering the spinodal region, a physical system would immediately undergo liquid-liquid phase separation, and thus the modelling of these systems was only possible because of the incorporation of the gradient term. Low values of the gradient coefficient allowed to recover the physical separated configuration, whereas larger values led to a homogeneously mixed final system due to the finite nature of the system. Moreover, it was found that in a phase-split system the solvent accumulated at the interface, leading to this region deviating from the tie line despite the coexistence compositions of the bulk phases maintaining the expected symmetry. Examining the supersaturation, it was found that the incorporation of the interfacial free energy term into a system representative of a typical antisolvent crystallisation process predicted a larger spike at the interface upon the first contact between the two streams, leading to the interfacial region becoming supersaturated. Moreover, it was found that the extent to which supersaturation occurred is also dependent on both the API-antisolvent non-ideality, since it affects the placement of the solubility curve in the diagram, and the diffusivity between species, since this alters the composition pathways observed during diffusion. Overall, these results prove that neglecting the gradient contribution to the free energy can lead to erroneous predictions of supersaturation, and thus, of the time and place where nucleation could occur, and of nucleation and growth rates.

- **To develop an experimental framework isolating diffusion as the dominant mass transfer mechanism in order to facilitate the qualitative validation of the predictions of the proposed model.**

  The developed platform leveraged the advantageous hydrodynamics that a microfluidic geometry presents for this purpose, in combination with Raman microscopy for the quantitative translation of spectra into composition. This platform was applied to different ethanol–water binary systems, proving able to capture composition mixing maps across

the microfluidic channel that, in principle, constitute an exact representation of the composition values in the physical system. While there were several experimental sources of error outside the author's control which compromised the quantitative accuracy of the experimental measurements, these maps still followed the expected qualitative trends. Moreover, an in-silico optimisation framework was built, leveraging the captured data to help inform benchmark parameters of mass transfer models. It was tested through the estimation of Fickian diffusion coefficients in ethanol–water systems, with the predicted values remaining on the same order of magnitude as those available in literature. It was found that the velocity profile of the experimental system exerted the largest effect on the predicted diffusion coefficient, highlighting the importance of accuracy in its measurement. Despite the encountered challenges, this experimental platform successfully isolated diffusion as the dominant contributing mechanism to mass transfer in the system. Thus, in the future it could serve to qualitatively validate the outcomes of the advanced mass transfer models developed in this work, helping elucidate whether the predictions of certain events, such as liquid-liquid phase separation, are observed during the mixing.

6.2 Future work

Upon reflection on the limitations and potential areas of improvement of the results attained during the completion of this PhD, the following recommendations are provided for future scientists wanting to build upon this work. The first section presented is applicable to both the development of the binary and the ternary models, whereas the second one focuses on the limitations and recommendations unique to the ternary case. Lastly, the third section contains the advice pertaining to the developed experimental framework.

6.2.1 General model development

The one-parameter Margules activity model was selected for this work because it is the simplest model that allowed to capture non-ideal interactions. However, the application of the developed mass transfer model to a real system may require its substitution by a more advanced activity model, such as NRTL or UNIQUAC. The modularity of the model should avoid this transition affecting any other terms in the free energy definition.

The simulations conducted in this work were limited to a one-dimensional mesh. However, the gradient term may show anisotropy, that is, unsymmetrical behaviour across dimensions. Therefore, investigating the performance of the model in 2D or 3D could be an area of interest for future exploration.

The mesh size considered in this work was not large enough to allow the nondimensional gradient coefficients to take values consistent with what a physical system would require, due to a constraint in the computing power and time required to complete each simulation. Future work conducted in this area would benefit from implementing an adaptive mesh, in order to obtain both a sufficient resolution at the interfacial region and a coarser mesh at the boundaries of the system, where the effect of the gradient term fades.

Spontaneous phase separation occurs because the system is linearly unstable to all fluctuations, which are a normal occurrence in a system due to thermal noise. However, the present work relied on the small numerical fluctuations inherent to computation to provide this noise. While this same method has been applied across a wide range of literature [10, 121, 123], it would be beneficial to incorporate a thermal noise term for enhanced physical accuracy.

The proposed model did not consider the effect of temperature on diffusion. Upon mixing, certain species may release or consume heat, which will affect the value of the diffusion coefficient and the value of the binary interaction parameters, and thus, the shape and location of the miscibility gap. Therefore, incorporating this effect may result in a change in the pathways across the ternary phase diagram; it could potentially show that a system predicted to cross into the miscibility gap in this work does not actually do so, or vice versa. Hence, incorporating the effect of temperature into the governing equations of the system should be a priority for future development.

6.2.2 Development of a ternary model

The binary model developed in Chapter 3 was able to find a form of the composition dependence for the interfacial free energy coefficient, κ, that allowed to recover a flat chemical potential in equilibrium for a phase-split system; however, due to time constraints it was not possible to do the same for the ternary model of Chapter 4. Appendix F summarises the current ideas of the author on the topic. While accuracy of the mass transfer predictions were not compromised by this limitation, finding the form of the composition dependence that complies with this condition may lead to important insights on the theory. Therefore, it should be explored in the future.

The binary model possesses only two parameters that affect the mass transfer dynamics: the degree of non-ideality between species and the interfacial free energy coefficient. However, introducing a third species substantially increased the number of input parameters, now grown from two to seven: $D_{10}, D_{20}, D_{12}, \kappa_{10}, \kappa_{20}, \kappa_{12}, A$. Due to time and length considerations, certain constraints were applied to their values in this work. However, a deeper understanding of their effect upon mass transfer may be attained by performing more simulations for a wider combination of parameters. Moreover, it would be beneficial to test the effect of the weight given to the counter-species gradient term: κ_{aa}/κ_{ab} and κ_{bb}/κ_{ab}.

One of the assumptions made to simplify the system was that the interactions between solvent and antisolvent, as well as API and solvent, were ideal. While in a physical antisolvent system it is not expected to find non-idealities large enough to cause a miscibility gap between either of these two pairs, it may not be uncommon for them to show a small degree of non-ideality. Therefore, future work should consider this, and study the effect that non-idealities in the interactions of these other two pairs have upon mass transfer.

6.2.3 Leveraging microfluidics and Raman microscopy to isolate diffusion

The semicircular cross-sectional profile of the microfluidic channel used in this work resulted in the recovery of different Raman intensities across the channel height, due to the different amounts

of liquid passing through them. This had to be dealt with through the development and training of one PLS model per node measured, forcing the same resolution and points to be used for any test or experiment. This could be avoided altogether by switching to a microfluidic channel with a rectangular cross-sectional profile.

The velocity profile was found to be one of the most important factors in the determination of the diffusion coefficient between solvents. It is highly sensitive to the presence of gas bubbles inside the system, and thus every precaution should be taken to avoid them. For this purpose, it is recommended to degas any solutions prior to loading them in the system, and to change the tubing connecting the syringes with the channel regularly. In this work, this was also caused by the gas pockets that appeared due to wetting problems on the channel wall. However, this is a limitation specific to the microfluidic channel used, and is not expected to pose a problem for other scientists.

On the topic of velocity, in this work it was approximated through the quotient between flowrate and cross-sectional area. This was chosen because the estimation of the velocity profile through the Hagen-Poiseuille equation led to a significant overestimation of the mean velocity, which in turn considerably increased the error in the estimated diffusion coefficient. However, this approximation does not consider the effect of friction against the walls, which will naturally cause a lower velocity near the top and bottom of the channel. This could be causing an increased error in the estimation of the diffusion coefficient. Therefore, it is recommended that more suitable methods be investigated for the determination of the velocity profile inside the microchannel.

The confocal Raman microscope employed to conduct this work presented several challenges. Among the most relevant were its inaccuracies in the software visualisation when showing the point in space it was measuring, that led to the need to develop a bespoke procedure relying exclusively on the Raman signal. In addition, during the latter experiments, the system was unable to auto-calibrate without a very specific sequence of prior steps. These hurdles are specific to the instrument available for this work, and are not expected to become problematic for any future scientists.

To enhance the robustness of the PLS calibration model, it would be advantageous to expand the calibration dataset through more measurements, as well as validate the composition of the stock solutions used to build it through a suitable method, such as Karl Fischer titration.

The extremely low flowrates employed in this work were observed to cause an oscillation of the interface at the entrance to the channel. This will most likely have contributed to inaccuracies in the measured composition in that region, since the oscillation period was shorter than the Raman collection time at a particular point. To mitigate the effect of this oscillation, it is recommended to perform several repeats of the same measurement. As an alternative, this oscillation could be avoided altogether if working at larger flowrates. To ensure a sufficient degree of mixing is achieved, a longer microfluidic channel would have to be employed. These measures could be implemented without making the experimental time prohibitively long by reducing the range of wavenumbers measured, coarsening or reducing the grid, or performing the repeated experiments on separate days; this would also help quantify the reproducibility of the results.

Lastly, while the Fickian interdiffusion coefficient has been predicted under the assumption that it does not depend on composition, this data could be leveraged to inform a more complex model, such as Fickian diffusion incorporating a composition dependence in D, Maxwell-Stefan, or, qualitatively, CaHiMaS. The qualitative validation of CaHiMaS would benefit from the selection of a system that exhibits a miscibility gap, in the case of binary systems; an example of this could be salicylic acid–n-heptane, as shown in Chapter 2. Similarly, the validation of the ternary model requires extending the system to three components.

Bibliography

[1] S. Jia, P. Yang, Z. Gao, Z. Li, C. Fang, and J. Gong, "Recent progress in antisolvent crystallization", *CrystEngComm*, 24 (17 2022), 3122–3135, DOI: 10.1039/D2CE00059H.

[2] Z. Gao, S. Rohani, J. Gong, and J. Wang, "Recent Developments in the Crystallization Process: Toward the Pharmaceutical Industry", *Engineering*, 3, 3 (2017), 343–353, DOI: https://doi.org/10.1016/J.ENG.2017.03.022.

[3] Y. Yang and Z. K. Nagy, "Model-Based Systematic Design and Analysis Approach for Unseeded Combined Cooling and Antisolvent Crystallization (CCAC) Systems", *Crystal Growth & Design*, 14, 2 (2014), 687–698, DOI: 10.1021/cg401562t.

[4] A. Lewis, M. Seckler, H. Kramer, and G. van Rosmalen, "Precipitation and anti-solvent crystallization", *Industrial Crystallization: Fundamentals and Applications*, Cambridge University Press, 2015, 234–260.

[5] A. Haghighizadeh, H. Mahdavi, and O. Rajabi, "Recent Progress in Antisolvent Crystallization of Pharmaceuticals with a Focus on the Membrane-Based Technologies", *Chemical Engineering & Technology*, 47, 5 (2024), 750–763.

[6] Z. Meng, Y. Huang, S. Cheng, and J. Wang, "Investigation of Oiling-Out Phenomenon of Small Organic Molecules in Crystallization Processes: A Review", *ChemistrySelect*, 5, 26 (2020), 7855–7866, DOI: https://doi.org/10.1002/slct.202001255.

[7] B. Szilagyi, A. Majumder, and Z. K. Nagy, "Fundamentals of Population Balance Based Crystallization Process Modeling", *The Handbook of Continuous Crystallization*, ed. by N. Yazdanpanah and Z. K. Nagy, The Royal Society of Chemistry, Feb. 2020, DOI: 10.1039/9781788013581-00051.

[8] R. Miller, J. Sefcik, and L. Lue, "Modeling Diffusive Mixing in Antisolvent Crystallization", *Cryst. Growth Des.*, 22 (2022), 2192–2207, DOI: 10.1021/acs.cgd.1c01269.

[9] Z. Zhang, J.-F. Audibert, W. Wang, V. Génot, S. Y. Park, A. Spasojević-de Biré, and R. B. Pansu, "Thermodynamics of Oiling-Out in Antisolvent Crystallization. II. Diffusion toward Spinodal Decomposition", *Crystal Growth & Design*, 24, 8 (2024), 3501–3516, DOI: 10.1021/acs.cgd.4c00231.

[10] Y. Tsugawa, K. Kadota, M. Yoshida, and Y. Shirakawa, "Utilizing the phase-field method to investigate liquid-liquid phase separation in the ternary system of water/ethanol/butylparaben", *Chemical Engineering Research and Design*, 210 (2024), 339–351, DOI: https://doi.org/10.1016/j.cherd.2024.08.040.

[11] R. Krishna, "Uphill diffusion in multicomponent mixtures", *Chem. Soc. Rev.*, 44 (10 2015), 2812–2836, DOI: 10.1039/C4CS00440J.

[12] J. C. Maxwell, "On the Dynamical Theory of Gases", *Philosophical Transactions of the Royal Society of London*, 157 (1867), 49–88.

[13] J. Stefan, "Über das Gleichgewicht und die Bewegung, insbesondere die Diffusion von Gasgemengen", *Sitzber. Akad. Wiss. Wien*, 63 (1871), 63–124.

[14] J. W. Cahn and J. E. Hilliard, "Free Energy of a Nonuniform System. I. Interfacial Free Energy", *The Journal of Chemical Physics*, 28 (2 1958), 267, DOI: 10.1063/1.1744102.

[15] J. Ulrich and T. Stelzer, "Crystallization", *Kirk-Othmer Encyclopedia of Chemical Technology*, John Wiley '&' Sons, Ltd, 2011, 1–63, DOI: 10.1002/0471238961.0318251918152119.A01.PUB3.

[16] A. S. Myerson, D. Erdemir, and A. Y. Lee, eds., *Handbook of Industrial Crystallization*, 3rd, Cambridge University Press, 2019, DOI: 10.1017/9781139026949.

[17] K. Carpenter and W. Wood, "Industrial crystallization for fine chemicals", *Advanced Powder Technology*, 15, 6 (2004), 657–672.

[18] J. B. Lee, G.-E. Kim, S.-Y. Kim, B.-C. Park, J.-H. Cha, J.-W. Kwak, Y.-J. Kim, I.-P. Hong, Y.-P. Jeon, S. G. Jeon, et al., "A Comprehensive Review of Applied Crystallization Methods in Industrial Waste Recycling and Perspectives Toward Advanced Applications", *Journal of Environmental Chemical Engineering* (2026), 122515.

[19] Q. Guan, Y. Li, Y. Zhong, W. Liu, J. Zhang, X. Yu, R. Ou, and G. Zeng, "A review of struvite crystallization for nutrient source recovery from wastewater", *Journal of Environmental Management*, 344 (2023), 118383, DOI: https://doi.org/10.1016/j.jenvman.2023.118383.

[20] W. Mu and C. Chen, *Crystallization of High-Performance Metallic Materials*, 2025.

[21] R. L. Earle, *Unit operations in food processing*, Elsevier, 1983, chap. Contact-equilibrium separation processes, 116–142.

[22] L. Yu and S. Reutzel-Edens, "CRYSTALLIZATION | Basic Principles", *Encyclopedia of Food Sciences and Nutrition (Second Edition)*, ed. by B. Caballero, Second Edition, Oxford: Academic Press, 2003, 1697–1702, DOI: https://doi.org/10.1016/B0-12-227055-X/00313-8.

[23] A. Lewis, M. Seckler, H. Kramer, and G. Van Rosmalen, *Industrial crystallization: fundamentals and applications*, Cambridge University Press, 2015.

[24] M. Ammar, S. Ashraf, D. A. Gonzalez-Casamachin, and J. Baltrusaitis, "Sustainable by (crystal) design: novel materials for agriculture via active ingredient cocrystallization", *RSC Sustainability*, 3, 2 (2025), 781–803.

[25] X. Niu, R. Yang, H. Zhang, and J. Yang, "Crystal engineering in the development of improved pesticide products", *Advanced Agrochem*, 1, 1 (2022), 39–60.

[26] L. E. Hatcher, A. J. Burgess, P. Payne, and C. C. Wilson, "From structure to crystallisation and pharmaceutical manufacturing: the CSD in CMAC workflows", *CrystEngComm*, 22, 43 (2020), 7475–7489.

[27] J. Chen, B. Sarma, J. M. Evans, and A. S. Myerson, "Pharmaceutical crystallization", *Cryst. Growth Des.*, 11, 4 (2011), 887–895.

[28] Mettler Toledo, *Crystallization & Precipitation*, URL: https://www.mt.com/ch/en/home/applications/L1_AutoChem_Applications/L2_Crystallization.html.

[29] A. H. Bari, A. Chawla, and A. B. Pandit, "Sono-crystallization kinetics of K2SO4: Estimation of nucleation, growth, breakage and agglomeration kinetics", *Ultrasonics Sonochemistry*, 35 (2017), 196–203, DOI: https://doi.org/10.1016/j.ultsonch.2016.09.018.

[30] B. Biscans, "Impact attrition in crystallization processes. Analysis of repeated impacts events of individual crystals", *Powder Technology*, 143-144 (2004), 264–272, DOI: https://doi.org/10.1016/j.powtec.2004.04.025.

[31] R. Censi and P. D. Martino, "Polymorph Impact on the Bioavailability and Stability of Poorly Soluble Drugs", *Molecules*, 20 (10 Oct. 2015), 18759, DOI: 10.3390/MOLECULES201018759.

[32] J. W. Mullin, "Crystallization and Precipitation", *Ullmann's Encyclopedia of Industrial Chemistry*, vol. 10, Wiley-VCH Verlag GmbH 'I&' Co. KGaA, 2012, 581–630, DOI: 10.1002/14356007.B02_03.

[33] R. Kumar, A. K. Thakur, N. Banerjee, A. Kumar, G. K. Gaurav, and R. K. Arya, "Liquid antisolvent crystallization of pharmaceutical compounds: current status and future perspectives", *Drug Delivery and Translational Research*, 13, 2 (2023), 400–418.

[34] N. Abzan, M. Kharaziha, S. Labbaf, and N. Saeidi, "Modulation of the mechanical, physical and chemical properties of polyvinylidene fluoride scaffold via non-solvent induced phase separation process for nerve tissue engineering applications", *Eur. Polym. J.*, 104 (2018), 115–127, DOI: 10.1016/J.EURPOLYMJ.2018.05.004.

[35] C. T.-C. Wan, R. R. Jacquemond, Y.-M. Chiang, K. Nijmeijer, F. R. Brushett, A. Forner-Cuenca, C. T.-C. Wan, Y m Chiang, F. R. Brushett, R. R. Jacquemond, K Nijmeijer, and A Forner-Cuenca, "Non-Solvent Induced Phase Separation Enables Designer Redox Flow Battery Electrodes", *Advanced Materials*, 33 (16 2021), 2006716, DOI: 10.1002/ADMA.202006716.

[36] M. Konstantakou, D. Perganti, P. Falaras, and T. Stergiopoulos, "Anti-Solvent Crystallization Strategies for Highly Efficient Perovskite Solar Cells", *Crystals*, 7 (10 2017), 291–311, DOI: 10.3390/CRYST7100291.

[37] G. R. Guillen, Y. Pan, M. Li, and E. M. Hoek, "Preparation and characterization of membranes formed by nonsolvent induced phase separation: a review", *Industrial & Engineering Chemistry Research*, 50, 7 (2011), 3798–3817.

[38] A. A. Lonare and S. R. Patel, "Antisolvent Crystallisation of Poorly Water Soluble Drugs", *International Journal of Chemical Engineering and Applications*, 4 (5 2013), 337–341.

[39] H. Takiyama, T. Minamisono, Y. Osada, and M. Matsuoka, "Operation design for controlling polymorphism in the anti-solvent crystallization by using ternary phase diagram", *Chemical Engineering Research and Design*, 88, 9 (2010), 1242–1247.

[40] H. Digarse and D. Sarkar, "Production of the metastable δ-polymorphic form of pyrazinamide by isothermal internal seeding anti-solvent crystallization", *Journal of Crystal Growth*, 526 (2019), 125245.

[41] Z. Ma, C. Li, R. Wu, R. Chen, and Z. Gu, "Preparation and characterization of superfine ammonium perchlorate (AP) crystals through ceramic membrane anti-solvent crystallization", *Journal of Crystal Growth*, 311, 21 (2009), 4575–4580, DOI: https://doi.org/10.1016/j.jcrysgro.2009.06.008.

[42] X.-S. Li, J.-X. Wang, Z.-G. Shen, P.-Y. Zhang, J.-F. Chen, and J. Yun, "Preparation of uniform prednisolone microcrystals by a controlled microprecipitation method", *International Journal of Pharmaceutics*, 342 (1-2 2007), 26–32, DOI: 10.1016/J.IJPHARM.2007.04.025.

[43] D. Chen, D. Singh, K. K. Sirkar, and R. Pfeffer, "Porous Hollow Fiber Membrane-Based Continuous Technique of Polymer Coating on Submicron and Nanoparticles via Antisolvent Crystallization", *Ind. Eng. Chem. Res.*, 54 (19 2015), 5237–5245, DOI: 10.1021/ACS.IECR.5B00155.

[44] D. Chen, D. Singh, K. K. Sirkar, and R. Pfeffer, "Continuous synthesis of polymer-coated drug particles by porous hollow fiber membrane-based antisolvent crystallization", *Langmuir*, 31 (1 2015), 432–441, DOI: 10.1021/LA503179T/ASSET/IMAGES/LA503179T.SOCIAL.JPEG_V03.

[45] Z. Yu, R. Tan, and P. Chow, "Effects of operating conditions on agglomeration and habit of paracetamol crystals in anti-solvent crystallization", *Journal of Crystal Growth*, 279, 3-4 (2005), 477–488.

[46] A. Paulino, G. Rauber, C. Campos, M. Maurício, R. De Avillez, S. Cuffini, and S. Cardoso, "Hollow crystal anti-solvent preparation process as a promising technique to improve dissolution of poorly soluble drugs", *Journal of crystal growth*, 366 (2013), 76–81.

[47] D. Xia, M. Ouyang, J. X. Wu, Y. Jiang, H. Piao, S. Sun, L. Zheng, J. Rantanen, F. Cui, and M. Yang, "Polymer-mediated anti-solvent crystallization of nitrendipine: Monodispersed spherical crystals and growth mechanism", *Pharmaceutical Research*, 29 (1 2012), 158–169, DOI: 10.1007/S11095-011-0522-6/FIGURES/9.

[48] V. Bhamidi, S. H. Lee, G. He, P. S. Chow, R. B. H. Tan, C. F. Zukoski, and P. J. A. Kenis, "Antisolvent Crystallization and Polymorph Screening of Glycine in Microfluidic Channels Using Hydrodynamic Focusing", *Cryst. Growth Des.*, 15, 7 (2015), 3299–3306, DOI: 10.1021/acs.cgd.5b00420.

[49] M. Knox, M. Trifkovic, and S. Rohani, "Combining anti-solvent and cooling crystallization: Effect of solvent composition on yield and meta stable zone width", *Chemical Engineering Science*, 64, 16 (2009), 3555–3563, DOI: https://doi.org/10.1016/j.ces.2009.04.045.

[50] M. Lenka and D. Sarkar, "Combined cooling and antisolvent crystallization of l-asparagine monohydrate", *Powder Technology*, 334 (2018), 106–116, DOI: https://doi.org/10.1016/j.powtec.2018.04.038.

[51] C. Lindenberg, M. Krättli, J. Cornel, M. Mazzotti, and J. Brozio, "Design and Optimization of a Combined Cooling/Antisolvent Crystallization Process", *Crystal Growth & Design*, 9, 2 (Dec. 2008), 1124–1136, DOI: 10.1021/cg800934h.

[52] P. H. Karpiński and J. Bałdyga, "Batch Crystallization", *Handbook of Industrial Crystallization*, ed. by A. S. Myerson, D. Erdemir, and A. Y. Lee, Cambridge University Press, 2019, 346–379.

[53] J. McGinty, N. Yazdanpanah, C. Price, J. H. ter Horst, and J. Sefcik, "Nucleation and Crystal Growth in Continuous Crystallization", *The Handbook of Continuous Crystallization*, ed. by N. Yazdanpanah and Z. K. Nagy, The Royal Society of Chemistry, Feb. 2020, DOI: 10.1039/9781788013581-00001.

[54] J. H. ter Horst, C. Schmidt, and J. Ulrich, "32 - Fundamentals of Industrial Crystallization", *Handbook of Crystal Growth (Second Edition)*, ed. by P. Rudolph, Second Edition, Handbook of Crystal Growth, Boston: Elsevier, 2015, 1317–1349, DOI: https://doi.org/10.1016/B978-0-444-63303-3.00032-8.

[55] A. J. Alvarez and A. S. Myerson, "Continuous plug flow crystallization of pharmaceutical compounds", *Crystal Growth & Design*, 10, 5 (2010), 2219–2228.

[56] J. Jang, W.-S. Kim, T. S. Seo, and B. J. Park, "Over a decade of progress: Crystallization in microfluidic systems", *Chemical Engineering Journal*, 495 (2024), 153657.

[57] H.-h. Shi, Y. Xiao, S. Ferguson, X. Huang, N. Wang, and H.-x. Hao, "Progress of crystallization in microfluidic devices", *Lab on a Chip*, 17, 13 (2017), 2167–2185.

[58] C. for Drug Evaluation and Research, *Guidance for Industry PAT - A Framework for Innovative Pharmaceutical Development, manufacturing, and Quality Assurance*, Food and Drug Administration, 2004.

[59] E. M. Agency, *ICH Topic Q7. Good Manufacturing Practice for Active Pharmaceutical Ingredients*, European Medicines Agency, 2000.

[60] A. S. Rathore and H. Winkle, "Quality by design for biopharmaceuticals", *Nat. Biotechnol.*, 27 (1 2009), 26–34, DOI: 10.1038/NBT0109-26.

[61] C. L. Mustoe, A. J. Turner, S. J. Urwin, I. Houson, H. Feilden, D. Markl, M. M. Al Qaraghuli, M. W. Chong, M. Robertson, A. Nordon, B. F. Johnston, C. J. Brown, J. Robertson, C. Adjiman, H. Batchelor, B. Benyahia, M. Bresciani, C. L. Burcham, J. Cardona, C. Cottini, A. S. Dunn, D. Fradet, G. W. Halbert, M. Henson, P. Hidber, M. Langston, Y. S. Lee, W. Li, J. Mantanus, J. McGinty, B. Mehta, T. Naz, S. Ottoboni, E. Prasad, P.-O. Quist, G. K. Reynolds, C. Rielly, M. Rowland, W. Schlindwein, S. L. Schroeder, J. Sefcik, E. Settanni, H. Siddique, K. Smith, R. Smith, J. S. Srai, A. A. Thorat, A. Vassileiou, and A. J. Florence, "Quality by digital design to accelerate sustainable medicines development", *International Journal of Pharmaceutics*, 681 (2025), 125625, DOI: https://doi.org/10.1016/j.ijpharm.2025.125625.

[62] I. Houson, H. Siddique, M. W. Chong, M. Robertson, A. J. Turner, A. Nordon, A. Osman, A. Galindo, A. S. Dunn, B. Johnston, B. Benyahia, C. J. Brown, C. L. Mustoe, C. J. Price, C. D. Reilly, C. Adjiman, G. Jackson, E. Prasad, G. Halbert, H. Feilden, J. Sefcik, J. McGinty, J. Robertson, K. Smith, M. Al-Attili, M. McGowan, M. Siddique, M. Pathan, N. Rajoub, N. Hamilton, R. Feeney, S. Brown, S. J. Urwin, T. Bernet, T. Pickles, W. Li, and A. J. Florence, "Quality by digital design in action: a workflow for crystallisation and isolation", *International Journal of Pharmaceutics*, 686 (2025), 126343, DOI: https://doi.org/10.1016/j.ijpharm.2025.126343.

[63] C. Pirkle, L. Foguth, S. Brenek, K. Girard, and R. Braatz, "Computational Fluid Dynamics Modeling of Mixing Effects for Crystallization in Coaxial Nozzles", *Chem. Eng. Process.: Process Intensif.*, 97 (2015), 213–232, DOI: 10.1016/j.cep.2015.07.006.

[64] P. Liu, L. Yang, Y. Ma, Y. Zhang, H. Wang, J. Cheng, and C. Yang, "Continuous Antisolvent Crystallization of L-Histidine: Impact of Process Parameters and Kinetic Estimation", *Industrial & Engineering Chemistry Research*, 63, 6 (2024), 2831–2841.

[65] M. Thorson, S. Goyal, Y. Gong, G. Zhang, and P. Kenis, "Microfluidic approach to polymorph screening through antisolvent crystallization", *CrystEngComm*, 14 (2012), 2404–2412, DOI: 10.1039/C2CE06167H.

[66] Y. Qu, J. Cheng, Z.-S. Mao, and C. Yang, "A perspective review on mixing effect for modeling and simulation of reactive and antisolvent crystallization processes", *React. Chem. Eng.*, 6 (2 2021), 183–196, DOI: 10.1039/D0RE00223B.

[67] T. Pickles, V. Svoboda, I. Marziano, C. J. Brown, and A. J. Florence, "Integration of a model-driven workflow into an industrial pharmaceutical facility: supporting process development of API crystallisation", *CrystEngComm*, 26, 34 (Sept. 2024), 4678–4689, DOI: 10.1039/d4ce00358f.

[68] T. Pickles, Y. Leghrib, M. Weisshaar, M. Goncharuk, P. Timperman, T. Doherty, D. D. Ford, J. Moores, A. J. Florence, and C. J. Brown, "Automated scale-up crystallisation DataFactory for model-based pharmaceutical process development: a Bayesian case study", *Digital Discovery*, 4, 8 (Aug. 2025), 2025–2032, DOI: 10.1039/d4dd00406j.

[69] H. Groen and K. J. Roberts, "Nucleation, Growth, and Pseudo-Polymorphic Behavior of Citric Acid As Monitored in Situ by Attenuated Total Reflection Fourier Transform Infrared Spectroscopy", *The Journal of Physical Chemistry B*, 105, 43 (2001), 10723–10730, DOI: 10.1021/jp011281.

[70] I. de Albuquerque and M. Mazzotti, "Crystallization Process Design Using Thermodynamics To Avoid Oiling Out in a Mixture of Vanillin and Water", *Cryst. Growth Des.*, 14, 11 (2014), 5617–5625, DOI: 10.1021/cg500904v.

[71] W. H. Lin, Z. Q. Yu, P. S. Chow, and R. B. H. Tan, "The Crystallization of Active Pharmaceutical Ingredients with Low Melting Points in the Presence of Liquid–Liquid Phase Separation", *Crystals*, 11 (11 2021), 1326–1336, DOI: 10.3390/CRYST11111326.

[72] S. Zhou, Z. Cen, D. Han, B. Zhang, and J. Gong, "Oiling-Out in Industrial Crystallization of Organic Small Molecules: Mechanisms, Characterization, Regulation, and Applications", *Crystal Research and Technology*, 59, 8 (2024), 2400092.

[73] S. Veesler, E. Revalor, O. Bottini, and C. Hoff, "Crystallization in the presence of a liquid-liquid phase separation", *Organic process research & development*, 10, 4 (2006), 841–845.

[74] I. de Albuquerque and M. Mazzotti, "Influence of Liquid-Liquid Phase Separation on the Crystallization of L-Menthol from Water", *Chemical Engineering & Technology*, 40, 7 (2017), 1339–1346.

[75] M. Takasuga and H. Ooshima, "Control of crystal size during oiling out crystallization of an API", *Crystal Growth & Design*, 14, 11 (2014), 6006–6011.

[76] M. Takasuga and H. Ooshima, "Control of crystal aspect ratio and size by changing solvent composition in oiling out crystallization of an active pharmaceutical ingredient", *Crystal Growth & Design*, 15, 12 (2015), 5834–5838.

[77] E. Favvas and A. C. Mitropoulos, "What is spinodal decomposition", *J. Eng. Sci. Technol. Rev*, 1, 1 (2008), 25–27.

[78] D. Ramkrishna and M. R. Singh, "Population Balance Modeling: Current Status and Future Prospects", *Annual Review of Chemical and Biomolecular Engineering*, 5, Volume 5, 2014 (2014), 123–146, DOI: https://doi.org/10.1146/annurev-chembioeng-060713-040241.

[79] H. M. Omar and S. Rohani, "Crystal Population Balance Formulation and Solution Methods: A Review", *Crystal Growth & Design*, 17, 7 (June 2017), 4028–4041, DOI: 10.1021/acs.cgd.7b00645.

[80] Y. Qu, J. Cheng, Z.-S. Mao, and C. Yang, "A perspective review on mixing effect for modeling and simulation of reactive and antisolvent crystallization processes", *React. Chem. Eng.*, 6 (2 2021), 183–196, DOI: 10.1039/D0RE00223B.

[81] Z. Mao and C. Yang, "Micro-mixing in chemical reactors: A perspective", *Chinese Journal of Chemical Engineering*, 25 (4 2017), 381–390, DOI: 10.1016/J.CJCHE.2016.09.012.

[82] S. Zhao, C. Chen, P. Zhu, H. Xia, J. Shi, F. Yan, and R. Shen, "Passive Micromixer Platform for Size-and Shape-Controllable Preparation of Ultrafine HNS", *Ind. Eng. Chem. Res.*, 58 (2019), 16709–16718, DOI: 10.1021/acs.iecr.9b02396.

[83] Z. Wu, N.-T. Nguyen, and X. Huang, "Nonlinear diffusive mixing in microchannels: theory and experiments", *Journal of Micromechanics and Microengineering*, 14 (2004), 604–611.

[84] Z. Wu and N. T. Nguyen, "Hydrodynamic focusing in microchannels under consideration of diffusive dispersion: Theories and experiments", *Sens. Actuators B Chem.*, 107 (2 2005), 965–974, DOI: 10.1016/J.SNB.2004.11.014.

[85] S. Sullivan, B. Akpa, S. Matthews, A. Fisher, L. Gladden, and M. Johns, "Simulation of miscible diffusive mixing in microchannels", *Sens. Actuators B Chem.*, 123 (2 May 2007), 1142–1152, DOI: 10.1016/j.snb.2006.10.025.

[86] X. Liu, A. Martín-Calvo, E. McGarrity, S. K. Schnell, S. Calero, J.-M. Simon, D. Bedeaux, S. Kjelstrup, A. Bardow, and T. J. H. Vlugt, "Fick diffusion coefficients in ternary liquid systems from equilibrium molecular dynamics simulations", *Ind. Eng. Chem. Res.*, 51 (2012), 10247–10258.

[87] Y. Gaponenko, V. Gousselnikov, C. I. Santos, and V. Shevtsova, "Near-Critical Behavior of Fick Diffusion Coefficient in Taylor Dispersion Experiments", *Microgravity Sci. Technol.*, 31 (5 2019), 475–486, DOI: 10.1007/S12217-019-09736-4/FIGURES/10.

[88] G. Guevara-Carrion, R. Fingerhut, and J. Vrabec, "Fick Diffusion Coefficient Matrix of a Quaternary Liquid Mixture by Molecular Dynamics", *J. Phys. Chem*, 2020 (2022), 4527–4535, DOI: 10.1021/acs.jpcb.0c01625.

[89] T. J. dos Santos, F. W. Tavares, and C. R. Abreu, "Fick diffusion coefficients via molecular dynamics: An alternative approach in the Fourier domain", *J. Mol. Liq.*, 329 (2021), 115460, DOI: 10.1016/J.MOLLIQ.2021.115460.

[90] T. Klein, M. Piszko, C. J. Kankanamge, G. Kasapis, and A. P. Fröba, "Fick Diffusion Coefficient in Binary Mixtures of [HMIM][NTf] 2] and Carbon Dioxide by Dynamic Light Scattering and Molecular Dynamics Simulations", *J. Phys. Chem. B*, 125 (2021), 5100–5113, DOI: 10.1021/acs.jpcb.1c01616.

[91] R. Krishna, "Problems and pitfalls in the use of the Fick formulation for intraparticle diffusion", *Chem. Eng. Sci.*, 48 (5 1993), 845–861, DOI: 10.1016/0009-2509(93)80324-J.

[92] R. Taylor and R. Krishna, *Multicomponent Mass Transfer*, 1st, John Wiley & Sons, Inc., 1993, 13–26.

[93] R. Krishna and J. Wesselingh, "The Maxwell-Stefan approach to mass transfer", *Chem. Eng. Sci.*, 52, 6 (1997), 861–911, DOI: https://doi.org/10.1016/S0009-2509(96)00458-7.

[94] E. L. Cussler, *Diffusion: Mass Transfer in Fluid Systems*, 3rd, Cambridge University Press, 2009.

[95] R. Miller, J. Sefcik, and L. Lue, "Modeling Diffusive Mixing in Antisolvent Crystallization", *Crystal Growth & Design*, 22, 4 (2022), 2192–2207, DOI: 10.1021/acs.cgd.1c01269.

[96] Z. Zhang, R. Bi, J.-F. Audibert, W. Wang, S. Y. Park, A. Spasojević-de Biré, and R. B. Pansu, "Thermodynamics of Oiling-Out in Antisolvent Crystallization. I. Extrapolation of Ternary Phase Diagram from Solubility to Instability", *Crystal Growth & Design*, 24, 1 (2024), 224–237, DOI: 10.1021/acs.cgd.3c00916.

[97] M. R. Tonks and L. K. Aagesen, "The phase field method: mesoscale simulation aiding material discovery", *Annual Review of Materials Research*, 49, 1 (2019), 79–102.

[98] N. Provatas and K. Elder, *Phase-field methods in materials science and engineering*, John Wiley & Sons, 2011.

[99] S. M. Allen and J. W. Cahn, "A microscopic theory for antiphase boundary motion and its application to antiphase domain coarsening", *Acta metallurgica*, 27, 6 (1979), 1085–1095.

[100] N. Provatas, T. Pinomaa, and N. Ofori-Opoku, *Quantitative phase field modelling of solidification*, CRC Press, 2021.

[101] J. Li, D. Zheng, and W. Zhang, "Advances of phase-field model in the numerical simulation of multiphase flows: A review", *Atmosphere*, 14, 8 (2023), 1311.

[102] W. J. Boettinger, J. A. Warren, C. Beckermann, and A. Karma, "Phase-field simulation of solidification", *Annual review of materials research*, 32, 1 (2002), 163–194.

[103] P. Mathis, "Phase-field modelling of solidification microstructures", *Journal of the Indian Institute of Science*, 96, 3 (2016), 179–198.

[104] X.-l. Dong, H. Xing, K.-r. Weng, and H.-l. Zhao, "Current development in quantitative phase-field modeling of solidification", *Journal of Iron and Steel Research International*, 24, 9 (2017), 865–878.

[105] I. Steinbach, "Phase-field model for microstructure evolution at the mesoscopic scale", *Annual Review of Materials Research*, 43, 1 (2013), 89–107.

[106] D. Tourret, H. Liu, and J. LLorca, "Phase-field modeling of microstructure evolution: Recent applications, perspectives and challenges", *Progress in Materials Science*, 123 (2022), 100810.

[107] T. Q. Bui and X. Hu, "A review of phase-field models, fundamentals and their applications to composite laminates", *Engineering Fracture Mechanics*, 248 (2021), 107705.

[108] A. C. Hansen-Dörr, R. de Borst, P. Hennig, and M. Kästner, "Phase-field modelling of interface failure in brittle materials", *Computer Methods in Applied Mechanics and Engineering*, 346 (2019), 25–42.

[109] R. Cavuoto, P. Lenarda, A. Tampieri, D. Bigoni, and M. Paggi, "Phase-field modelling of failure in ceramics with multiscale porosity", *Materials & Design*, 238 (2024), 112708.

[110] Y. Yu, C. Hou, X. Zheng, and M. Zhao, "Phase field modeling for composite material failure", *Fatigue & Fracture of Engineering Materials & Structures*, 47, 11 (2024), 4176–4195.

[111] M. Xue and M. Yi, "Phase-field simulation of sintering process: A review", *Computer Modeling in Engineering & Sciences*, 140, 2 (2024), 1165.

[112] M. Yi, W. Wang, M. Xue, Q. Gong, and B.-X. Xu, "Modeling and simulation of sintering process across scales", *Archives of Computational Methods in Engineering*, 30, 5 (2023), 3325–3358.

[113] N. Bieberdorf, M. Asta, and L. Capolungo, "Grain boundary effects in high-temperature liquid-metal dealloying: a multi-phase field study", *npj computational materials*, 9, 1 (2023), 127.

[114] L. Lai, P.-A. Geslin, and A. Karma, "Microstructural pattern formation during liquid metal dealloying: Phase-field simulations and theoretical analyses", *Physical Review Materials*, 6, 9 (2022), 093803.

[115] S. J. Bohr, F. Wang, M. Metze, J. L. Vukušić, A. Sapalidis, M. Ulbricht, B. Nestler, and S. Barbe, "State-of-the-art review of porous polymer membrane formation characterization—How numerical and experimental approaches dovetail to drive innovation", *Frontiers in Sustainability*, 4 (2023), 1093911.

[116] S. Monfared, A. Ardaševa, and A. Doostmohammadi, "Multiphase-field models of tissues", *Annual Review of Condensed Matter Physics*, 17 (2025).

[117] R. D. Travasso, M. Castro, and J. C. Oliveira, "The phase-field model in tumor growth", *Philosophical Magazine*, 91, 1 (2011), 183–206.

[118] M. Fritz, "Tumor evolution models of phase-field type with nonlocal effects and angiogenesis", *Bulletin of Mathematical Biology*, 85, 6 (2023), 44, DOI: 10.1007/s11538-023-01151-6.

[119] S. Najem and M. Grant, "Phase-field model for collective cell migration", *Physical Review E*, 93, 5 (2016), 052405.

[120] A. Moure and H. Gomez, "Phase-Field Modeling of Individual and Collective Cell Migration: A. Moure, H. Gomez", *Archives of Computational Methods in Engineering*, 28, 2 (2021), 311–344.

[121] E. Petrishcheva and R. Abart, "Exsolution by spinodal decomposition in multicomponent mineral solutions", *Acta Materialia*, 60, 15 (2012), 5481–5493, DOI: https://doi.org/10.1016/j.actamat.2012.07.006.

[122] E. B. Nauman and D. Q. He, "Morphology predictions for ternary polymer blends undergoing spinodal decomposition", *Polymer*, 35, 11 (1994), 2243–2255.

[123] P. K. Inguva, P. J. Walker, H. W. Yew, K. Zhu, A. J. Haslam, and O. K. Matar, "Continuum-scale modelling of polymer blends using the Cahn–Hilliard equation: transport and thermodynamics", *Soft Matter*, 17 (23 2021), 5645–5665, DOI: 10.1039/D1SM00272D.

[124] S. Zhou, Z. Cen, D. Han, B. Zhang, and J. Gong, "Oiling-Out in Industrial Crystallization of Organic Small Molecules: Mechanisms, Characterization, Regulation, and Applications", *Crystal Research and Technology*, 59, 8 (2024), 2400092.

[125] L. Codan, S. Casillo, M. U. Babler, and M. Mazzotti, "Phase diagram of a chiral substance exhibiting oiling out. 2. Racemic compound forming ibuprofen in water", *Crystal Growth & Design*, 12, 11 (2012), 5298–5310.

[126] C. Peters, L. Wolff, S. Haase, J. Thien, T. Brands, H.-J. Koß, and A. Bardow, "Multicomponent diffusion coefficients from microfluidics using Raman microspectroscopy", *Lab on a Chip*, 17, 16 (2017), 2768–2776.

[127] C. Peters, J. Thien, L. Wolff, H.-J. Koß, and A. Bardow, "Quaternary diffusion coefficients in liquids from microfluidics and Raman microspectroscopy: cyclohexane+ toluene+ acetone+ methanol", *Journal of Chemical & Engineering Data*, 65, 3 (2019), 1273–1288.

[128] M. Colangeli, C. Giberti, and C. Vernia, "Uphill diffusions in single and multi-species systems", *Journal of Physics A: Mathematical and Theoretical*, 56, 39 (2023), 393001.

[129] S. M. Walas, *Phase Equilibria in Chemical Engineering*, Elsevier, 1985.

[130] P. Debye, "Angular dissymmetry of the critical opalescence in liquid mixtures", *The Journal of Chemical Physics*, 31, 3 (1959), 680–687.

[131] M. Ariyapadi and E. Nauman, "Gradient energy parameters for polymer–polymer–solvent systems and their application to spinodal decomposition in true ternary systems", *Journal of Polymer Science Part B: Polymer Physics*, 28, 12 (1990), 2395–2409.

[132] J. Simmons, C Shen, and Y Wang, "Phase field modeling of simultaneous nucleation and growth by explicitly incorporating nucleation events", *Scripta Materialia*, 43, 10 (2000), 935–942, DOI: https://doi.org/10.1016/S1359-6462(00)00517-0.

[133] L. Gránásy, T. Börzsönyi, and T. Pusztai, "Nucleation and Bulk Crystallization in Binary Phase Field Theory", *Phys. Rev. Lett.*, 88 (20 May 2002), 206105, DOI: 10.1103/PhysRevLett.88.206105.

[134] L. Gránásy, G. I. Tóth, J. A. Warren, F. Podmaniczky, G. Tegze, L. Rátkai, and T. Pusztai, "Phase-field modeling of crystal nucleation in undercooled liquids – A review", *Progress in Materials Science*, 106 (2019), 100569, DOI: https://doi.org/10.1016/j.pmatsci.2019.05.002.

[135] M. Ode and I. Ohnuma, "A thermal fluctuation-based nucleation method for phase-field models", *Computational Materials Science*, 194 (2021), 110448, DOI: https://doi.org/10.1016/j.commatsci.2021.110448.

[136] S. DeWitt, S. Rudraraju, D. Montiel, W. B. Andrews, and K. Thornton, "PRISMS-PF: A general framework for phase-field modeling with a matrix-free finite element method", *npj Computational Materials*, 6, 1 (2020), 29.

[137] E. Nauman and N. P. Balsara, "Phase equilibria and the Landau—Ginzburg functional", *Fluid Phase Equilibria*, 45, 2 (1989), 229–250, DOI: https://doi.org/10.1016/0378-3812(89)80260-2.

[138] R. Krishna and J. A. Wesselingh, "The Maxwell-Stefan approach to mass transfer", *Chemical engineering science*, 52, 6 (1997), 861–911.

[139] H. K. Versteeg and W. Malalasekera, *An Introduction to Computational Fluid Dynamics: The Finite Volume Method*, 2nd, Harlow, England: Pearson Education Ltd, 2007.

[140] J. E. Guyer, D. Wheeler, and J. A. Warren, "FiPy: Partial Differential Equations with Python", *Computing in Science & Engineering*, 11, 3 (2009), 6–15, DOI: 10.1109/MCSE.2009.52.

[141] P. Virtanen, R. Gommers, T. E. Oliphant, M. Haberland, T. Reddy, D. Cournapeau, E. Burovski, P. Peterson, W. Weckesser, J. Bright, S. J. van der Walt, M. Brett, J. Wilson, K. J. Millman, N. Mayorov, A. R. J. Nelson, E. Jones, R. Kern, E. Larson, C. J. Carey, İ. Polat, Y. Feng, E. W. Moore, J. VanderPlas, D. Laxalde, J. Perktold, R. Cimrman, I. Henriksen, E. A. Quintero, C. R. Harris, A. M. Archibald, A. H. Ribeiro, F. Pedregosa, P. van Mulbregt, and SciPy 1.0 Contributors, "SciPy 1.0: Fundamental Algorithms for Scientific Computing in Python", *Nature Methods*, 17 (2020), 261–272, DOI: 10.1038/s41592-019-0686-2.

[142] M. Olshanskii, Y. Palzhanov, and A. Quaini, "A scalar auxiliary variable unfitted FEM for the surface Cahn–Hilliard equation", *Journal of Scientific Computing*, 97, 3 (2023), 57.

[143] E. Nauman and D. Q. He, "Nonlinear diffusion and phase separation", *Chemical Engineering Science*, 56, 6 (2001), 1999–2018, DOI: https://doi.org/10.1016/S0009-2509(01)00005-7.

[144] A. Lewis, M. Seckler, H. Kramer, and G. Van Rosmalen, *Industrial crystallization: fundamentals and applications*, Cambridge University Press, 2015.

[145] A. K. Thakur, R. Kumar, V. V. Kumar, A. Kumar, G. K. Gaurav, and K. N. Gupta, "A critical review on thermodynamic and hydrodynamic modeling and simulation of liquid antisolvent crystallization of pharmaceutical compounds", *Journal of Molecular Liquids*, 362 (2022), 119663.

[146] W. Gong, P. Li, and S. Rohani, "Spherical Crystallization Based on Liquid-Liquid Phase Separation in a Reverse Antisolvent Crystallization Process", *Journal of Pharmaceutical Sciences*, 113, 6 (2024), 1616–1623, DOI: https://doi.org/10.1016/j.xphs.2024.01.016.

[147] X. Liu, H. Li, and M. Zhan, "A review on the modeling and simulations of solid-state diffusional phase transformations in metals and alloys", *Manufacturing Review*, 5 (2018), 10.

[148] E. O. Avila-Davila, V. M. Lopez-Hirata, and M. L. Saucedo-Muñoz, "Application of Phase-Field Method to the Analysis of Phase Decomposition of Alloys", *Modeling and Simulation in Engineering Sciences*, ed. by N. S. Akbar and O. A. Beg, London: IntechOpen, 2016, chap. 10, DOI: 10.5772/64153.

[149] Y. Wang, D. Zhang, Z. Pi, J. Lin, and C. Wen, "Phase field simulation of spinodal decomposition in Zr–Nb alloys for implant materials", *Journal of Applied Physics*, 126, 8 (2019).

[150] J. S. Higgins and J. T. Cabral, *A thorny problem? Spinodal decomposition in polymer blends*, 2020.

[151] R. Krishna, "Serpentine diffusion trajectories and the Ouzo effect in partially miscible ternary liquid mixtures", *Phys. Chem. Chem. Phys.*, 17 (41 2015), 27428–27436, DOI: 10.1039/C5CP04520G.

[152] L. A. Ramakers, J. McGinty, W. Beckmann, G. Levilain, M. Lee, H. Wheatcroft, I. Houson, and J. Sefcik, "Investigation of metastable zones and induction times in glycine crystallization across three different antisolvents", *Crystal Growth & Design*, 20, 8 (2020), 4935–4944.

[153] N. Matsushima, Y. Tsugawa, K. Kadota, M. Yoshida, and Y. Shirakawa, "Non-equilibrium phase behavior of localized LLPS driven by solute concentration and anti-solvent addition rate", *Journal of Molecular Liquids*, 444 (2026), 129224, DOI: https://doi.org/10.1016/j.molliq.2025.129224.

[154] L. Evans, *Partial Differential Equations*, Graduate studies in mathematics, American Mathematical Society, 2010.

[155] P. Cui and S. Wang, "Application of microfluidic chip technology in pharmaceutical analysis: A review", *Journal of Pharmaceutical Analysis*, 9, 4 (2019), Special Issue: Advances in Pharmaceutical Analysis 2018, 238–247, DOI: https://doi.org/10.1016/j.jpha.2018.12.001.

[156] K. Dodo, K. Fujita, and M. Sodeoka, "Raman Spectroscopy for Chemical Biology Research", *Journal of the American Chemical Society*, 144, 43 (Oct. 2022), 19651–19667, DOI: 10.1021/jacs.2c05359.

[157] K. Roetmann, W. Schmunk, C. S. Garbe, and V. Beushausen, "Micro-flow analysis by molecular tagging velocimetry and planar Raman-scattering", *Experiments in fluids*, 44 (2008), 419–430.

[158] K. A. Esmonde-White, M. Cuellar, C. Uerpmann, B. Lenain, and I. R. Lewis, "Raman spectroscopy as a process analytical technology for pharmaceutical manufacturing and bioprocessing", *Analytical and bioanalytical chemistry*, 409, 3 (2017), 637–649.

[159] G. Rinke, A. Wenka, K. Roetmann, and H. Wackerbarth, "In situ Raman imaging combined with computational fluid dynamics for measuring concentration profiles during mixing processes", *Chemical Engineering Journal*, 179 (2012), 338–348, DOI: https://doi.org/10.1016/j.cej.2011.11.016.

[160] M. Wellhausen, G. Rinke, and H. Wackerbarth, "Combined measurement of concentration distribution and velocity field of two components in a micromixing process", *Microfluidics and nanofluidics*, 12, 6 (2012), 917–926.

[161] D. Schafer, M. Müller, M. Bonn, D. W. Marr, J. van Maarseveen, and J. Squier, "Coherent anti-Stokes Raman scattering microscopy for quantitative characterization of mixing and flow in microfluidics", *Optics letters*, 34, 2 (2009), 211–213.

[162] A. Bouchaudy, C. Loussert, and J.-B. Salmon, "Steady microfluidic measurements of mutual diffusion coefficients of liquid binary mixtures", *AIChE Journal*, 64, 1 (2018), 358–366.

[163] J.-B. Salmon, A. Ajdari, P. Tabeling, L. Servant, D. Talaga, and M. Joanicot, "In situ Raman imaging of interdiffusion in a microchannel", *Applied physics letters*, 86, 9 (2005).

[164] K. O'Hare and P. Spedding, "Evaporation of a binary liquid mixture", *The Chemical Engineering Journal*, 48, 1 (1992), 1–9, DOI: https://doi.org/10.1016/0300-9467(92)85001-P.

[165] E. Smith and G. Dent, *Modern Raman Spectroscopy: A Practical Approach*, Wiley, 2019.

[166] P. J. Larkin, "Chapter 2 - Basic Principles", *Infrared and Raman Spectroscopy (Second Edition)*, ed. by P. J. Larkin, Second Edition, Elsevier, 2018, 7–28, DOI: https://doi.org/10.1016/B978-0-12-804162-8.00002-1.

[167] O. Hollricher and W. Ibach, "High-Resolution Optical and Confocal Microscopy", *Confocal Raman Microscopy*, ed. by T. Dieing, O. Hollricher, and J. Toporski, Berlin, Heidelberg: Springer Berlin Heidelberg, 2011, 1–20, DOI: 10.1007/978-3-642-12522-5_1.

[168] J. Thyr and T. Edvinsson, "Evading the Illusions: Identification of False Peaks in Micro-Raman Spectroscopy and Guidelines for Scientific Best Practice", *Angewandte Chemie International Edition*, 62, 43 (2023), e202219047, DOI: https://doi.org/10.1002/anie.202219047.

[169] The Dolomite Centre Ltd, *Y Junction Chips*, Product datasheet MAR-000059 v1.3, Accessed March 2023, Royston, Hertfordshire, UK: The Dolomite Centre Ltd, n.d.

[170] HORIBA, *XploRA PLUS, Specifications*, Accessed: 2025-06-03, 2025, URL: https://www.horiba.com/gbr/scientific/products/detail/action/show/Product/xploratm-plus-1528/.

[171] Z.-M. Zhang, S. Chen, and Y.-Z. Liang, "Baseline correction using adaptive iteratively reweighted penalized least squares", *Analyst*, 135 (5 2010), 1138–1146, DOI: 10.1039/B922045C.

[172] M. A. Haque, "Feature Engineering & Selection for Explainable Models A Second Course for Data Scientists", *LULU Internacional* (2022).

[173] B. Illowsky and S. Dean, "Introductory Statistics 2e", Accessed online, Houston, Texas: OpenStax, 2023, chap. 2 Descriptive Statistics, 116.

[174] F. Pedregosa, G. Varoquaux, A. Gramfort, V. Michel, B. Thirion, O. Grisel, M. Blondel, P. Prettenhofer, R. Weiss, V. Dubourg, J. Vanderplas, A. Passos, D. Cournapeau, M. Brucher, M. Perrot, and E. Duchesnay, "Scikit-learn: Machine Learning in Python", *Journal of Machine Learning Research*, 12 (2011), 2825–2830.

[175] Y. Numata, Y. Iida, and H. Tanaka, "Quantitative analysis of alcohol–water binary solutions using Raman spectroscopy", *Journal of Quantitative Spectroscopy and Radiative Transfer*, 112, 6 (2011), 1043–1049.

[176] D. Green and R. Perry, "Physical and Chemical Data", *Perry's Chemical Engineers' Handbook, Eighth Edition*, McGraw Hill professional, McGraw Hill LLC, 2007.

[177] P. Inguva, V. J. Bhute, T. N. Cheng, and P. J. Walker, "Introducing students to research codes: A short course on solving partial differential equations in Python", *Education for Chemical Engineers*, 36 (2021), 1–11, DOI: https://doi.org/10.1016/j.ece.2021.01.011.

[178] C. R. Harris, K. J. Millman, S. J. van der Walt, R. Gommers, P. Virtanen, D. Cournapeau, E. Wieser, J. Taylor, S. Berg, N. J. Smith, R. Kern, M. Picus, S. Hoyer, M. H. van Kerkwijk, M. Brett, A. Haldane, J. F. del Río, M. Wiebe, P. Peterson, P. Gérard-Marchant, K. Sheppard, T. Reddy, W. Weckesser, H. Abbasi, C. Gohlke, and T. E. Oliphant, "Array programming with NumPy", *Nature*, 585, 7825 (Sept. 2020), 357–362, DOI: 10.1038/s41586-020-2649-2.

[179] T. pandas development team, *pandas-dev/pandas: Pandas*, version 2.2.2, Feb. 2020, DOI: 10.5281/zenodo.3509134.

[180] Wes McKinney, "Data Structures for Statistical Computing in Python", *Proceedings of the 9th Python in Science Conference*, ed. by Stéfan van der Walt and Jarrod Millman, 2010, 56 –61, DOI: 10.25080/Majora-92bf1922-00a.

[181] J. A. Nelder and R. Mead, "A Simplex Method for Function Minimization", *The Computer Journal*, 7, 4 (1965), 308–313, DOI: 10.1093/comjnl/7.4.308.

[182] Y. Lin, X. Yu, Z. Wang, S.-T. Tu, and Z. Wang, "Laminar flow diffusion interface control in a microchannel with accurate Raman measurement", *Chemical Engineering and Processing: Process Intensification*, 57-58 (2012), 1–7, DOI: https://doi.org/10.1016/j.cep.2012.04.008.

[183] B. R. Hammond and R. H. Stokes, "Diffusion in binary liquid mixtures. Part 1.—Diffusion coefficients in the system ethanol + water at 25°", *Trans. Faraday Soc.*, 49 (0 1953), 890–895, DOI: 10.1039/TF9534900890.

[184] M. T. Tyn and W. F. Calus, "Temperature and concentration dependence of mutual diffusion coefficients of some binary liquid systems", *Journal of Chemical and Engineering Data*, 20, 3 (1975), 310–316.

[185] K. C. Pratt and W. A. Wakeham, "The mutual diffusion coefficient of ethanol–water mixtures: determination by a rapid, new method", *Proceedings of the Royal Society of London. A. Mathematical and Physical Sciences*, 336, 1606 (1974), 393–406, DOI: 10.1098/rspa.1974.0026.

[186] K. R. Harris, T. Goscinska, and H. N. Lam, "Mutual diffusion coefficients for the systems water–enthanol and water–propan-1-ol at 25°C", *J. Chem. Soc., Faraday Trans.*, 89 (12 1993), 1969–1974, DOI: 10.1039/FT9938901969.

[187] P. Kolodner, H. Williams, and C. Moe, "Optical measurement of the Soret coefficient of ethanol/water solutions", *The Journal of chemical physics*, 88, 10 (1988), 6512–6524, DOI: 10.1063/1.454436.

[188] S. Wiegand, H. Ning, and H. Kriegs, "Thermal Diffusion Forced Rayleigh Scattering Setup Optimized for Aqueous Mixtures", *The Journal of Physical Chemistry B*, 111, 51 (2007), PMID: 18052276, 14169–14174, DOI: 10.1021/jp076913y.

[189] A. Königer, B. Meier, and W. Köhler, "Measurement of the Soret, diffusion, and thermal diffusion coefficients of three binary organic benchmark mixtures and of ethanol–water mixtures using a beam deflection technique", *Philosophical Magazine*, 89, 10 (2009), 907–923, DOI: 10.1080/14786430902814029.

[190] J. C. Legros, Y. Gaponenko, A. Mialdun, T. Triller, A. Hammon, C. Bauer, W. Köhler, and V. Shevtsova, "Investigation of Fickian diffusion in the ternary mixtures of water–ethanol–triethylene glycol and its binary pairs", *Phys. Chem. Chem. Phys.*, 17 (41 2015), 27713–27725, DOI: 10.1039/C5CP04745E.

Appendix A

The fundamental diffusion models

This section aims to serve as a theoretical background for two of the main diffusion models involved in this project: the first and second Fick's laws, and the Maxwell-Stefan equation. A mathematical derivation of these models is performed, providing valuable insight on their advantages and limitations. With this purpose, the mass balance over the control volume shown in Figure A.1 is presented.

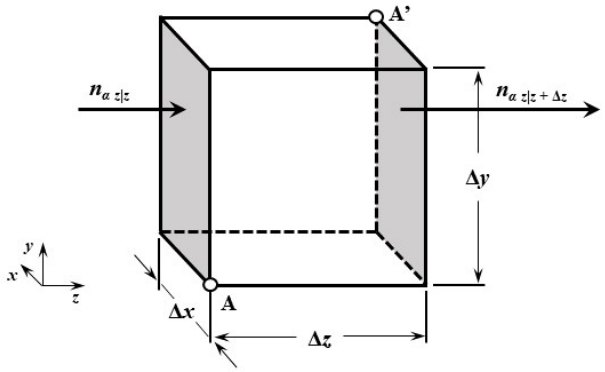


FIGURE A.1: Differential volume element over which the mass balance is performed. Adapted from Byron et al. [1]

The notation used in Figure A.1 is as follows: $n_{\alpha\ z|z}$ represents the mass flux of component α along the x axis due to both convection and molecular diffusion evaluated on the coordinate $z = z$; its definition is included in Equation (A.1). In the same way, $n_{\alpha\ z|z+\Delta z}$ corresponds to the combined mass flux of α on the z direction, evaluated on the coordinate $z = z + \Delta z$. Finally, the points A and A' have, respectively, the coordinates (x, y, z) and $(x + \Delta x, y + \Delta y, z + \Delta z)$.

$$n_{\alpha z|z} = v_z \rho_\alpha + j_{\alpha z} \tag{A.1}$$

where the first term corresponds to the mass transport due to convection: v_z is the z component of the mass average velocity ($\boldsymbol{v}$) of the fluid, measured in $\mathrm{m\,s^{-1}}$, which vector is defined in Equation (A.2), and ρ_α ($\mathrm{kg\,m^{-3}}$) is the mass concentration of component α. The second term, $j_{\alpha z}$, represents the mass transport along the z direction occurring due to molecular diffusion, and

is measured, as the first one, in $\mathrm{kg\,m^{-2}\,s^{-1}}$.

$$\boldsymbol{v} = \sum_{\alpha=1}^{N} w_\alpha \boldsymbol{v_\alpha} \tag{A.2}$$

where w_α is the mass fraction of α in the mixture, and $\boldsymbol{v_\alpha}$ (m/s) is the average velocity of all the molecules of component α present in the control volume.

The general mass balance equation of a system is depicted in Equation (A.3). For generalisation purposes, the first step considers a multicomponent system, and the development of a chemical reaction within the boundaries of the volume element.

$$I + P = O + C + A \tag{A.3}$$

where I and O represent the mass flowrate of component that enters and exits the system, respectively; A refers to the mass that is accumulated within the system; and, finally, P and C correspond with the production and consumption of component due to homogeneous chemical reactions. It is worth mentioning that the production or consumption of component as a consequence of a heterogeneous reaction would instead be considered in the boundary conditions used to evaluate the differential equation that results from the mass balance.

The contributors to the mass balance are described, in the above-mentioned order, in Equations (A.4 – A.7). This step only presents the equations in relation to the x component for the inlet and outlet terms, although analogous expressions for the y and z directions can be deduced. Production and consumption have been combined in only one term, R, which overall sign will be positive or negative depending on which one of the two it corresponds with, respectively. These two terms do not depend on the direction of the flux, and, therefore, they are evaluated for the whole volume element studied.

$$I_{\alpha z} = n_{\alpha z|z} \cdot \Delta x \Delta y \tag{A.4}$$

$$O_{\alpha z} = n_{\alpha z|+\Delta z} \cdot \Delta x \Delta y \tag{A.5}$$

$$R_\alpha = r_\alpha \cdot \Delta x \Delta y \Delta z \tag{A.6}$$

$$A_\alpha = \frac{\partial \rho_\alpha}{\partial t} \cdot \Delta x \Delta y \Delta z \tag{A.7}$$

where $\alpha = 1, 2, ..., N$ and r_α is the rate of production of component α. The z component of the inlet and outlet terms can be found, according to Figure A.1, across the whole surface of the shaded faces, since all the points comprised in them have the same z coordinate.

The next step in this deduction is the consideration of the inlet and outlet terms along the x and y axis. After dividing by the volume of the control element, $\Delta x \Delta y \Delta z$, and allowing this volume to become infinitesimally small, the continuity equation for α is found. This is shown in Equation (A.8), where all the terms have units of $\mathrm{kg\,m^{-3}\,s^{-1}}$.

$$\frac{\partial \rho_\alpha}{\partial t} = -\left(\frac{\partial n_{\alpha z}}{\partial z} + \frac{\partial n_{\alpha x}}{\partial x} + \frac{\partial n_{\alpha y}}{\partial y} \right) + r_\alpha \tag{A.8}$$

Rewriting this expression so that the mass flux of α is expressed as a vector, instead of through its three components, and considering Equation (A.1), it is possible to obtain the vectorial continuity equation of α in terms of the convective and molecular diffusive transport, as shown in Equation (A.9). Finally, in Equation (A.10) this expression is written in terms of the mass fraction of α, making use of the fact that $\rho_\alpha = w_\alpha \cdot \rho$, and considering that ρ is constant throughout the control volume. Equation (A.11) shows the molar equivalent of this continuity expression.

$$\frac{\partial \rho_\alpha}{\partial t} = -(\nabla \cdot \mathbf{v}\rho_\alpha) - (\nabla \cdot \mathbf{j}_\alpha) + r_\alpha \tag{A.9}$$

$$\rho\left(\frac{\partial w_\alpha}{\partial t} + (\mathbf{v} \cdot \nabla w_\alpha)\right) = -(\nabla \cdot \mathbf{j}_\alpha) + r_\alpha \tag{A.10}$$

$$c\left(\frac{\partial x_\alpha}{\partial t} + (\mathbf{v} \cdot \nabla x_\alpha)\right) = -(\nabla \cdot \mathbf{j}_\alpha) + r_\alpha \tag{A.11}$$

A.1 Fick's law of binary diffusion

The deduction of Fick's first law follows, in general, an empirical reasoning, and therefore that is how it will be covered in this report. A more in-depth explanation of the scenario presented here can be found in [94].

Let us imagine two bulbs full with gaseous nitrogen and carbon dioxide, respectively, and connected by a capillary tube. Fick defined the flux of a component as the amount of that species that flows through a certain area in a certain time. He stated that, as Equation (A.12) shows, this quantity was proportional to the difference between the concentration measured in the bulbs poor and rich in α, respectively, and relative to the length of the capillary tube.

$$\mathbf{J}_\alpha = -D_{\alpha\beta} \cdot \frac{\Delta c_\alpha}{\Delta z} \tag{A.12}$$

where $D_{\alpha\beta}$ is the proportionality constant. Physically, it corresponds with the diffusion coefficient of one component in another, and it indicates how miscible the two species are. As for the negative sign, it appears to keep the flux positive, since the difference in concentration is a negative quantity.

Considering that the concentration varies in the other two dimensions, and that the length of the studied capillary is infinitesimal, Fick's first law (A.13), (A.14), in molar and mass units, respectively, is obtained.

$$\mathbf{J}_\alpha = -D_{\alpha\beta} \cdot \nabla c_\alpha \tag{A.13}$$

$$\mathbf{J}_\alpha = -D_{\alpha\beta} \cdot \nabla \rho_\alpha \tag{A.14}$$

A.2 Fick's second law of diffusion

This derivation is based on a simple combination of the final expressions obtained for the mass balance and Fick's first law of binary diffusion. Firstly, it is possible to substitute Equation (A.14)

into Equation (A.10). Considering the density of the solution as constant, Equation (A.15) is obtained.

$$\rho\left(\frac{\partial w_\alpha}{\partial t}+(\mathbf{v}\cdot\nabla w_\alpha)\right)=\rho D_{\alpha\beta}\nabla^2 w_\alpha+r_\alpha \tag{A.15}$$

This equation adequately describes diffusion in dilute liquid solutions, provided that the pressure and temperature of the system are constant. If, additionally, no chemical reactions are taking place, and the velocity of the system can be considered zero, this expression can be further simplified into Equation (A.16), Fick's second law of diffusion in mass units. Analogously, substituting Equation (A.13) into Equation (A.11) and considering the mentioned approximations, Fick's second law in molar units would be obtained.

$$\frac{\partial \rho_\alpha}{\partial t}=D_{\alpha\beta}\nabla^2\rho_\alpha \tag{A.16}$$

A.3 Maxwell-Stefan model

The Maxwell-Stefan model is derived along the lines of the studies presented in [92, 93]. Let us consider a binary system formed by species α and β. For mass transfer to occur, there must exist a driving force in the system that allows the molecule of α in movement to overcome the molecular friction exerted on it. Specifically, this friction is caused exclusively by molecules of a different species, which is this case corresponds to β. This can be proven through collision theory, since this molecular friction corresponds with the linear momentum transferred from a molecule of α to β, shown in Equation (A.17).

$$\mathbf{M}_\alpha=\frac{m_\alpha m_\beta}{m_\alpha+m_\beta}\cdot(\mathbf{v}_\alpha-\mathbf{v}_\beta) \tag{A.17}$$

where $\mathbf{M}_\alpha$ is the transferred linear momentum, and m_i and $\mathbf{v_i}$ are the mass and velocity of species i, respectively.

Equation (A.17) shows that, in order to have a transfer of momentum, the velocity of the two molecules must be different. This proves that the momentum transferred in an $\alpha-\alpha$ collision is zero, and that the system will only exhibit molecular friction if the species are in movement with respect to each other. It is also worth noting that the rationale behind this kinetic analysis is only applicable to low-density gases. In denser fluids, such as liquids, the amount of linear momentum transferred cannot be validly approximated to that corresponding to two-particle collisions. Nonetheless, the physical significance of Equation (A.17) remains intact, and therefore can be applied to the deduction of the Maxwell-Stefan model for liquids [93].

This equation is derived below through a force analysis following Newton's second law (A.18), which states that the sum of the forces imposed on a system is proportional to the time rate of change of the momentum in that system.

$$\sum \mathbf{F_i}\propto\frac{d(m\mathbf{v_i})}{dt} \tag{A.18}$$

Intuitively, the right term must correspond with the average momentum exchanged in a collision, written in Equation (A.17), multiplied by the number of $\alpha-\beta$ collisions in the system per unit of time. In turn, the latter should be proportional to the molar fraction of both components, since a higher number of particles will increase the probability of an $\alpha-\beta$ collision. Substituting these within Newton's law, Equation (A.19) is obtained.

$$\sum \mathbf{F}_\alpha = f_{\alpha\beta} x_\alpha x_\beta \left(\mathbf{v}_\alpha - \mathbf{v}_\beta\right) \tag{A.19}$$

where $\mathbf{f}_{\alpha\beta}$ is a proportionality constant manually included in the expression. Physically, it can be understood as a drag coefficient, since this term corresponds with the molecular friction experienced by the moving molecule.

The analysis of the left term requires the performance of a force balance on species α, illustrated in Figure A.2, over the control volume shown in Figure A.1. Only the pressure forces are considered for this derivation, and therefore the Maxwell-Stefan model is invalid when other external forces, such as an electric field, are acting on the system.

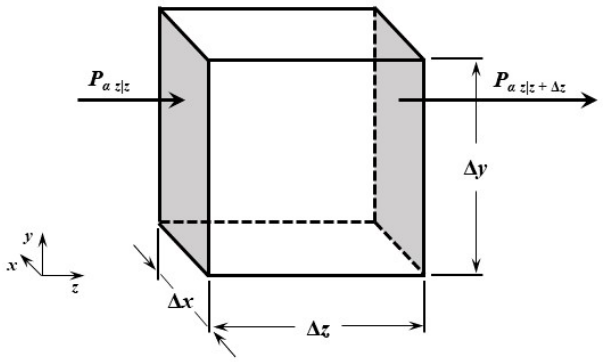


FIGURE A.2: Differential volume element over which the force balance is performed.

The terms in this force analysis, presented in Equation (A.20), are analogous to those in the mass balance at the beginning of this section. In this case, the homogeneous chemical reaction and accumulation are zero, being the only contributors the partial pressure of α evaluated in z (in) and $z+\Delta z$ (out).

$$\sum \mathbf{F}_\alpha = \left(P_{\alpha z|z} - P_{\alpha z|z+\Delta z}\right) \cdot \Delta y \cdot \Delta x \tag{A.20}$$

Dividing by the volume of the system, $\Delta x \cdot \Delta y \cdot \Delta z$, Equation (A.21) is obtained. Finally, allowing this volume to become infinitesimally small, and generalising for the x and y directions, the sum of the forces per volume acting on α in the system is written in Equation (A.22).

$$\sum \mathbf{F}_\alpha = \frac{P_{\alpha z|z} - P_{\alpha z|z+\Delta z}}{\Delta z} \tag{A.21}$$

$$\sum \mathbf{F}_\alpha = -\nabla P_\alpha \tag{A.22}$$

If the system is considered to be isobaric, it is still possible to further operate the left term expressing it as a function of the composition gradient of α, as shown in Equation (A.25). To

continue developing this term, it is necessary to consider the derivative of the chemical potential with respect to space, presented in equations (A.23) and (A.24).

$$\frac{\partial \mu_\alpha}{\partial z} = RT \frac{\partial \log x_\alpha}{\partial x_\alpha} \cdot \frac{\partial x_\alpha}{\partial z} \tag{A.23}$$

$$\nabla x_\alpha = \frac{x_\alpha}{RT} \nabla \mu_\alpha \tag{A.24}$$

Introducing these expressions, Equation (A.25) can be rewritten in terms of the chemical potential gradient of α, as Equation (A.26) describes.

$$\sum \mathbf{F}_\alpha = -P \cdot \nabla x_\alpha \tag{A.25}$$

$$\sum \mathbf{F}_\alpha = -P \cdot \frac{x_\alpha}{RT} \cdot \nabla_{T,P} \mu_\alpha \tag{A.26}$$

At this point, it is convenient to combine the developed expressions for the left and right term of Newton's second law, which correspond with equations (A.19) and (A.26), respectively. This is presented in Equation (A.27).

$$-P \cdot \frac{\mathbf{x}_\alpha}{RT} \cdot \nabla_{T,P} \mu_\alpha = f_{\alpha\beta} x_\alpha x_\beta \left(\mathbf{v}_\alpha - \mathbf{v}_\beta \right) \tag{A.27}$$

One last mathematical operation is required. Until now, a diffusion coefficient has not appeared in any of the equations obtained in this derivation, and the proportionality constant $f_{\alpha\beta}$ has not been defined either. In this case, $f_{\alpha\beta}$ is considered as the inverse of the Maxwell-Stefan diffusion coefficient, $Đ_{\alpha\beta}$, multiplied by the global pressure of the system, P. Considering this, defining $\beta = 1/RT$ and simplifying x_α from both sides, the final version of the Maxwell-Stefan model (A.28) for a liquid binary mixture is obtained.

$$\nabla_{T,P} \beta \mu_\alpha = \frac{x_\beta}{Đ_{\alpha\beta}} \cdot \left(\mathbf{v}_\beta - \mathbf{v}_\alpha \right) \tag{A.28}$$

This expression can be re-written in order to obtain the diffusive fluxes of both components of the mixture, $\boldsymbol{J}_\alpha$ and $\boldsymbol{J}_\beta$. Multiplying both sides by x_α and considering that $\mathbf{N}_\alpha = c x_\alpha \mathbf{v}_\alpha$ and $\mathbf{N}_\beta = c x_\beta \mathbf{v}_\beta$:

$$-x_\alpha \nabla_{T,P} \beta \mu_\alpha = \frac{x_\beta \mathbf{N}_\alpha - x_\alpha \mathbf{N}_\beta}{c\, Đ_{\alpha\beta}} \tag{A.29}$$

The left term of this expression can be further developed by considering that, for a non-ideal fluid mixture, the chemical potential can be defined in terms of activity coefficients, as Equation (**??**) shows. Therefore, introducing this in Equation (A.29), and applying the chain rule to the subsequent derivative, Equation (A.31) is obtained.

$$-x_\alpha \nabla_{T,P} \beta \mu_\alpha = -x_\alpha \nabla_{T,P} \left(\ln x_\alpha + \ln \gamma_\alpha \right) \tag{A.30}$$

$$-x_\alpha \nabla_{T,P} \beta \mu_\alpha = -x_\alpha \left(\frac{1}{x_\alpha} \nabla_{T,P} x_\alpha + \frac{\partial \ln \gamma_\alpha}{\partial x_\alpha} \nabla_{T,P} x_\alpha \right) \tag{A.31}$$

Grouping the terms multiplying the gradient of x_α, it is possible to obtain Equation (A.32).

The parameter formed as a result of this operation corresponds with the thermodynamic factor, defined by $\Gamma = 1 + x_\alpha \frac{\partial \ln \gamma_\alpha}{\partial x_\alpha}$. It is used to account for the non-linear behaviour present in non-ideal mixtures.

$$-x_\alpha \nabla_{T,P} \beta \mu_\alpha = -\Gamma \, \nabla_{T,P} x_\alpha \tag{A.32}$$

In order to derive the individual diffusive fluxes, it is required to transform the right term of Equation (A.29) by considering $x_\beta = 1 - x_\alpha$, $N_\beta = N_t - N_\alpha$ and that $\mathbf{N}_\alpha = \mathbf{J}_\alpha + x_\alpha \mathbf{N_t}$. This way, Equation (A.33) is obtained.

$$-x_\alpha \beta \nabla_{T,P} \mu_\alpha = \frac{\mathbf{J}_\alpha}{c \, Đ_{\alpha\beta}} \tag{A.33}$$

Therefore, knowing that $c_\alpha = c x_\alpha$, it is possible to express the diffusive flux of species α both in terms of the gradient of its chemical potential and of its molar fraction, as Equation (A.34) shows.

$$\mathbf{J}_\alpha = -Đ_{\alpha\beta} \, c_\alpha \nabla_{T,P} \beta \mu_\alpha = -c \, Đ_{\alpha\beta} \, \Gamma \, \nabla_{T,P} x_\alpha \tag{A.34}$$

Comparing this expression with Fick's law ($\mathbf{J}_\alpha = -c \, D_{\alpha\beta} \, \nabla_{T,P} x_\alpha$), the relationship between Fick's and Maxwell-Stefan's diffusion coefficient, included in Equation (A.35), can be deduced.

$$D = Đ_{\alpha\beta} \, \Gamma \tag{A.35}$$

As Krishna and Wesselingh [93] stated, the Maxwell-Stefan coefficient can be interpreted as an inverse drag coefficient, whereas Fick's coefficient is a group of two different effects: the drag phenomenon covered in Maxwell-Stefan's and non-ideal mixture behaviour. Therefore, Fick's law and the Maxwell-Stefan model will yield identical resutls when the value of the thermodynamic factor is one, in which case the Maxwell-Stefan diffusion coefficient will not be a function of composition. According to these authors, this assumption is only feasible for gaseous mixtures provided that their pressure is not high, and for thermodynamically ideal liquid mixtures.

Appendix B

Formulation of the nondimensional Helmholtz free energy density

The aim of this appendix is to demonstrate how the Helmholtz free energy density of a nonideal multicomponent system, with units of $(1/V)$, can be derived from its nondimensional Gibbs free energy. In particular, the nonideality has been described through the Margules activity model, since this is the simplest nontrivial model for the intended application of this work. We start by defining the Gibbs free energy of the system in Equation (B.1).

$$\beta G = \sum_{i=0}^{n} N_i[\beta\mu_i^\circ(T,p) + \ln x_i] + \frac{N}{2}\sum_{i\neq j}^{n} A_{ij}x_i x_j \tag{B.1}$$

where βG is the nondimensional Gibbs free energy, and $\beta = 1/kT$; N and N_i are the total number of molecules in the system, and the molecules of species i, respectively; μ_i° is the chemical potential of the pure species i; $A_{ij}ij$ is the Margules interaction coefficient between species i and j; and x_i is the mole fraction of species i.

In the Gibbs framework, the temperature (T) and pressure (p) of the system are independent variables, and this free energy can only be minimised in a system in which these are kept constant. In contrast, the thermodynamic volume (V) of the system is allowed to vary. The volume of the system in equilibrium can thus be calculated through Equation (B.2).

$$\beta V = \left.\frac{\partial \beta G}{\partial p}\right|_{T,N_i} \tag{B.2}$$

It is possible to leverage this to reach a definition of the thermodynamic β in this system. Considering that $\partial\mu_i^\circ/\partial p = \overline{V}_i^\circ$, the substitution of Equation (B.1) into the expression above can be expanded into Equation (B.3). Then, dividing this resulting expression by V, the definition of β is reached, as shown in Equation (B.4).

$$\beta V = \sum_{i=0}^{n} N_i\beta\overline{V}_i^\circ(T,p) + \frac{N}{2}\sum_{i\neq j}^{n}\frac{\partial A_{ij}}{\partial p}x_i x_j \tag{B.3}$$

$$\beta = \sum_{i=0}^{n} c_i\beta\overline{V}_i^\circ(T,p) + \frac{c}{2}\sum_{i\neq j}^{n}\frac{\partial A_{ij}}{\partial p}x_i x_j \tag{B.4}$$

Now, the aim of this derivation is to reach an expression for the nondimensional Helmholtz free energy density, $f = F/V$, which, again, has units of $(1/V)$. Considering first the definitions of the Helmholtz and Gibbs free energies, given in Equations (B.5) and (B.6), respectively, it becomes clear that the two can be related through $F = G - pV$.

$$F = U - TS \tag{B.5}$$

$$G = U + pV - TS \tag{B.6}$$

where U is the internal energy of the system, and S is its entropy.

This way, the nondimensional Helmholtz free energy density can be defined as $f = \beta(G - pV)/V$, which in turn can be expanded into Equation (B.7) by substituting in it Equation (B.1).

$$f = \sum_{i=0}^{n} c_i \left[\beta \mu_i^\circ(T,p) + \ln x_i\right] + \frac{c}{2} \sum_{i \neq j}^{n} A_{ij}(T,p) x_i x_j - \beta p \tag{B.7}$$

The Helmholtz formulation assumes that the temperature and the volume of the system are independent variables, and can only be minimised in equilibrium for a system in which they are kept constant. On the other hand, the pressure of the system is allowed to vary. Therefore, the pressure dependency of the Margules parameters and of μ_i° needs to be accounted for. For simplicity, in this work the pressure dependency of these two variables have been expanded through a first-order Taylor series, as shown in Equations (B.8) and (B.9). This is equivalent to assuming that the system is incompressible.

$$\mu_i^\circ(T,p) \approx \mu_i^\circ(T,p_0) + V_i^\circ(T,p_0)(p - p_0) + \cdots \tag{B.8}$$

$$A_{ij}(T,p) \approx A_{ij}(T,p_0) + \frac{\partial A_{ij}(T,p_0)}{\partial p}(p - p_0) + \cdots \tag{B.9}$$

where p_0 has been chosen to be the initial pressure of the system.

Substituting these definitions within Equation (B.7), Equation (B.10) is reached. Grouping then its terms into zero and first-order contributions, Equation (B.11) is obtained.

$$\begin{aligned} f = &\sum_{i=0}^{n} c_i [\beta \mu_i^\circ(T,p_0) + \beta V_i^\circ(T,p_0)(p - p_0) + \cdots + \ln x_i] \\ &+ \frac{c}{2} \sum_{i \neq j}^{n} A_{ij}(T,p_0) x_i x_j + \frac{c}{2} \sum_{i \neq j} \frac{\partial A_{ij}(T,p_0)}{\partial p}(p - p_0) x_i x_j + \cdots - \beta p \end{aligned} \tag{B.10}$$

$$\begin{aligned} f = &\sum_{i=0}^{n} c_i [\beta \mu_i^\circ(T,p_0) + \ln x_i] + \frac{c}{2} \sum_{i \neq j}^{n} A_{ij}(T,p_0) x_i x_j - \beta p \\ &+ \left[\sum_{i=0}^{n} c_i \beta V_i^\circ(T,p_0) + \frac{c}{2} \sum_{i \neq j}^{n} \frac{\partial A_{ij}(T,p_0)}{\partial p} x_i x_j \right] (p - p_0) + \cdots \end{aligned} \tag{B.11}$$

The last term of the right-hand side in Equation (B.11) corresponds exactly with the definition of the thermodynamic β in this system, given in Equation (B.4). Substituting this in,

Equation (B.12) emerges. This constitutes the final version of the nondimensional Helmholtz free energy density used in this work.

$$f = \sum_{i=0}^{n} c_i[\beta\mu_i^\circ(T, p_0) + \ln x_i] + \frac{c}{2}\sum_{i\neq j}^{n} A_{ij}(T, p_0)x_i x_j - \beta p_0 \tag{B.12}$$

Note that all thermodynamic variables within this expression depend only on the temperature of the system and its initial pressure, both of which are constant. Thus, the free energy used in this work is independent of pressure.

Appendix C

Interfacial tension in one-dimensional multicomponent systems

We are concerned with the derivation of an expression for the interfacial tension of a system of infinite length, formed by n number of species, and divided into two bulk phases joined by an interface, all in thermodynamic equilibrium. Its non-dimensional Helmholtz free energy functional is given in Equation (C.1), which integrand corresponds with the free energy density of the system. While it has been attempted to provide all detail needed for the algebra to be understandable, the reader is advised to work backwards if stuck on a particular step, taking note on what terms changed and which remained constant.

$$F = \int d\mathbf{r} \left[f(\mathbf{r}) + \frac{1}{2} \sum_{ij}^{n} \kappa_{ij} \nabla c_i(\mathbf{r}) \cdot \nabla c_j(\mathbf{r}) \right] \tag{C.1}$$

where f corresponds with the free energy associated to the pure species and their ideal and non-ideal mixtures; c is the concentration, in units of particle density; and in the second term, which corresponds with the interfacial free energy, κ_{ij} is defined as the interfacial free energy coefficient.

The chemical potential of the system for a species α, obtained by performing a variational derivative of the free energy functional with respect to c_α, is given in Equations (C.2) and (C.3) for the generalised and one-dimensional forms, respectively. Note that because of the system being in equilibrium, the chemical potentials of all species, denoted as γ_i, must be spatially constant.

$$\gamma_\alpha = \frac{\partial f}{\partial c_\alpha} - \sum_{i}^{n} \nabla \cdot [\kappa_{\alpha i} \nabla c_i(\mathbf{r})] + \frac{1}{2} \sum_{ij}^{n} \frac{\partial \kappa_{ij}}{\partial c_\alpha} \nabla c_i(\mathbf{r}) \cdot \nabla c_j(\mathbf{r}) \tag{C.2}$$

$$\gamma_\alpha = \frac{\partial f}{\partial c_\alpha} - \sum_{i}^{n} [\kappa_{\alpha i} c_i'(z)]' + \frac{1}{2} \sum_{ij}^{n} \frac{\partial \kappa_{ij}}{\partial c_\alpha} c_i'(z) c_j'(z) \tag{C.3}$$

The interfacial tension of a system is defined as the work per unit area required to form an interface between two bulk phases. This can be expressed as the difference between the free energy of the heterogeneous system and that of the two individual bulk phases when disconnected from each other, as seen in Equations (C.4) and A for the generalised and one-dimensional cases,

respectively.

$$\beta\sigma A_I = F - \int_I f\left(c_1^I(\mathbf{r}),\ldots,c_n^I(\mathbf{r})\right)d\mathbf{r} - \int_{II} f\left(c_1^{II}(\mathbf{r}),\ldots,c_n^{II}(\mathbf{r})\right)d\mathbf{r} \tag{C.4}$$

$$\beta\sigma = F - \int_I f\left(c_1^I(z),\ldots,c_n^I(z)\right)dz - \int_{II} f\left(c_1^{II}(z),\ldots,c_n^{II}(z)\right)dz \tag{C.5}$$

where I goes from $-\infty$ to the interface location, and II, from the interface location to $+\infty$; and A_I corresponds with the area of the interface.

Substituting the free energy functional F into Equation (C.4), Equation (C.6) is reached. This expression can be further simplified by relating the obtained differences in free energy densities with the chemical potential.

$$\beta\sigma = \int_I dz\left(f - f(c_0^I,\ldots,c_n^I)\right) + \int_{II} dz\left(f - f(c_0^{II},\ldots,c_n^{II})\right) + \frac{1}{2}\int dz\sum_{ij}\kappa_{ij}c_i'(z)c_j'(z) \tag{C.6}$$

Therefore, the equilibrium Helmholtz free energy densities of these two contributions must be calculated in order to reach an expression for the surface tension. We will focus first on f, since the expressions for $f(c_0^I,\ldots,c_n^I)$ and $f(c_0^{II},\ldots,c_n^{II})$ can be derived from its definition.

A general equilibrium Gibbs free energy density can be defined through $\sum_{i=0}^{n} c_i(\mathbf{r})\gamma_i$. Since the equilibrium composition profile in the system ($c_i(\mathbf{r})$) is not known, and not constant, the free energy density must be calculated by summing over the product of the equilibrium chemical potential of all species with the spatial derivative of the concentration of that species, as presented in Equation (C.7), and subsequently integrating this expression.

$$\sum_i^n c_i'\gamma_i = \sum_i^n c_i'\frac{\partial f}{\partial c_i} - \sum_{ij}^n c_i'\left[\kappa_{ij}c_j'\right]' + \frac{1}{2}\sum_{ijk}^n c_i'\frac{\partial\kappa_{jk}}{\partial c_i}c_j'c_k' \tag{C.7}$$

The first and third terms of the right-hand side in this expression constitutes an expansion of the chain rule for the spatial derivative of f and κ, respectively. The expression becomes

$$\sum_i^n c_i'\gamma_i = f' - \sum_{ij}^n \kappa_{ij}c_i'c_j'' - \sum_{ij}^n \kappa_{ij}'c_i'c_j' + \frac{1}{2}\sum_{jk}^n \kappa_{jk}'c_j'c_k'$$

The last two terms can be summed, and the second term on the right-hand side can be rewritten as the result of a product rule. In turn, the two terms resulting from these two simplifications also constitute the expansion of a product rule, and thus can be collapsed this way.

$$\begin{aligned}\sum_i^n c_i'\gamma_i &= f' - \frac{1}{2}\sum_{ij}^n \kappa_{ij}\left(c_i'c_j'\right)' - \frac{1}{2}\sum_{ij}^n \kappa_{ij}'c_i'c_j' \\ &= f' - \frac{1}{2}\sum_{ij}^n \left[\kappa_{ij}c_i'c_j'\right]'\end{aligned}$$

Lastly, considering that the chemical potentials are constant, and therefore their derivative is zero, the derivatives in the expression can be generalised for the entire left and right-hand sides.

$$\left[\sum_{i}^{n} c_i \gamma_i\right]' = \left[f - \frac{1}{2}\sum_{ij}^{n}\left[\kappa_{ij} c_i' c_j'\right]\right]'$$

Integrating both sides with respect to $\mathbf{r}$, Equation (C.8) is reached. This expression relates the Gibbs and Helmholtz free energy densities of the system in equilibrium, and will only be fulfilled if the chemical potentials of all species in the system are constant.

$$\sum_{i}^{n} c_i \gamma_i = f - \frac{1}{2}\sum_{ij}^{n} \kappa_{ij} c_i' c_j' + \beta p_0 \tag{C.8}$$

where βp_0 appears as an integration constant when evaluating the result at the integral limits, at which the composition is constant and that of equilibrium, and thus, at which the gradient term becomes zero. In this case, the LHS and RHS of the expression correspond with the equilibrium Gibbs and Helmholtz free energy densities, respectively. The reason why this term is constant is because of the specific pressure dependency considered in this work, which has been detailed in Appendix B.

Equation (C.8) yields a definition of f that can be substituted into Equation (C.6). The free energy densities of the bulk phases can also be defined from this expression, taking into account that there will be no contribution from the interface in this case, and considering that the compositions will be the coexistence values. These have been defined in Equations (C.9) and (C.10).

$$f(c_0^I, \ldots, c_n^I) = \sum_{i=0}^{n} c_i^I \gamma_i - \beta p_0 \tag{C.9}$$

$$f(c_0^{II}, \ldots, c_n^{II}) = \sum_{i=0}^{n} c_i^{II} \gamma_i - \beta p_0 \tag{C.10}$$

Moreover, Equation (C.8) also leads to a differential expression through which to solve for the equilibrium composition profile, by integrating dc_i/dz and dc_j/dz. This equilibrium composition profile must be used to calculate the coexistence compositions, which in turn are needed to calculate $f(c_0^I, \ldots, c_n^I)$ and $(c_0^{II}, \ldots, c_n^{II})$.

Substituting these free energy densities into Equation (C.6), Equation (C.11) is reached.

$$\beta\sigma = \int_I dz \sum_{i}^{n} \gamma_i \left(c_i - c_i^I\right) + \int_{II} dz \sum_{i}^{n} \gamma_i \left(c_i - c_i^{II}\right) + \int dz \sum_{ij} \kappa_{ij} c_i' c_j' \tag{C.11}$$

Lastly, this expression can be further simplified by placing the interface so that the area between the concentration profile of each species within the heterogeneous system and its concentration in the two bulk phases is equal in magnitude, but of opposite sign. This concept is illustrated in Figure C.1.

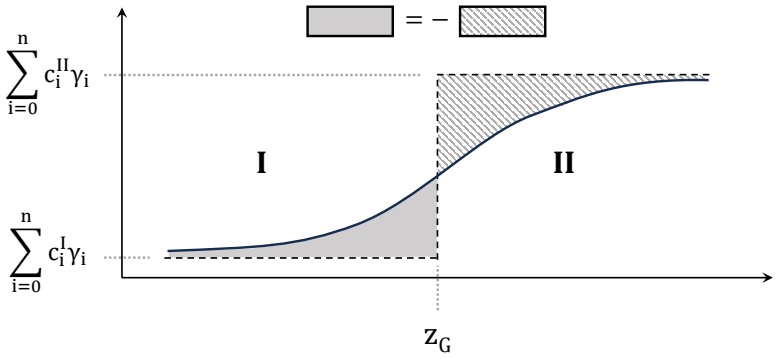


FIGURE C.1: Diagram of the heterogeneous system in equilibrium. The continuous black line depicts its concentration profile, whereas the dashed lines correspond with the concentration of the individual, unconnected bulk phases: c_i^I and c_i^{II}. The location of the interface, z_G, is chosen so that the shaded grey and striped areas are equal in magnitude but of opposite sign.

This way, the final expression for the interfacial tension of a one-dimensional multicomponent system is given in Equation (C.12).

$$\beta\sigma = \int dz \sum_{ij} \kappa_{ij} c_i' c_j' \tag{C.12}$$

This equation can be specialised for both binary and ternary systems, as given in equations (C.13) and (C.14), respectively; note that species 0 was considered to be the dependent one in both cases. Note that the binary κ corresponds with $\kappa_{00} + \kappa_{11} - 2\kappa_{10}$. In the ternary case, we have that $\kappa_{aa} = \kappa_{11} + \kappa_{00} - 2\kappa_{10}$; $\kappa_{bb} = \kappa_{22} + \kappa_{00} - 2\kappa_{20}$; and $\kappa_{ab} = \kappa_{12} + \kappa_{00} - \kappa_{10} - \kappa_{20}$.

$$\beta\sigma = \int \kappa \left(c_1'\right)^2 dz \tag{C.13}$$

$$\beta\sigma = \int dz \left[\kappa_{aa}\left(c_1'\right)^2 + \kappa_{bb}\left(c_2'\right)^2 + 2\kappa_{ab}\left(c_1' c_2'\right)\right] \tag{C.14}$$

Appendix D

Supplementary material on the experimental microfluidic platform

The following section includes the comparison between the experimental and the best-fit simulation profiles obtained from the optimisation of Fickian diffusion to the collected experimental maps. Figure D.1 presents this comparison for experiment 7. Figure D.2 presents these results for experiments 1–3. Figure D.3 presents these results for experiments 4–6. Figure D.4 presents these results for experiments 8–13.

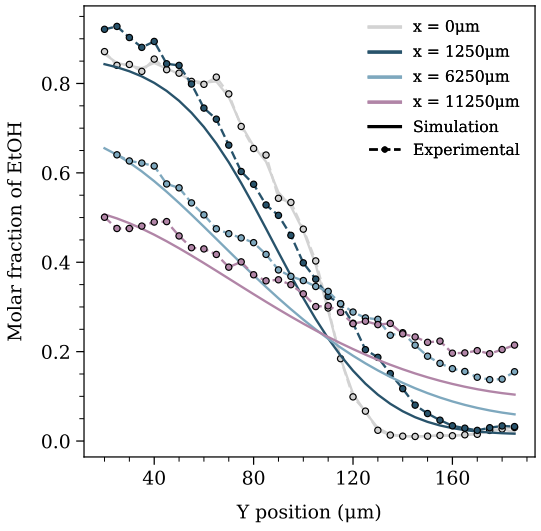


FIGURE D.1: Comparison between the experimental and the best-fit simulation profiles for experiment 7.

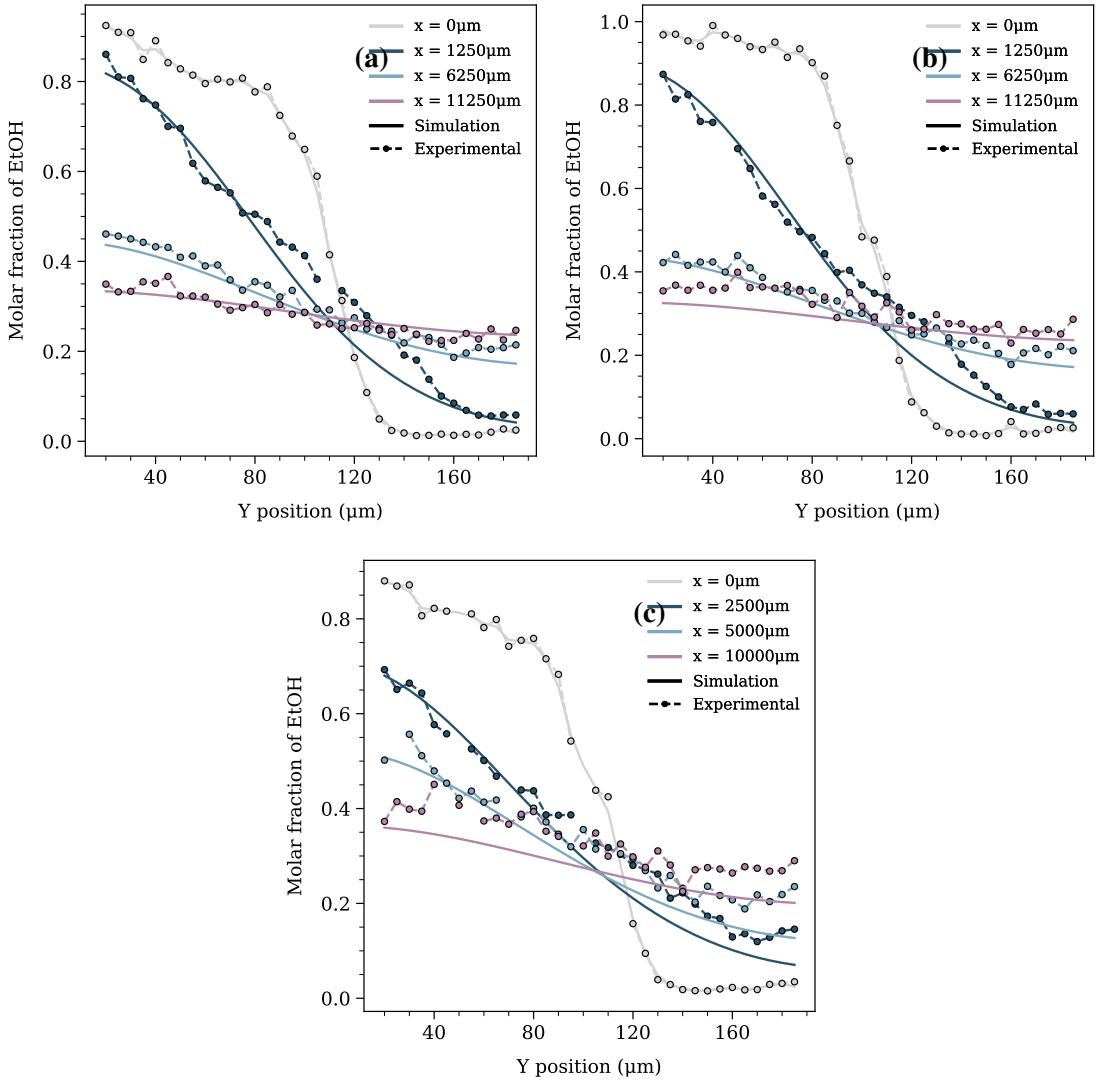


FIGURE D.2: Comparison between the experimental and the best-fit simulation profiles for experiments 1 (a), 2 (b) and 3 (c).

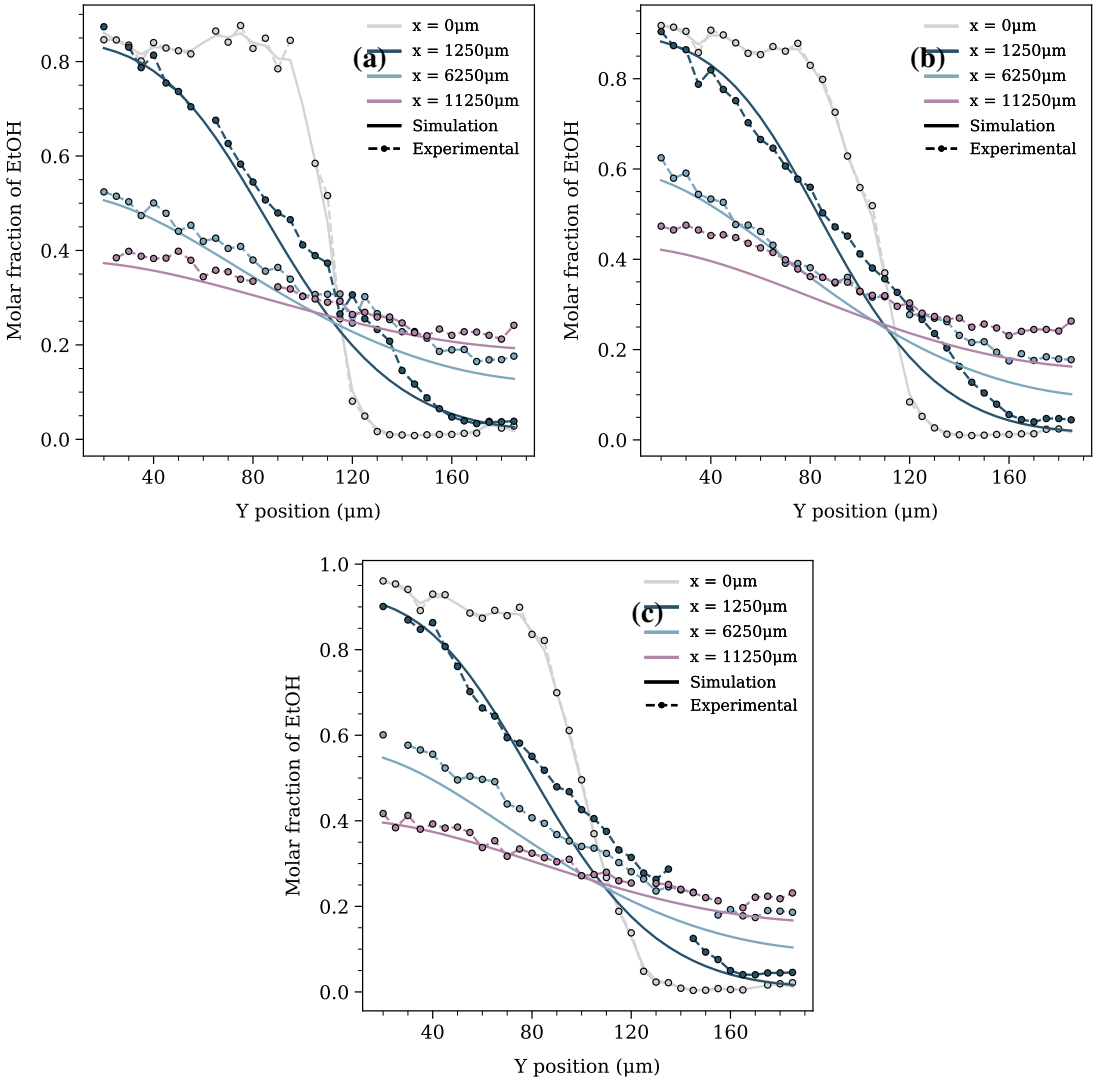


FIGURE D.3: Comparison between the experimental and the best-fit simulation profiles for experiments 4 (a), 5 (b) and 6 (c).

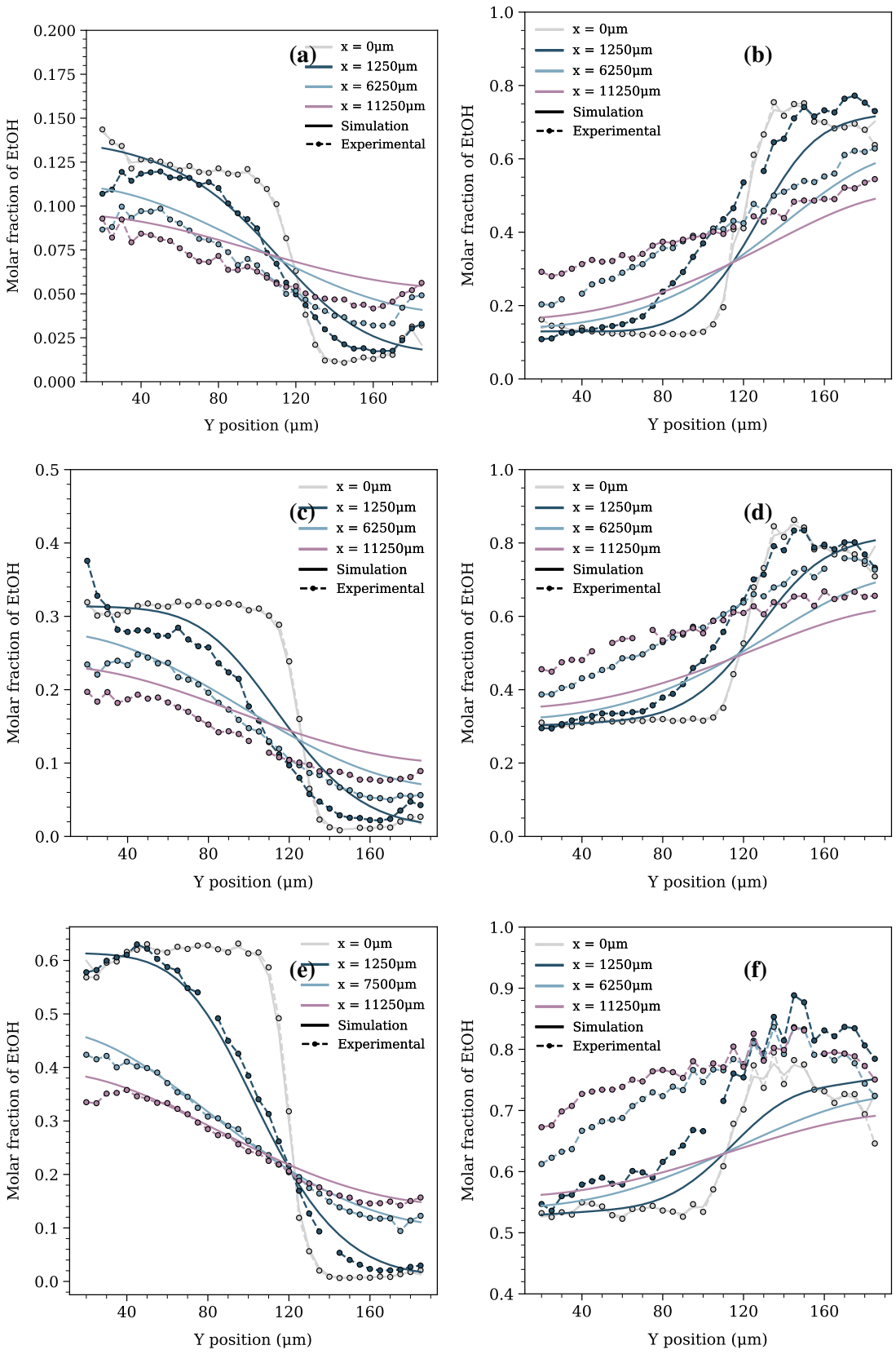


FIGURE D.4: Comparison between the experimental and the best-fit simulation profiles for experiments 11 (a), 8 (b), 12 (c), 9 (d), 13 (e), 10 (f).

Appendix E

Building the ternary diagram

This section describes how to obtain the relevant curves and features of the ternary diagram, according to the thermodynamic models proposed in this work. In particular, it focuses first on the spinodal curve, followed by the binodal and solubility ones.

There are three components in our system: the API, the solvent and the antisolvent, which mole fractions have been defined in this section, respectively, as x_{API}, x_S and x_A. The interactions between API and solvent, as well as between solvent and antisolvent, have been considered ideal, and the one-parameter Margules activity model has been used to describe the nonideality in the interactions between API and antisolvent. The nondimensional molar Helmholtz free energy, $\overline{F}^*$, is given in Equation (E.1). Note that this nondimensionalisation is achieved through multiplying β to the original free energy, F_{og}: $F^* = \beta F_{og}$.

$$\overline{F}^* = x_S\left(\beta\mu_S^\circ + \ln x_S\right) + x_A\left(\beta\mu_A^\circ + \ln x_A\right) + x_{API}\left(\beta\mu_{API}^\circ + \ln x_{API}\right) + Ax_Ax_{API} - \beta p_0 \quad \text{(E.1)}$$

where $\beta\mu_i^\circ = \beta\mu_i^\circ(T, p_0)$ and $A = A(T, p_0)$, p_0 being a reference pressure of the system, constant.

Since both the free energy and the chemical potential are defined only up to an additive constant, any constants and terms linearly dependent on composition—which become constants in the chemical potential equation—do not have an impact on the system. Thus, the molar nondimensional Helmholtz free energy of the system can be defined as $\overline{F} = \overline{F}^* + \beta p_0 - x_S\beta\mu_S^\circ - x_A\beta\mu_A^\circ - x_{API}\beta\mu_{API}^\circ$, and Equation (E.1) can be rewritten as Equation (E.2):

$$\begin{aligned}\overline{F} &= x_S \ln x_S + x_A \ln x_A + x_{API} \ln x_{API} + Ax_Ax_{API} \\ &= (1 - x_A - x_{API})\ln(1 - x_A - x_{API}) + x_A \ln x_A + x_{API} \ln x_{API} + Ax_Ax_{API}\end{aligned} \quad \text{(E.2)}$$

The chemical potential of a species i can be defined with respect to $\beta\overline{F}$ through Equation (E.3). Performing this derivative, the chemical potentials of the three species are found in Equations (E.4)-(E.6).

$$\beta\mu_i = \left.\frac{\partial(n\beta\overline{F})}{\partial n_i}\right|_{T,V,n_{j\neq i}} \quad \text{(E.3)}$$

$$\beta\mu_A = \ln x_A + Ax_{API}(1 - x_A) \quad \text{(E.4)}$$

$$\beta\mu_{API} = \ln x_{API} + Ax_A(1 - x_{API}) \quad \text{(E.5)}$$

$$\beta\mu_S = \ln x_S \quad \text{(E.6)}$$

E.1 Binodal curve and tie lines

The binodal curve encloses the miscibility gap, and defines the coexistence compositions in the two-phase equilibrium within it. These compositions correspond with the intersection between the free energy density curve and the common tangent between the two wells in this curve. Since the activity model considered in this work leads to a symmetric free energy density, this intersection corresponds with the minima of the two wells.

The tie lines relate the equilibrium between the two phases, joining the two coexistence compositions of one equilibrium state. In order to determine where the tie lines sit, the condition of chemical equilibrium must be enforced. This entails the chemical potentials of all components being equal in both phases, as per Equations (E.7)-(E.9).

$$\beta\mu_S(x_A^I, x_{API}^I) = \beta\mu_S(x_A^{II}, x_{API}^{II}) \tag{E.7}$$

$$\beta\mu_A(x_A^I, x_{API}^I) = \beta\mu_A(x_A^{II}, x_{API}^{II}) \tag{E.8}$$

$$\beta\mu_{API}(x_A^I, x_{API}^I) = \beta\mu_{API}(x_A^{II}, x_{API}^{II}) \tag{E.9}$$

In the case of the solvent, which does not have a nonideality term, the condition of equilibrium becomes $\ln x_S^I = \ln x_S^{II}$. Therefore, in equilibrium, $x_S^I = x_S^{II}$, which indicates that the tie lines inside the binodal are horizontal for this system.

Now, the free energy will have critical points at those compositions for which its first derivatives become zero: $\partial(\overline{F})/\partial x_A = \partial(\overline{F})/\partial x_{API} = 0$. These first derivatives are given in Equations (E.10) and (E.11).

$$\begin{aligned}\frac{\partial(\overline{F})}{\partial x_A} &= \left[-\ln(1-x_A-x_{API}) + (1-x_A-x_{API})\frac{-1}{(1-x_A-x_{API})} + \ln x_A + x_A\frac{1}{x_A} + Ax_{API} \right] \\ &= [\ln x_A - \ln(1-x_A-x_{API}) + Ax_{API}]\end{aligned} \tag{E.10}$$

$$\frac{\partial(\overline{F})}{\partial x_{API}} = [\ln x_{API} - \ln(1-x_A-x_{API}) + Ax_A] \tag{E.11}$$

Expanding the condition for critical points above,

$$\ln x_A^I - \ln x_S^I + Ax_{API}^I = \ln x_{API}^I - \ln x_S^I + Ax_A^I \tag{E.12a}$$

$$\ln x_A^I - \ln x_{API}^I + A\left[x_{API}^I - x_A^I\right] = 0 \tag{E.12b}$$

$$\ln x_A^I - \ln x_{API}^I + A\left[1 - x_S^I - 2x_A^I\right] = 0 \tag{E.12c}$$

This is the final identity that we will use to determine the binodal, knowing also that the tie lines are horizontal. The methodology used to determine this curve is: (1) Give values to x_S^I in the interval $[0,1]$. (2) From Equation (E.12c), calculate x_A^I. (3) The dependent composition comes as $1-x_S^I-x_A^I$. (4) Finally, since the tie lines are horizontal: $x_A^{II} = x_{API}^I$, and $x_{API}^{II} = x_A^I$.

E.2 Spinodal curve

The lower and upper composition bounds of the spinodal region, what is referred to as the spinodal curve, are delimited by the inflexion points of the molar Helmholtz free energy surface. In a ternary system this molar free energy has two variables, the two independent compositions. Therefore, its inflexion points are determined as those that make zero the determinant of its Hessian matrix. For a function $f(x,y)$ this matrix is given by

$$H = \begin{bmatrix} f_{xx} & f_{yx} \\ f_{xy} & f_{yy} \end{bmatrix}$$

and its determinant is given by $det(H) = f_{xx}f_{yy} - f_{xy}f_{yx}$.

Therefore, the first step to obtain the spinodal curve is to calculate the second-order derivatives of the molar Helmholtz free energy, given in Equations (E.13)-(E.16). Note that the first-order ones were given in Equations (E.10) and (E.11).

$$\begin{aligned} \frac{\partial^2(\overline{F})}{\partial x_A^2} &= \frac{\partial}{\partial x_A}\frac{\partial(\overline{F})}{\partial x_A} \\ &= \frac{\partial}{\partial x_A}\left[\ln x_A - \ln(1-x_A-x_{API}) + Ax_{API}\right] \\ &= \frac{1}{x_A} + \frac{1}{1-x_A-x_{API}} \\ &= \frac{1}{x_A} + \frac{1}{x_S} \end{aligned} \tag{E.13}$$

$$\frac{\partial^2(\overline{F})}{\partial x_{API}^2} = \frac{1}{x_{API}} + \frac{1}{x_S} \tag{E.14}$$

$$\frac{\partial^2(\overline{F})}{\partial x_{API}\partial x_A} = A + \frac{1}{x_S} \tag{E.15}$$

$$\frac{\partial^2(\overline{F})}{\partial x_A\partial x_{API}} = A + \frac{1}{x_S} \tag{E.16}$$

Following the equation for the determinant of the Hessian given above, we get that the free energy density will have inflexion points for the compositions that make the following relation true:

$$\left[\frac{1}{x_A} + \frac{1}{x_S}\right]\left[\frac{1}{x_{API}} + \frac{1}{x_S}\right] - \left[A + \frac{1}{x_S}\right]^2 = 0 \tag{E.17a}$$

$$\left[\frac{x_S + x_A}{x_A x_S}\right]\left[\frac{x_S + x_{API}}{x_{API} x_S}\right] - \left[\frac{1 + Ax_S}{x_S}\right]^2 = 0 \tag{E.17b}$$

$$\frac{1}{x_S}\left[\left[\frac{x_S + x_A}{x_A}\right]\left[\frac{x_S + x_{API}}{x_{API}}\right] - \left[1 + Ax_S\right]^2\right] = 0 \tag{E.17c}$$

$$\frac{(x_S + x_A)(1 - x_A)}{x_A x_{API}} - \frac{x_A x_{API}(1 + Ax_S)^2}{x_A x_{API}} = 0 \tag{E.17d}$$

$$(x_S + x_A)(1 - x_A) - x_A x_{API}(1 + A x_S)^2 = 0 \tag{E.17e}$$

$$(x_S + x_A)(1 - x_A) - x_A(1 - x_A - x_S)(1 + A x_S)^2 = 0 \tag{E.17f}$$

Equation (E.17f) has become an expression that relates the two independent compositions, from which the spinodal curve can be plotted. The methodology is as follows: (1) Give values to x_S in the interval $[0, 1]$. (2) For each of these x_S, use the condition derived for the inflexion points to calculate x_A. (3) Apply $x_{API} = 1 - x_A - x_S$ to get the third composition missing.

E.3 Solubility curve

The solubility marks the point at which the liquid and solid phases of the API are in equilibrium. Thus, from the chemical equilibrium condition, $\beta\mu_{API}^{(S)} = \beta\mu_{API}^{(L)}$. The expressions for these are given in Equations (E.18) and (E.19).

$$\beta\mu_{API}^{(S)} = \beta\mu_{API}^{0,(S)} + \ln x_{API}^{(S)} \tag{E.18}$$

$$\beta\mu_{API}^{(L)} = \beta\mu_{API}^{0,(L)} + \ln x_{API}^{(L)} + A\left(1 - x_{API}^{(L)}\right)x_A^{(L)} \tag{E.19}$$

Considering that the crystals that form in the solid phase are completely pure, $x_{API}^{(S)} = 1$, and in turn, $\ln x_{API}^{(S)} = 0$. This means that the equilibrium condition now reads

$$\beta\mu_{API}^{0,(S)} = \beta\mu_{API}^{0,(L)} + \ln x_{API}^{(L)} + A\left(1 - x_{API}^{(L)}\right)x_A^{(L)} \tag{E.20}$$

$$\beta\mu_{API}^{0,(S)} - \beta\mu_{API}^{0,(L)} = \ln x_{API}^{(L)} + A\left(1 - x_{API}^{(L)}\right)x_A^{(L)} \tag{E.21}$$

$$\tag{E.22}$$

where the compositions in the liquid phase are those we had been looking at in the rest of the sections.

This provides all the tools needed to plot the solubility, considering that the entire LHS is a quantity defined by the specific system being studied, and thus defined by the user. The methodology is: (1) Pick the LHS value. (2) Give values to x_A in the interval $[0, 1]$. (3) Use the equilibrium condition to calculate x_{API}. (4) Apply $x_S = 1 - x_A - x_{API}$ to get the third composition missing.

Appendix F

Supplementary material on the ternary mass transfer model development

F.1 Towards defining the correct chemical potential

This appendix summarises the current progress made towards the discovery of a form of the composition-dependent interfacial free energy coefficient that produces a flat profile in equilibrium in a phase-separated system. The author makes all the effort to provide clarity on her thoughts; however, the reader must note this is unfinished investigation—not all the answers are available.

The first thing to assert is that the chemical potential of a system which does not present phase separation does remain flat. Two equations have been tested so far for the calculation of the chemical potential, both calculating it in terms of (c, x_1, x_2). The first form is that proposed by Petrischeva and Abart [121], and the second is a preliminary form proposed in this work, based on Equation (C.8). These two forms share common expressions for $\delta F/\delta x_1$ and $\delta F/\delta x_2$—also referred to as $\beta\mu_a$ and $\beta\mu_b$—which are defined in Equations (F.2) and (F.2), respectively. However, their expressions for $\delta F/\delta c$ are different, with their form given in Equation (F.3) and ours in Equation (F.4).

$$\beta\mu_a = \frac{\partial f}{\partial x_1} - \kappa_{aa}\nabla^2 x_1 - \kappa_{ab}\nabla^2 x_2 \tag{F.1}$$

$$\beta\mu_b = \frac{\partial f}{\partial x_1} - \kappa_{aa}\nabla^2 x_1 - \kappa_{ab}\nabla^2 x_2 \tag{F.2}$$

$$\frac{\delta F}{\delta c} = \frac{\partial f}{\partial c} + \frac{\kappa_{aa}}{2}(\nabla x_1)^2 + \kappa_{ab}(\nabla x_1 \nabla x_2) + \frac{\kappa_{bb}}{2}(\nabla x_2)^2 \tag{F.3}$$

$$\frac{\delta F}{\delta c} = \frac{\partial f}{\partial c} - \frac{\kappa_{aa}}{2}(\nabla x_1)^2 - \kappa_{ab}(\nabla x_1 \nabla x_2) - \frac{\kappa_{bb}}{2}(\nabla x_2)^2 \tag{F.4}$$

Thus, this preliminary form takes the same expression proposed by Petrischeva and Abart, but inverts the sign of the first-order terms to negative, in order to comply with the equilibrium condition found in Equation (C.8). Figure F.1 presents the chemical potentials of experiments 1 and 2, calculated through both expressions.

Considering the Y scales, Figure F.1 proves that the chemical potentials in a homogeneous system do remain flat in equilibrium. The reason why both equation forms reach exactly the

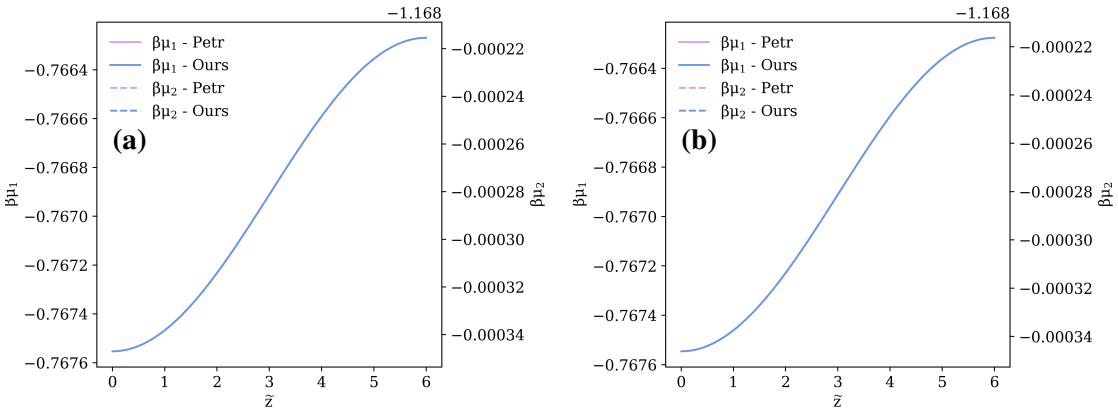


FIGURE F.1: Chemical potentials of the two independent species, 1 and 2, for the equilibrium state of a system in which a stream of pure antisolvent was mixed with a solution of 25% API. The results obtained with the form posed by Petrischeva and Abart [121] and with the form initially explored in this work are both presented. The degree of non-ideality was $A = 3$, and the interfacial free energy coefficients correspond with (a) $(\kappa_{aa}, \kappa_{ab}, \kappa_{bb}) = (0, 0, 0)$ and (b) $(\kappa_{aa}, \kappa_{ab}, \kappa_{bb}) = (0.025, 0.008, 0.025)$.

same output here is that, in the absence of a composition gradient, the interfacial terms become zero and both equations are the same.

The next thing to ascertain is that the differences in chemical potential used to define the driving force in this work, $\beta\mu_a = \beta\mu_1 - \beta\mu_0$ and $\beta\mu_b = \beta\mu_2 - \beta\mu_0$, do return a flat profile when in equilibrium, for a phase-separated state. For this purpose, Figure F.2 presents these profiles for experiments 3 and 4, which correspond, respectively, with $(\tilde{\kappa}_{aa}, \tilde{\kappa}_{ab}, \tilde{\kappa}_{bb}) = (0.025, 0.008, 0.025)$ and $(\tilde{\kappa}_{aa}, \tilde{\kappa}_{ab}, \tilde{\kappa}_{bb}) = (0.1, 0.032, 0.1)$.

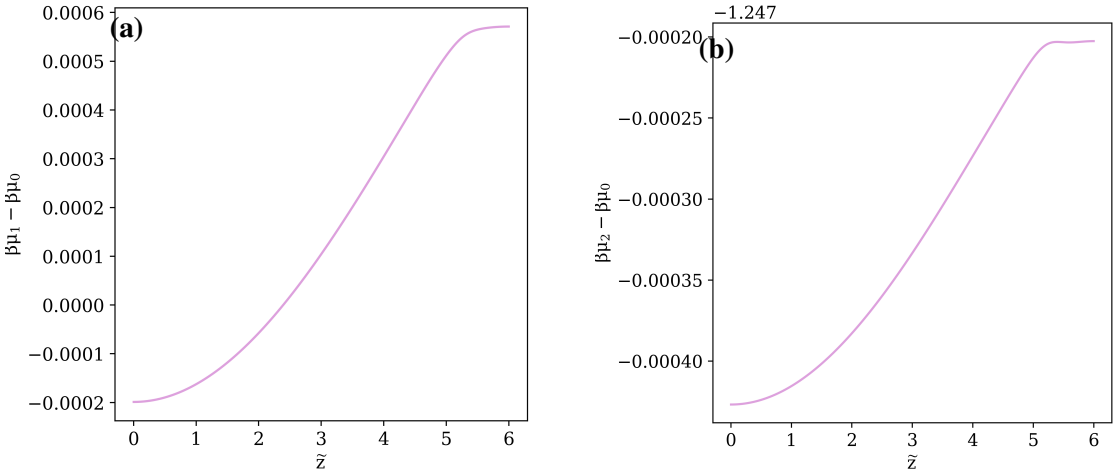


FIGURE F.2: Chemical potential differences between the independent and the dependent species for the equilibrium state of a system in which a stream of pure antisolvent was mixed with a solution of 45% API. In particular, (a) presents $\beta\mu_a = \beta\mu_1 - \beta\mu_0$, and (b), $\beta\mu_b = \beta\mu_2 - \beta\mu_0$. The results obtained with the form posed by Petrischeva and Abart [121] and with the form initially explored in this work are both presented. The degree of non-ideality was $A = 3$, and the interfacial free energy coefficients correspond with $(\kappa_{aa}, \kappa_{ab}, \kappa_{bb}) = (0.025, 0.008, 0.025)$.

The outputs of Figure F.2 prove that the chemical potential differences do remain constant, which is consistent with the dynamic evolution of mass transfer. The composition had ceased

evolving, which can only occur when the driving force for diffusion is depleted. In this case, this corresponds with $\beta\mu_a$ and $\beta\mu_b$.

As for the individual chemical potentials pertaining to experiments 3 and 4, they are presented in Figure F.3(a) and (b), respectively. These outputs make clear that, while the higher value of the gradient free energy coefficient can retrieve a flat profile—given that it led to fully homogeneous mixing—this is not the case for the lower value, when the system phase-separated.

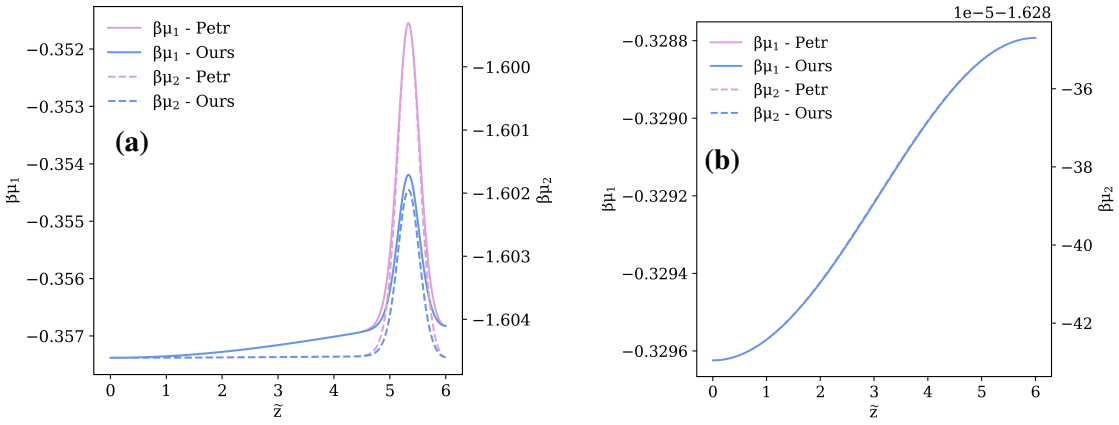


FIGURE F.3: Chemical potentials of the two independent species for the equilibrium state of a system in which a stream of pure antisolvent was mixed with a solution of 45% API. The results obtained with the form posed by Petrischeva and Abart [121] and with the form initially explored in this work are both presented. The degree of non-ideality was $A = 3$, and the interfacial free energy coefficients correspond with (a) $(\kappa_{aa}, \kappa_{ab}, \kappa_{bb}) = (0.025, 0.008, 0.025)$ and (b) $(\kappa_{aa}, \kappa_{ab}, \kappa_{bb}) = (0.1, 0.032, 0.1)$.

The most prominent trends in Figure F.3(a) are the fact that Petrischeva and Abart's form of the chemical potential returned a very similar overshoot at the interface for both species, and that the form proposed in this work does manage to reduce this overshoot, although it does not flatten it completely. The reason why $\beta\mu_1$ shows a slight slope before the peak while $\beta\mu_2$ is completely flat may be because the API needed slightly more simulation time to fully reach equilibrium. Since the changes occurring at these stage of the simulation were imperceptible in the composition profiles, this does not compromise the accuracy of those results.

After establishing what is correct and what still needs to be worked on, we can turn our attention towards the equation defining the chemical potential. By definition, it must correspond with the variational derivative of the free energy with respect to the concentration of the species of interest. The specific expressions that this derivative takes for the three species in the system, species 0 being the dependent one, are given in Equations (F.5)–(F.7). Therefore, calculating $\beta\mu_1$ by parsing the composition profile to this expression will, undoubtedly, return a flat profile.

$$\frac{\delta F}{\delta c_1} = \frac{\partial f}{\partial c_1} + \left(\nabla c_1\right)^2 \frac{1}{2}\frac{\partial \kappa_{aa}}{\partial c_1} + \left(\nabla c_2\right)^2 \frac{1}{2}\frac{\partial \kappa_{bb}}{\partial c_1} + \left(\nabla c_1 \cdot \nabla c_2\right)\frac{\partial \kappa_{ab}}{\partial c_1} - \nabla\cdot[(\kappa_{11}-\kappa_{10})\nabla c_1] - \nabla\cdot[(\kappa_{12}-\kappa_{10})\nabla c_2] \tag{F.5}$$

$$\begin{aligned}\frac{\delta F}{\delta c_2} = \frac{\partial f}{\partial c_2} + \left(\nabla c_1\right)^2 \frac{1}{2}\frac{\partial \kappa_{aa}}{\partial c_2} + \left(\nabla c_2\right)^2 \frac{1}{2}\frac{\partial \kappa_{bb}}{\partial c_2} + \left(\nabla c_1 \cdot \nabla c_2\right)\frac{\partial \kappa_{ab}}{\partial c_2} \\ - \nabla \cdot [(\kappa_{21} - \kappa_{20})\nabla c_1] - \nabla \cdot [(\kappa_{22} - \kappa_{20})\nabla c_2]\end{aligned} \tag{F.6}$$

$$\begin{aligned}\frac{\delta F}{\delta c_0} = \frac{\partial f}{\partial c_0} + \left(\nabla c_1\right)^2 \frac{1}{2}\frac{\partial \kappa_{aa}}{\partial c_0} + \left(\nabla c_2\right)^2 \frac{1}{2}\frac{\partial \kappa_{bb}}{\partial c_0} + \left(\nabla c_1 \cdot \nabla c_2\right)\frac{\partial \kappa_{ab}}{\partial c_0} \\ - \nabla \cdot [(\kappa_{10} - \kappa_{00})\nabla c_1] - \nabla \cdot [(\kappa_{20} - \kappa_{00})\nabla c_2]\end{aligned} \tag{F.7}$$

Moreover, the definition of the chemical potential in terms of (c, x_1, x_2) through the application of the chain rule is also correct. Hence, a direct calculation of $\delta F/\delta c$, $\delta F/\delta x_1$ and $\delta F/\delta x_2$ (Equations (F.8)–(F.10)) will also, by definition, produce a flat profile.

$$\begin{aligned}\frac{\delta F}{\delta x_1} = \frac{\partial f}{\partial x_1} + \left(\nabla x_1\right)^2 \frac{c^2}{2}\frac{\partial \kappa_{aa}}{\partial x_1} + \left(\nabla x_2\right)^2 \frac{c^2}{2}\frac{\partial \kappa_{00}}{\partial x_1} + \left(\nabla x_1 \cdot \nabla x_2\right) c^2 \frac{\partial \kappa_{ab}}{\partial x_1} \\ - c^2 \nabla \cdot [\kappa_{aa}\nabla x_1] - c^2 \nabla \cdot [\kappa_{ab}\nabla x_2]\end{aligned} \tag{F.8}$$

$$\begin{aligned}\frac{\delta F}{\delta x_2} = \frac{\partial f}{\partial x_2} + \left(\nabla x_2\right)^2 \frac{c^2}{2}\frac{\partial \kappa_{bb}}{\partial x_2} + \left(\nabla x_1\right)^2 \frac{c^2}{2}\frac{\partial \kappa_{00}}{\partial x_2} + \left(\nabla x_1 \cdot \nabla x_2\right) c^2 \frac{\partial \kappa_{ab}}{\partial x_2} \\ - c^2 \nabla \cdot [\kappa_{ab}\nabla x_1] - c^2 \nabla \cdot [\kappa_{bb}\nabla x_2]\end{aligned} \tag{F.9}$$

$$\begin{aligned}\frac{\delta F}{\delta c} = \frac{\partial f}{\partial c} + \left(\nabla x_1\right)^2 \frac{c^2}{2}\frac{\partial \kappa_{aa}}{\partial c} + \left(\nabla x_2\right)^2 \frac{c^2}{2}\frac{\partial \kappa_{bb}}{\partial c} + \left(\nabla x_1 \cdot \nabla x_2\right) c^2 \frac{\partial \kappa_{ab}}{\partial c} \\ + c\kappa_{aa}\left(\nabla x_1\right)^2 + c\kappa_{bb}\left(\nabla x_2\right)^2 + 2c\kappa_{ab}\left(\nabla x_1 \cdot \nabla x_2\right) \\ - cx_1 \nabla \cdot [\kappa_{aa}\nabla x_1] - cx_1 \nabla \cdot [\kappa_{ab}\nabla x_2] \\ - cx_2 \nabla \cdot [\kappa_{ab}\nabla x_1] - cx_2 \nabla \cdot [\kappa_{bb}\nabla x_2] \\ + c\nabla \cdot [\kappa_{00}\nabla x_1] + c\nabla \cdot [\kappa_{00}\nabla x_2]\end{aligned} \tag{F.10}$$

The problem arises through the definition of the interfacial free energy coefficients in these expressions. The reason why Equation (F.5) could not be used directly was because the dynamics of the model had been built upon differences between chemical potentials as the driving force, corresponding exactly to Equations (F.8) and (F.9). In them, the interfacial free energy coefficients naturally group into the three groups represented as κ_{aa}, κ_{ab} and κ_{bb}. Therefore, the dynamics were defined based on these three values. It is not possible to determine the value of $(\kappa_{11} - \kappa_{10})$ or $(\kappa_{22} - \kappa_{20})$ from them.

Calculating it through the chain rule, rewriting its definition in terms of (c, x_1, x_2), is an easier choice, since, as mentioned, Equations (F.8) and (F.9) were embedded into the continuity equations. Therefore, the only outstanding expression to define is $\delta F/\delta c$, which corresponds with the contribution of the bulk phase to the chemical potential. However, attending to its definition in Equation (F.10), we can see that this expression is not defined exclusively in terms of κ_{aa}, κ_{ab} and κ_{bb}, but instead also counts with a lone term at the end that depends only on κ_{00}. While at a first glance it may appear odd, that term is correct, and needed in order to recover Equation (F.5) from the chain rule expression.

This indicates that the definition of the gradient coefficient of the dependent species is non-trivial, and might be the key component for producing a flat equilibrium chemical potential profile in a phase-split system. It may be the case that sampling a sufficiently large range of values for κ_{00} is enough to land on one that enables this, since the groups of parameters κ_{aa}, κ_{ab} and κ_{bb} could maintain their value through adjusting the relative value of the other interfacial coefficients. However, a suitable value for κ_{00} obtained in this way may be specific to the profile it was designed to flatten. Therefore, perhaps a more robust approach would be to test different forms of the composition dependence of this parameter.

F.2 Additional results

Figure F.4(a) presents the composition evolution through the ternary diagram of a system without non-ideal or gradient contributions, meaning that $A = 0$ and $(\kappa_{aa}, \kappa_{ab}, \kappa_{bb}) = (0, 0, 0)$. In particular, the system is formed by a stream of pure antisolvent and a solution of 25% API. Similarly, Figure F.4(b) presents the evolution of this system when the gradient contributions are acknowledged, with the coefficients being $(\kappa_{aa}, \kappa_{ab}, \kappa_{bb}) = (0.1, 0.032, 0.1)$. Lastly, it was considered that $\beta\mu_1^{\circ,(S)} - \beta\mu_1^{\circ,(L)} = -1$.

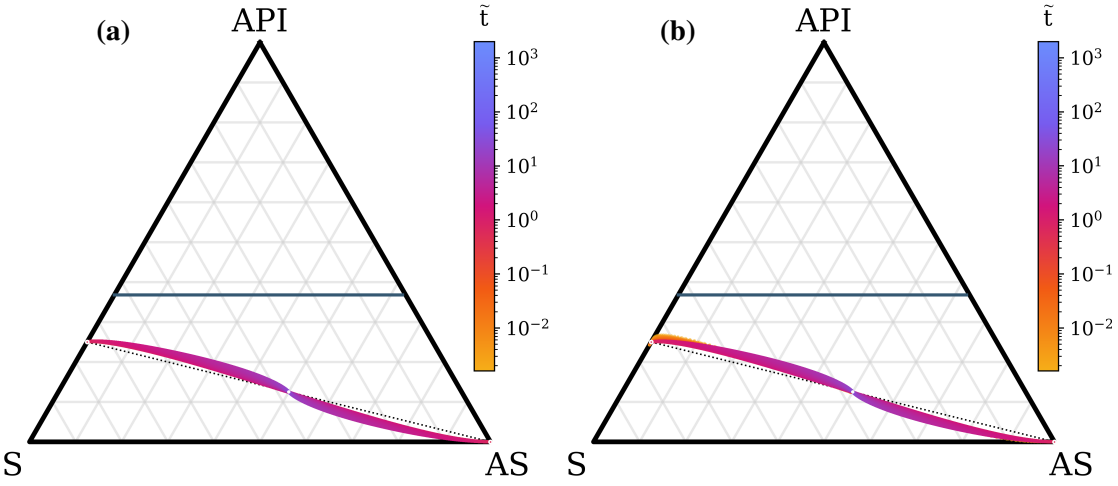


FIGURE F.4: Evolution of the composition with time in a system mixing pure antisolvent with a 45% API solution, considering that $A = 0$ and $\beta\mu_1^{\circ,(S)} - \beta\mu_1^{\circ,(L)} = -1$. The gradient coefficient values are (a) $(\tilde{\kappa}_{aa}, \tilde{\kappa}_{ab}, \tilde{\kappa}_{bb}) = (0, 0, 0)$ and (b) $(\tilde{\kappa}_{aa}, \tilde{\kappa}_{ab}, \tilde{\kappa}_{bb}) = (0.1, 0.032, 0.1)$. In particular, (a, b) depict the compositional pathways through the ternary diagram. The blue line in them is the solubility curve, and the dotted line joins the two initial compositions, marked by a white circle. To ease visualisation, the last recorded profile has been plotted in white.

The pathway in this case is not fully linear, as Fickian diffusion would indicate, because the form of the flux employed in this work—defined by Petrischeva and Abart [121]—does not reduce exactly to Fick's law. Nonetheless, the trajectories are still considerably more linear than they are when there interactions between the API and the antisolvent are nonideal.

Figure F.5 presents the composition evolution through the phase diagram (a) and in space (b) of a system in which a solution of 55% API and 45% solvent is mixed with pure antisolvent.

It was considered that $A = 3$ and that $\beta\mu_1^{\circ,(S)} - \beta\mu_1^{\circ,(L)}$; the interfacial free energy coefficients had values of $(\kappa_{aa}, \kappa_{ab}, \kappa_{bb}) = (0.05, 0.016, 0.05)$.

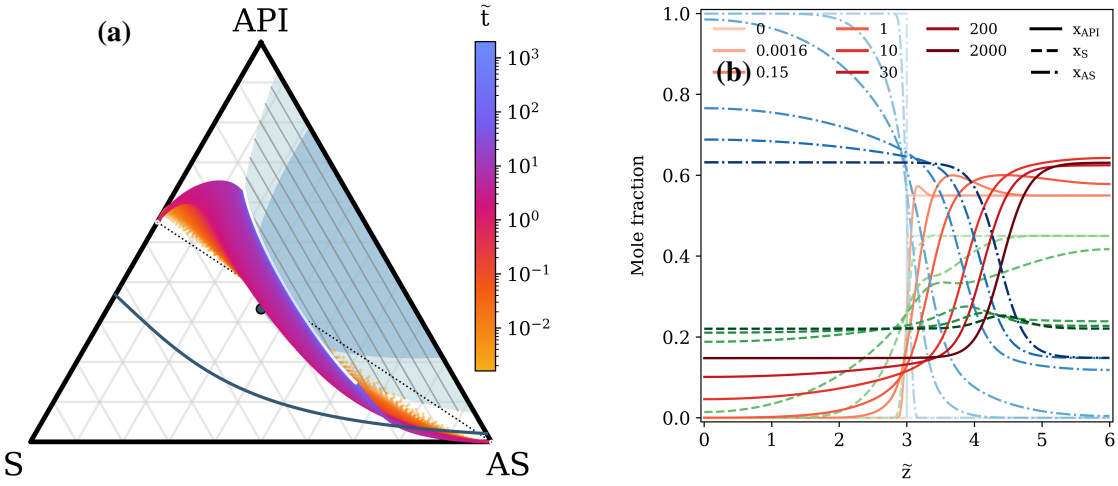


FIGURE F.5: Evolution of the composition with time in a system mixing pure antisolvent with a 45% API solution, considering that $A = 3$ and $\beta\mu_1^{\circ,(S)} - \beta\mu_1^{\circ,(L)} = -1$. The gradient coefficient values are $(\tilde{\kappa}_{aa}, \tilde{\kappa}_{ab}, \tilde{\kappa}_{bb}) = (0.05, 0.016, 0.05)$. In particular, (a) depicts the compositional pathways through the ternary diagram. The blue line in them is the solubility curve, and the dotted line joins the two initial compositions, marked by a white circle. To ease visualisation, the last recorded profile has been plotted in white. (b) Spatial evolution of the composition profile.

Figure F.6(a) presents the composition evolution through the ternary diagram of a system in which a stream of 45/55% API/solvent is mixed with a solution of 80/20% antisolvent/solvent. In it, $A = 3$, and $\beta\mu_1^{\circ,(S)} - \beta\mu_1^{\circ,(L)} = -1$. Two sets of values of the gradient free energy coefficient have been tested: (a) $(\kappa_{aa}, \kappa_{ab}, \kappa_{bb}) = (0, 0, 0)$, and (b) $(\kappa_{aa}, \kappa_{ab}, \kappa_{bb}) = (0.1, 0.032, 0.1)$. Its purpose was to assert the dilution of the antisolvent stream with solvent as an effective means of reducing the possibility of phase separation, which these results prove it is.

Lastly, Figure F.7 presents the composition evolution through the ternary diagram of a system in which a solution of 25/75% API/solvent is mixed with a stream of pure antisolvent. In it, $A = 3$, and $\beta\mu_1^{\circ,(S)} - \beta\mu_1^{\circ,(L)} = -1$. Two sets of values of the gradient free energy coefficient have been tested: (a) $(\kappa_{aa}, \kappa_{ab}, \kappa_{bb}) = (0, 0, 0)$, and (b) $(\kappa_{aa}, \kappa_{ab}, \kappa_{bb}) = (0.1, 0.032, 0.1)$.

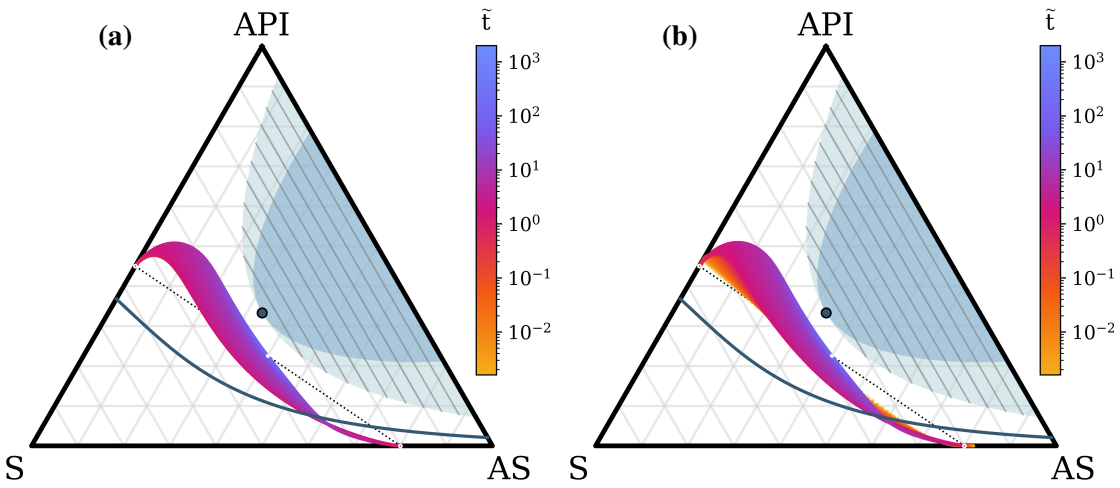


FIGURE F.6: Evolution of the composition with time in a system mixing a 45% API solution with a solution of 80/20% antisolvent/solvent, considering that $A = 3$ and $\beta\mu_1^{\circ,(S)} - \beta\mu_1^{\circ,(L)} = -1$. The gradient coefficient values are (a) $(\tilde{\kappa}_{aa}, \tilde{\kappa}_{ab}, \tilde{\kappa}_{bb}) = (0,0,0)$ and (b) $(\tilde{\kappa}_{aa}, \tilde{\kappa}_{ab}, \tilde{\kappa}_{bb}) = (0.1, 0.032, 0.1)$. The blue line in them is the solubility curve, and the dotted line joins the two initial compositions, marked by a white circle. To ease visualisation, the last recorded profile has been plotted in white.

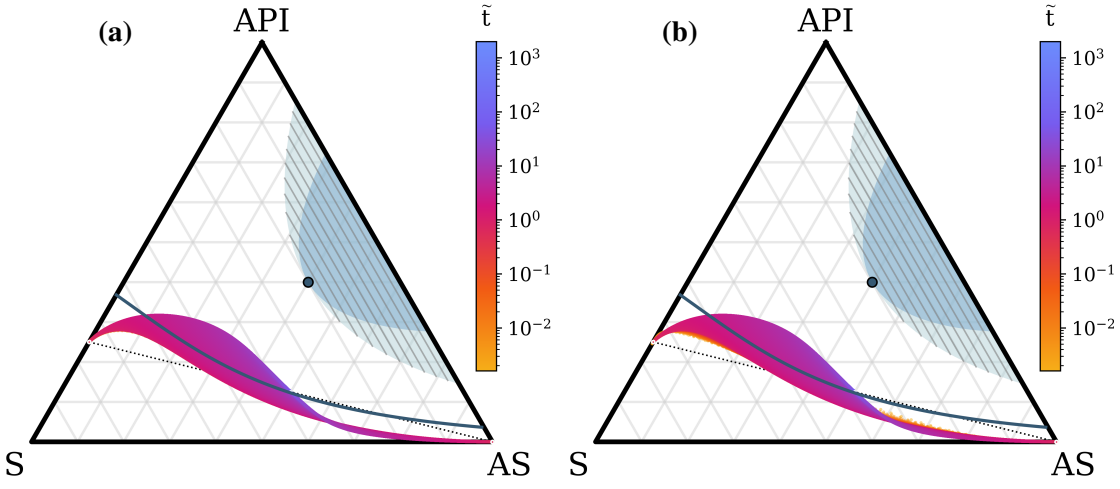


FIGURE F.7: Evolution of the composition with time in a system mixing a 25/75% API/solvent solution with a stream of pure antisolvent, considering that $A = 2.5$ and $\beta\mu_1^{\circ,(S)} - \beta\mu_1^{\circ,(L)} = -1$. The gradient coefficient values are (a) $(\tilde{\kappa}_{aa}, \tilde{\kappa}_{ab}, \tilde{\kappa}_{bb}) = (0,0,0)$ and (b) $(\tilde{\kappa}_{aa}, \tilde{\kappa}_{ab}, \tilde{\kappa}_{bb}) = (0.025, 0.008, 0.025)$. The blue line in them is the solubility curve, and the dotted line joins the two initial compositions, marked by a white circle. To ease visualisation, the last recorded profile has been plotted in white.